

The Hamlyn Symposium on Medical Robotics

2023

IMMERSIVE TECH: THE FUTURE OF MEDICINE



Proceedings

26 - 29th June 2023

Salzitsa Anastasova-Ivanova, Ana Cruz Ruiz, Daniel Elson, Stamatia Giannarou, George Mylonas, Ferdinando Rodriguez y Baena, Alexander Thompson (Editors)

Proceedings of the 15th

Hamlyn Symposium on Medical Robotics

2023

Imperial College London,
London, United Kingdom
26th- 29th June, 2023

Published by:

The Hamlyn Centre, Imperial College London
E- Print, London, United Kingdom — June 2023
<https://www.imperial.ac.uk/hamlyn-centre/>
ISSN 2755-0036

Preface

We are delighted to have hosted the 15th [Hamlyn Symposium on Medical Robotics](#) led by Professor the Lord Ara Darzi, who holds the Paul Hamlyn Chair of Surgery at Imperial College London, the Royal Marsden Hospital and the Institute of Cancer Research, London and Professor Ferdinando Rodriguez y Baena, Professor of Medical Robotics in the Department of Mechanical Engineering at Imperial College, and Co-Director of the Hamlyn Centre.

This year's symposium was held at the Royal Geographical Society on the 26th to 29th June 2023. The theme of the meeting was "Immersive Tech: The Future of Medicine", and covered several topics including bioinspired robots, wearable robots, virtual/augmented reality, imaging/navigation, smart devices, all with a strong focus on clinical translation challenges. The event was supported by world-renowned international programme committee, who ensured a timely and robust peer review of the submitted papers. Out of the 111 papers submitted, 79 were selected either as oral or poster presentations.

We were delighted to have distinguished keynote speakers from the USA, UK, and Hong Kong. We were honoured to have two keynotes on the first day of the symposium, the first by Dr Timothy Ferris, NHS National Director of Transformation and previously, non-executive director of NHS Improvement, who is internationally renowned for his pioneering work on improving health and care in both hospital and community settings. We were equally delighted to feature a keynote talk by Professor Esther Rodriguez-Villegas, an academic and an entrepreneur, who is founder of two active life-sciences companies, Acurable and TainiTec. Acurable focuses on creating and commercialising disruptive wearable medical devices to facilitate and improve the diagnosis and management of chronic cardiovascular conditions, among which, the first wearable medical device to have been granted the CE-mark for fully automatic diagnosis of Obstructive Sleep Apnoea (OSA). TainiTec develops and commercialises the, currently, smallest preclinical wireless neural recording systems on the market.

The second day of the symposium featured two more keynote talks by prominent academics in their field: the first by Professor Allison Okamura, who is professor in the Mechanical Engineering Department at Stanford University, with a courtesy appointment in Computer Science. She is currently the Editor-in-Chief of the journal IEEE Robotics and Automation Letters. She has been an Associate Editor of the IEEE Transactions on Haptics, Editor-in-Chief of the IEEE International Conference on Robotics and Automation Editorial Board, an editor of the International Journal of Robotics Research, and co-chair of the IEEE Haptics Symposium. Lastly, we were delighted to close the symposium with our final keynote speaker, Professor Philip Chiu, who is Professor of the Division of Upper GI and Metabolic Surgery, Department of Surgery, Director of the Multi-Scale Medical Robotics Centre, Director of the Endoscopy Centre, Institute of Digestive Disease, Director of the CUHK Jockey Club Minimal Invasive Surgical Skills Centre, Director of the CUHK Chow Yuk Ho Technology Centre for Innovative Medicine, and Associate Dean (External Affairs), Faculty of Medicine, all within the Chinese University of Hong Kong.

During this year's Industry Forum, we had the opportunity to engage subject experts in a lively discussion on '*Harnessing the potential of digital surgery: challenges and opportunities*'. The healthcare industry is responsible for generating over 30% of the world's data volume and, with an

expected compound annual growth rate of 36% by 2025, effective management and analysis of this massive amount of data is crucial. We were incredibly excited to have the following speakers on the panel:

- Kevin Jarrold, Chief Information Officer at Imperial College Healthcare NHS Trust
- Shan Jegatheeswaran, Head of MedTech Digital for Johnson and Johnson
- Matthew Howard, International Lead, Public Sector Healthcare Data Science & AI, Amazon Web Services
- Clíodhna Ní Ghuidhir, Principal Scientific Adviser for AI, NICE
- Rich Mahoney, Vice President Research, Intuitive Surgical
- Alex Maret, Vice President, Robotics & Digital Surgery at Cambridge Consultants
- George Murgatroyd, Vice President, Digital Technologies, Medtronic

The panel was moderated by James Kinross, Senior Lecturer at Imperial College and Consultant in Colorectal Surgery, and Ferdinando Rodriguez y Baena.

This year we also featured a Clinical Forum centred on the *complexities associated to the clinical translation of robotic technology*. During this Forum, we had the opportunity to engage clinical and engineering experts in a lively discussion about the challenges and opportunities of translating medical robots by exploring questions such as:

- How could biomedical engineering and clinical sciences work together to enable effective translation?
- How could a quality management system support translation?
- How do we tackle patient interest and acceptance?
- Who should pay for novel technologies?
- How to deal with regulatory approval, clinical trials, and reimbursement?

Our esteemed panellists were leaders in their field:

1. Arianna Menciassi, BME, Sant'Anna School of Advanced Studies, Italy
2. William Anderson, Neurosurgeon, John's Hopkins University, USA
3. Mark Slack, Gynaecologist, Chief Medical Officer of CMR Surgical, UK
4. Kevin Cleary, Technical Director, Bioengineering Initiative, Childrens National Medical Centre, USA
5. Gernot Kronreif, Chief Scientific Officer, ACMIT GmbH, Austria

The panel was moderated by Professor Andreas Melzer, MD DDS, ICCAS University Leipzig and IMSaT University Dundee.

We were delighted to see that the affiliated workshops to the Symposium have continued to grow and flourish, with many of them organised by early career researchers. A total of 12 workshops were organised and they covered the areas of: soft robotics for endoscopy, micro nano robotics, robotic systems for surgery training, computer assisted interventions, robotic awareness and autonomy in surgery and open-source software for surgical technologies. We continued to receive CPD accreditation for these workshops from the Royal College of Surgeons and we are proud to deliver a programme that enables to continued professional development of clinicians and engineers in these fields. A detailed programme of the workshops is listed on our [website](#). We believe these workshops

have played a crucial role in providing a platform for the formulation of new ideas and future collaborations.

One of our continued highlights of the Symposium was the Surgical Robot Challenge, which encourages researchers to push their technologies a little further than writing journals and conference papers allows, and more importantly, share those developments with the community to help test out novel ideas and help steer trends in the wider surgical robotic community. This year we had 9 finalist teams, from all around the world including Italy, China, USA, United Kingdom, and others.

The challenge was sponsored by Intuitive Surgical, Cambridge Consultants and the Wellcome Trust. We were grateful for the sponsorship we received and to our esteem judges, Robert Merrifield, from Imperial College London (and founder of the challenge in 2015), Riccardo Secoli, from Cambridge Consultants and Rich Mahoney, from Intuitive Surgical.

We showcased the entries at the Hamlyn Symposium via a highlights video and announced the winners at the award ceremony. All entries can be also viewed on our Hamlyn Symposium [website](#) and [YouTube](#) channel, where a digital recording of the award ceremony is also accessible.

Organising an international meeting of this scale involves a huge amount of effort and requires a dedicated team. We would like to thank the International Programme Committee for dedicating their valuable time to ensure timely review of the submitted papers and to the Workshop Organisers who, through joint effort, helped put together an excellent symposium programme. We are grateful to all our sponsors and exhibitors for supporting the Symposium and affiliated Workshops. Special thanks go to the Royal College of Surgeons of England for arranging CPD accreditation of the Symposium workshops.

Finally, we would like to take this opportunity to express our gratitude to the Hamlyn Centre team who have worked so hard behind the scenes, managing all aspects of the Symposium organisation, from programme preparation and publicity to registration and logistics. In particular, we would like to thank, Alia Talaat Ahmed, Salzitsa Anastasova-Ivanova, Nazia Bharde, Ana Cruz Ruiz, Marianne Knight, and Robert Merrifield, as well as all of the Hamlyn Centre, especially our many volunteers, who have helped to make the Symposium a great success. Lastly, special thanks go to Lady Hamlyn. None of this would be possible without the generous philanthropic support from both the Helen Hamlyn Trust and Lady Hamlyn herself. It remains a great honour and privilege to have had the opportunity to establish, develop and lead the Hamlyn Centre to its current internationally recognised status, supported by so many talented researchers.

Professor The Lord Ara Darzi and Professor Ferdinando Rodriguez y Baena
Co-Chairs, Programme Committee
Hamlyn Symposium on Medical Robotics 2023

Organisation

Co-Chairs

Professor The Lord Darzi of Denham
Professor Ferdinando Rodriguez y Baena

Programme Committee

Ferdinando Rodriguez y Baena (Chair) Imperial College London, UK
William Anderson John Hopkins Medicine, USA
Christos Bergeles King's College London, UK
Darwin Caldwell Instituto Italiano di Tecnologia, Italy
Philip Chiu The Chinese University of Hong Kong, China
Howie Choset Carnegie Mellon University, USA
Kevin Cleary Children's National Hospital, USA
Dana Damian The University of Sheffield, UK
Brian Davies Imperial College London, UK
Elena De Momi Politecnico di Milano, Italy
Simon DiMaio Intuitive Surgical Inc, USA
Sanja Dogramadzi University of Sheffield, UK
Pierre DuPont Harvard University, USA
Leonard Fass Imperial College London, UK
Gabor Fichtinge Queen's University, Canada
Fanny Ficuciello University of Naples Federico II, Italy
Paolo Fiorini University of Verona, Italy
Kanako Harada University of Tokyo, Japan
S. Duke Herrell Vanderbilt University, USA
Jaesung Hong DGIST, South Korea
Pierre Jannin INSERM, France
Branko Jaramaz Blue Belt Technologies, USA
Leo Joskowicz Hebrew University of Jerusalem, Israel
Peter Kazanzides Johns Hopkins University, USA
James Kinross Imperial College London, UK
Gernot Kronreif ACMIT, Austria
Daniel Leff Imperial College London, UK
Thomas Looi Sick Kids Toronto, Canada
Leonardo Mattos Istituto Italiano di Tecnologia, Italy
Andreas Melzer University Dundee, UK
Arianna Menciassi Scuola Superiore Sant'Anna, Italy
Marcia O' Malley Rice University, USA
Nisha Patel Imperial College London, UK
Rajni Patel Western University, Canada
Kawal Rhode King's College London, UK
Cameron Riviere Carnegie Mellon University, USA
Ichiro Sakuma University of Tokyo, Japan
Simone Schuerle ETH Zurich, Switzerland
Riccardo Secoli Cambridge Consultants, UK
Bruno Siciliano University of Naples Federico II, Italy
Stefanie Speidel National Center for Tumor Diseases, Germany
Danail Stoyanov University College London, UK
Amir Szold Assia Medical Group, Israel
Russell Taylor Johns Hopkins University, USA

Pietro Valdastri University of Leeds, UK
Bob Webster Vanderbilt University, USA
Helge Wurdemann University College London, UK

Additional Reviewers

Catherine Abraham	Junlei Hu	Nikita Murasovs
Nishanth Arun	Sajjad Hussain	Ravi Naik
Muhammad Adeel Azam	Antonella Imperato	Wang Ning
Ananya Bal	Jayender Jagadeesan	Filipe Pedrosa
Sophia Bano	Laszlo Jaksa	Veronica Penza
Yilin Cai	Edward Johns	Giovanni Pittiglio
Marco Caianiello	Lianne Johnson	Hadi Sadati
Lin Cao	Dominic Jones	Mohammad Salehizadeh
Kai Fung Chan	Shane King	Mohamed Sallam
Sara Condino	Maria Koskinopoulou	Fan Shao
Laura Connolly	Zaneta Koszowska	Azadeh Shariati
Remi Delaunay	Shunlei Li	Jialei Shi
Michele Di Lecce	Zheng Li	Jason Shrand
Tayfun Efe Ertop	Lukas Lindenroth	Avinash Kumar Singh
Navid Feizi	Peter Lloyd	Edoardo Sinibaldi
Martina Finocchiaro	Erin Mahan	Zeyu Song
Enrico Franco	Luigi Manfredi	Agostino Stilli
Bhoomika Gandhi	Nils Marahrens	Izadyar Tamadon
Gautam Gare	Andrea Mariani	Fabio Tatti
Arnaud Garriga Casanovas	Evangelos Mazomenos	Damith Vithanage
Bruno Gil	Aoife McDonald-Bowyer	Yaxi Wang
Nikita Greenidge	Rocco Moccia	Zicong Wu
Vincent Groenhuis	Sara Moccia	Hon Chi Yip
Ajay Gunalan	Hasan Dad Ansari Mohammad	
Rebecca Hissey	Konstantinos Mountris	

Local Organising Team

Salzitsa Anastasova-Ivanova
Nazia Bharde
Ana Cruz Ruiz
Dan Elson
Stamatia Giannarou
James Kinross
Marianne Knight
Robert Merrifield
George Mylonas
Alia Talaat
Alexander Thompson

Table of Contents

Tuesday, June 27th

Session 1: Navigation

1 SLAM-based Surgical Guidance For Breast Reconstruction Surgery

Elise Fu (Brigham and Women's Hospital, Harvard Medical School, US)
Ángela Alarcón de la Lastra (Brigham and Women's Hospital, Harvard Medical School, US)
Haoyin Zhou (Brigham and Women's Hospital, Harvard Medical School, US)
Ruisi Zhang (Brigham and Women's Hospital, Harvard Medical School, US)
Justin Broyles (Brigham and Women's Hospital, Harvard Medical School, US)
Haripriya Ayyala (Yale Medical School, US)
Bohdan Pomahac (Yale Medical School, US)
Jagadeesan Jayender (Brigham and Women's Hospital, Harvard Medical School, US)

3 SLAM-based Trackerless Navigation System for Lateral Skull base Surgery: A Pilot Cadaver Study

Haoyin Zhou (Brigham and Women's Hospital, US)
Ryan Bartholomew (Brigham and Women's Hospital; Massachusetts Eye and Ear Infirmary, US)
Maud Boreel (Brigham and Women's Hospital; Massachusetts Eye and Ear Infirmary, US)
Alejandro Garcia (Brigham and Women's Hospital; Massachusetts Eye and Ear Infirmary, US)
Krish Suresh (Brigham and Women's Hospital; Massachusetts Eye and Ear Infirmary, US)
Saksham Gupta (Brigham and Women's Hospital, US)
Jeffrey Guenette (Brigham and Women's Hospital, US)
Daniel Lee (Massachusetts Eye and Ear Infirmary, US)
C. Eduardo Corrales (Brigham and Women's Hospital, US)
Jayender Jagadeesan (Harvard University, US)

5 dvrk-Based Teleoperation of a CTR Robot with Stereovision Feedback for Neurosurgery

Changyan He (The Hospital for Sick Children, Canada)
Robert Nguyen (The Hospital for Sick Children, Canada)
Eric Diller (University of Toronto, Canada)
James Drake (The Hospital for Sick Children, Canada)
Thomas Looi (The Hospital for Sick Children, Canada)

7 Proof of Concept Implementation of Forbidden Region Dynamic Active Constraints in Minimally Invasive Surgery

Zejian Cui (Imperial College London, UK)
Ferdinando Rodriguez Y Baena (Imperial College London, UK)

9

How Insights from In Vivo Human Pilot Studies with da Vinci Image Guidance are Informing Next Generation System Design

Piper Cannon (Vanderbilt University, US)

Shaan Setia (Vanderbilt University Medical Center, US)

Nicholas Kavoussi (Vanderbilt University Medical Center, US)

S. Duke Herrell (Vanderbilt University Medical Center, US)

Robert Webster (Vanderbilt University, US)

Session 2: Robotic Systems & Devices

11

MRI-Guided Robotic Prostate Biopsy

Haipeng Liang (Queen Mary University of London, UK)

Wanli Zuo (Ningbo University, China)

Dimitri Kessler (University of Cambridge, UK)

Tristan Barrett (University of Cambridge, UK)

Zion Tsz Ho Tse (Queen Mary University of London, UK)

13

Toward Robotic Craniosynostosis Surgery: Development of a Novel Articulated Minimally Invasive Bone Cutting Tool

Jones Law (The University of Toronto, Canada)

Dale Podolsky (The University of Toronto, Canada)

15

Robotic Assistant for Image-Guided Treatment of Ankle Joint Dislocations: A Feasibility Study

Gang Li (Children's National Hospital, US)

Rohan Vijayan (Johns Hopkins University, US)

Ali Uneri (Johns Hopkins University, US)

Babar Shafiq (Johns Hopkins Medicine, US)

Jeffrey Siewersdseen (The University of Texas MD Anderson Cancer Center, US)

Kevin Cleary (Children's National Hospital, US)

17

Towards Cellular Level Microsurgery: Design And Testing Of A High Presision Delta Robot For Medical Applications

Xiaoyu Huang (Robotics and Mechatronics Systems Research Centre, School of Engineering and Informatics, University of Sussex, UK)

Elizabeth Rendon-Morales (Robotics and Mechatronics Systems Research Centre, School of Engineering and Informatics, University of Sussex, UK)

Rodrigo Aviles-Espinosa (Robotics and Mechatronics Systems Research Centre, School of Engineering and Informatics, University of Sussex, UK)

19

Computational Analysis of Design Parameters for a Bimanual Concentric Push-Pull Robot

Tony Qin (University of North Carolina at Chapel Hill, US)

Peter Connor (Vanderbilt University, US)

Khoa Dang (University of Tennessee, Knoxville, US)

Ron Alterovitz (University of North Carolina at Chapel Hill, US)

Robert Webster (Vanderbilt University, US)

Caleb Rucker (University of Tennessee, Knoxville, US)

Session 3: Surgical Needles & Catheters

21 **Toward Multiple-Point Stiffness Changing Surgical Needle for Eye Surgery Robotic System**

Rongwan Chen (Chonnam National University, South Korea)
Seong Young Ko (Chonnam National University, South Korea)

23 **Ultrasonically-Lubricated Catheters: A Proof of Concept**

Mostafa A. Atalla (Delft University of Technology, Netherlands)
Jeroen J. Tuijp (Delft University of Technology, Netherlands)
Michaël Wiertlewski (Delft University of Technology, Netherlands)
Aimée Sakes (Delft University of Technology, Netherlands)

25 **Augmented Reality-assisted Epidural Needle Insertion: User Experience and Performance**

Negar Kazemipour (CONCORDIA University, Canada)
Amir Sayadi (McGill University, Canada)
Renzo Cecere (McGill University, Canada)
Jake Barralet (McGill University, Canada)
Amir Hooshiar (McGill University, Canada)

27 **Workspace Characterization for Hybrid Tendon and Ball Chain Continuum Robots**

Giovanni Pittiglio (Boston Children's Hospital - Harvard Medical School, US)
Margherita Mencatelli (Boston Children's Hospital - Harvard Medical School, US)
Abdulhamit Dondur (Boston Children's Hospital - Harvard Medical School, US)
Yash Chitalia (University of Louisville, US)
Pierre E. Dupont (Boston Children's Hospital - Harvard Medical School, US)

29 **A Comparison of the Workspace and Dexterity of Hybrid Concentric Tube Robot and Notched Wrist Systems**

Paul H. Kang (University of Toronto, Canada)
Robert H. Nguyen (The Hospital for Sick Children, Canada)
Thomas Looi (The Hospital for Sick Children, Canada)
James Drake (The Hospital for Sick Children, Canada)

Poster Teasers 1

31 **Design and Control of a Tele-operated Soft Instrument in Minimally Invasive Surgery**

Jialei Shi (University College London, UK)
Helge Wurdemann (University College London, UK)

33 **A Deep Learning Model for Tip Force Estimation on Steerable Catheters Via Learning-From-Simulation**

Majid Roshanfar (Concordia University, Canada)
Pedram Fekri (Concordia University, Canada)
Javad Dargahi (Concordia University, Canada)

35 DEBI: A New Mechanical Device for Safer Needle Insertions

Ayhan Aktas (Imperial College London, UK)
Enrico Franco (Imperial College London, UK)

37 Valvuloplasty Balloon Catheter Sizing Approach for Calcified Aortic Valve with Different Annulus Ratios

Junke Yao (University College London, China)
Giorgia Bosi (Department of Mechanical Engineering, University College London, UK)
Gaetano Burriesci (University College London, UK)
Helge Wurdemann (University College London, UK)

39 Implementation of a Novel Handheld Endoscopic Operation Platform (EndoGRASP)

Chun Ping Lam (The Chinese University of Hong Kong, Hong Kong)
Ming Ho Ho (Multi-scale Medical Robotics Center, Hong Kong)
Shi Pan Siu (Multi-scale Medical Robotics Center, Hong Kong)
Ka Chun Lau (Multi-scale Medical Robotics Center, Hong Kong)
Yeung Yam (The Chinese University of Hong Kong, Hong Kong)
Philip Wai Yan Chiu (The Chinese University of Hong Kong, Hong Kong)

41 Magnetic Anchored and Cable Driven Endoscope for Minimally Invasive Surgery

Jixiu Li (The Chinese University of Hong Kong, Hong Kong)
Tao Zhang (Multi-scale Medical Robotics Center (MRC), Hong Kong)
Truman Cheng (Multi-scale Medical Robotics Center (MRC), Hong Kong)
Calvin Sze Hang Ng (The Chinese University of Hong Kong and Multi-scale Medical Robotics Center (MRC), Hong Kong)
Philip Wai Yan Chiu (The Chinese University of Hong Kong and Multi-scale Medical Robotics Center (MRC), Hong Kong)
Zheng Li (The Chinese University of Hong Kong and Multi-scale Medical Robotics Center (MRC), Hong Kong)

43 SciKit-Surgery for Augmented Reality Surgery Research

Stephen Thompson (UCL, UK)
Miquel Xochicale (UCL, UK)
Thomas Dowrick (UCL, UK)
Matthew Clarkson (UCL, UK)

45 Flexible Magnetic Soft Stent for Mobile Flow Diversion

Tianlu Wang (Max Planck Institute for Intelligent Systems, Germany)
Metin Sitti (Max Planck Institute for Intelligent Systems, Germany)

47

A Novel Stereoscopic Thermal Endoscope for Tissue Damage Prevention

Dumitru Scutelnic (University of Verona, Italy)
Giacomo De Rossi (University of Verona, Italy)
Nicola Piccinelli (University of Verona, Italy)
Claudia Daffara (University of Verona, Italy)
Salvatore Siracusano (University of L'Aquila, Italy)
Riccardo Muradore (University of Verona, Italy)

49

Augmented Reality-Based Surgical Guidance for Anterior and Posterior Cruciate Ligament Reconstruction

Deokgi Jeung (Department of Robotics and Mechatronics Engineering, DGIST, South Korea)
Hyun-Joo Lee (Department of Orthopaedic Surgery, Kyungpook National University Hospital, South Korea)
Hee-June Kim (Department of Orthopaedic Surgery, Kyungpook National University Hospital, South Korea)
Jaesung Hong (Department of Robotics and Mechatronics Engineering, DGIST, South Korea)

51

Meshless Modelling for Heat-based Robotic Navigation of Radio Frequency Catheter Ablation

Konstantinos Mountris (Mechanical Engineering Dept., University College London, UK)
Richard Schilling (Barts Heart Centre, St Bartholomew's Hospital, UK)
Alicia Casals (Research Center for Biomedical Engineering, Universitat Politècnica de Catalunya, Spain)
Helge Wurdemann (Mechanical Engineering Dept., University College London, UK)

53

Computer-Based Assessment of The Operator's Experience in Obstetric Ultrasound Examination Based on Hand Movements and Applied Forces

Veronica Penza (Istituto Italiano di Tecnologia, Italy)
Andrea Santangelo (Istituto Italiano di Tecnologia, Italy)
Dario Paladini (Istituto Giannina Gaslini, IRCCS, Italy)
Leonardo S. Mattos (Istituto Italiano di Tecnologia, Italy)

55

Dual Robot System for Autonomous Needle Insertion into Deep Vessels

Lorenzo Civati (Advanced Robotics, Istituto Italiano di Tecnologia (IIT), Italy)
Maria Koskinopoulou (Advanced Robotics, Istituto Italiano di Tecnologia (IIT), Italy)
Andrea Santangelo (Advanced Robotics, Istituto Italiano di Tecnologia (IIT), Italy)
Leonardo S. Mattos (Advanced Robotics, Istituto Italiano di Tecnologia (IIT), Italy)

57

Design of a Flexible Bone Drill Using a Hydraulic Pressure Wave

Esther P. de Kater (TU Delft, Netherlands)

Tjalling G. Kaptijn (TU Delft, Netherlands)

Aimée Sakes (TU Delft, Netherlands) *Paul Breedveld* (TU Delft, Netherlands)

59

Toward a Millimeter-Scale Tendon-Driven Continuum Wrist with Integrated Gripper for Microsurgical Applications

Alexandra Leavitt (Robotics Center and Kahlert School of Computing, University of Utah, US)

Ryan Lam (Robotics Center and Kahlert School of Computing, University of Utah, US)

Nichols Crawford Taylor (Robotics Center and Kahlert School of Computing, University of Utah, US)

Daniel S. Drew (Robotics Center and Department of Electrical and Computer Engineering, University of Utah, US)

Alan Kuntz (Robotics Center and Kahlert School of Computing, University of Utah, US)

61

Extracting Unusual Movements during Robotic Surgical Tasks: A Semi-Supervised Learning Approach

Yi Zheng (University of Texas at Austin, United States)

Ann Majewicz-Fey (University of Texas at Austin, United States)

63

Evolutionary Deep Learning Using Hybrid EEG-Fnirs-ECG Signals to Cognitive Workload Classification in Laparoscopic Surgeries *Adrian*

Rubio Solis (Imperial College London, UK)

Kaizhe Jin (Imperial College London, UK)

Ravi Naik (Imperial College London, UK)

George Mylonas (Imperial College London, UK)

65

WaveLeNet: Transfer Neural Calibration for Embedded Sensing in Soft Robots

Navid Masoumi (CONCORDIA University, Canada)

Negar Kazemipour (CONCORDIA University, Canada)

Sarvin Ghiasi (McGill University, Canada)

Tannaz Torkaman (CONCORDIA University, Canada)

Amir Sayadi (McGill University, Canada)

Javad Darqahi (CONCORDIA University, Canada)

Amir Hooshair (McGill University, Canada)

Session 4: Machine Learning Approaches for Healthcare

67

SimPS-Net: Simultaneous Pose & Segmentation Network of Surgical Tools

Spyridon Soukas (Imperial College London, UK)

Anh Nguyen (University of Liverpool, UK)

Stephen Laws (Imperial College London, UK)

Brian Davies (Imperial College London, UK)
Ferdinando Rodriguez Y Baena (Imperial College London, UK)

69 Deep Imitation Learning for Automated Drop-In Gamma Probe Manipulation

Kaizhong Deng (The Hamlyn Centre for Robotic Surgery, Imperial College London, UK)
Baoru Huang (The Hamlyn Centre for Robotic Surgery, Imperial College London, UK)
Daniel S. Elson (The Hamlyn Centre for Robotic Surgery, Imperial College London, UK)

71 Enhancing Fluoroscopy-Guided Interventions: a Neural Network to Predict Vessel Deformation without Contrast Agents

François Lecomte (Inria, France)
Valentina Scarponi (Inria, France)
Pablo Alvarez (Inria, France)
Juan Verde (IHU Strasbourg, France)
Jean-Louis Dillenseger (Univ Rennes, France)
Eric Vibert (Paul Brousse Hospital, Paris, France)
Stéphane Cotin (Inria, France)

73 Comparison of Denoising Methods for Synthetic Low-Field Neurological MRI

Anthony O'Brien (Imperial College London, UK)
Ferdinando M Rodriguez Y Baena (Imperial College London, UK)

75 Learning Robotic Ultrasound through Coaching

Mythra Balakuntala (Purdue University, US)
Deepak Raina (Purdue University, US)
Juan Wachs (Purdue University, US)
Richard Voyles (Purdue University, US)

Wednesday, June 28th

Session 5: Simulation & Training

77 Global Versus Local Kinematic Skills Assessment on Robotic Assisted Hysterectomies

Arnaud Huaulm   (Univ Rennes,INSERM, LTSI - UMR 1099, France)

Krystel Nyangoh Timoh (Department of Obstetrics and Gynecology, Rennes University Hospital, Rennes, France, France)

Victor Jan (Univ Rennes,INSERM, LTSI - UMR 1099, France)

Sonia Guerin (Department of Obstetrics and Gynecology, Rennes University Hospital, Rennes, France, France)

Pierre Jannin (Univ Rennes,INSERM, LTSI - UMR 1099, France)

79 Using LOR Syringe Probes as a Method to Reduce Errors in Epidural Analgesia - a Robotic Simulation Study

Nitsan Davidor (Ben-Gurion University of the Negev, Israel)

Yair Binyamin (Soroka Medical Center, Israel)

Tamar Hayuni (Soroka Medical Center, Israel)

Ilana Nisky (Ben-Gurion University of the Negev, Israel)

81 Design of an Ex-Vivo Experimental Setup for Spine Surgery Based on in-Vivo Identification of Respiration-induced Spine Movement

Elie Saghbiny (Armand-Trousseau Hospital, Paris, France; Sorbonne Universit  , CNRS UMR 7222, INSERM U1150, ISIR, France)

Saman Vafadar (Sorbonne Universit  , CNRS UMR 7222, INSERM U1150, ISIR, France)

Antoine Harl   (Sorbonne Universit  , CNRS UMR 7222, INSERM U1150, ISIR, France)

Guillaume Morel (Sorbonne Universit  , CNRS UMR 7222, INSERM U1150, ISIR, France)

83 Towards a Robotic Minimally Invasive Surgery Assessment and Augmentation Platform for Visual-Haptic Acuity Development

Sergio Machaca (Johns Hopkins University, US)

Jeremy D. Brown (Johns Hopkins University, US)

85 Integrating a Real-time Surgical Robot Dynamic Simulator with 3D Slicer

Hongyi Fan (Johns Hopkins University, US)

Adnan Munawar (Johns Hopkins University, US)

Manish Sahu (Johns Hopkins University, US)

Russell Taylor (Johns Hopkins University, US)

Peter Kazanzides (Johns Hopkins University, US)

Session 6: Soft Robotics

87 A Soft Continuum Robot with Multi-Modal Shape and Contact Force Sensing for Minimally Invasive Surgery

Max McCandless (Boston University, US)
Frank Julia Wise (Boston University, US)
Sheila Russo (Boston University, US)

89 Soft Artificial Bladder with Volume Monitoring Capabilities

Federica Semproni (Scuola Superiore Sant'Anna, Pisa, Italy)
Veronica Iacovacci (Scuola Superiore Sant'Anna, Pisa, Italy)
Sabina Maglio (Scuola Superiore Sant'Anna, Pisa, Italy)
Simone Onorati (Scuola Superiore Sant'Anna, Pisa, Italy)
Michele Ibrahim (Scuola Superiore Sant'Anna, Pisa, Italy)
Arianna Menciassi (Scuola Superiore Sant'Anna, Pisa, Italy)

91 A Fluidic Actuated Soft Robot for Improving Bronchoscopic Biopsy

Daniel Van Lewen (Boston University, US)
Taylor Janke (Boston University, US)
Harin Lee (Boston University, US)
Ryan Austin (Boston University, US)
Ehab Billatos (Boston University, US)
Sheila Russo (Boston University, US)

93 Soft Robotic Pneumatic Actuators Assist Diaphragmatic Dysfunction in a Respiratory Simulator

Diego Quevedo-Moreno (Department of Mechanical Engineering, Massachusetts Institute of Technology, US)
Jonathan Tagoe (Department of Mechanical Engineering, Massachusetts Institute of Technology, US)
Ellen Roche (Department of Mechanical Engineering, Massachusetts Institute of Technology, US)

95 Computational Predictive Model for Full Body Controlled Soft Continuum Magnetic Robots under Hybrid Actuation

Kiana Abolfathi (School of Computer Science and Electronic Engineering, University of Essex, Colchester, UK)
James Chandler (School of Electronic and Electrical Engineering, University of Leeds, UK)
Keyoumars Ashkan (Department of Neurosurgery, King's College Hospital, London, UK)
Luca Citi (School of Computer Science and Electronic Engineering, University of Essex, Colchester, UK)
Pietro Valdastri (School of Electronic and Electrical Engineering, University of Leeds, UK)
Ali Kafash Hoshiar (School of Computer Science and Electronic Engineering, University of Essex, Colchester, UK)

97 A Soft Laparoscopic Grasper for Retraction of the Small Intestine

Lorenzo Kinnicutt (Boston University College of Engineering, US)
Jungjae Lee (Boston University College of Engineering, US)
Janae Oden (Boston University College of Engineering, US)
Leah Gaeta (Boston University College of Engineering, US)

Sean Carroll (Boston University College of Engineering, US)
Anushka Rathi (Boston University College of Engineering, US)
Zi Heng Lim (Boston University College of Engineering, US)
Megan Lee (Boston University College of Engineering, US)
Chisom Orakwue (Boston University College of Engineering, US)
Kevin McDonald (Boston University College of Engineering, US)
Donald Hess (Boston Medical Center, US)
Tommaso Ranzani (Boston University College of Engineering, US)

99 A Pop-Up Soft Robot Driven by Hydraulic Folded Actuators for Minimally Invasive Surgery

Jianlin Yang (College of Aerospace Engineering, Nanjing University of Aeronautics and Astronautics, China)
Mark Runciman (Hamlyn Centre, Imperial College London, UK)
James Avery (Hamlyn Centre, Imperial College London, UK)
Zhijun Sun (College of Aerospace Engineering, Nanjing University of Aeronautics and Astronautics, China)
George Mylonas (Hamlyn Centre, Imperial College London, UK)

101 Development of an Untethered Inflatable Capsule Robot for Stricture Dilation - a Preliminary Study

Kaan Esen dag (Automatic Control and Systems Engineering Department, The University of Sheffield, UK)
Mark McAlindon (Royal Hallamshire Hospital, Sheffield Teaching Hospitals NHS Foundation Trust, UK)
Daniela Rus (Computer Science and Artificial Intelligence Laboratory, Massachusetts Institute of Technology, United States)
Shuhei Miyashita (Automatic Control and Systems Engineering Department, The University of Sheffield, UK)
Dana Damian (Automatic Control and Systems Engineering Department, The University of Sheffield, UK)

103 Proof of Concept of a Novel Growing Soft Robot for Colonoscopy

Cem Tutcu (Department of Mechanical Engineering, Bogazici University, Turkey)
Seref Kemal Talas (Department of Mechanical Engineering, Bogazici University, Turkey)
Ozgur Kocaturk (Institute of Biomedical Engineering, Bogazici University, Turkey)
Nurdan Tozun (Department of Gastroenterology, Acibadem Mehmet Ali Aydinlar University School of Medicine, Turkey)
Evren Samur (Department of Mechanical Engineering, Bogazici University, Turkey)

105 Scalable and Spatially Selective Actuation of Living Microrobots

Seyed Nima Mirkhani (ETH Zurich, Switzerland)
Tinotenda Gwisai (ETH Zurich, Switzerland)
Michael G. Christiansen (ETH Zurich, Switzerland)
Simone Schuerle (ETH Zurich, Switzerland)

Poster Teasers 2

107

Real-Time Cognitive Workload States Recognition from Ultra Short-Term ECG Signals on Trainee Surgeons Using 1D Convolutional Neural Networks

Kaizhe Jin (Imperial College London, UK)
Ravi Naik (Imperial College London, UK)
Adrian Rubio Solis (Imperial College London, UK)
George Mylonas (Imperial College London, UK)

109

Priority-Based Shared Control for Peg Transfer Task

Zhaoyang Jacopo Hu (Imperial College London, UK)
Longrui Chen (Imperial College London, UK)
Yanpei Huang (Imperial College London, UK)
Etienne Burdet (Imperial College London, UK)
Ferdinando Rodriguez Y Baena (Imperial College London, UK)

111

Incident Angle Study for Designing an Endoscopic Tool for Intraoperative Brain Tumor Detection

Kent Yamamoto (Duke University, Department of Mechanical Engineering and Materials Science, US)
Tanner Zachem (Duke University, Department of Mechanical Engineering and Materials Science, US)
Weston Ross (Duke University School of Medicine, Department of Neurosurgery, US)
Patrick Codd (Duke University Department of Mechanical Engineering and Materials Science, Duke University School of Medicine, US)

113

Comparative Usability Study of Human-computer Interfaces for 3D Model Manipulation in Surgical Augmented Reality Applications

Alberto Neri (Istituto Italiano di Tecnologia, Italy)
Veronica Penza (Istituto Italiano di Tecnologia, Italy)
Leonardo S. Mattos (Istituto Italiano di Tecnologia, Italy)

115

Area-Based Total Length Estimation for Position Control in Soft Growing Robots

Korn Borvorntanajanya (Ph.D. Student, Imperial College London, UK)
Shen Treratanakulchai (Mahidol University, Thailand)
Enrico Franco (Senior Research Associate, Imperial College London, UK)
Ferdinando Rodriguez Y Baena (Professor, Imperial College London, UK)

117

A Novel Handheld Robotic System for Endoscopic Neurosurgery: A Cadaver Pilot Study

Emmanouil Dimitrakakis (Wellcome/EPSRC Centre for Surgical and Interventional Sciences (WEISS), University College London (UCL), London, UK)
George Dwyer (Wellcome/EPSRC Centre for Surgical and Interventional Sciences (WEISS), University College London (UCL), London, UK)
Nicola Newall (National Hospital for Neurology and Neurosurgery, London, UK)
Danyal Khan (National Hospital for Neurology and Neurosurgery, London, UK)

Hani Marcus (National Hospital for Neurology and Neurosurgery, London, UK)
Danail Stoyanov (Wellcome/EPSRC Centre for Surgical and Interventional Sciences (WEISS), University College London (UCL), London, UK)

119

Developing a Personalised Inflatable Rectal Obturator

Aryan Niknam Maleki (The Hamlyn Centre, Department of Surgery and Cancer, Imperial College London, London, UK)
Mark Runciman (The Hamlyn Centre, Department of Surgery and Cancer, Imperial College London, London, UK)
Alexander Thompson (The Hamlyn Centre, Department of Surgery and Cancer, Imperial College London, London, UK)
Julia Murray (The Institute of Cancer Research and Royal Marsden NHS Foundation Trust, Dept of Radiotherapy and Imaging, London, UK)
George Mylonas (The Hamlyn Centre, Department of Surgery and Cancer, Imperial College London, London, UK)

121

Feasibility of Mobile Application for Surgical Robot Teleoperation

Akhil Deo (Johns Hopkins University, US)
Peter Kazanzides (Johns Hopkins University, US)

123

An application of SlicerROS2: Haptic latency evaluation for virtual fixture guidance in breast conserving surgery

Laura Connolly (Queen's University, Canada)
Anton Deguet (Johns Hopkins University, US)
Tamas Ungi (Queen's University, Canada)
Aravind Kumar (Johns Hopkins University, US)
Andras Lasso (Queen's University, Canada)
Kyle Sunderland (Queen's University, Canada)
Axel Krieger (Johns Hopkins University, US)
Simon Leonard (Johns Hopkins University, US)
Gabor Fichtinger (Queen's University, Canada)
Parvin Mousavi (Queen's University, Canada)
Russell H. Taylor (Johns Hopkins University, US)

125

Optimizing Heart Valve Surgery with Model-Free Catheter Control

Anna Bicchi (Politecnico di Milano, Italy)
Francesca Fati (Politecnico di Milano, Italy)
Mariagrazia Fati (Politecnico di Milano, Italy)
Emiliano Votta (Politecnico di Milano, Italy)
Elena De Momi (Politecnico di Milano, Italy)

127

Percutaneous Focal Tumour Ablation Assisted by Mini-Stereotactic Frame: Proof-of-Concept

Joeana Cambranis-Romero (Western University, Canada)
Terry Peters (Western University/Robarts Research Institute, Canada)
Elvis Chen (Western University/Robarts Research Institute, Canada)

129

AI-based Agents for Automated Robotic Endovascular Guidewire Manipulation

Young-Ho Kim (Siemens Healthineers, US)
Eric Lluch (Siemens Healthineers, Germany)
Gulsun Mehmet (Siemens Healthineers, US)
Florin Ghesu (Siemens Healthineers, Germany)
Ankur Kapoor (Siemens Healthineers, US)

131 Losing Focus: Can It Be Useful in Robotic Laser Surgery?

Nicholas Pacheco (Worcester Polytechnic Institute, US)
Yash Garje (Worcester Polytechnic Institute, United US)
Aakash Rohra (Worcester Polytechnic Institute, US)
Loris Fichera (Worcester Polytechnic Institute, US)

133 Design and Evaluation of a Sealing Valve Mechanism for Stoma Patients

Maleeha Al-Hamadani (School for Biomedical Engineering and Imaging Sciences, King's College London, UK)
Carlo Seneci (School for Biomedical Engineering and Imaging Sciences, King's College London, UK)

135 Simulating Mesh Cutting with the dVRK in Unity

Kanishkan Senthilkumar (Indian Institute of Technology Madras, India)
Radian Gondokaryono (Department of Computer Science, University of Toronto, Canada)
Mustafa Haiderbhai (Department of Computer Science, University of Toronto, Canada)
Lueder Kahrs (Department of Computer Science, University of Toronto, Canada)

137 Design and Calibration of a Robot-Driven Catheter Actuation System

Navid Feizi (Western University, Canada)
Filipe C. Pedrosa (Western University, Canada)
Elaheh Arefinia (Western University, Canada)
Jagadeesan Jayender (Harvard Medical School, US)
Rajni V. Patel (Western University, Canada)

139 Handheld Concentric Tube Robot for Percutaneous Nephrolithotomy

Filipe Pedrosa (Western University, Canada)
Ruisi Zhang (Intuitive Surgical, US)
Navid Feizi (Western University, Canada)
Dianne Sacco (Massachusetts General Hospital, US)
Rajni Patel (Western University, Canada)
Jagadeesan Jayender (Harvard Medical School, US)

141 Non-local Dependencies and Contextual Information in the Interpretation of Procedural Surgical Text

Maria-Camilla Fiazza (University of Verona, Italy)

143 Miniaturisation, Modularization and Evaluation of the SoftSCREEN System

Vanni Consumi (UCL, UK)
Danail Stoyanov (UCL, UK)
Agostino Stilli (UCL, UK)

Session 7: Imaging & Sensing

145 Surface-Enhanced Raman Spectroscopy and Transfer Learning Toward Accurate Reconstruction of the Surgical

Zone *Ashutosh Raman* (Duke University, US)
Ren Odion (Duke University, US)
Kent Yamamoto (Duke University, US)
Weston Ross (Duke University, US)
Patrick Codd (Duke University, US)
Tuan Vo-Dinh (Duke University, US)

147 Breast Surface Reconstruction Utilising Autonomous Robotic Assisted Ultrasound Image Acquisition

A.G. de Groot (University of Twente, Netherlands)
V. Groenhuis (University of Twente, Netherlands)
S. Stramigioli (University of Twente, Netherlands)
F.J. Siepel (University of Twente, Netherlands)

149 From 4D Transesophageal Echocardiography to Patient Specific Mitral Valve Models

Patrick Carnahan (Western University, Canada)
Elvis Chen (Western University, Canada)
Terry Peters (Western University, Canada)

151 3-D Visualization and Inter-Session Comparison for Robotic Assisted Bladder Cancer Screening

Vincent Groenhuis (Robotics and Mechatronics, University of Twente, Netherlands)
Antonius G. de Groot (Robotics and Mechatronics, University of Twente, Netherlands)
Erik B. Cornel (Ziekenhuisgroep Twente, Netherlands)
Stefano Stramigioli (Robotics and Mechatronics, University of Twente, Netherlands)
Françoise J. Siepel (Robotics and Mechatronics, University of Twente, Netherlands)

153 A New Suture Needle State Estimation Method Based on Electrical Impedance Sensing

Kim Schwaner (University of Southern Denmark, Denmark)
Zhuoqi Cheng (University of Southern Denmark, Denmark)
Thiusius Savarimuthu (University of Southern Denmark, Denmark)

155 Index of Authors

SLAM-based Surgical Guidance For Breast Reconstruction Surgery

Elise Fu¹, Ángela Alarcón de la Lastra¹, Haoyin Zhou¹, Ruisi Zhang¹,
 Justin Broyles¹, Haripriya Ayyala², Bohdan Pomahac², Jagadeesan Jayender¹

¹Brigham and Women's Hospital, Harvard Medical School, Boston, USA

²Yale Medical School, New Haven, USA

jayender@bwh.harvard.edu

INTRODUCTION

In 2018, 31.3% of the patients with stage I and stage II cancer underwent mastectomy in the United States. The loss of the breast mound post mastectomy alters the physical appearance of the patient and can have significant detrimental effect on the body image and mental health of patients [1]. Breast reconstruction surgery (BRS) using DIEP (deep inferior epigastric perforators) flap utilizes redundant lower abdominal skin and fat for reconstruction of breast mound. Due to its composition of fat similar to native breast, the flap has the advantage of superior aesthetic contours of the reconstructed breast [2], [3]. However, in order to establish the best flap shape and volume, the surgeon must have finesse and intuition [4]. Asymmetry of the breast can lead to a lower quality of life and a badly reconstructed breast is a constant reminder of the disease. Thus, it is crucial to have an accurate, reliable and accessible method to assess breast volume and shape to plan the reconstruction. Our study proposes the use of a low-cost RGB-D camera to scan the contralateral breast of a patient who has undergone mastectomy and 3D print a mirrored mold to guide the surgeon to establish the best shape (see Figure 1).

MATERIALS AND METHODS

A. SLAM-based Mosaicking Algorithm

We propose to use the simultaneous localization and mapping (SLAM) method to mosaic the RGB-D data at different time steps without the use of an external tracker. Most existing RGB-D camera-based dense reconstruction methods, such as KinectFusion [5], depend on the truncated signed distance function (TSDF) algorithm [6] to generate the mesh model, which uses volumetric grids to represent the 3D environment. To improve the accuracy of breast reconstruction, we use volumetric grids with a small sampling step of 2 mm. The small sampling step significantly increases the number of volumetric grids, and in turn increases the computational burden and memory usage. Hence, it is essential to restrict the boundaries of the area-of-interest to reduce the number of grids. Another problem of using the traditional volumetric grid-based TSDF algorithm is that it relies heavily on GPU parallel computation to achieve real-time performance. However, in practice, it is often difficult to bring the GPU-equipped computers

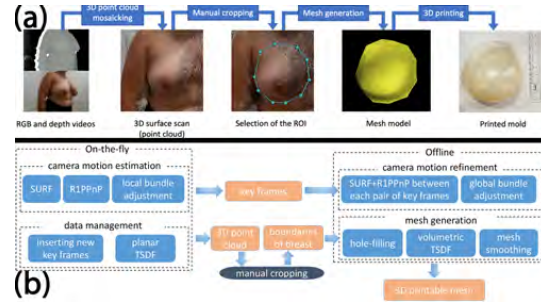


Fig. 1 (a) Workflow of the SLAM-Based Breast surface scanning system, (b) Overview of the SLAM algorithms used for reconstructing the breast surface

to the congested clinical work spaces. To solve the above problems, we propose to split our 3D dense reconstruction algorithm into on-the-fly and offline steps that can be run on a regular laptop. The on-the-fly step builds the model of the environment from the raw RGB-D data in real-time using a real-time planar TSDF algorithm to generate a dense point cloud with high resolution color texture. This step avoids the use of volumetric grids and can provide the user with a real-time map of the anatomy to delineate the breast boundaries. After manually cropping the boundaries of the breast, the offline step refines the results and generates a 3D printable mesh model using the volumetric grids-based TSDF algorithm with a small sampling step of 2mm.

B. Hardware, Software and 3D Printing

The hardware setup consists of an Intel RealSense D415 camera to scan the patient, a wireless clicker to control the software remotely, and a MacBook Pro (connected to the camera using a cable) to run the software. We have developed a software module in 3D Slicer to provide an intuitive workflow for the surgeons to input the patient details and scan the patient with minimal software interaction. The initial 3D reconstruction result is a point cloud with high-resolution color texture, which can be viewed in real-time on the software to confirm that the entire breast has been covered (Figure 2(a)). The cropped point cloud model (Figure 2(b)) is converted into a mesh model of the breast surface (Figure 2(c)),

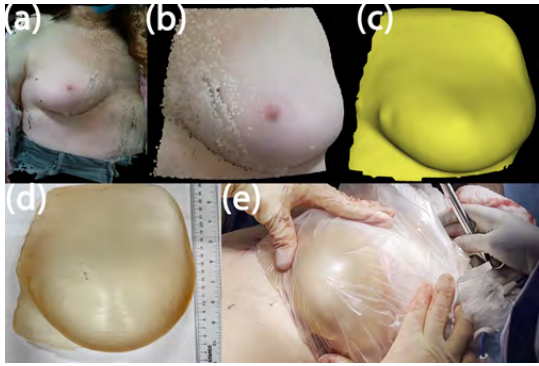


Fig. 2 Example of a patient scan. (a) 3D point cloud scan, (b) Cropped and reflected point cloud of breast to be reconstructed, (c) Mesh model, (d) 3D printed mold, (e) Intraoperative use of the mold for shaping the breast

which is then 3D printed to create a rigid mold for shaping the DIEP flap during BRS (Figure 2(d)). This mold is used to shape the abdominal fat that is harvested to create the breast mound and mimic the patient's native breast (Figure 2(e)).

C. Validation

We have conducted experiments to measure the repeatability and accuracy of the surface scan. A chest phantom (The Chamberlain Group, MA, USA) was used for validating the system. Eight CT skin markers (Beekley Medical, CT) with a diameter of 4.0 mm were placed on the acromial extremity of the clavicles, suprasternal notch, lower sternum, abdomen and umbilicus. To validate the mosaicking algorithm, a larger and smaller area of the phantom were scanned. The entire front side of the phantom was scanned to represent a larger area, and the right and left side to represent a smaller area. Three scans ($n=3$) of each side were performed for a total of 9 scans. Note that depending on the side of the phantom scanned, only the fiducial points visible on that side were used. We validate the repeatability and accuracy of the surface scans.

D. Patient Case Studies

Under an IRB approved study, fifteen patients ($n=15$) were scanned using the 3D surface reconstruction system to validate the system in a multi-center trial (BWH and Yale). These patients were of different ages, skin types, and breast sizes. Each patient during their surgery consult stood in front of a flat wall. Using the RGB-D camera, their breasts were individually scanned following the same workflow as described above and shown in Figure 1. In one patient, the rigid mold that was 3D printed from the surface scan was used intraoperatively to reconstruct the breast.

RESULTS

Repeatability and Accuracy: The 3D surface reconstruction was validated through repeatability and accuracy

tests. When comparing the surface scans between each other through landmark pair distance error and fiducial registration error, the repeatability values were 0.88 ± 0.49 mm and 1.10 ± 0.35 mm, respectively. The landmark pair distance error and fiducial registration error when compared to the CT images had an average value of 1.38 ± 0.79 mm and 1.46 ± 0.48 mm, respectively.

Clinical studies: To validate the system on real patients, breast scans were completed on eight patients with different breast sizes, skin types, and ages. A point-cloud and mesh model were created for each patient. The entire breast was scanned successfully, including the inframammary fold. Although the breasts of different sizes were able to be scanned correctly, it was faster and more feasible to scan smaller ones.

Intraoperative Guidance: The breast mold was also used intraoperatively on one patient under an IRB-approved protocol. The patient underwent mastectomy and was scheduled for a BRS. A week before the procedure, the patient was scanned using the RGB-D camera integrated with the SLAM algorithms and a 3D point cloud of the healthy breast was created. Thereafter, the mesh model was created and flipped to represent the reconstructed breast, as shown in Figure 2(b). The flipped mesh model was then 3D printed to create a rigid mold for reconstructing the breast. On the day of the surgery, the flap was harvested from the abdomen and placed into the rigid mold to shape the flap to mimic the contralateral healthy breast. The procedure did not result in any complications.

DISCUSSION

We proposed the use of the Intel RealSense D415 RGB-D camera integrated with a mosaicking algorithm based on the SLAM method, to scan the entire breast surface and assist in BRS. The repeatability and accuracy of the 3D surface reconstruction presented optimal results, with average errors all under 1.46 mm. Initial clinical results show the utility of the system for assisting surgeons during BRS.

REFERENCES

- [1] K. E. Türk and M. Yilmaz, "The effect on quality of life and body image of mastectomy among breast cancer survivors," *European journal of breast health*, vol. 14, no. 4, p. 205, 2018.
- [2] J. H. Yueh and et. al, "Patient satisfaction in postmastectomy breast reconstruction: a comparative evaluation of diep, tram, latissimus flap, and implant techniques," *Plastic and reconstructive surgery*, vol. 125, no. 6, pp. 1585–1595, 2010.
- [3] A. Thorarinsson and et. al, "Long-term health-related quality of life after breast reconstruction: comparing 4 different methods of reconstruction," *Plastic and reconstructive surgery Global open*, vol. 5, no. 6, 2017.
- [4] P. N. Blondefel and et. al, "Shaping the breast in aesthetic and reconstructive breast surgery: An easy three-step principle. part ii—breast reconstruction after total mastectomy," *Plastic and reconstructive surgery*, vol. 123, no. 3, pp. 794–805, 2009.
- [5] S. Izadi and et. al, "Kinectfusion: real-time 3d reconstruction and interaction using a moving depth camera," in *Proceedings of the 24th annual ACM symposium on User interface software and technology*, 2011, pp. 559–568.
- [6] B. Curless and M. Levoy, "A volumetric method for building complex models from range images," in *Proceedings of the 23rd annual conference on Computer graphics and interactive techniques*, 1996, pp. 303–312.

SLAM-based Trackerless Navigation System for Lateral Skull base Surgery: A Pilot Cadaver Study

Haoyin Zhou¹, Ryan A. Bartholomew^{1,2}, Maud Boreel¹, Alejandro Garcia^{1,2}, Krish Suresh^{1,2}, Saksham Gupta¹, Jeffrey P Guenette¹, Daniel J Lee², C. Eduardo Corrales¹, Jagadeesan Jayender¹

¹*Brigham and Women's Hospital, Harvard Medical School, Boston, USA*

²*Massachusetts Eye and Ear Infirmary, Harvard Medical School, Boston, USA*

INTRODUCTION

Lateral skull base surgery requires drilling near delicate structures with high accuracy. Misidentification of anatomy within the opaque temporal bone can lead to inadvertent surgical complications with high morbidity including facial paralysis, hearing loss, and dysequilibrium. Given that benign pathology is typically the indication for surgery, it is of elevated importance for the lateral skull base surgeon to deftly tread the line between underexposure, which risks persistent disease, and overexposure, which risks iatrogenic injury. The safety and efficacy of lateral skull base surgery may be improved with a viable surgical navigation system.

Despite the availability of surgical navigation systems for nearly three decades, they are infrequently used for lateral skull base surgeries. The navigation systems depend on external tracking equipment and can suffer from cumbersome registration and calibration steps, and suffer from metallic interference or line-of-sight issues. Moreover, for lateral skull base surgery, the patient head position may be adjusted intraoperatively and result in a significant registration error.

In this paper, we have developed a novel Simultaneous Localization and Mapping (SLAM)-based navigation system that localizes the anatomy in real-time based on images without the use of a tracking system. Using this technology, a brief pan of the endoscope can create a 3D surface model of the operative field in real time from the surgeon's perspective. This computerized surface model is then fused to preoperatively acquired CT images of the temporal bone, providing information about the relationship of the exposed tissue surface to underlying anatomic structures. Thereafter, the endoscope is tracked in real-time with respect to the reconstructed surface using video-based features to localize the anatomical structures.

METHODS

A. Trackerless Surgical Navigation

The navigation system consists of three components - a) surface reconstruction of the exposed anatomy, b) registration of the surface to the preoperative CT images, and c) localization of the endoscope in real-time based on features extracted from the video images. The details of the steps are given below.

Surface Reconstruction: Our real-time 3D reconstruction algorithm first extracts 3D information from video frames via stereo matching, and then aligns the resultant 3D models using a novel feature-based SLAM method and a novel dense point cloud merging method [1]. In the current work, we have made significant modifications to improve its robustness and accuracy for lateral skull base surgery, as follows: (1) We have combined ORB and Superpoint image features to improve the tracking of video frames and endoscope. We observed that ORB is more robust for tracking adjacent video frames especially when the tissue surface has poor color texture. However, it is difficult to restore the loss of endoscope tracking using the ORB features, often encountered during surgery when the surgeon removes the endoscope from the surgical field. On the other hand, Superpoint, which is a deep learning-based method, is more robust for restoring the lost tracking of the endoscope but has an unpredictable behavior for tracking video frames. (2) We consider the uncertainty of the stereo-matching results for dense point cloud merging due to the limited range of depth perception of the standard 4 mm endoscope. A weight factor is applied for each pixel for merging and mosaicking, which is computed as the reciprocal value of the depth. (3) For each video frame, we added a feature-based sparse bundle adjustment (SBA) step for adjacent video frames according to the results of R1PPnP-based feature matches selection [2], and then perform SBA using all neighboring video frames.

Registration: Since not all landmarks are visible in both CT and intraoperative anatomy, we used half of the screw fiducials to compute the rigid 6-DoF transform for CT-endoscope registration. After the reconstruction of the initial surface scan followed by the CT-endoscope registration, the anatomical structures segmented from the CT images are aligned with the surface scan.

Real-time localization of anatomical structures: To provide surgical navigation on-the-fly, we have developed an intuitive software interface to provide augmented visualization of the CT structures overlaid on the reconstructed surface. The endoscope is continuously tracked based on the acquired video frames. We match the live video frame to the previously recorded video frames during surface reconstruction using Superpoint+R1PPnP. During this step, the dense point cloud mosaicking is disabled, and

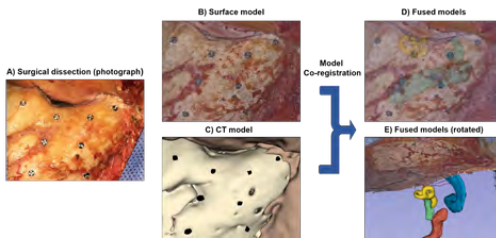


Fig. 1 Experimental Protocol Summary. For each surgical step of a translabyrinthine dissection (A), a surface model is reconstructed from 3D-endoscopic video (B) and a CT model is segmented from high-resolution temporal bone CT images (C). The models are co-registered, and the surface model can be made semi-transparent (D) or rotated (E) to permit visualization of the underlying segmented structures.

the CT data is reprojected to the live endoscopy video frame in real-time using the GPU.

B. Surgery and fiducial placement

Fresh human cadaveric heads were used for experiments and translabyrinthine dissections were completed in five discrete steps. The first surgical step was presentation of the undisturbed pinna, the second surgical step was exposure of the mastoid bone, the third surgical step was a cortical mastoidectomy using a surgical drill to expose the aditus ad antrum with preservation of the tegmen mastoideum and sigmoid sinus, the fourth surgical step was a labyrinthectomy with complete removal of the semicircular canals, and the fifth and final surgical step was an internal auditory canal drill out whereby inferior and superior troughs were drilled and a thin layer of bone was left overlying the internal auditory canal. Following completion of each surgical step, 8 to 10 titanium screws (1.2mm, Stryker) were fixed to bone to serve as fiducials for quantifying the surface reconstruction, registration and localization errors.

C. CT imaging and anatomical model segmentation

Following completion of each surgical step and placement of fiducials, a 3D endoscope (4 mm, 0 degree, Karl Storz TipCam 3D Endoscopy system) was used to capture and reconstruct the exposed surface using the SLAM algorithm on a Titan V GPU. High resolution CT images of the cadaveric temporal bone (0.6 mm slice thickness) were acquired. Lateral skull base structures were manually segmented using semi-automatic image intensity-based methods. Segmented structures included bone, skin and soft tissue, ossicles, inner ear labyrinth, otic capsule, facial nerve, internal auditory canal, sigmoid sinus and jugular bulb, internal carotid artery, and screw fiducials.

RESULTS

For each ear, we performed 5 surgical steps and for each step, we placed 8-10 screw fiducials. Each fiducial has three coordinates in the SLAM, EM and CT spaces

	Reconstruction	Registration	Localization
Pinna	0.57	0.72	1.67
Exposed bone	0.42	0.6	1.56
Mastoidectomy	0.78	0.99	2.06
Labyrinthectomy	0.75	0.91	1.86
IAC drillout	0.77	0.97	1.71

TABLE I Overall average error (mm)

respectively. In addition, we have attached another EM tracker on the endoscope to record its motion, which is not needed by the SLAM algorithm and only used for validating the localization accuracy.

Three types of errors are reported in this paper: (1) Reconstruction error, which quantifies the accuracy of the endoscopy video-based 3D reconstruction, computed using the coordinates of the screw fiducials in CT images and endoscopy scans. (2) Registration error, which quantifies the error of aligning the reconstructed surface and the preoperative CT images. (3) Localization error that quantifies the accuracy in localizing the anatomical structures when the endoscope is in motion. Two electromagnetic trackers were used in our experiments. One localizes the coordinates of the fiducials, and the second one was attached to the endoscope. For each surgical step, we scan the anatomy twice. The first scan was used to build the 3D model, register the surface to the preoperative CT and obtain the EM-endoscope calibration. We then use the second scan to report the localization error. The ability to use two different scan also demonstrates the ability to restore lost tracking of the endoscope. The average surface reconstruction, registration and localization errors of 8 ears \times 5 steps \times 8 or 10 fiducials are reported in Table I.

DISCUSSION

We proposed the use of a novel trackerless navigation system integrated with a mosaicking algorithm based on SLAM to provide intraoperative navigation for lateral skull base surgery. The reconstruction, registration and localization errors are less than 0.78 mm, 0.99mm, and 2.06 mm respectively. Initial results show the utility of the trackerless system for accurately localizing lateral skull base anatomy during surgery.

REFERENCES

- [1] H. Zhou and J. Jagadeesan, "Real-time dense reconstruction of tissue surface from stereo optical video," *IEEE Transactions on Medical Imaging*, vol. 39, no. 2, pp. 400–412, 2019.
- [2] H. Zhou, T. Zhang, and J. Jagadeesan, "Re-weighting and 1-point ransac-based pnp solution to handle outliers," *IEEE TPAMI*, vol. 41, no. 12, pp. 3022–3033, 2019.
- [3] N. Ben-Shlomo *et al.*, "Incidence of iatrogenic inner ear breaches from vestibular schwannoma surgery: a review of 1,153 hearing preservation approaches," *Journal of Neurological Surgery Part B: Skull Base*, vol. 81, no. S 01, p. A073, 2020.
- [4] D. Schneider *et al.*, "Evolution and stagnation of image guidance for surgery in the lateral skull: a systematic review 1989–2020," *Frontiers in surgery*, vol. 7, p. 604362, 2021.
- [5] R. F. Labadie *et al.*, "In vitro assessment of image-guided otologic surgery: submillimeter accuracy within the region of the temporal bone," *Otolaryngology-Head and Neck Surgery*, vol. 132, no. 3, pp. 435–442, 2005.
- [6] R. F. Labadie, B. M. Davis, and J. M. Fitzpatrick, "Image-guided surgery: what is the accuracy?" *Current opinion in otolaryngology & head and neck surgery*, vol. 13, no. 1, pp. 27–31, 2005.

dVRK-based teleoperation of a CTR robot with stereovision feedback for neurosurgery

Changyan He^{1,2}, Robert H. Nguyen¹,
Eric Diller², James Drake¹, and Thomas Looi¹

¹*PCIGITI Center, the Hospital for Sick Children*

²*Microrobotics Lab, University of Toronto, Toronto, Canada
changyan.he@utoronto.ca*

INTRODUCTION

Decades of efforts have been made to minimize the invasiveness of the procedures inside the patient's brain. Endoscopic tools are first developed and applied in neurosurgery, which significantly reduce the trauma to a limited number of small holes but also limit the surgeon's reachability to the target tissue inside of the brain due to the tool's rigidity. Flexible robotic tools are then introduced to perform the procedures with a minimally invasive approach [1] by providing enhanced dexterity with their tentacle-like body. However, intuitive and efficient manipulation of the robotic tools remains challenging because currently the surgeon manipulates the robotic tools with feedback of the monocular vision from a standard clinical neuro-endoscope suffering from lack of depth perception. In this paper, we propose a robotic system with a flexible end-effector and stereovision feedback for neurosurgery by integrating our previously-developed Concentric Tube Robot (CTR)[2], the da Vinci Robot Research Kit (dVRK) [3] and a customized dual endoscope camera subsystem. The CTR manipulator was teleoperated with the dVRK master tool manipulator (MTM). A virtual motion boundary was applied for the MTM by haptic feedback based on the CTR's workspace to guide the operator to control the CTR within its motion range. The manipulation performance of the proposed system was experimentally evaluated and the results of that showed under the stereovision feedback the manipulation accuracy of the CTR is 2.8 mm and the image transmission latency is 1.5 seconds. This preliminary study suggests that our proposed system has the potential of improving surgeons' manipulation performance in robot-assisted minimally invasive neurosurgery.

MATERIALS AND METHODS

A. Robotic system

The proposed robotic system mainly consists of three components, as shown in Fig. 1, including the MTM, the CTR manipulator, and a customized dual camera endoscope. The MTM is a haptic console with 7

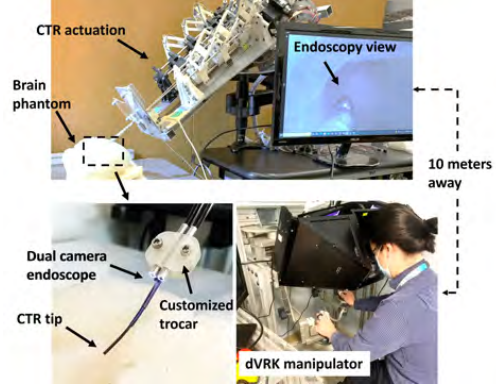


Fig. 1 Overview of the robotic system. (a) CTR, (b) dual endoscopy cameras, (c) master manipulator of the dVRK.

degrees-of-freedom (DoFs) and was used to operate the CTR manipulator remotely. A vision system with two monitors was mounted above the MTM and was utilized to provide stereo visual perception for the operator. The CTR manipulator was developed with three concentric deployed NiTi tubes and has six DoFs at its tip. The workspace of the CTR is obtained as the shape of an inverted bell with bottom diameter of 32 mm and height of 35 mm. The absolute error of the CTR's tip positioning is 2.8 mm with a standard deviation 1.5 mm [2]. Two USB mini-camera probes (MODOSON, China) with the diameter of 3.9 mm and resolution of 720p were selected as the endoscopes. The two camera probes were aligned manually to provide the images with proper orientations for stereo vision reconstruction, which were then fixed side-by-side by a 3D-printed trocar, and deployed parallelly with the CTR's tube holder.

B. Control architecture

The control architecture of the robotic system is shown in Fig. 2. The operator sits beside the MTM and teleoper-

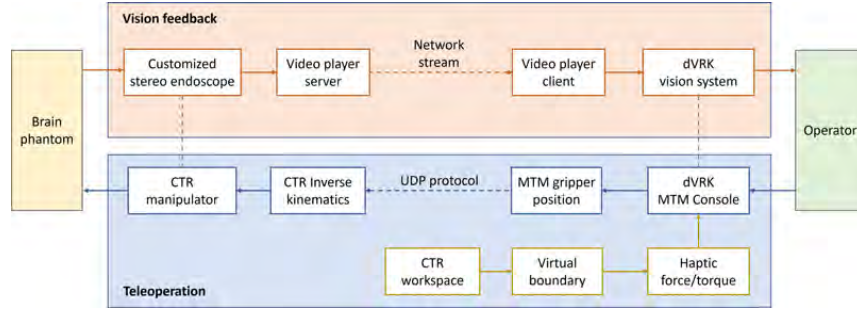


Fig. 2 Control architecture of the robotic system. The operator controls the CTR manipulator via the dVRK MTM and gets the stereo vision feedback from the customized dual endoscope cameras at the CTR side.

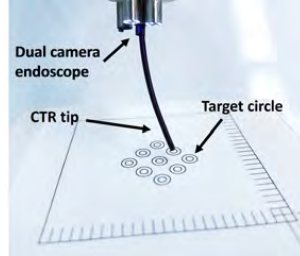


Fig. 3 Experimental setup. A group of concentric circles is printed on a sheet paper and is used to evaluate the CTR's teleoperation accuracy.

ates the CTR, while obtaining the stereo vision feedback from the customized dual-camera endoscope at the CTR side. The control command, i.e., the MTM's gripper real-time position, is converted from ROS messages to UDP messages and then sent to the CTR system via the local area network (LAN). The received data is fed into the CTR's inverse kinematic model to generate the CTR's desired position. The real-time images from the two USB camera probes are fetched with a video player sever (VLC media player, VideoLAN) and then streamed through the LAN to a video player client. The received images are projected on the two screens of the dVRK vision system. We set virtual boundaries for the MTM based on the CTR's reachable workspace using haptic feedback. The operator is guided to control the CTR within its motion range all the time. This feature avoids invalid command positions sent to the CTR and thus can improve the operation efficiency.

C. Experiments

A set of experiments were carried out to evaluate the teleoperation accuracy of the CTR manipulator. Nine groups of two concentric circles with diameters of 2 mm and 4 mm were printed on a sheet of paper. The paper was stuck to a stage and placed under the CTR, as shown in Fig. 3. In the experiment, a human operator was expected to maneuver the MTM with the stereo feedback to control the CTR's tip to touch all circle

TABLE I Evaluation Result

	Mean value	Standard deviation
Teleoperation accuracy	2.8 mm	0.3 mm
Stereovision latency	1.5 second	0.2 second
Completion time	9 minutes	1.2minutes

centers in sequence. The hit locations of the CTR's tip were recorded and used to calculate the accuracy with the below rules: the accuracy is 1 mm if the CTR's tip was located inside of the inner circle and 2 mm if the CTR's tip was located inside of the outer circle but out of the inner circle. One engineer who was familiar with both CTR and MTM was recruited to perform the experiment. The experiment was repeated 5 times.

RESULTS

The experimental results are shown in Table I. The accuracy of the CTR's tip localization under teleoperation was 2 mm with a standard deviation of 0.5 mm. The image stream latency is also evaluated with a timer and the result showed the delay was 1.5 second. The average completion time for the experiments was 9 minutes.

DISCUSSION

This preliminary study indicates that our proposed robotic system has the potential to be used in brain surgery, although the performance could be further improved. Future study will investigate the minimization of the customized trocar and real-time video transmission. Simulated procedures on a brain phantom will also be explored.

REFERENCES

- [1] C. Faria, W. Erhagen, M. Rito, E. De Momi, G. Ferrigno, and E. Bicho, "Review of robotic technology for stereotactic neurosurgery," *IEEE Reviews in Biomedical Engineering*, vol. 8, pp. 125–137, 2015.
- [2] C. He, R. Nguyen, C. Forbigger, J. Drake, T. Looi, and E. Diller, "A hybrid steerable robot with magnetic wrist for minimally invasive epilepsy surgery," in *2023 International Conference on Robotics and Automation (ICRA)*. IEEE, 2023.
- [3] P. Kazanzides, Z. Chen, A. Deguet, G. S. Fischer, R. H. Taylor, and S. P. DiMaio, "An open-source research kit for the da vinci surgical system," in *IEEE Intl. Conf. on Robotics and Auto. (ICRA)*, Hong Kong, China, 2014, pp. 6434–6439.

Proof of Concept Implementation of Forbidden Region Dynamic Active Constraints in Minimally Invasive Surgery

Zejian Cui¹ and Ferdinando Rodriguez Y Baena¹

¹*Department of Mechanical Engineering, Imperial College London*
{zejian.cui, f.rodriguez}@imperial.ac.uk

INTRODUCTION

Active Constraints (AC), also named as Virtual Fixtures (VF), are a strategy to provide anisotropic haptic guidance for surgeons during use so that motions that comply with safety requirements are permitted, while those that breach safety requirements are negated. AC can be helpful also in a teleoperative surgical scenario, in which surgeons operating on the surgeon-side interface are separated from the patient-side, where surgical instruments are held and manipulated by a robot. One challenging aspect of incorporating AC into a modern clinical setting is how to efficiently update pre-constructed AC geometries in real time to account for dynamic tissue movement. In this study, we designed a pipeline for implementing Forbidden Region AC (FRAC), where tissue movement is constantly captured by a depth-sensing camera. The effectiveness of the pipeline has been confirmed through *in vitro* trajectory tracking experiments along a deforming aorta phantom. Our experimental results demonstrate the capability of our method to provide timely corrective guidance when a violation of the safety region is detected.

MATERIALS AND METHODS

Bowyer *et. al* [1] proposed that the implementation of AC can be summarised into three stages: AC generation, AC evaluation and AC enforcement. In these processes, the tissue to be protected is represented using geometry, the violation of safety region is determined, and an AC force is generated. In the rest of this section, we present the design of each of these for our proposed dynamic AC pipeline.

A. AC generation

AC generation is the foundation of the AC implementation, where anatomical areas of interest must be geometrically represented, either through simple geometries such as lines and points or through complex geometries such as triangular or quadrilateral meshes. Although complex geometries provide a more accurate description of the anatomical structure, they come at the cost of higher computational requirements for the subsequent AC evaluation step. To enable real-time updates of AC when tissue undergoes deformation, we utilize a depth sensing camera, Acusense 3D (Revopoint 3D Inc.), with



Fig. 1 Hardware setup, consisting of an Acusense 3D camera, an aorta silicon phantom and a pair of forceps held by dVRK Patient Side Manipulator1 (PSM1)

a resolution of 0.5mm at a working distance of 0.5m. The Acusense camera streams a point cloud representing the tissue surface at a rate of 10fps, which is then registered with a pre-scanned tissue model. Assuming that the deformation of soft tissue caused by the respiratory movements of a patient can be modelled as an affine transformation, we leverage the robust global registration method TEASER++ [2] to accelerate this step.

B. AC evaluation

AC evaluation is responsible for conducting a proximity query between a surgical instrument and the soft tissue to be protected. The returned minimum distance is compared with a safety distance to determine if a violation of the safety region has occurred. Different AC geometrical representations result in different levels of difficulty when performing AC evaluation. For mesh representations, proximity queries require a significant amount of computational effort. To accelerate the proximity query process, we incorporate the Deformation Invariant Bounding Spheres (DIBS) method [3] in our pipeline design.

C. AC enforcement

AC enforcement involves computing the magnitude and direction of an AC force/torque to be sensed by surgeons

so that surgical tools can be retracted into the safety region promptly when a violation occurs. Although a simple elastic-plastic model is the most widely adopted for generating haptic cues, it is not always dissipative, which can introduce safety concerns. Therefore, in this study, we adopt a dynamic frictional constraint model [4] that is able to compensate for this shortcoming.

D. Experiment design

To test the effectiveness of the proposed AC strategy in assisting teleoperational surgical tasks, trajectory tracking experiments were designed and implemented on the first generation da Vinci Research Kit (dVRK) [5]. In this controlled study, we assume that when an AC force is generated, a surgical tool (Forceps 400036E) should be effectively pulled out of the forbidden region along the direction of the AC force by a "virtual surgeon". Specifically, instead of recruiting users to operate on the patient side, we directly feed the AC force into a hybrid force-position controller, which in turn generates positional commands to be received by the tool. Before the experiment, we defined a reference dynamic trajectory, consisting of 500 points in total, which is constantly updated as the tool moves above the surface of a pulsating phantom, maintaining a safety distance of 8mm.

RESULTS

Throughout the experiment, a total of $N = 726$ points were gathered on the actual tool tip trajectory. The average distance between the tool tip and updated target point on the reference trajectory is $\frac{1}{N} \sum_{i=1}^N \|P_i - Q_i\| = 13.28\text{mm}$, where P_i and Q_i denote the i th point on the actual tool tip trajectory and its corresponding target point on the updated reference trajectory, respectively. To demonstrate the effectiveness of the proposed AC strategy in assisting the task, 4 timestamps along the trajectory were selected, which are depicted in Fig.2 to show how the tool tip was retracted from the forbidden region when a safety condition was breached. The updated reference trajectory was also overlaid onto the updated phantom model at these four timestamps to illustrate the deformation of the phantom. Fig 3 provides a more detailed demonstration of the tool tip movement when a violation of the safety region is detected.

DISCUSSION AND CONCLUSION

The average distance between the tool tip and its corresponding target point on the reference trajectory is greater than the defined safety distance, which indicates the effectiveness of the proposed AC strategy in maintaining task safety. Our results also show that when the safety condition is breached due to dynamic tissue deformation, the proposed AC strategy is able to prioritize task safety and guide the tool tip to move out of the forbidden region. One limitation of this study is that a hybrid force-position controller was used to remove the human element from these initial experiments. Hence, the (virtual) surgeon was assumed to be able to perfectly act upon the

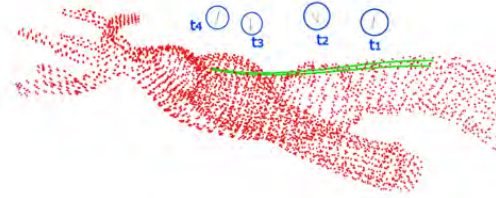


Fig. 2 Tool tip positions at four timestamps t_1, t_2, t_3, t_4 . The green lines represent the updated reference trajectories at each timestamp, while the red points represent the updated phantom models. The misalignment between them indicates movement of the phantom. The blue circles represent the tool tip positions, with highlight in Fig.3

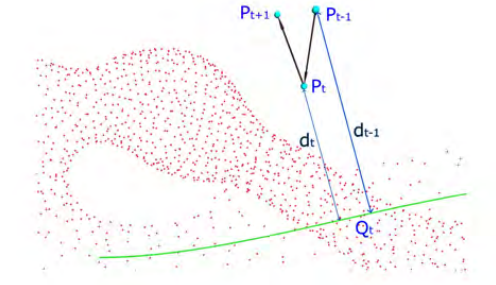


Fig. 3 Tool tip movement when safety condition is breached. At time $t - 1$, the tool tip is located at P_{t-1} , and its distance from the phantom surface is greater than the safety distance ($d_{t-1} >$ safety distance), hence movement towards P_t is allowed. However, at P_t , when the minimum distance reduces to less than the safety distance ($d_t <$ safety distance), the AC controller generates an AC force to guide the tool tip away from forbidden region and towards P_{t+1}

generated AC force and respond promptly. Future work will involve conducting user studies and evaluating the effectiveness of the proposed AC strategy in assisting actual teleoperational surgical tasks.

REFERENCES

- [1] S. A. Bowyer, B. L. Davies, and F. Rodriguez y Baena, "Active constraints/virtual fixtures: A survey," *IEEE Transactions on Robotics*, vol. 30, no. 1, pp. 138–157, 2014.
- [2] H. Yang, J. Shi, and L. Carlone, "TEASER: Fast and Certifiable Point Cloud Registration," *IEEE Trans. Robotics*, 2020.
- [3] S. A. Bowyer and F. R. y Baena, "Deformation invariant bounding spheres for dynamic active constraints in surgery," *Proceedings of the Institution of Mechanical Engineers, Part H: Journal of Engineering in Medicine*, vol. 228, no. 4, pp. 350–361, 2014.
- [4] S. A. Bowyer and F. Rodriguez y Baena, "Dynamic frictional constraints in translation and rotation," in *2014 IEEE International Conference on Robotics and Automation (ICRA)*, 2014, pp. 2685–2692.
- [5] P. Kazanzides, Z. Chen, A. Deguet, G. S. Fischer, R. H. Taylor, and S. P. DiMaio, "An open-source research kit for the da vinci® surgical system," in *2014 IEEE international conference on robotics and automation (ICRA)*. IEEE, 2014, pp. 6434–6439.

How Insights from In Vivo Human Pilot Studies with da Vinci Image Guidance are Informing Next Generation System Design

P. C. Cannon^{1,3}, S. A. Setia^{2,3}, N. L. Kavoussi^{2,3}, S. D. Herrell III^{1,2,3},
 and R. J. Webster III^{1,2,3}

¹Vanderbilt University, Department of Mechanical Engineering

²Vanderbilt University Medical Center, Department of Urologic Surgery

³Vanderbilt Institute for Surgery and Engineering (VISE)

piper.c.cannon@vanderbilt.edu

INTRODUCTION

Using an image guidance system constructed over the past several years [1], [2] we have recently collected our first in vivo human pilot study data on the use of the da Vinci for image guided partial nephrectomy [3]. Others have also previously created da Vinci image guidance systems (IGS) for various organs, using a variety of approaches [4]. Our system uses touch-based registration, in which the da Vinci's tool tips lightly trace over the tissue surface and collect a point cloud. This point cloud is then registered to segmented medical images. We provide the surgeon a picture-in-picture 3D Slicer display, in which animated da Vinci tools move exactly as the real tools do in the endoscope view (see [2] for illustrations of this). The purpose of this paper is to discuss recent in vivo experiences and how they are informing future research on robotic IGS systems, particularly the use of ultrasound.

MATERIALS AND METHODS

In a recent set of in vivo experiments, we deployed our IGS system during robot-assisted partial nephrectomy, using a bystander study protocol [3]. This protocol enables us to test the IGS system without changing the therapeutic process. We do this by using two surgeons, one who solely uses the IGS display to collect data, and one who solely conducts the surgery according to the standard of care without ever seeing the IGS display. This isolates the testing of the IGS system from the therapeutic process, enabling the IGS system to be tested earlier in vivo, to obtain quick data and surgeon feedback on whether various approaches or aspects of the system are likely to be useful to the surgeon. Before conducting our in vivo studies we assessed accuracy in phantoms [1], [2]. Then, to determine whether accuracy improvements translate to the in vivo setting, we performed the following experiments. Surgeons used the da Vinci tool tips to touch (or point the tool jaws at, for subsurface locations) specific anatomical targets, both with and without IGS. Our first observation was that there was error in the pointing process itself, which we

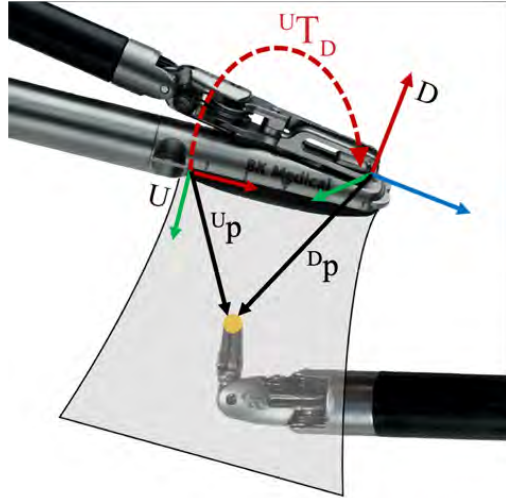


Fig. 1 Proposed hand-eye calibration approach to compute the transformation, ${}^U T_D$, between the ultrasound image plane, U, and the da Vinci tool tip coordinate system, D, using the tip of another da Vinci tool.

found we could reduce with a virtual pointer (i.e. a line in the virtual environment that extends the length of the tool jaws) [5]. Overall, our in vivo studies enabled us to quantitatively assess our robotic IGS system in the context of partial nephrectomy, but our results were not statistically significant with respect to demonstrating surgeon accuracy improvement [3]. Note that these experiments were conducted using rigid registration and considered the part of the surgery where the kidney is mobilized from the surrounding fat. Based on these studies, future work will be needed to integrate tissue deformation and cutting models into our IGS system to capture subsequent steps in the procedure.

We saw larger errors at the vein and artery than at the tumor, and these were also larger than we had observed



Fig. 2 Example ultrasound image of da Vinci Large Needle Driver tool tip, which provides one calibration point.

in prior phantom studies. These error levels, combined with qualitative observations of tissue deformation during surgery, led us to hypothesize that tissue deformation is responsible.

To address this in this paper, we take the first steps toward the use of intraoperative ultrasound to acquire subsurface points to assist in registration (see e.g. [6]), and inform future tissue deformation models. Our goal is to calibrate the “drop in” ultrasound probe used with the da Vinci robot in a new way, i.e. by placing the da Vinci tool tips of the other arm into the ultrasound image to obtain a set of known points for calibration. This is a robotic adaptation of a technique suggested for use with tracked pointers [7].

Before the ultrasound data can be incorporated into the IGS display, calibration must be performed to determine the transformation between the da Vinci tool holding the probe and the resulting ultrasound image plane (see Fig. 1). Note that this technique eliminates the need for additional calibration phantoms, using the sterilized robotic tool tip that is already present in the surgical scene. Thus it is a practical and efficient solution for the intraoperative hand-eye calibration between the da Vinci Xi and ultrasound image plane.

To perform data collection for calibration the drop-in ultrasound transducer is held by a da Vinci Prograsp tool, via a custom attachment. The tip of a da Vinci Large Needle Driver tool is then repeatedly imaged as shown in Fig. 1, with an example of one of these images shown in Fig. 2. ${}^U T_D$ is computed using an iterative least-squares solver which adjusts the parameters in the transformation to minimize the difference between observed robot tip positions in the ultrasound images and those reported by the da Vinci’s encoders. After the calibration is complete, a set of points collected the same way, but not used in the calibration process, is used to assess error via the leave-one-out cross-validation approach.

RESULTS

We determined the feasibility of this calibration method by imaging the Large Needle Driver 60 times with the ultrasound probe held by the Prograsp tool. Employing the leave-one-out cross-validation approach, we found the mean target registration error across the 60 data points to be 2.14 mm.

DISCUSSION

Our in vivo pilot studies have revealed significant soft tissue deformation. Based on this, we plan to pursue future tissue deformation models and use subsurface points to augment our current surface-based registration processes. In this paper we have taken a first step toward such a system by addressing the ultrasound calibration challenge. By using the da Vinci’s other tool to collect points that are known in both Cartesian and ultrasound image space, we performed a hand-eye calibration. This approach provides a practical method for calibration that does not rely on external tracking systems or a calibration phantom. The average error in our calibrated ultrasound system was 2.14 mm which is in line with the errors observed in past research on ultrasound calibration. This opens the door to future research on use of ultrasound for registration and display of ultrasound images in our IGS system, as well as the creation and incorporation of models for tissue deformation and cutting.

REFERENCES

- [1] J. M. Ferguson, E. B. Pitt, A. Kuntz, J. Granna, N. L. Kavoussi, N. Nimmagadda, E. J. Barth, I. S. Duke Herrell, and I. R. J. Webster, “Comparing the accuracy of the da vinci xi and da vinci si for image guidance and automation,” *The International Journal of Medical Robotics and Computer Assisted Surgery*, vol. 16, no. 6, pp. 1–10 e2149, 2020.
- [2] J. M. Ferguson, E. B. Pitt, A. A. Remirez, M. A. Siebold, A. Kuntz, N. L. Kavoussi, E. J. Barth, I. S. D. Herrell, and I. R. J. Webster, “Toward practical and accurate touch-based image guidance for robotic partial nephrectomy,” *IEEE Transactions on Medical Robotics and Bionics*, vol. 2, no. 2, pp. 196–205, 2020.
- [3] P. C. Cannon, J. M. Ferguson, B. E. Pitt, J. A. Shrand, S. A. Setia, N. Nimmagadda, E. J. Barth, N. L. Kavoussi, R. L. Galloway, S. D. Herrell, and R. J. Webster, “A safe framework for quantitative in vivo human evaluation of image guidance,” *IEEE Open Journal of Engineering in Medicine and Biology*, accepted.
- [4] S. D. Herrell, R. L. Galloway, and L. M. Su, “Image-guided robotic surgery: update on research and potential applications in urologic surgery,” *Current Opinion in Urology*, vol. 22, no. 1, pp. 47–54, 2012.
- [5] J. A. Shrand, J. M. Ferguson, P. C. Cannon, N. Nimmagadda, S. Setia, N. L. Kavoussi, R. J. Webster III, and S. D. Herrell, “A Visual Guide Improves Pointing Accuracy in Image-Guided Robotic Surgery,” in *35th Engineering and Urology Society Annual Meeting*, 2022, p. 53.
- [6] O. Moharerri, C. Schneider, T. K. Adebar, M. C. Yip, P. Black, C. Y. Nguan, D. Bergman, J. Seroger, S. DiMaio, and S. E. Salcudean, “Ultrasound-based image guidance for robot-assisted laparoscopic radical prostatectomy: Initial in-vivo results,” in *Information Processing in Computer-Assisted Interventions*. Berlin, Heidelberg: Springer Berlin Heidelberg, 2013, pp. 40–50.
- [7] M. Welch, J. Andrea, T. Ungi, and G. Fichtinger, “Freehand ultrasound calibration: phantom versus tracked pointer,” in *Proc. SPIE 8671, Medical Imaging 2013: Image-Guided Procedures, Robotic Interventions, and Modeling*, vol. C, 2013.

MRI-Guided Robotic for Prostate Biopsy

Haipeng Liang¹⁺, Wanli Zuo^{1,2+}, Dimitri Kessler³, Tristan Barrett³, Zion Tsz HoTse¹

¹*School of Engineering and Materials Science, Queen Mary University of London, London, E1 4NS*

²*School of Mechanical Engineering and Mechanics, Ningbo University, 315211, China*

³*Department of Radiology, University of Cambridge School of Clinical Medicine, CB2 0QQ*

⁺co-first author haipeng.liang@qmul.ac.uk

Introduction

Prostate cancer is one of the most common malignancies and the second leading cause of cancer death in men [1]. Approximately 52,300 new cases of prostate cancer are detected in the UK every year, that's more than 140 every day.

Magnetic resonance imaging (MRI) has been widely used in the diagnosis of prostate cancer, as it can offer high-resolution tissue imaging at arbitrary orientations and monitor therapeutic agents, surgical tools, and tissue properties. Therefore, a robot - under the guidance of MRI - can target the tumor regions with high accuracy to obtain the biopsy samples for diagnosis, thus reducing unnecessary gland punctures and maximizing the utility of a minimally invasive system.

However, as MR scanners require a strong magnetic field, ferromagnetic materials are precluded as they can cause a hazard to the device and patients, and paramagnetic materials can generate their own magnetic field which will distort the image quality. As a result, MR-safe actuators are required to power the robot. Plus, due to the limited size of the MR bores, the robot operating inside should be as compact as possible [2].

In this paper, a robotic system for MRI-guided prostate biopsy is proposed. Comparing with the existing designs, it has a compact size, with the workspace covering the whole prostate. The use of pneumatically powered actuators can avoid the influence of electromagnetic interference. The working principle, mathematical model, and mechanism design are presented. The needle insertion experiment under an MR environment was conducted.

Materials and Methods

A. Robot Design and Actuator

With a compact size of $23 \times 12 \times 11.5$ cm, the presented design has three motorized degrees of freedom (DoF) and one passive DoF that allow the needle to be positioned to the prostate in different directions. After arriving at the desired position, surgeons manually insert the needle to get into the targeted area. For the requirement of MR compatibility, all the components are made of plastic materials using 3D printing and laser cutting. Two motors are used to control the horizontal and vertical movements of the needle in a work plane, while the third motor is to control the rotation of the work plane. Two sets of bevel gears connected to the bars are applied to control the position of the needle

guide in the work plane, so that the work plane rotates around the centre of the bevel gears. Fig. 1 shows the CAD drawing and the photo of the robot.

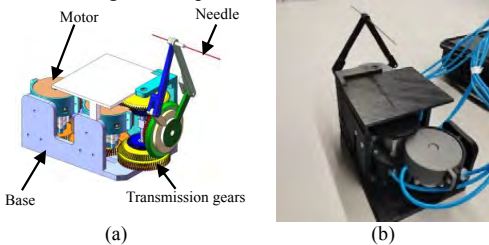


Fig. 1. (a) CAD drawing of the robot; (b) Photo of the robot.

The stepper motor used in this system was recently reported in [3], in which the housing is separated into three closed chambers. Three hoses and solenoid valves are used to fill and exhaust the air from the relevant chambers. The compressed air in each chamber drives the rotor to rotate by 60° , resulting in the output shaft rotating by 120° .

B. Kinematic Analysis

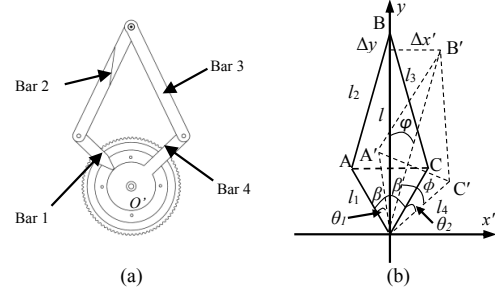


Fig. 2 Translational motion of the prostate robot. (a) CAD drawing. (b) Schematic diagram.

For the movement in the work plane, a multi-bar mechanism is applied, in which the needle guide is attached to joint B at the end of the two bars, allowing it to move horizontally and vertically, as shown in Fig. 2a. Bar 1 and Bar 4 can rotate around point o' and are powered by two motors through the transmission of various gears. Fig. 2b depicts the schematic diagram of the translational movement on the plane, from which the rotating angles of the two bars with respect to the position of the needle guide are expressed as:

$$\begin{cases} \theta_1 = \phi + \varphi - \beta \\ \theta_2 = \phi - \varphi + \beta \end{cases} \quad (1)$$

and

$$\begin{cases} \phi = \angle BOB' = \arctan \frac{\Delta x}{l - \Delta y} \\ \varphi = \arccos \frac{l_1^2 + (OB')^2 - l_2^2}{2(OB')l_1} \\ \beta = \angle AO'B = \arccos \frac{l_1^2 + l^2 - l_2^2}{2l_1l} \\ (OB')^2 = \Delta x'^2 + (l + \Delta y)^2 \end{cases} \quad (2)$$

where $l_1 = l_4$, $l_2 = l_3$, are the lengths of the four bars, respectively. l is the original length of the centre bar OB . θ_1 , θ_2 are the rotation angles of Bar 1 and Bar 4, respectively.

The third DoF of the robot is applied to drive the rotation of the work plane, which is controlled by Motor 3. As shown in Fig. 3 the horizontal movement of the needle in the work plane is also affected by the rotation of the work plane and is expressed as:

$$\Delta x = (a + r)\sin\gamma + b\cos\gamma \quad (3)$$

where a and b depict the position of the target point relative to the work plane, r is the radius of the work plane's rotating circle, and γ is its rotating angle.

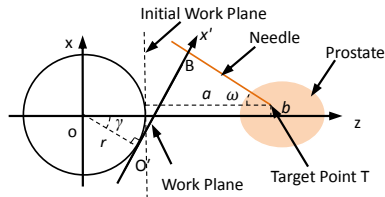


Fig. 3. Schematic diagram of the rotation of the work plane and needle insertions.

According to Eqs. (1) – (3), the rotating angles of the three motors can be obtained with the position of the needle guide relative to the target point and the insertion angle.

C. Workspace analysis

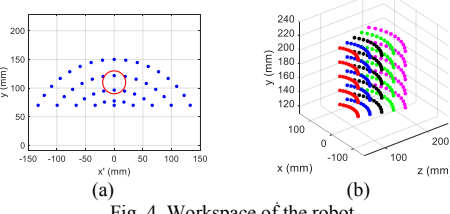


Fig. 4. Workspace of the robot.

The workspace of the robot is determined by the planar movement and the rotation of the work plane. Fig. 4a depicts the workspace of the needle guide in the work plane. Fig. 4b shows the workspace with the vertical movement and the rotation of the work plane at insertion depths of 80 – 150 mm, in which the width of workspace at each point is shown as Fig. 4a.

Results

Three drivers were applied to control nine valves connected to the motors, then a user interface was

developed to manipulate the multifunction I/O device to generate the signal to control the rotation of each motor.

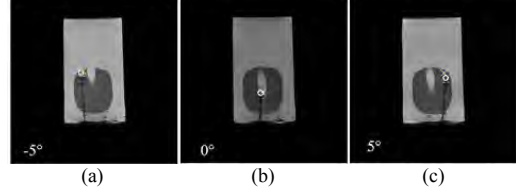


Fig. 5. The insertion of eight points from three different directions: (a) -5°; (b) 0°; (c) 5°

The accuracy of the robot was measured by inserting a needle into the prostate phantom from different directions. In the open-air test, the needle was pointed to eight targeted points in the prostate phantom, showing that the robot has an accuracy of 1.13 mm. The MR test was conducted with a 3T MR scanner, in which the needle was inserted into the prostate phantom from different directions. Fig. 5 shows some of the MR images of the test, the mean error was measured as 2.33 mm with a standard deviation of 2.28 mm.

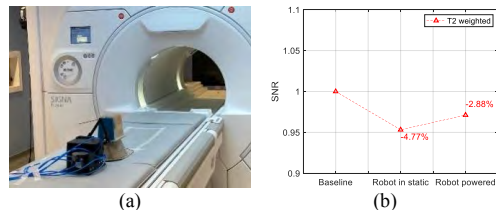


Fig. 6. (a) Photo of the robot in the MR scanner. (b) SNR of T2 MR images under three scenarios.

The signal-to-noise ratio (SNR) reduction was calculated using the mean value of the image centre dividing the standard deviation of the corner area. Fig. 6 shows the photo of the robot in an MR scanner, and the SNR reduction under different scenarios. The SNR reduction was measured as less than 5%, which is acceptable for clinical use.

Discussion

This study proposed a 4-Dof robot used for prostate biopsy in the MR environment. It is powered by three pneumatic stepper motors, allowing the needle to be inserted into the prostate with different orientations. The main contribution of this work is its compact size, making it easy to be placed inside the MR scanner. The SNR result shows it is suitable for clinical application.

References

- [1] F. Allameh, A. H. Rahavian, and S. Ghiasi, "Prevalence of Castration Success Rate in Iranian Metastatic Prostate Cancer Patients: A Referral Center Statistics," International Journal of Cancer Management, vol. 11, no. 10, Oct, 2018.
- [2] H. Su et al., "Piezoelectrically Actuated Robotic System for MRI-Guided Prostate Percutaneous Therapy," IEEE/ASME Transactions on Mechatronics, vol. 20, no. 4, pp. 1920-1932, 2015.
- [3] H. P. Liang and Z. T. H. Tse, "Cycloidal Stepper Motor: A Systematic Approach for Designing a Nonmagnetic Rotary Actuator," Ieee-Asme T Mech, vol. 28, no. 1, pp. 71-79, Feb 2023.

Toward Robotic Craniosynostosis Surgery: Development of a Novel Articulated Minimally Invasive Bone Cutting Tool

J. Law^{1,2}, D. Podolsky^{1,2}

¹*Center for Image Guided Innovation and Therapeutic Intervention, The Hospital for Sick Children, Canada,*

²*Institute of Biomedical Engineering, University of Toronto, Canada,
jones.law@mail.utoronto.ca*

INTRODUCTION

Craniosynostosis involves premature fusion of the cranial sutures resulting in an abnormal head shape and functional sequelae such as raised intracranial pressure [1]. Surgery is required and can be performed open or endoscopically. Both approaches require osteotomies to either remove the fused suture or to remodel the bone. The endoscopic approach is performed using smaller incisions and has reduced blood loss, operative time and cost in comparison to the open approach [2]. However, with the endoscopic approach, the osteotomy extent is limited due to reduced access using currently available surgical tools [3]. As a result, the patient is required to wear a molding helmet post-operatively and only certain types of craniosynostosis can be treated using this approach.

Conventional instruments for craniosynostosis surgery consists of straight rigid tools. They are simple and intuitive to manipulate with open accessibility, but are difficult to use in restricted areas. Furthermore, the unique curvature of the skull limits the reach of the instruments during craniosynostosis surgery.

A novel steerable instrument would allow performance of extensive osteotomies on the skull using key-hole incisions. Such a device would eliminate the need for a molding helmet and can be used to treat all types of craniosynostosis. The following paper describes a novel articulating bone cutting device specifically designed for keyhole craniosynostosis surgery that can also be utilized for any procedure requiring a craniotomy. This device would represent a paradigm shift in minimal access cranial surgery.

MATERIALS AND METHODS

Tool design and function

The tool comprises a flexible bending section, a rigid shaft, an end-effector, a driving unit, and a channel for inserting a flexible endoscope and is shown in Fig. 1(a). The flexible bending section (Fig. 1(d)) is constructed with three hinge joints in the pitch direction. The range of the bending radius of the mechanism was determined from the average curvature of a patient specific craniosynostosis skull model. The curvature of the bending section can be adjusted to conform to different regions of the skull.

The bending section is connected to a handle by a rigid shaft, which comprises a straight and a curved

section. The end-effector comprises a bone punch, dural protector, scalp retractor and endoscope for visualization (Fig 1(c)). The bone punch comprises two jaws: a static lower jaw and a cable actuated upper jaw that uses a three-bar-linkage mechanism (Fig 1(c)). The dural protector shields the brain and dura and the scalp retractor creates a soft tissue pocket for visualization.

Three cables are used for actuation: a pair of cables to drive the bending section, and a cable to actuate the bone punch. The cable pair passes through the bending section linkages and is fixed to the distal end while the proximal end is connected to a worm gear mechanism at the driving unit (Fig. 1(b)).

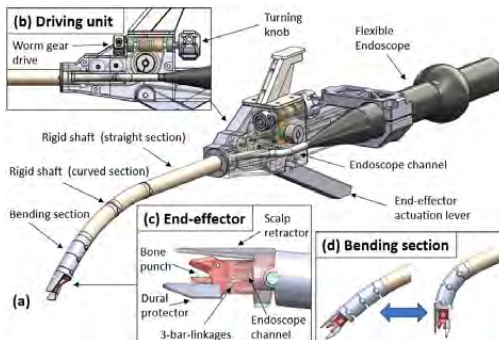


Fig. 1 System overview of the bone cutting tool: (a) the overall tool design, (b) the driving unit with an imbedded worm gear mechanism, and (c) the end-effector components including bone punch mechanism, scalp retractor, and dural protector. (d) The bending section can articulate to conform to different curvatures of the skull.

Prototype development

A prototype of the tool was developed using computer-aided-design (CAD) in SolidWorks (patent pending). Component parts were three-dimensionally (3D) printed in polylactic acid (PLA) and computer numerical control (CNC) machined in aluminum and stainless-steel.

Kinematic analysis and workspace simulation

The tool comprises three degrees-of-freedom (dof): (1) yaw at the insertion point $\theta_1 = [-65^\circ, 65^\circ]$, (2) longitudinal movement along the curved shaft and (3) articulation of the bending section in the pitch direction. The range of motion is defined by the arc length, which has a corresponding range of $\theta_2 = [0^\circ, 30^\circ]$. The articulating section is modelled by constraining the

bending angles of the three linkage joints to be evenly distributed due to the stiffness of the internal components, with a range of $\theta_3 = \theta_4 = \theta_5 = [5^\circ, 20^\circ]$. Denavit-Hartenberg (DH) parameters were used to determine the forward kinematics and the workspace was plotted visually using MATLAB.

Phantom model development and testing

A craniosynostosis phantom model was developed using patient specific imaging of an infant with craniosynostosis. The phantom was developed using a 3D printed skull in PLA and a casted silicone scalp. The phantom was used to simulate the workspace constraints. The tool was inserted through a keyhole vertex incision and tested for its ability to reach distal areas of the frontal, parietal, and occipital bones.

Mechanical testing

The force required to dissect simulated cranial bone was evaluated. A digital force gauge (BTE-500, HFBTE) was connected to the end-effector actuation cable to measure the cable tension required to cut the simulated bone (2mm thick biomechanical polyurethane foam sheet with 2 levels of density (PCF 30 and 40, Sawbones)).

EVALUATION AND RESULTS

The physical prototype was successfully developed and is shown in Fig 2.



Fig. 2 Physical prototype of the tool with coupled flexible endoscope.

The results of the workspace analysis can be seen in Fig. 3(a) and 3(b). The maximum deflection of the tool tip is 23.7 mm. The sweep angle of the fan shape is 120 degrees reflecting the yaw angle (θ_4) range at insertion. The downward curve represents the insertion movement along the curved shaft arc (θ_2).

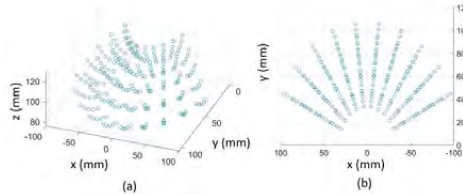


Fig. 3 Workspace analysis of the instrument: (a) Isometric view, and (b) top view of the reachable points of the workspace with the given joint range.

Phantom testing demonstrated the ability of the device to reach distal targets along the parietal, frontal, and occipital bones Fig. 4 (a,b and c).

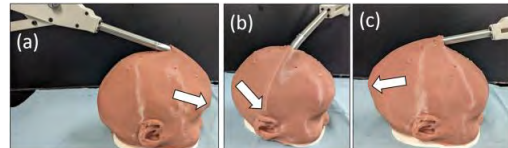


Fig. 4 The tool was inserted through a keyhole vertex incision on the phantom model, demonstrating reachability to the distal (a) frontal, (b) parietal and (c) occipital bone. Arrow used to indicate the maximum reach of the tool tip.

Fig. 5 demonstrates the cable tension required to cut the simulated bone (30 PCF density: 133N to 164N and 40 PCF density: 236N to 272N). The cutting force increased to less than 40N when the bending angles increased from a minimum (0°) to a maximum (45°).

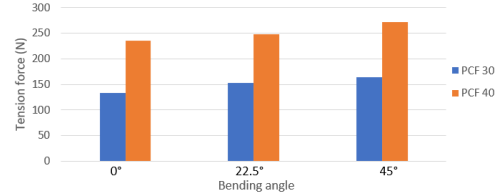


Fig. 5 The bone cutting force of the actuation cable when cutting simulated bone.

DISCUSSION

The presented tool demonstrates the ability to provide accessibility to a skull surface with varying curvature using a keyhole incision. The prototype also demonstrated that the design mechanism can deliver the required force to cut bone, and it is consistent when operating at different areas of the skull.

This tool represents a first step toward robotic craniosynostosis surgery by introducing a mechanism that offers both the necessary reach and mechanical capabilities. Future research will aim to enhance the system through the integration of motorized actuation, navigation and robotic manipulation.

REFERENCES

- [1] N. A. Shlobin et al., "Global Epidemiology of Craniosynostosis: A Systematic Review and Meta-Analysis," *World Neurosurgery*, vol. 164, pp. 413-423, 2022.
- [2] R. H. Han et al., "Characterization of complications associated with open and endoscopic craniosynostosis surgery at a single institution," *Journal of neurosurgery. Pediatrics*, vol. 17, no. 3, pp. 361–370, 2016.
- [3] M. A. Clayman, G. J. Murad, M. H. Steele, M. B. Seagle, and D. W. Pincus, "History of craniosynostosis surgery and the evolution of minimally invasive endoscopic techniques: The University of Florida experience," *Annals of plastic surgery*, vol. 58, no. 3, pp. 285–287, 2007.
- [4] Sawbones. (2023, 10th, Feb). Biomechanical Materials for Precise, Repeatable Testing. Available: <https://www.sawbones.com/biomechanical-product-info>.

Robotic Assistant for Image-Guided Treatment of Ankle Joint Dislocations: A Feasibility Study

G. Li¹, R. Vijayan², A. Uneri², B. Shafiq³, J.H. Siewerdsen⁴, and K. Cleary¹

¹*Sheikh Zayed Institute for Pediatric Surgical Innovation, Children's National Hospital*

²*Biomedical Engineering Department, Johns Hopkins University*

³*Orthopaedic Surgery Department, Johns Hopkins Medicine*

⁴*Department of Imaging Physics, The University of Texas MD Anderson Cancer Center*

gli2@cnmc.org

INTRODUCTION

Trauma to the ankle is an increasingly common injury and is a major source of long-term debility [1]. Over two million ankle injuries occur each year in the United States alone [2]. Over half a million ankle injuries require surgeries [1]. Multiple studies have demonstrated accurate reduction of the distal tibiofibular joint (syndesmosis) as a critical predictor of good clinical outcome [3], [4]. Surgical manipulation of the tibia and fibula is necessary to properly align and reduce the syndesmosis space in ankle fractures involving sprains of the syndesmosis. However, current techniques of manual reduction utilizing open or percutaneous approaches have been shown to result in inaccurate reduction of the syndesmosis [3], [4]. We propose a novel system that combines intraoperative imaging based on low-dose cone-beam computed tomography (CBCT) and 3D-2D image registration with robotic manipulation of the fibula to precisely restore its anatomical relationship with the tibial incisura. Our long-term goal is to develop robotic assistance with intraoperative imaging for precise reduction of the syndesmosis, while minimizing radiation exposure to the patient and the surgical staff. The focus of this study is to investigate the feasibility of the robot design and the potential clinical workflow.

MATERIALS AND METHODS

We designed and constructed a novel low-profile robotic device with a radiolucent end effector to manipulate the distal fibula, and a passive fixture to secure the tibia, as shown in Fig. 1. The robot was designed to provide 3 degrees-of-freedom (DOF) motion to precisely manipulate the fibula, while providing the range of forces required to carry out the reduction. The robot design illustrated in Fig. 2 provides two translational motions and one rotational motion. A distal fibula plate was used to fix the injured fibula, and the robot was attached to the plate via two threaded drill guides (DePuySynthes, USA). A 6-DOF force/torque sensor (ATI Industrial Automation, USA) was attached to the end of the robot

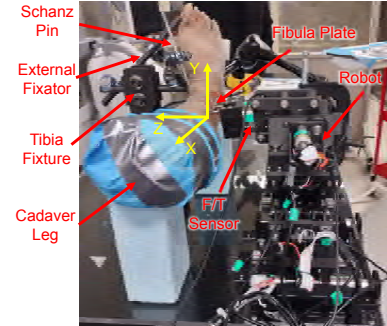


Fig. 1 Illustration of robot prototype and setup for cadaver study. The tibia was secured by the passive fixture via a Schanz pin and the fibula was manipulated by the robot.

to measure the force/torque applied to the fibula during the reduction. The end effector was designed with an offset of 50 mm away from the main body of the robot and was made of mostly radiolucent material, such that it does not occlude the anatomical structures in the fluoroscopic images and also provide sufficient space for the surgeon to operate surgical tools (e.g., drill, K-wires, and screws). A passive fixture was designed to secure the tibia using a Schanz pin and prevent it from moving during the reduction. The major parts of the robot and the passive fixture were printed with radiolucent Onyx plastic with carbon fiber reinforcement material (Mark Two, Markforged, USA). Manipulation of the distal fibula is subject to high forces that may result in unintended motion of the tibia and/or mechanical flex of the robot. To correct for such motion, a registration algorithm has been developed to localize the fibula and tibia using intraoperative fluoroscopy. The algorithm can compute the discrepancy between the intended fibula-tibia pose servoed to the robot and subsequently instruct the robot to alter and/or extend its path to achieve the desired pose.

Initial cadaveric studies were performed to assess the feasibility of the robot design and potential workflow. A lower right cadaver leg was used as specimen, which was placed in a supine position on an operating table. An incision was made to expose the proximal fibula region, and the tibia and fibula were separated by cutting four syndesmotic ligaments to reduce sprain of ankle syndesmosis. The fibula was manipulated by the robot on three principal directions of reduction, i.e. pulling-compressing, anterior-posterior translation, and external-internal rotation, as shown in Fig. 2. Manipulation forces/torques were measured by the F/T sensor and the displacements were monitored with 3D CBCT images. The registration algorithm was evaluated separately using a UR3e robot with a similar setup.

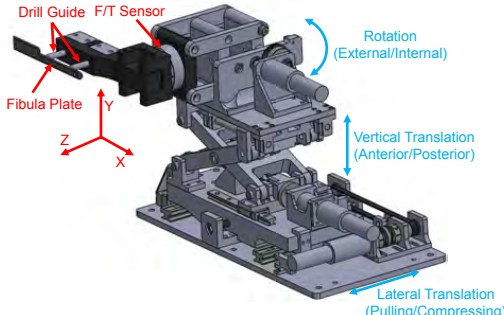


Fig. 2 CAD model of the robot design.

RESULTS

The robot was able to manipulate the fibula in the commanded directions and the presence of the robot did not affect the imaging quality. Fig. 3 demonstrates the neutral pose of the ankle and corresponding displacement after pulling and compressing the fibula. The results indicate a discrepancy between the commanded and the actual displacement. For instance, the commanded displacement for pulling was 14 mm, and the actual displacement of the fibula was 8.4 mm. The main source of the discrepancy was the deformation of the robot structure, due to the relatively low stiffness of the 3D printed plastic material. The imaging guidance algorithm was evaluated separately using a UR3e robot. Fig. 4 shows the error in estimating the separation between the fibula-tibia after servoing 7 mm of lateral pull to the robot, clearly indicating that use of image guidance allows accurate localization of the true fibula-tibia separation in the presence of motion and flexion.

DISCUSSION

This initial cadaveric study demonstrated that the robot is able to provide the required motion to manipulate the fibula, and the passive fixture can secure the tibia with minimal displacement. However, this proof-of-concept prototype was constructed with less rigid material, which leads to deformation of the structure.

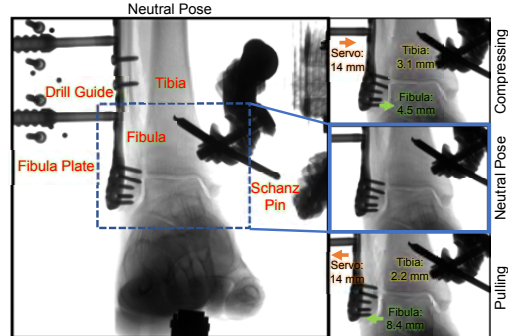


Fig. 3 Fluoroscopic images of the ankle showing its neutral pose and corresponding displacements obtained from 3D CBCT images after pulling and compressing the fibula.

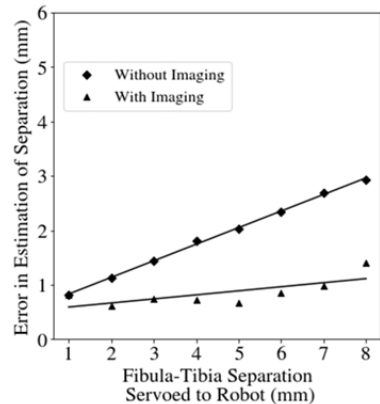


Fig. 4 Comparison of fibula-tibia separation with and without imaging guidance.

Future work will increase the rigidity of the robot by using engineering grade material and improving the structure design. We will also integrate the imaging guidance algorithm with the proposed robot to provide accurate manipulation of the fibula. The concept of robotic precision guided by intraoperative imaging may have other applications in procedures where precise manipulation of bony anatomy is required.

REFERENCES

- [1] S. Koehler, "Ankle fractures in adults," <https://www.uptodate.com/contents/ankle-fractures-in-adults>, 2023.
- [2] M. M. Herzog, Z. Y. Kerr, S. W. Marshall, and E. A. Wikstrom, "Epidemiology of ankle sprains and chronic ankle instability," *Journal of athletic training*, vol. 54, no. 6, pp. 603–610, 2019.
- [3] G. A. Naqvi, P. Cunningham, B. Lynch, R. Galvin, and N. Awan, "Fixation of ankle syndesmotic injuries: comparison of tightrope fixation and syndesmotic screw fixation for accuracy of syndesmotic reduction," *The American journal of sports medicine*, vol. 40, no. 12, pp. 2828–2835, 2012.
- [4] H. C. Sagi, A. R. Shah, and R. W. Sanders, "The functional consequence of syndesmotic joint malreduction at a minimum 2-year follow-up," *Journal of orthopaedic trauma*, vol. 26, no. 7, pp. 439–443, 2012.

TOWARDS CELLULAR LEVEL MICROSURGERY: DESIGN AND TESTING OF A HIGH PRECISION DELTA ROBOT FOR MEDICAL APPLICATIONS

Xiaoyu Huang¹, Elizabeth Rendon-Morales¹ Rodrigo Aviles-Espinosa ¹

¹ *Robotics and Mechatronics Systems Research Centre, School of Engineering and Informatics, University of Sussex, UK*

ra408@sussex.ac.uk

INTRODUCTION

The development of future surgical therapies has driven the efforts to increase the precision of robot-guided manipulators beyond sub-millimetre accuracies. Medical applications such as reconstructive microsurgery, vitreoretinal eye surgery and cellular level neurosurgery still require achieving precision comparable to the size of human cells [1]. Most commercially available systems can achieve millimetre accuracies with a few examples of higher precision instruments including ophthalmic and reconstructive microsurgery robots achieving accuracies within the range of hundreds of microns [1].

A parallel robot is a closed-loop mechanism where the end-effector is coupled to the base via multiple sequences of links. These devices are mostly used in industrial pick and place applications due their advantages including high precision, stiffness, speed, and low moving inertia [2]. However, a major disadvantage is their limited workspace and rotational capabilities. In the context of cellular level surgical applications, having a reduced workspace does not represent a disadvantage given that, as in most of the cases, the surgical procedure is to be performed within a reduced manipulation volume.

This paper presents an integrated methodology outlining the design and testing of a delta robot based on linear actuators achieving micron level end effector positioning accuracy. The main application of the here presented design is to perform superficial tissue optical biopsy with future prospects of being able to conduct cellular level surgeries. The design methodology considers two parameters determining the robot geometry and dimensions these are: the end-effector workspace ($\sim 5 \text{ mm}^3$) and the end-effector motion resolution ($1 \mu\text{m}$). The robot performance was evaluated using a non-contact metrology approach based on bright field microscopy (BFM) to characterize the precision and kinematic performance. Our results demonstrate that the presented methodology can be used for designing high precision robots achieving accuracies $< 1 \mu\text{m}$.

MATERIALS AND METHODS

The design methodology of the high precision delta robot presented in this work is divided into two stages: robot design and implementation followed by experimental evaluation.

Robot design and implementation

Figure 1 shows the geometric analysis of a simplified model of our linear delta robot. The end-effector of the

robot is connected to the driving leadscrews (a, b, c) through 3D printed joints attached to the robotic arms having a set of ball joints attached at both ends. To keep the stability of the end-effector, the robotic arms adopt a parallelogram structure as shown in Fig 1.

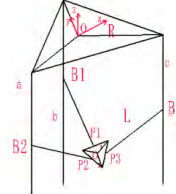


Fig.1 Simplified model of a linear delta robot

The centre of the base platform is formed by three stepper motors O with coordinates $(0,0,0)$. The coordinate of the end-effector O' is (x, y, z) , and the coordinates of the connect joints B_1, B_2, B_3 are $(0, \sqrt{3}/2, z_1)$, $(-\sqrt{3}/2, z_2)$, $(\sqrt{3}/2, 0, z_3)$ respectively. Then the relationship between the arm length L , radius of the base platform R , and radius of the end-effector platform r can be obtained.

$$\overrightarrow{OO'} = \overrightarrow{OB_1} + \overrightarrow{B_1P_1} + \overrightarrow{P_1O'} \quad (\text{Eq. 1})$$

$$x^2 + (y + r - R)^2 + (z - z_1)^2 = L^2 \quad (\text{Eq. 2})$$

$$(x - \frac{\sqrt{3}}{2}(r - R))^2 + (y - \frac{1}{2}(r - R))^2 + (z - z_2)^2 = L^2 \quad (\text{Eq. 3})$$

$$(x - \frac{\sqrt{3}}{2}(r - R))^2 + (y - \frac{1}{2}(r - R))^2 + (z - z_3)^2 = L^2 \quad (\text{Eq. 4})$$

By combining equations 1 to 4, the end-effector position (O') with coordinates B_1, B_2 and B_3 can be expressed. As a result, the main factors affecting the end-effector displacement and moving resolution are the arm length L and the base platform radius R . Using equations 1 to 4 while defining the motion limits of B_1, B_2 and B_3 , the motion state of O' can be represented dynamically though simulations. The robot design, including the kinematics modelling and simulation was based on-MATLAB 2020 (MathWorks, USA) and CATIA V5-6R2018 (Dassault systems, France). Simulation results showed that the dimensions satisfying the design requirement resulted in the following arm length and radius of the base platform of $R = 250\text{mm}$, $L=235\text{mm}$, $r=20\text{mm}$.

RESULTS

Considering the stepper motor operation parameters of $0.2\mu\text{m}/\text{step}$ under 1/8 micro stepping (rotational steps of 0.225°) and $1.75\mu\text{m}/\text{step}$ under full stepping (rotational steps of 1.8°) and tracing the trajectories of the end-

effector O' using the obtained R, L parameters, resulted in a simulated workspace of $4.01\text{mm} \times 4.43\text{mm} \times 5.61\text{mm}$. We then consider that the robot design requires to withstand a total mass of 2kg where the end-effector will integrate a bright field microscope and vision tools. Using the simulated model developed in Fig 2. The torque values for single joints were obtained tough the inverse kinematics. Results showed that the maximum torque requirement for the application is 0.09 N.m per joint. These theoretical values were used for the selection of the robot actuators providing a maximum torque up to 0.12 Nm.

Figure 2 shows the delta robot implementation. This was built using extruded aluminium beams (MakerBeam B.V., Netherlands), injection moulded brackets, sealed chrome Steel bearings and built-in-house 3D printed joints. The drive system uses a 35mm SH3533-12U40 unipolar stepper motor (Sanyo Denki, Japan) and a BSD 02.V motor driver (RTA Pavia, Italy). The robotic system is controlled though a custom-made GUI operated though an FPGA (NI MyRIO 1900 NI, Austin, Texas, USA).

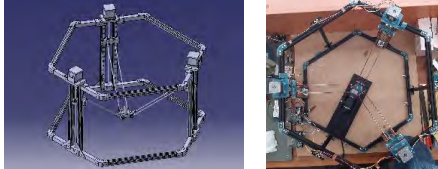


Fig.2 3D model of the delta robot (left) and final robot prototype tested using bright field microscopy system

Experimental evaluation

To characterize the precision and kinematic performance of the linear delta robot manipulator, a non-contact metrology approach based on BFM was implemented. The BFM system is based on a 5 elements microscope objective lens (Celestron LLC, Torrance, California, United States) having an equivalent focal length of 15.8mm. Magnification is adjusted though a tube slider adjusting the lens distance between a 5 MP camera and the object. The device is mounted in two positions: for lateral and planar motion characterization as shown in Fig 3. The BFM system is used to track the robot motion within its workspace obtaining images for set trajectories.

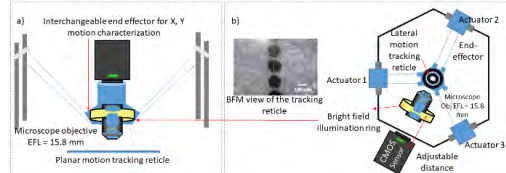


Fig.3 Experimental setup of the delta robot and BFM system a) lateral view, (b) top view.

Evaluation of the delta robot manipulator was conducted to assess the X, Y and Z axis end-effector moving resolution. The test parameters include discrete steps motion (1 to 12 steps), three velocity settings (Low 103.8 $\mu\text{m/s}$, Medium 207.6 $\mu\text{m/s}$ and High 311.4 $\mu\text{m/s}$) as well as two micro stepping settings (1/2 and 1/8).

Simulations were performed using discrete steps of 1, 4, and 12, to obtain the base line theoretical displacements for each set of steps yielding 0.625 μm , 2.5 μm , 7.5 μm respectively.

Table 1 shows practical results when assessing Z axis end-effector moving resolution considering Low, Medium and High speeds with the actuators set to 1/8 micro-stepping.

Speed [$\mu\text{m/s}$]	Stepper motor steps	Simulation results [μm]	Practical results [μm]	Error [μm]
Low 103.8	1	0.625 μm	1.32	± 0.02
	4	2.5 μm	2.62	± 0.07
	12	7.5 μm	7.81	± 0.09
Medium 207.6	1	0.625 μm	1.72	± 0.05
	4	2.5 μm	2.61	± 0.07
	12	7.5 μm	8.18	± 0.26
High 311.4	1	0.625 μm	1.75	± 0.03
	4	2.5 μm	2.63	± 0.04
	12	7.5 μm	8.08	± 0.24

Table 1.

DISCUSSION

From the results presented in table 1, when the robot is driven in single steps, the actual displacement results in a motion of 2.1 to 2.8 times the theoretical obtained value. This result is expected given that the motion involves acceleration and de acceleration, being more evident while operating the system at higher speeds. However, in real working conditions, the robotic system will follow a set trajectory defined by the medical procedure. When setting the system to move in continuous stepping mode i.e., 4 by 4-steps and 12 by 12-steps, the error between the actual value and the theoretical value is reduced to 4.8% while performing movements of 4 by 4 steps and 6.9% (considering the three speed settings results average) while performing movements of 12 by 12 steps compared to our theoretical baseline.

In this paper a design methodology outlining the numerical calculations and simulation of a linear delta robot requiring to achieve a specific end effector-motion resolution and workspace has been presented. The design was validated through simulations and kinematic tests assessing its performance using a BFM. The developed system is capable of producing micron level precision end effector motion demonstrating that the current prototype is has the potential to be used for cellular level surgical procedures.

REFERENCES

- [1]. Brodie A, Vasdev N. The future of robotic surgery[J]. The Annals of The Royal College of Surgeons of England, 2018, 100(Supplement 7): 4-13.
- [2]. Rodriguez E, Riaño C, Alvares A, et al. Design and dimensional synthesis of a Linear Delta robot with single legs for additive manufacturing[J]. Journal of the Brazilian Society of Mechanical Sciences and Engineering, 2019, 41(11): 1-23.

Computational Analysis of Design Parameters for a Bimanual Concentric Push-Pull Robot

T. Qin¹, P. Connor², K. Dang³, R. Alterovitz¹, R. J. Webster², and C. Rucker³

¹*Department of Computer Science, University of North Carolina at Chapel Hill*

²*Department of Mechanical Engineering, Vanderbilt University*

³*Department of Mechanical Engineering, University of Tennessee, Knoxville*

tonyqin@cs.unc.edu

INTRODUCTION

Colorectal cancer is a pervasive disease: an estimated 4.6% of men and 4.2% of women will suffer from it in their lifetime [1]. Precancerous polyps can be small (<5 mm) medium (6-9 mm) or large (>10 mm) [2]. Small polyps are most frequent, but polyps too large for immediate endoscopic removal during screening occur 135,000 times per year in the US alone [1]. There are two primary options for removing these polyps: endoscopic removal or partial colectomy. Endoscopic procedures, such as endoscopic submucosal dissection (ESD), are less invasive and reduce the risk of infection, reoccurrence, and other adverse events [3]. Despite this, approximately 50,000 patients each year undergo partial colectomies for polyps which could have been removed endoscopically [4].

A primary obstacle to wider use of endoscopic procedures is how challenging they are for physicians to perform, due to the limited dexterity of existing trans-endoscopic tools [5]. Currently tools come straight out the tip of the colonoscope and moving them requires moving the tip of the colonoscope [6]. To enable tools to move independent of the colonoscope, we propose an endoscopically deployable, flexible robotic system, as shown in Fig. 1. This system deploys a flexible robotic arm through each channel of a standard 2-channel colonoscope. Each arm is composed of a setup sheath followed by a steerable sheath, with each sheath built using a concentric push-pull robot (CPPR) [7]. Each arm has a hollow central lumen through which tools (e.g. forceps, electrosurgery probes, etc.) can be passed. This design adds dexterity and provides the physician with two independent manipulators, with the goal of making ESD easier to perform.

In this paper, to inform the design of the system, we computationally analyze the relationship between the reachable workspace of the push-pull robot and its design parameters. We note there are inherent trade-offs in the design parameters, e.g., increasing the length parameters of the setup sheaths increases the distal reachable workspace but may limit the proximal reachable workspace. For a candidate design, we evaluate the

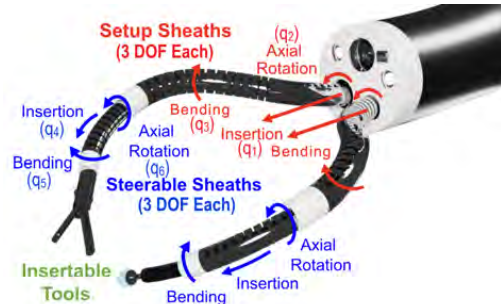


Fig. 1 Degrees of Freedom of a Bi-manual Push-Pull Robot with Setup and Steerable Sheaths.

reachable workspace by running forward kinematics over a wide range of actuatable configurations and compare the resulting reachable workspace to the field of view of an endoscopic camera. We conduct this evaluation for a wide range of candidate designs. This work will inform future work on tube design for the proposed system.

MATERIALS AND METHODS

The proposed bimanual system is based on using multiple CPPRs, each composed of a nested pair of Nitinol (NiTi) tubes, which are asymmetrically laser patterned to offset the neutral bending axes from each other, and joined at their tips, such that relative translation of the tube bases results in bending [7].

The proximal and distal setup sheaths are actuated into an “S” shape. The proximal segment will have a length, L_1 , and curvature, q_3 . The distal segment will have a length, L_2 , and the same curvature in the opposite direction, $-q_3$. The two curved segments are separated by a short straight segment of length L_s .

For the setup sheaths, the design parameters are the following geometric properties:

- Max curvature of the setup sheaths ($q_3 < \kappa_{max}$),
- Length of the curved proximal segment (L_1), and
- Length of the curved distal segment (L_2).

For the steerable sheaths, greater curvature and insertion capabilities will improve the reachability in the workspace of the robot, so we assume maximal values. The limits

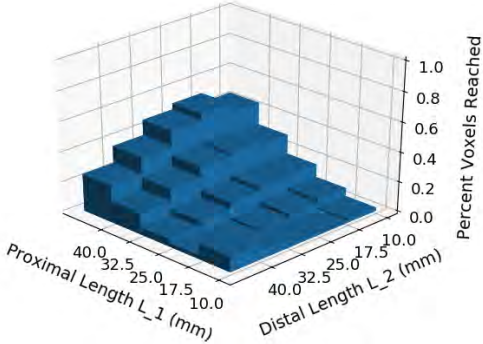


Fig. 2 This plot shows the percentage of workspace voxels reached with a maximum setup sheath curvature of 0.4mm^{-1} as a function of the two setup curvature lengths.

i	1	2	3	4	5
L	q_1	L_1	L_s	L_2	q_4
κ	0	q_3	0	$-q_3$	q_5
ϕ	q_2	0	0	0	q_6

TABLE I Parameters used for Evaluation of each Constant Curvature Transformation Matrix $T_{cc,i}(L, \kappa, \phi)$

for curvatures and lengths were selected based on prior experience with maximum manufacturable values. The robot can actuate the DOF shown in Fig. 1. For the setup sheaths, the DOF are base insertion (q_1), axial rotation (q_2), and curvature (q_3). For the tip steerable sheaths, the DOF are insertion (q_4), curvature (q_5), and axial rotation (q_6). The target workspace is determined by the field of view for a commercial colonoscope. Based on the Olympus CF-2T160I, the field of view is 140 degrees and depth of field is 3-100 mm respectively. We discretized the resultant volume into cubic voxels with edge length 5 mm. To evaluate the reachable voxels of each design, we iteratively computed the results of the forward kinematics. The forward kinematics is based on a constant curvature model with a transformation matrix T_{cc} allowing for length L , curvature κ , and axial rotation ϕ as denoted in Table I. [8]: $T_{base}^{\text{tip}} = \prod_{i=1}^5 T_{cc,i}^{\sim}$

We computed the resulting tip location for each combination of design parameters and actuation variables. The tip location was then used to mark a corresponding voxel in an occupancy array. The best design was then determined by the highest coverage percentage of reachable voxels in the workspace.

RESULTS

Figure 2 illustrates the trends in the reachable workspace as a function of each design parameter. The plot shows that increases in the length of the proximal section generally lead to a larger proportion of the target workspace being reached. The largest reachable workspace was achieved with a setup sheath having proximal length of $L_1 = 40$ mm and distal length of $L_2 = 10$ mm. Fig. 3 shows the workspace and example configurations of this design,

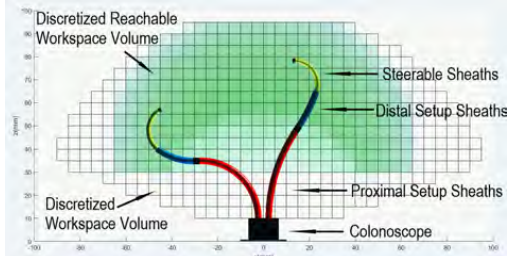


Fig. 3 Bi-manual CPPR system and its workspace. The boxes show a 2D slice of the voxels of the workspace. The green indicates the voxels that are reached. Darker green regions indicate higher sampled point density.

which is able to reach 50.1% of the camera's field of view.

A maximum setup sheath curvature of 0.04mm^{-1} was chosen as an estimated maximum based on previous work on tube cut pattern designs. Further experiments showed that more voxels are reached with a higher maximum curvature up to 0.10mm^{-1} , beyond which there are diminishing returns.

DISCUSSION

This paper outlines early work toward designing a bi-manual CPPR capable of completing ESD. Proceeding with the resulting design parameters of tubes, we can continue work on modeling, actuation, and control of the robotic manipulators. Future work will involve the implementation of intuitive controls for surgeons, modeling of the robotic system, and optimizing the transfer of actuation actions through the length of the colonoscope. Additionally, testing in live porcine models is planned for validation of in-vivo ESD performance. With this work as a cornerstone, we ultimately hope to realize the potential benefits of ESD and improve surgical outcomes.

REFERENCES

- [1] W. Street, "Colorectal cancer facts & figures 2017-2019."
- [2] D. Joseph et al., "Colorectal cancer screening: Estimated future colonoscopy need and current volume and capacity," *Cancer*, vol. 122, no. 16, pp. 2479–2486.
- [3] H. Ono, "Endoscopic mucosal resection for treatment of early gastric cancer," *Gut*, vol. 48, no. 2, pp. 225–229.
- [4] K. D. Miller, R. L. Siegel, C. C. Lin, A. B. Mariotto, J. L. Kramer, J. H. Rowland, K. D. Stein, R. Alteri, and A. Jemal, "Cancer treatment and survivorship statistics, 2016," *CA: A Cancer Journal for Clinicians*, vol. 66, no. 4, pp. 271–289.
- [5] Y. Cui, C. C. Thompson, P. W. Y. Chiu, and S. A. Gross, "Robotics in therapeutic endoscopy (with video)," *Gastrointestinal Endoscopy*, vol. 96, no. 3, pp. 402–410, 2022.
- [6] M. Kranzfelder, A. Schneider, A. Fiolka, S. Koller, D. Wilhelm, S. Reiser, A. Meining, and H. Feussner, "What do we really need? visions of an ideal human-machine interface for NOTES mechatronic support systems from the view of surgeons, gastroenterologists, and medical engineers," *Journal of Medical Devices*, vol. 22, no. 4, pp. 432–440.
- [7] K. Oliver-Butler, J. A. Childs, A. Daniel, and D. C. Rucker, "Concentric push-pull robots: Planar modeling and design," *IEEE Transactions on Robotics*, vol. 38, no. 2, pp. 1186–1200.
- [8] R. J. Webster and B. A. Jones, "Design and kinematic modeling of constant curvature continuum robots: A review," *IEEE Transactions on Robotics*, vol. 29, no. 13, pp. 1661–1683.

Toward Multiple-Point Stiffness Changing Surgical Needle for Eye Surgery Robotic System

Rongwan Chen¹, Seong Young KO¹

¹Department of Mechanical Engineering, Chonnam National University, South Korea
rwchen@jnu.ac.kr, sko@jnu.ac.kr

INTRODUCTION

Nowadays, minimally invasive surgeries require thin and slender instruments, such as needles and catheters, which can reach the surgical sites inside the human body. Especially, eye surgery requires high precision and steady manipulation of the inside of the the human eyeball. Through this manipulation, diseases such as epiretinal membrane, retinal detachment, diabetic retinopathy, and macular holes can be treated, and drugs can be delivered to the target sites for effective treatment [1].

There are two classifications of stiffness change robots that can be used for ophthalmic surgery. One is to use two or more pre-curved elastic material tubes and control it by the insertion/retraction and axial rotation motions. Another one is to use the tendon-pulley mechanism [2],[3]. Ravigopal *et al.* proposed the mechanism using one tendon and notched tube [4] and Jeong *et al.* utilized one tendon and two notched tubes [5], which are for cardiovascular diseases. Kim *et al.* presented interaction forces of one inner tube and one outer tube with a specific pattern to change the stiffness of wires with diameters of 8~10mm[6] and 1~2mm[7]. In this paper, we propose a mechanism that can change change the stiffness of the needle at two different points independantly.

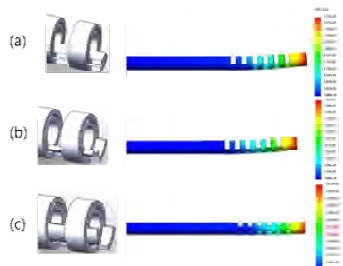


Fig. 1 Simulation on different rotation position with inner and outer tubes having one notched section. (a) Fully overlapped case (weak case), (b) case with 60° rotation, (c) case with 120° rotation.



Fig. 2 Sectional view: (a) None is notched (b) Outer tube is notched, (c) Inner tube is notched, (d) Both are notched (adjustable case), (e) Both are notched and completely overlapped (weakest case).

DESIGNE AND SIMULATION

The robotic surgical tools with a smaller diameter cause less damage to the patient and the easier recovery. In this study, we propose the robotic tool that can change its stiffness and its tip position. For this purpose, it is designed so that it includes an outer tube with an outer diameter (OD) of 0.5 mm (<21 G), an inner tube, and a tendon. To explain the concept, first, Figure 1 shows the change in stiffness according to three different rotational positions of the notched inner tube and the notched outer tube. A 1 N force is applied at the distal tip. Figure 1 shows that the stiffness of the needles can be changed more than 4 times by changing their relative rotational angle.

Based on the simulation results, the stiffness value of the needle can be estimated according to the relative position of the notched tube as shown in Fig 2. As shown in Fig. 2(a), if both the inner tube and the outer tube do not have notches, the stiffness is the highest. If either tube does not have notches as shown in Fig. 2(b) and 2(c), the stiffness will be slightly smaller. The stiffness becomes smaller if both tubes have notches as shown in Fig. 2(d) and 2(e), and the smallest when the two completely overlap as in Fig. 2(e).

Using these characteristics, we propose the novel stiffness changing mechanism. The mechanism has two tubes and one wire. Each tube has two notched sessions (one is a distal and the other is a proximal). By changing the relative position (rotation/translation) between the tubes, the stiffness of the robotic needle system can be adjusted. Fig. 3 shows a simplified conceptual working principle. Fig. 3(a) shows the case in which the distal notched session (Part 1) becomes weak, and Fig. 3(b) shows the case in which the proximal notched session (Part 2) becomes weak. In Fig. 3(c), both notched sessions become stronger. Since the weaker notched

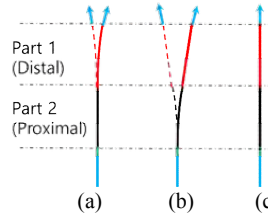


Fig. 3 Concept figures of the distal and proximal part: (a) the distal notched session (Part 1) bends easily, (b) the proximal notched session (Part 2) bends easily. (c) Both bends less, strongest case.

session bends easier, when the wire is pulled, the needle moves further in the case of Fig. 3(b) than case of Fig. 3(a). Fig 3(c) is considered as a stronger version by using a symmetrical design. This case can be used during the robotic needle system is inserted into the eyeball. The adjustable case as shown in Fig 2(d) will be used mainly to change the stiffness actively. The different rotation of inner tube and outer tube can change the stiffness.

MANUFACTURE AND EXPERIMENT

The needles are manufactured by a femtosecond laser machine as shown in Fig 4. The initial shape of tubes is not straight, which may be caused by the thermal effect during the femtosecond laser manufacture processing. It will be further modified by changing manufacturing parameters.

The tendon (or wire) will be fixed at region A of the inner tube using a glue as shown in Fig 5. The force will be applied by putting this tendon to activate the bending motion of the needle body. The experiment setup was designed so as to precisely adjust their relative pose manually as shown in Fig 5. Here X_1 is the position of the outer tube, X_2 and R_2 are the position and rotation of the inner tube respectively. X_3 is the tendon's position. Currently, one simple experiment of adding a 2g weight to the tip of the needle has been performed using the

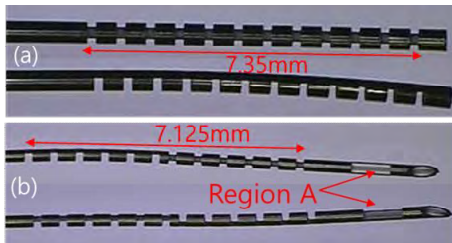


Fig. 4 Processed prototype of superelastic nitinol tube (front and top views): (a) Outer tube (OD/ID = 0.5/0.4mm), (b) Inner tube (OD/ID = 0.33/0.23mm).

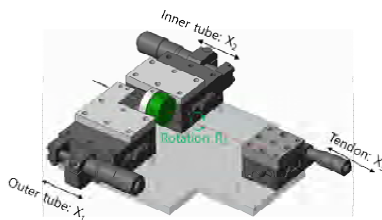


Fig. 5 Experiment setup. Relative positions of the tubes and tendon are adjusted manually.

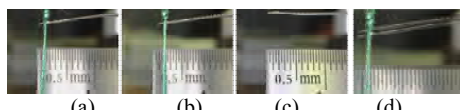


Fig. 6 Stiffness change by 2g weight: (a) Part 1 is weak, (b) Part 2 is weak, (c) Relax statue, (d) Partially overlap the (a) & (b) needles.

experimental setup as shown in Fig. 5. Fig 6(a-c) shows three cases corresponding to Fig 3. The deflection amount will be obtained by comparing the force-applied cases (Fig 6(a)(b)) to the relaxed case (Fig 6(c)). Fig. 6(d) shows the overlapped image of Fig. 6(a) and 6(b) for easier comparison.

RESULTS

This paper proposes the novel stiffness changing needle mechanism combining two notched tubes and one tendon. By changing the relative position between the tubes, we can change the stiffness of the specific parts of needles independently. In this paper, we only showed the first prototype and feasibility of this concept.

DISCUSSION

During the preliminary experiment, the deflection amount could be obtained easily in real-time when changing the stiffness using the experimental setup as in Fig. 5. This means that the proposed structure shows its feasibility. Further simulation on the custom size and machining of high quality will be carried out to prove its efficacy during the eye surgery. More accurate observation equipment will be fabricated to evaluate the system's performance.

ACKNOWLEDGEMENT

This paper was supported by the National Research Foundation of Korea (NRF) grant funded by the Korea government (MSIT) (No. 2022R1A2C2008422).

REFERENCES

- [1] Fleming I, Balicki M, Koo J, Iordachita I, Mitchell B, Handa J, Hager G, Taylor R. Cooperative robot assistant for retinal microsurgery. *Med Image Comput Comput Assist Interv*. 2008;11(Pt 2):543-50.
- [2] Gilbert HB, Rucker DC, Webster III R J. Concentric tube robots: The state of the art and future directions. *Robotics Research*, 2016; 253-269.
- [3] Burgner-Kahrs J, Rucker DC, Choset H. Continuum robots for medical applications: A survey[J]. *IEEE Transactions on Robotics*. 2015; 31(6): 1261-1280.
- [4] Ravigopal SR, Brumfiel TA, Desai JP. Automated Motion Control of the COAST Robotic Guidewire under Fluoroscopic Guidance. *IEEE 2021 International Symposium on Medical Robotics (ISMR)*. 2021: 1-7.
- [5] Jeong S, Chitalia Y, Desai JP. Design, modeling, and control of a coaxially aligned steerable (coast) guidewire robot. *IEEE Robotics and Automation Letters*, 2020; 5(3): 4947-4954.
- [6] Kim J, Choi WY, Kang S, et al. Continuously variable stiffness mechanism using nonuniform patterns on coaxial tubes for continuum microsurgical robot. *IEEE Transactions on Robotics*. 2019; 35(6): 1475-1487.
- [7] Kim J, Kim C, Kang S, et al. A novel variable stiffness mechanism for minimally invasive surgery using concentric anisotropic tube structure. *The Hamlyn Symposium on Medical Robotics*. 2017: 43-44.

Ultrasonically-Lubricated Catheters: A Proof of Concept

Mostafa A. Atalla^{1,2}, Jeroen J. Tuijp¹, Michaël Wiertlewski², and Aimée Sakes¹

¹ Department of BioMechanical Engineering, TU Delft,

² Department of Cognitive Robotics, TU Delft

m.a.a.atalla@tudelft.nl

INTRODUCTION

Over the past few decades, minimally-invasive endovascular interventions have proved its benefits over conventional open heart surgeries, leading to shorter recovery times and lower infection rates. In a typical endovascular procedure, the interventionist inserts a catheter in the radial or femoral artery and navigates it through the arteries to the heart, where the intervention is performed. In order to safely reach the heart, the catheters (and guidewires) used during these procedures need to easily follow the curves in the vascular system, while creating as little friction as possible with the blood vessel wall. If these devices exhibit high friction, there is a risk of damage to the mucous membranes or the intima of the blood vessels, which may lead to infectious diseases or thrombus formation [1], [2]. While low friction is beneficial to avoid damage to the membranes and blood vessel wall, it makes holding a specific location in open spaces, such as inside the heart, difficult. This is particularly true when high forces need to be applied, such as when cutting or puncturing tissues. This suggests the need for new advanced catheters whose frictional properties are controllable and can be adjusted depending on the phase of the catheterization procedure; for instance, having low friction while navigating through the vasculature and switching to a high friction state while executing the surgical task.

In this work, we propose a novel concept of a variable friction catheter, which comprises discrete modules for friction control. We hereby present the proof-of-concept of the friction control modules, which we characterized in simulation and experimentally. Finally, we present the preliminary results of the sliding friction experiments.

MATERIALS AND METHODS

A. Ultrasonic Lubrication

When two objects slide over each other, it was found that inducing transverse ultrasonic vibration, in one of those objects, can reduce the effective friction force experienced by the sliding bodies, in what is called Ultrasonic Friction Modulation (UFM). This ultrasonic excitation creates a pressurized thin cushion of the surrounding fluid medium, which separates the two surfaces

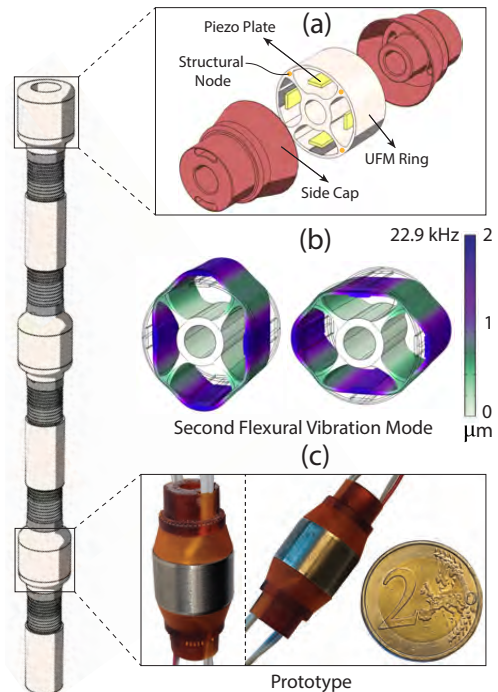


Fig. 1 Illustration of the concept of ultrasonically lubricated catheters (a) Design of the friction control module (b) Eigenfrequency simulation of the designed module (c) Module prototype.

away from each other, resulting in controllable active lubrication at the interface [3]. This technology proved its effectiveness in different applications where modulating friction is desirable, such as haptic touch displays and squeeze film air bearings. The capability of UFM to switch between high and low friction states, suggests the potential of this technology to fulfill the friction modulation requirement of future smart catheters.

B. Design of Friction Control Module

To enable friction control in catheters, we propose a discrete module design concept in which UFM modules

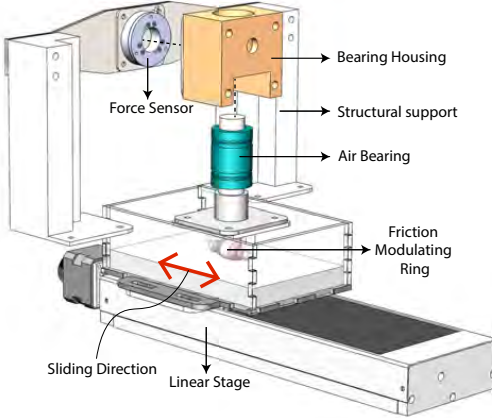


Fig. 2 Experimental setup for testing the friction modulation capabilities of the proposed system.

are integrated along the catheter's shaft as shown in Fig.1. The design requirements for the UFM modules, to ensure proper functionality, includes technology and application requirements. The technology requires the modules to achieve around ($2 \mu\text{m}$) transverse vibration amplitude at ultrasonic frequency ($> 20 \text{ kHz}$), while the application requires the design to be tubular, to have a lumen and to have the potential to be downsized. To tackle these requirements, we designed a resonating ring which comprises four piezoelectric plates, as shown in Fig.1(a), such that when the piezo plates are activated, a standing flexural wave is induced in the ring as shown in Fig.1(b). The frequency of this wave coincides with the second flexural resonance mode (second harmonic) of the ring structure, which is governed by diameter and wall thickness of the ring. To properly support the ring, the inner structure is connected to the ring at the nodes of the standing wave as shown in Fig.1(a) to ensure minimal interference with the generated wave.

C. Experiment

To validate the concept, we fabricated a scaled-up titanium ring prototype of diameter (15 mm), wall thickness (0.5 mm) and length (10 mm). We carried out a computational FEM simulation estimating the resonance frequency of this prototype to be (22.9 kHz) and the amplitude potentially reaching ($1.8 \mu\text{m}$) as shown in Fig.1(b). To characterize the performance of the prototype, we conducted a frequency-sweep experiment using a laser Doppler vibrometer to reveal the actual resonance frequency and maximum achievable amplitude of the ring. Furthermore, we designed a feasibility experiment, shown in Fig.2, in which we measured the sliding friction force experienced by the ring in both on and off cases, over a PMMA surface in a container partially filled with water, at a sliding speed of (0.1 mm/s), for a stroke of (2 mm) forward and backward and under a (1.1 N) load which lies in the range of critical contact forces for catheters [4].

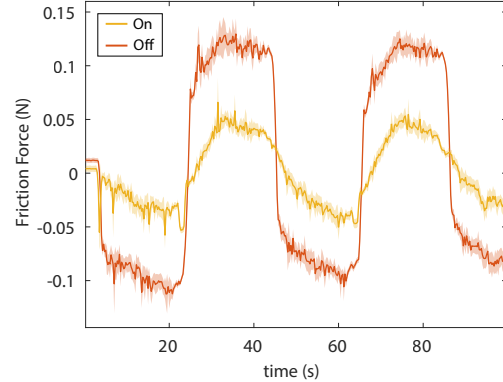


Fig. 3 Experimental measurements showing a comparison between the friction force when the UFM module is on (yellow) versus when it is off (red) under loading of (1.1 N). Solid lines represent the mean of five trials while the shades represent their standard deviation.

RESULTS

The vibration characterization experiments showed that the actual frequency of the desired mode is (19.7 kHz) and the maximum vibration amplitude is ($0.9 \mu\text{m}$). The preliminary friction experiments, repeated five times, showed that the UFM ring prototype achieved up to 50% friction reduction, when activated, while sliding over solid PMMA surface, as shown in Fig.3.

DISCUSSION

The preliminary experimental results showed that the prototype successfully achieved a significant friction reduction in the designed feasibility experiment, validating the design concept and further demonstrating its potential for medical applications. In the future, we plan to further develop the system to achieve higher vibration amplitudes, which could potentially lead to increased friction reduction. In addition, we plan to test the system in a clinically-relevant environment in tissue phantoms and ex-vivo animal tissues.

Please contact the following e-mail address with any questions: m.a.a.atalla@tudelft.nl

REFERENCES

- [1] R. M. Wagner, R. Maiti, M. J. Carré, C. M. Perrault, P. C. Evans, and R. Lewis, "Bio-tribology of vascular devices: A review of tissue/device friction research," *Bioribotology*, vol. 25, p. 100169, 2021.
- [2] K. Takashima, R. Shimomura, T. Kitou, H. Terada, K. Yoshinaka, and K. Ikeuchi, "Contact and friction between catheter and blood vessel," *Tribology International*, vol. 40, no. 2, pp. 319–328, 2007.
- [3] M. Wiertlewski, R. F. Friesen, and J. E. Colgate, "Partial squeeze film levitation modulates fingertip friction," *Proceedings of the National Academy of Sciences of the United States of America*, vol. 113, no. 33, pp. 9210–9215, 2016.
- [4] N. Xiao, J. Guo, S. Guo, and T. Tamiya, "A robotic catheter system with real-time force feedback and monitor," *Australasian physical amp; engineering sciences in medicine*, vol. 35, no. 3, p. 283–289, 2012.

Augmented Reality-assisted Epidural Needle Insertion: User Experience and Performance

Negar Kazemipour^{1,2}, Amir Sayadi¹, Renzo Cecere¹, Jake Barralet¹, and Amir Hooshiar^{*1}

¹*Surgical Robotics Centre, McGill University, Montreal, QC, Canada*

²*Applied Perception Laboratory, Concordia University, Montreal, QC, Canada*

**seyed.hooshiarahmedi@mail.mcgill.ca*

INTRODUCTION

The epidural injection is a medical intervention to inject therapeutics directly in the vicinity of the spinal cord and the nerves branching from it. Epidural needle insertion is a blind procedure that relies merely on the physician's tactile feedback. Nevertheless, tactile feedback can be polluted with needle-tissue friction and may vary from patient to patient. In order to achieve sub-millimetre accuracy, preempt neurological damage, and reduce the radiation exposure time for patients and physicians, new technologies have been used. Most recently, augmented reality (AR)-based methods have shown promising results in reducing the need for intraoperative X-ray imaging, especially in spine surgery. AR navigation is based on displaying images directly on a wearable device or screen visualizing surgical instruments and patients' anatomy. Combined with robotic precision, AR shows an excellent prospect for increasing accuracy for spinal injection similar to that of spine surgery [1]. Studies have shown that the AR navigation systems, when compared to the free-hand methods, resulted in increased precision of pedicle screw placement without intraoperative fluoroscopy [1], [2] and decreased radiation [3]. Inspired by the recent developments in spine surgery, in this study we have studied the user experience who used our robot-assisted needle insertion system for epidural space localization and needle insertion. In addition, the accuracy and repeatability of augmented reality-assisted epidural needle insertion were compared to that of non-assisted robotic needle insertion. For user experience assessment, NASA Task Load Index (TLX) [4] was used and analyzed.

MATERIALS AND METHODS

Fig. 1 shows the needle insertion setup used in this study. For brevity, we have not provided details of the utilized needle insertion robotic system. The aim of the study was to evaluate the accuracy and repeatability of the AR-assisted system. To generate patient-specific 3D holograms that were projected to the physician's display, first, a patient-specific anatomical model was created based on a patient's lumbar CT scan using Mimics Medical (Materialise, Belgium) software. Afterward, the vertebral bones were extracted from the 3D model and were manufactured using the 3D printing technique. To generate multi-layered soft tissue covering the vertebrae,

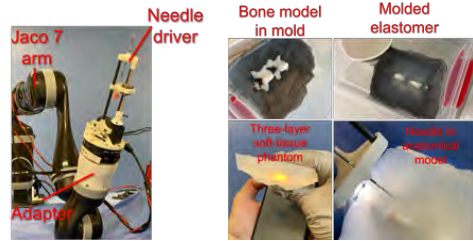


Fig. 1. Components of the epidural needle insertion setup and phantom spine.

a multi-level moulding technique was used using silicon elastomers (Ecoflex 00-30 and Ecoflex 00-10) as shown in Fig. 1(b). The seven-degree-of-freedom (7DoF) serial manipulator, and a custom-designed needle insertion end-effector. The needle was driven axially using a ball-screw mechanism with 50 μm step accuracy. For AR model registration, two regions of the 3D printed spinal model (crest of the spinal processes of L4 and L5) were localized using an electromagnetic probe (Polhemus Viper, Polhemus, USA) and were registered to their corresponding regions on the 3D model through static 3D registration. The residual error of this static registration was $0.85 \pm 0.33\text{mm}$. After model-to-phantom registration, the robotic arm's onboard VGA camera was used to register the arm with respect to a fiducial 2D marker (Vuforia). The center of the fiducial 2D marker was also registered with the electromagnetic tracker. This way, the arm's position with respect to the spine phantom was updated by the Vuforia Engine in the Unity environment. Also, the Unity environment was used to project the spine model onto the robotic arm's VGA camera.

For the experiments, a group of expert users ($n=5$) inserted a 19G epidural needle into the patient-specific model (L3-L4 and L4-L5 spaces) while looking at the augmented image feed from the arm's camera in Unity. Each subject repeated the task for five times with AR assistance (ROB+AR group). Also, the users repeated needle insertion without augmented reality assistance but with haptic feedback (ROB group). Haptic feedback was provided with a delta.3 haptic device with direct force reflection force rendering based on needle insertion force

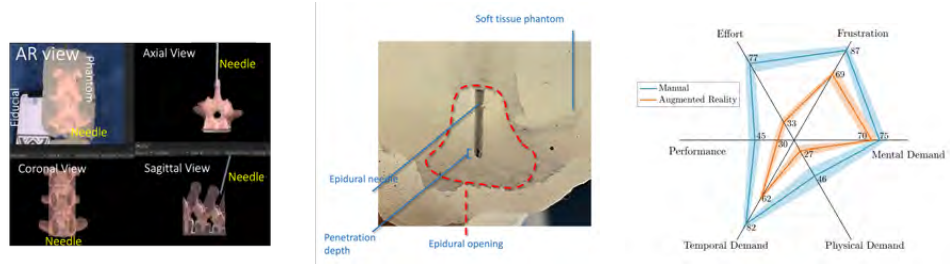


Fig. 2. Comparison of the sagittal and axial views of needle in spine model with virtual model, (b) internal view of the epidural space with needle tip penetration.

TABLE I
NASA TLX METRIC WEIGHTS

Weights	Demand			Performance	Effort	Frustration
	Mental	Physical	Temporal			
7	5	5	10	5	5	8

TABLE II
ACCURACY ASSESSMENT RESULTS

	Error (mm)	Repeatability (mm)	Success rate (%)	* T_c (sec)
ROB	4.3	1.8	70	16 ± 4
ROB+AR	1.03	0.77	100	7 ± 2
Change	-76%**	-57%**	+30%**	-56%**

* T_c : Time of completion.

**: $p < 0.05$

measured by an ATI Gamma force sensor installed on the robot's end-effector. The accuracy of needle insertion was quantified by measuring the needle position error and with/without assistance. The needle position error was assumed to be zero when it was 1mm into the epidural space. Moreover, the repeatability was quantified by measuring the standard deviation of the position error. To explore the usability of the system, participants were asked to complete the TLX questionnaire after the experiment. Mental, physical, and temporal demands, performance, frustration, and effort were asked on a scale of 0 to 100 with five increments for each setup. Based on the fact that the spinal needle insertion is a high-risk task to accomplish, we considered the metric weights provided in Table I for evaluation of the overall TLX score with AR assistance and without AR assistance groups. Afterwards, a statistical test was performed on the reported TLX outcomes to test significant differences between the two groups.

RESULTS AND DISCUSSION

Table II presents the results of the inspection of epidural space and manual needle penetration measurement after each needle insertion task. The ROB group showed an average needle position error (accuracy) of 4.3 mm while ROB+AR showed 1.03 mm (76% reduction). Also, the repeatability was 1.8mm in ROB and 0.77mm in ROB+AR group (57% reduction). In addition, the users had 100% success in localizing the epidural space on the

first try with AR and a 70% success rate without AR. Also, the time to completion of one needle insertion was 7 ± 2 s with assistance, while it was 16 ± 4 s without AR (56% reduction). The results of NASA TLX were statistically analyzed using a *t*-test with a confidence interval of 95% [5]. The results showed that the participants experienced significantly less temporal and physical demands, less effort and frustration, and perceived better success with the ROB+AR setup ($p < 0.05$). However, the mental demand did not show significant improvement ($p = 0.29$). The accuracy study results (Table II) are also in agreement with the TLX findings about temporal demand (T_c), effort (success rate), and performance (accuracy and repeatability).

CONCLUSIONS

In this study, an augmented reality guided system was designed and tested for robotic epidural needle injection. Fiducial 2D markers and electromagnetic tracker-based static registration were used to register the hologram on a patient-specific 3D-printed model. The proposed system improved the accuracy, repeatability, and success rate of epidural needle insertion on an anatomical model. In addition, it reduced procedural time and was more effective from the users' perspective. In future studies, using optical tracking systems may increase the accuracy of the registered hologram leading to a sub-millimetre accuracy potentially.

REFERENCES

- [1] G. Vadalà, S. De Salvatore, L. Ambrosio, F. Russo, R. Papalia, and V. Denaro, "Robotic spine surgery and augmented reality systems: a state of the art," *Neurospine*, vol. 17, no. 1, p. 88, 2020.
- [2] A. Elmi-Terander, H. Skulason, M. Söderman, J. Racadio, R. Homan, D. Babic, N. van der Vaart, and R. Nachabe, "Surgical navigation technology based on augmented reality and integrated 3d intraoperative imaging: a spine cadaveric feasibility and accuracy study," *Spine*, vol. 41, no. 21, p. E1303, 2016.
- [3] E. Edström, G. Burström, A. Omar, R. Nachabe, M. Söderman, O. Persson, P. Gerdhem, and A. Elmi-Terander, "Augmented reality surgical navigation in spine surgery to minimize staff radiation exposure," *Spine*, vol. 45, no. 1, pp. E45–E53, 2020.
- [4] S. G. Hart and L. E. Staveland, "Development of nasa-tlx (task load index): Results of empirical and theoretical research," in *Human Mental Workload*, ser. Advances in Psychology, P. A. Hancock and N. Meshkati, Eds., North-Holland, 1988, vol. 52, pp. 139–183.
- [5] B. R. Lowndes, K. L. Forsyth, R. C. Blocker, P. G. Dean, M. J. Truty, S. F. Heller, S. Blackmon, M. S. Hallbeck, and H. Nelson, "NASA-TLX assessment of surgeon workload variation across specialties," *Annals of surgery*, vol. 271, no. 4, pp. 686–692, 2020.

Workspace Characterization for Hybrid Tendon and Ball Chain Continuum Robots

G. Pittiglio¹, M. Mencattelli¹, A. Donder¹, Y. Chitalia², and P. E. Dupont¹

¹ *Boston Children's Hospital, Harvard Medical School,
giovanni.pittiglio@childrens.harvard.edu*

² *Department of Mechanical Engineering, University of Louisville*

INTRODUCTION

Continuum robots have attracted considerable attention for applications in minimally invasive diagnostics and therapeutics over the past decade [1]. The primary reason is their ability to navigate narrow and tortuous anatomical passageways, while guaranteeing safe interaction with the anatomy.

In designing such robots, an important goal is to create a robot with a workspace appropriate for the clinical task. A significant limitation of many continuum designs relates to the minimum radius of curvature that a particular design can achieve. While multiple bending sections can be concatenated to provide more degrees of freedom, the orientations by which a point in the workspace can be approached are often limited.

To overcome this limitation, this paper investigates a hybrid design that combines the advantages of tendon-actuated [2] and magnetic ball chain robots [3] as shown in Fig. 1. In this hybrid design, a proximal tendon-actuated section positions the robot with respect to the goal tip location while a distal ball chain section orients the robot tip with respect to the goal location. This abstract describes how the hybrid kinematics can be modeled and illustrates how the hybrid design possesses a dexterous workspace of finite extent.

MATERIALS AND METHODS

While beyond the scope of this abstract, a complete physics-based hybrid model can be derived by applying the distributed and magnetic forces and torques of the ball chain [3] to the tendon-actuation model of [2]. Assuming that magnetic loading does not significantly deflect the proximal tube, a simplified workspace characterization can be derived using a constant curvature assumption for the tendon-actuated segment [2] and a straight line approximation for the ball chain segment [3]. The latter assumption holds when the strength of the applied field is high enough to straighten the chain. Given these assumptions, the following approximate kinematic model can be used for a qualitative workspace analysis.

A ball chain robot is assumed to extend, for a length $l = n_s d$, as a straight line; here n_s is the number of spheres

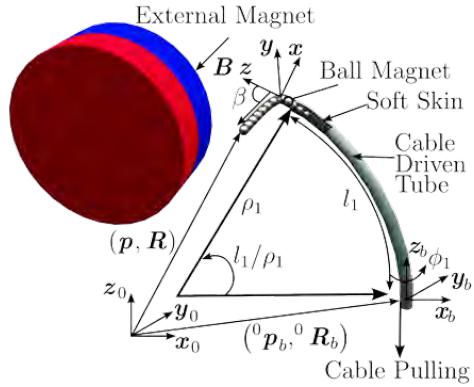


Fig. 1 Schematic representation of ball chain and tendon actuation.

(balls) and d their diameter. Given their base position and orientation in global reference frame, ${}^0\mathbf{p}_b$ and ${}^0\mathbf{R}_b$, their tip position and orientation is

$$\mathbf{p} = {}^0\mathbf{p}_b + n_s d {}^0\mathbf{R}_b \mathbf{rot}_{e_2}(\beta) \mathbf{e}_3 \quad (1a)$$

$$\mathbf{R} = {}^0\mathbf{R}_b \mathbf{rot}_{e_2}(\beta) \quad (1b)$$

with $\mathbf{e}_i \in \mathbb{R}^3$ i -th element of the canonical basis of \mathbb{R}^3 , and $\mathbf{rot}_{e_i}(\beta)$ rotation of $\beta = \angle \mathbf{B}$ around the axis e_i ; \mathbf{B} magnetic field. We approximate a set of n_t telescoping cable driven tubes using piece wise constant curvature assumption,

$$\mathbf{p} = {}^0\mathbf{p}_b + {}^0\mathbf{R}_b \sum_{i=1}^{n_t} \mathbf{rot}_{e_3}(\phi_i) \mathbf{r}_i \quad (2a)$$

$$\mathbf{R} = {}^0\mathbf{R}_b \prod_{i=1}^{n_t} \mathbf{rot}_{e_3}(\phi_i) \mathbf{rot}_{e_2} \left(\frac{l_i}{\rho_i} \right) \quad (2b)$$

where $\mathbf{r}_i = \rho_i (1 - \cos(l_i/\rho_i)) \sin(l_i/\rho_i)^\top$, ρ_i and l_i respective radius of curvature and length of the i -th section.

By combining (1) with (2), we obtain the kinematics of a ball chain magnetic robot extending from one cable driven tube

$$\mathbf{p} = {}^0\mathbf{p}_b + {}^0\mathbf{R}_b \mathbf{rot}_{e_3}(\phi_1) (\mathbf{r}_1 + n_s d \mathbf{rot}_{e_2}(\beta) \mathbf{e}_3) \quad (3a)$$

$$\mathbf{R} = {}^0\mathbf{R}_b \mathbf{rot}_{e_3}(\phi_1) \mathbf{rot}_{e_2} \left(\frac{l_1}{\rho_1} + \beta \right) \quad (3b)$$

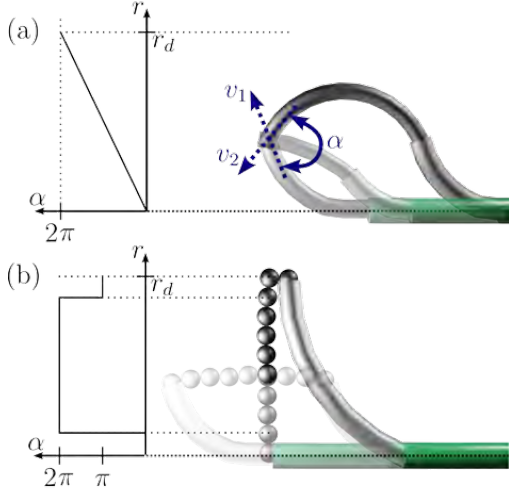


Fig. 2 Comparison of workspace dexterity for: (a) two-segment tendon-actuated robot; (b) tendon/ball-chain continuum robots. Plots on left indicate range of approach angles, α , as a function of distance, r , off of the longitudinal axis.

RESULTS

In Fig. 2, we compare the range of approach angles, α , spanned by a robot composed of 2 telescoping tendon driven sections with the proposed hybrid design, as a function of the distance, r , from the longitudinal axis of the proximal section at its base. For this comparison, we assume that the proximal and distal tendon-actuated sections have maximum bending angles of $\pi/2$ and π , respectively and that minimum radius of curvature of the distal tube is half that of the proximal tube. The minimum radius of curvature of the proximal tube is $r_d = 2l/\pi$. For any point located less than r_d from the base axis, the angle of approach is bounded by v_1 and v_2 (see Fig. 2). The former corresponds to the approach direction when the distal tube takes on its minimum bending radius while the latter corresponds to both tubes at their minimum radii of curvature. Any approach angle between these two extremes is possible as shown by the intermediate configuration. It can be shown that the range, α , increases linearly with r_d as shown on the left side of the plot with $\alpha = 2\pi$ only at $r = r_d$.

In contrast, since ball chains can achieve a very small radius of curvature as schematically depicted in Fig. 2 [3], the hybrid design can approach points from all directions, $\alpha = 2\pi$, for any r satisfying $d < r < r_d - d$. We see that the telescoping tubes achieve full dexterity only for $r = r_d$.

Fig. 3 provides an experimental validation of the dexterity of ball chain robots shown in Fig. 2. We consider the case $r = r_d$ (Fig. 3a) and the case $d < r \leq r_d - d$ (Fig. 3b), to validate the two extreme cases: $\alpha = \pi$ and $\alpha = 2\pi$, respectively. The tendon-actuated proximal

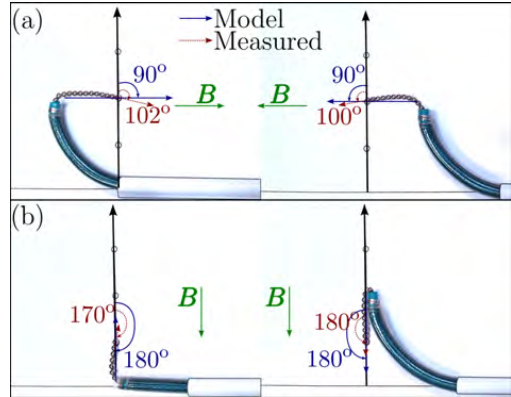


Fig. 3 Demonstration of dexterous workspace for hybrid tendon-actuated / ball chain continuum robot. Point at distance: (a) $r = r_d$; (b) $r \leq r_d - d$.

segment is 76mm long and the ball chain is 38mm long with the latter composed of 3.175mm diameter balls (N52 magnets). Using a magnetic field of 40 mT, by positioning a permanent magnet (N52, diameter 76.2 mm, height 38.1 mm) in the directions indicated in Fig. 3, we show that the ball chain can achieve the full dexterity predicted in Fig. 2 with mean percentage error between approximated model and experiments of 7.5%.

While we only have space to analyze and report experiments for the planar case here, by revolution around the robot's main axis (z_b), these results can be generalized to 3D. Specifically, we can show any point within distance $r_d - d$ from the robot's main axis can be approached from any direction.

DISCUSSION

The hybrid design presented in this paper is characterized by a large dexterous workspace. The design method, consisting of the combination of tendon driven and magnetic ball chain robots is perhaps the only continuum design capable of approaching a large set of tip positions from an arbitrary direction. This workspace can be approximated using a simple kinematic model, which is validated experimentally on a benchtop setup.

In the future, we will demonstrate the dexterous workspace in 3D and create an actuation platform for concurrent control of the tendon driven robot and magnetic chain.

REFERENCES

- [1] P. Dupont, N. Simaan, H. Choset, and C. Rucker, "Continuum Robots for Medical Interventions," *Proceedings of the IEEE*, 2022.
- [2] D. C. Rucker and R. J. Webster, "Statics and dynamics of continuum robots with general tendon routing and external loading," *IEEE Transactions on Robotics*, vol. 27, no. 6, pp. 1033–1044, 2011.
- [3] G. Pittiglio, M. Mencattelli, and P. E. Dupont, "Magnetic Ball Chain Robots for Endoluminal Interventions," 2023. [Online]. Available: [arXiv:2302.03728\[cs.RO\]](https://arxiv.org/abs/2302.03728)

A Comparison of the Workspace and Dexterity of Hybrid Concentric Tube Robot and Notched Wrist Systems

Paul H. Kang^{1,2}, Robert H. Nguyen², Thomas Looi², and James Drake^{1,2}

¹*Institute of Biomedical Engineering, University of Toronto, Canada*

²*The Wilfred and Joyce Posluns Centre for Image-Guided Intervention and Therapeutic Innovation, The Hospital for Sick Children, Canada*

hoseok.kang@mail.utoronto.ca

INTRODUCTION

Concentric tube robots (CTR) and notched wrists are two technologies that have been investigated for medical applications. CTRs consist of pre-curved super-elastic tubes that are nested concentrically, and are linearly translated and axially rotated with respect to one another for movement. Separately, notched wrists are tubular instruments that can achieve large bending angles via notches that are cut into the tube and shortening actuation cables that run along their length. These two robotic tools have been investigated independently, but very few studies have explored combining them [1], [2].

This paper compares the workspace and dexterity of a three-tube CTR with two hybrid CTR and notch-cut wrist systems in simulation. These metrics are key in measuring the performance of robots, and particularly so for surgical robots. To perform complicated surgical tasks, it is critical to increase the number of spatial points that the robot can reach, and the number of obtainable orientations at these points.

MATERIALS AND METHODS

This comparison investigated five systems: a three-tube CTR, a four-tube CTR where the inner-most tube had a precurvature of zero and square notches cut into the distal region of the tube to generate 1-degree-of-freedom (DOF) bending (Hybrid 1), a three-tube CTR that had a 2-DOF wrist fixed at the distal end of the inner-most CTR section (Hybrid 2), and two controls for each of the hybrid systems (Hybrid 1a and 2a) (see Fig. 1). The controls were identical to the hybrid systems but did not have any notches cut into the tubes. The notches used for both hybrid systems were commonly-used square cuts. The used 2-DOF wrist design was introduced in [3], and consisted of helically-wrapped notch-cuts in three bending planes that were 120° apart from each other. The design parameters that were chosen for the systems are shown in Table 1. The parameters for the CTR were chosen based on the values on our existing system. The wrist values were chosen based on literature and previous related designs [1], [2], [3], [4], as well as to constrain the maximum wrist lengths to be similar.

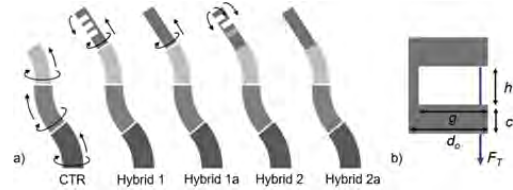


Fig. 1 a) The five systems investigated. Hybrid 1a and 2a served as the controls for Hybrid 1 and 2, respectively. b) A side view of a single square notch cut with labeled geometric parameters and cable actuation direction.

TABLE I CTR and wrist design parameters

Parameter	CTR			Hybrid Wrist	
	Outer Section	Middle Section	Inner Section	1	2
Outer diameter, d_o (mm)	2.45	1.91	1.48	0.63	0.63
Inner diameter (mm)	2.3	1.7	1.3	0.5	0.5
Curvature (mm ⁻¹)	1 / 81.00	1 / 69.67	1 / 55.67	0	—
Elastic modulus (GPa)	34.5	34.5	34.5	55.0	—
Max translation (mm)	20	20	40	45	—
Total number of notches	—	—	—	5	9
Notch cut height, h (mm)	—	—	—	0.6	0.6
Notch cut depth, g (mm)	—	—	—	1.07	1.07
Internotch space, c (mm)	—	—	—	0.6	0.6

The end-effector positions and orientations were then computed by performing forward kinematics on 10,000,000 randomly sampled joint configurations (i.e., the rotations and translations for each concentric tube, and the cable displacements to bend the notches). A torsionally-rigid forward kinematic model for the CTR was used [5], and a constant-curvature model for square-cut notches was used for the wrists [1], [3].

These end poses were used to compute the workspace and dexterity for each system. The workspace was defined as the volume of reachable points by the robot's end-effector. All space was first discretized into 3D voxels with dimensions 0.6 mm × 1.5 mm × 0.38 mm. The voxels that the robot's end-effector reached were marked, and the workspace volume was computed as the product of the voxel volume and the number of unique voxels reached. Secondly, the dexterity was defined as the fraction of orientations that the end-effector obtained at each point

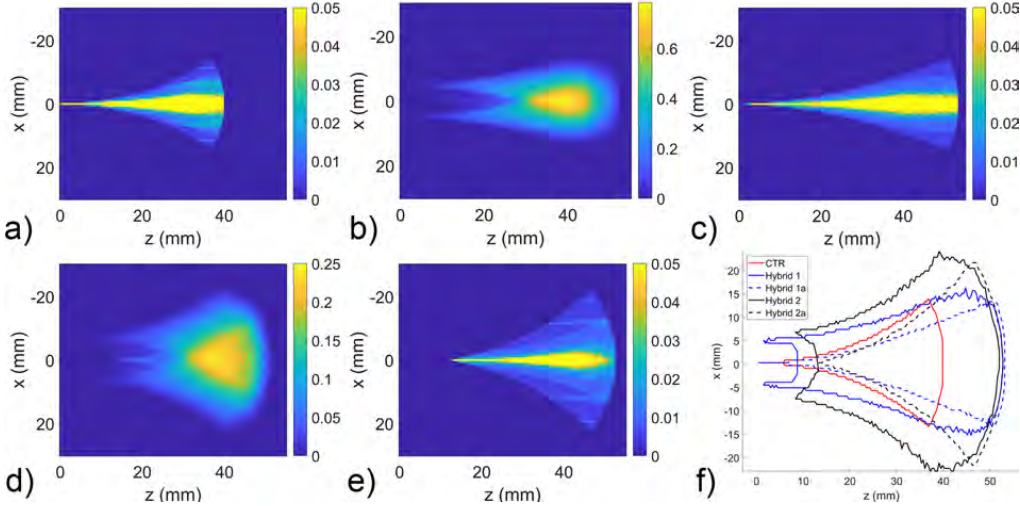


Fig. 2 a-e) The dexterity maps for a cross-section at the centerplane ($y=0$) for the CTR (a), Hybrid 1 (b), Hybrid 1a (c), Hybrid 2 (d), and Hybrid 2a (e) systems. f) The outline of the workspace at the cross-section $y=0$ for each system.

in the workspace. An arbitrary sphere at each point was discretized into 400 faces with equal surface area. The face that intersected with each end-effector's tangent vector was marked, and the dexterity at each point was expressed as the fraction of the number of unique faces marked over the total number of faces (see [6]).

RESULTS

The workspaces and dexterity heatmaps for each system are shown for a cross-section at the centerplane ($y=0$) in Fig. 2. Their total workspace volume and max dexterity is shown in Table 2. The workspaces for each system were rotationally symmetric around the z -axis. Hybrid 1 and 2 had higher workspace volumes and max dexterity values than their controls Hybrid 1a and 2a, respectively. Hybrid 2 displayed the greatest workspace volume (by at least a factor of two) while Hybrid 1 showed the greatest maximum dexterity (by at least a factor of three).

TABLE II Workspace volume and max dexterity results

System	Workspace Volume	Max Dexterity
CTR	5599 mm ³	0.05
Hybrid 1	17280 mm ³	0.78
Hybrid 1a	8187 mm ³	0.05
Hybrid 2	36332 mm ³	0.25
Hybrid 2a	16916 mm ³	0.05

DISCUSSION

This paper presented the improved workspace and dexterity of a CTR system when combined with notched wrists with either 1-DOF or 2-DOF bending capabilities. Compared to Hybrid 2, Hybrid 1's workspace was smaller because of the wrist's straight backbone. As the tube had zero curvature and was nested within the pre-curved tubes, the resultant curvatures were reduced for each section. This was not the case for Hybrid 2, and thus its design

may be more useful in cases where maintaining the pre-curvatures is important, e.g., obstacle avoidance of critical structures, or where a large workspace range is required, e.g., accessing large anatomical structures. Alternatively, Hybrid 1 generated higher dexterity values than Hybrid 2 as more notches were actuated in a single bending plane. A 2-DOF wrist requires notches to be cut in orthogonal bending planes which limits the maximum bending angle the wrist can achieve in a single direction (if constraining the wrist lengths to be the same). The Hybrid 1 system may be preferable for highly dexterous tasks and if the smaller workspace is not an issue. Overall, hybrid systems integrate the CTR's curvilinear shape and the notched wrist's sharp bends to access previously unreachable spatial points and to provide finer manipulability in its workspace. This is essential to execute complex surgeries and tasks. It is anticipated that further studies for design optimizations and medical applications will help to better understand how these hybrid designs can improve surgical techniques.

REFERENCES

- [1] P. A. York *et al.*, "A wrist for needle-sized surgical robots," in *2015 IEEE International Conference on Robotics and Automation (ICRA)*. Seattle, WA, USA: IEEE.
- [2] D. V. A. Nguyen *et al.*, "A Hybrid Concentric Tube Robot for Cholesteatoma Laser Surgery," *IEEE Robotics and Automation Letters*, vol. 7, no. 1.
- [3] P. Francis *et al.*, "Design, Modelling and Teleoperation of a 2 mm Diameter Compliant Instrument for the da Vinci Platform," *Annals of Biomedical Engineering*, vol. 46, no. 10.
- [4] K. W. Eastwood *et al.*, "Design of a Contact-Aided Compliant Notched-Tube Joint for Surgical Manipulation in Confined Workspaces," *Journal of Mechanisms and Robotics*, vol. 10, no. 1.
- [5] P. Sears and P. E. Dupont, "Inverse Kinematics of Concentric Tube Steerable Needles," in *Proceedings 2007 IEEE International Conference on Robotics and Automation*. Roma: IEEE, Apr. 2007, pp. 1887–1892.
- [6] L. Wu *et al.*, "Dexterity Analysis of Three 6-DOF Continuum Robots Combining Concentric Tube Mechanisms and Cable-Driven Mechanisms," *IEEE Robotics and Automation Letters*, vol. 2, no. 2.

Design and Control of a Tele-operated Soft Instrument in Minimally Invasive Surgery

J. Shi¹ and H. Wurdemann¹

¹*Mechanical Engineering, University College London, UK*
h.wurdemann@ucl.ac.uk

INTRODUCTION

The medical sector has emphasised increasing levels of autonomy to achieve safe and efficient robot-assisted surgeries [1]. In this case, robust and intuitive manipulation of medical robots is crucial, and many tele-operated surgical robots have been developed, e.g., the da Vinci robotic platform. The tele-operation can offer high operation precision and intuitive manipulation. In addition, soft robots have led to the development of inherently safe and flexible interventional tools for medical applications, e.g., the minimally invasive surgery (MIS). Soft instruments are particular advantageous to navigate in tortuous anatomical environments with constrained space [2]. Combining the tele-operation technology with soft robots might further result in a significant reduction in operation time and increase of surgeons' dexterity [3]. The contribution of this work lies in the design and control of a tele-operated soft instrument for laparoscopic examination proposed based on the miniaturised STIFF-FLOP manipulators (with a diameter of 11.5 mm) [4]. Specifically, the robot has two serially connected modules, which can seamlessly fit to commercially available 12 mm trocar ports used in MIS (see Fig. 1). The bending angle of the soft instrument can achieve 180°. We also preliminarily validate the feasibility of the soft instrument.

MATERIALS AND METHODS

A. System Overview

The robot body is made of a low shore hardness silicone (Ecoflex 00-50 Supersoft, SmoothOn). The robot has six fully fiber-reinforced circular chambers distributed evenly. Two adjacent chambers are internally connected via a 1 mm silicone pipes and actuated as one pair. An inner lumen of a 4.5 mm diameter is preserved to feed through a 4 mm endoscope camera (OV9734, China). The length of one robot module is 55 mm (see Fig. 1). The soft instrument is tele-operated by the Touch X (Geomagic, US). The command pose y_d is calculated by the relative linear position displacement of the Touch X,

$$y_d = k_d(y_c - y_s), \quad (1)$$

where y_s is the start position when the tele-operation begins, y_c is the current position and k_d is a 3×3 diagonal gain matrix to adjust the scale of the robot motion.

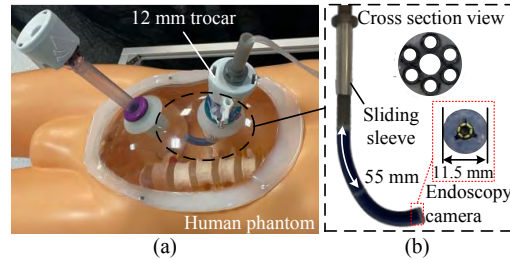


Fig. 1 (a) Human phantom with 12 mm disposable trocar ports. (b) The soft instrument has two identical robot segments, a 4 mm endoscopy camera is integrated at the tip of the robot. A sliding sleeve is designed to fully open the sealing part of the trocar before inserting the robot.

A PC with the Robot Operating System (ROS) is used as the host to achieve communication between the Touch X and a laptop running Matlab for achieving inverse kinematics, the calculated desired pressure is sent to an Arduino Due to regulate the chamber pressure via pressure regulators (Camoanzi K8P, Italy).

B. Inverse Kinematic Control

The spatial configuration of the robot's backbone can be described using a displacement vector $p(s)$ and a rotation matrix $R(s)$. Differentiating them with respect to the curve length s , denoted by $(\cdot)_{,s}$. This yields

$$p_{,s}(s) = R(s)v(s), \quad R_{,s}(s) = R(s)\hat{u}(s), \quad (2)$$

where $v(s)$ and $u(s)$ are the local strain vector and curvatures, with $\hat{u}(s)$ as a skew-symmetric matrix. The derivatives of force $n(s)$ and moment $m(s)$ are

$$n_{,s}(s) = f_e(s) + f_P(s), \quad m_{,s}(s) = -\hat{p}_{,s}n(s) - l_e(s) + l_P(s), \quad (3)$$

where $f_e(s)$ and $l_e(s)$ are the distributed external force and moment. $f_P(s)$ and $l_P(s)$ are the distributed force and moment resulting from pressurisation and equal

$$\begin{aligned} f_P(s) &= \sum_{i=1}^6 [P^i A_c R_s(s) e_3], \quad m_P(s) = \\ &\sum_{i=1}^6 P^i A_c R(s) [(v(s) + \hat{u}(s)d^i) \times e_3 + \hat{d}^i \hat{u}(s)e_3], \end{aligned} \quad (4)$$

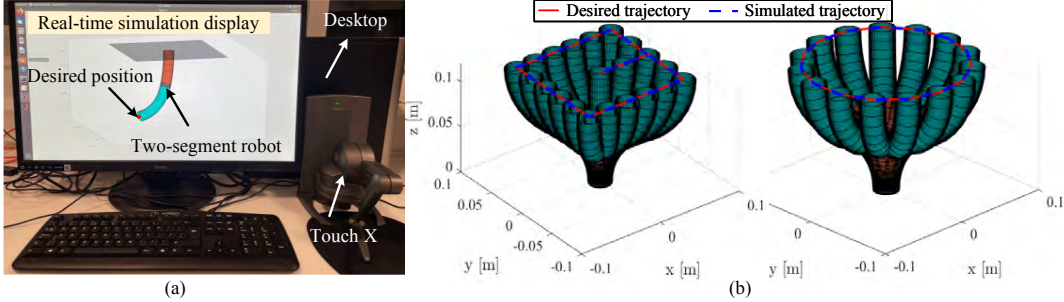


Fig. 2 (a) The simulated robot is visualised via Matlab interface and controlled by the Touch X. (b) The simulation results for the inverse kinematics when tracking a rectangular (side width of 120 mm) and circular shape (diameter of 160 mm), and the tip of the robot is kept vertically for demonstration.

where P^i is the pressure in the i th chamber, A_c is the chamber area, \hat{d}^i is the position vector of the i th chamber, $e_3 = [0, 0, 1]$. A linear constitutive material model is adopted to relate $n(s), m(s)$ to $v(s), u(s)$, yielding in (5)

$$n(s) = R(s)K_{se}(v(s) - e_3^T), \quad m(s) = R(s)K_{bt}u(s), \quad (5)$$

where K_{se} contains the shear and elongation stiffness, and K_{bt} contains the bending and torsion stiffness.

1) *Boundary Conditions:* For a two-segment robot with the length of L_1 and L_2 , the boundary conditions of the force and moment at the tip of the robot are

$$n(t^-) = F_P(t^-) + F_e(t^+), \quad m(t^-) = m_P(t^-) + m_e(t^+), \quad (6)$$

where $t = L_1 + L_2$, the subscripts P and e denote the force and torque from the pressurisation and external. Considering a rigid connection between two segments, the intermediate boundary conditions need to be satisfied

$$\begin{aligned} n(L_1^-) &= F_P(L_1^-) + n(L_1^+) + F_e(L_1^-) - F_P(L_1^+), \\ m(L_1^-) &= m_P(L_1^-) + m(L_1^+) + m_e(L_1^-) - m_P(L_1^+), \end{aligned} \quad (7)$$

where the superscripts $-$ and $+$ denote the left and right limits. For the inverse kinematics, the desired configuration can be y_d and R_d . As such,

$$p(t) = y_d, \quad R(t) = R_d. \quad (8)$$

2) *Numerical Implementation:* The shooting method can then be applied by assuming the initial guess as

$$g(0) = [n(0), m(0), P], \quad s.t. \quad P_{max} > P^i > 0, \quad i = 1 \dots 6. \quad (9)$$

where $n(0)$ and $m(0)$ are the force and moment at the base, P contains the actuation pressure in six chambers and P_{max} is the maximum allowed pressure. Specifically, by integrating (2) and (3) (using the fourth-order Runge-Kutta method) based on the initial condition (9) and satisfying (7)-(8). The problem is solved as a nonlinear least-square problem via Matlab.

RESULTS

The feasibility of the soft instrument is validated via a human phantom equipped with 12 mm trocar ports (see Fig. 1). The sliding sleeve can successfully prevent the

robot directly interacting with the sealing part of the trocar during the insertion process. As such, the robot doesn't suffer from buckling. In addition, the sliding sleeve is retractable to guarantee the sealing quality once the robot has passed. The simulation is visualised by Matlab, where the desired tip position is controlled by the Touch X (see Fig. 2(a)). The demonstration of the inverse kinematic control is exemplified by using two trajectories, i.e., rectangular and circular shapes. The tip of robot is kept towards the z -axis. The results are shown in Fig. 2(b), which shows the fidelity of the inverse control.

DISCUSSION

Compared with the robots from e.g., [2], [4] (diameter of 14.5 mm), our soft instrument (diameter of 11.5 mm) has the smallest diameter. This miniaturised dimension enables the robot seamlessly fit to the commonly available 12 mm trocar. The proposed inverse kinematic control is applicable to control the tip position and orientation with a frequency between 15-20 Hz in our PC (Intel i5, RAM 32 GB). It is worth mentioning that the problem generally can be solved within 3-5 optimisation iterations. As such, it is possible to improve the computation performance, e.g., using C++. We have also created soft robots with diameter of 8 mm. As such, we will further scale down the system dimension. In addition, we will evaluate the intuitiveness of the tele-operation system based on user tests and experimentally validate the accuracy of the inverse kinematic control.

REFERENCES

- [1] G.-Z. Yang, J. Cambias, K. Cleary, E. Daimler, and et al., "Medical robotics—regulatory, ethical, and legal considerations for increasing levels of autonomy," p. eaam8638, 2017.
- [2] A. Diodato, M. Brancadoro, G. De Rossi, and et al., "Soft robotic manipulator for improving dexterity in minimally invasive surgery," vol. 25, no. 1, pp. 69–76, 2018.
- [3] A. Arezzo, Y. Mintz, M. E. Allaix, and et al., "Total mesorectal excision using a soft and flexible robotic arm: a feasibility study in cadaver models," *Surgical endoscopy*, vol. 31, pp. 264–273, 2017.
- [4] J. Shi, W. Gaozhang, and H. A. Wurdemann, "Design and characterisation of cross-sectional geometries for soft robotic manipulators with fibre-reinforced chambers," in *Proc. IEEE Int. Conf. Soft Robot.*, 2022, pp. 125–131.

A Deep Learning Model for Tip Force Estimation on Steerable Catheters Via Learning-From-Simulation

Majid Roshanfar¹, Pedram Fekri¹, and Javad Dargahi¹

¹Robotic Surgery Lab., Concordia University, Montreal, QC, Canada

m_roshan@encs.concordia.ca

INTRODUCTION

Atrial Fibrillation (AFib) is the most common arrhythmia among the elderly population, where electrical activity becomes chaotic, leading to blood clots and strokes. During Radio Frequency Ablation (RFA), the arrhythmogenic sites within the cardiac tissue are burned off to reduce the undesired pulsation. Manual catheters are used for most atrial ablations, however, robotic catheter intervention systems provide more precise mapping. Several studies showed excessive contact forces (> 0.45 N) increase the incidence of tissue perforation, while inadequate force (< 0.1 N) results in ineffective ablation. Fig.1 shows a schematic of a cardiac RFA catheter used for AFib treatment. For robot-assisted RFA to be safe and effective, real-time force estimation of catheter's tip is required. As a solution, finite element (FE) analysis can provide a useful tool to estimate the real-time tip contact force. In this work, a nonlinear planar FE model of a steerable catheter was first developed with parametric material properties in ANSYS software. After that, a series of simulations based on each mechanical property was performed, and the deformed shape of the catheter was recorded. Next, validation was conducted by comparing the results of the simulation with experimental results between the range of 0-0.45 N to determine the material properties. Despite the previous work, which was a study to estimate the tip contact force of a catheter using a deep convolutional neural network [1], [2], the main contribution of this study was proposing a synthetic data generation, so as to train a light deep learning (DL) architecture for tip force estimation according to the FE simulations. Due to the availability of real-time X-ray images during RFA procedures (fluoroscopy), the shape of the catheter is available intraoperatively. The proposed solution not only feeds the data-hungry methods based on DL with a sufficient amount of data, but also shows the feasibility of replacing the fast, accurate, and light-weight learning-based methods with slow simulations.

MATERIALS AND METHODS

The catheter was modeled as a cantilever beam with a length of $L = 108$ mm and diameter $D = 2.33$ mm. These are the dimensions of the available catheter (Blazer II XP, Model 4770THK2, Boston Scientific). Due to the different materials used to prototype catheters, the

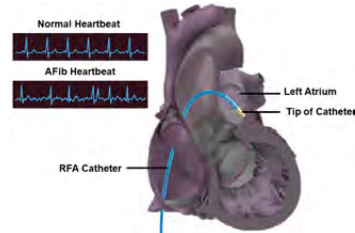


Fig. 1 Ablation catheter during RFA procedure and a comparison of normal and arrhythmic cardiac electrical activity. (3D Heart model from Zygote Media Group Inc.)

equivalent Young's modulus, Poisson's ratio, and density are considered as parameters in the simulations. Then based on the deformation of the catheter during the experimental setup, the values for these parameters are tuned. During the experiment, the tip of the catheter was 40 mm squeezed, and the reaction force at the base was recorded. Homogeneous Dirichlet and Neumann boundary conditions were applied at the right-most of the model to simulate the cantilever condition for the distal shaft of the catheter. The model was solved with 108 elements and with a large deformation assumption. To validate the parametric simulation and find the material properties, a range for every three parameters is considered. Young's modulus ranges from 120 to 200 MPa, Poisson's ratio from 0.3 to 0.4, and density from 7000 to 8000 kg/m³. The experimental setup in Fig.2 mimics the catheter simulation. Before the experiment, 108 mm of the catheter tip was measured and fixed in the holder of the linear actuator. The linear actuator was 3D printed in a way to align the center of the holder and 6-DoF force/torque sensor (ATI, Mini40). Next, a stepper motor controlled by an Arduino squeezed the catheter tip against the force sensor mounted at the end of the linear actuator. Simultaneously, a camera perpendicular to the deflection plane was used to record the deflection of the catheter. Fig.3(a) shows the recorded force during the experiment and Fig.3(b) compares the result of the experiment and simulation. By utilizing ANSYS's response surface optimization (RSO) module, the candidate point is selected with the aim of minimizing the error between the reaction force obtained from the force sensor and the simulation. After the optimization, Young's modulus, Poisson ratio, and density are set to

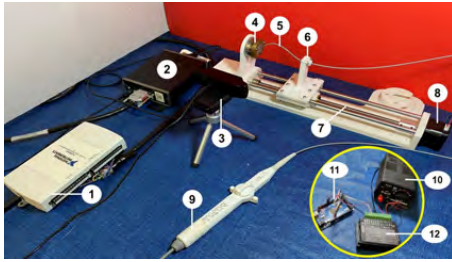


Fig. 2 Experimental setup, (1) data acquisition unit (2) power supply of sensor (3) camera (4) force/torque sensor (5) tip of the catheter (6) holder (7) linear actuator (8) stepper motor (9) steerable catheter (10) power supply (11) Arduino (12) microstep driver.

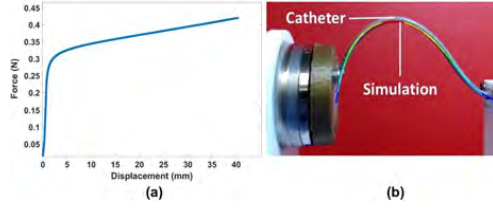


Fig. 3 (a) Recorded force (b) Simulation and experiment comparison. 137.6 MPa, 0.394, and 7736 kg/m^3 , respectively.

Considering FE simulation as a reference, the point is to create a model derived from the attained deflections and forces. In the previous studies [1]–[3], a huge effort was made to develop an experimental setup and carefully compile the required data by mechanically synthesizing different catheter's deflections. Instead of a force sensor, the models can learn from the simulation and be replaced with it. It can effectively facilitate the data compilation process while it provides more flexibility in producing various deflections. With this in mind, the intended model is meant to map the shape of deflections generated by the simulation to their corresponding forces. A dataset containing various deflections and their corresponding forces was compiled from the output of the simulation. The dataset comprises 10100 grey scale images with the shape of 224×224 . The total forces associated with each image is a vector norm attained from the forces along x and y direction with $\min = 0.015$, $\max = 0.419$, $std = 0.05$, and $mean = 0.362$. Given that, 70% of data was dedicated to the training set while the rest went for the test and validation set evenly. The goal is to create a model based on an image regression to map the input simulated images to the total force space. Inspired by [1], [2] a light-weight convolutional neural network is designed to model the data since the input images do not comprise complex shapes and regions. As shown in Fig.4, the input image is fed to the first convolution layer with 64 filters of size 7×7 and stride 2 followed by a max pooling 3×3 and stride 2. The output goes into 2 successive

TABLE I Benchmark for comparing the results with previous studies.

Models	inp	MSE	MAE	RMSE
Y-Net	3	2.83e-05	0.0039	0.005
ResNet	2	-	-	0.025
SimResNet	1	1.26e-05	0.0033	0.003

convolutional blocks with residual connections. Each of those blocks contains 2 convolution layers with 64 filters of size 3×3 along with a residual connection that adds the input channels to the output of the block. However, the first convolution layer of the first block diminishes the size of inputs with a stride 2 which reduces the input with size 224×224 to 64 feature maps of size 28×28 . Next, a global average pooling layer flattens the aforementioned feature maps into a vector that goes to a dense layer with 16 neurons. The ReLu activation function is applied to all convolutional and dense layers except the output layer which is one neuron to generate total forces. The architecture parameters are tuned by minimizing the Mean Square Error (MSE) loss function using Root Mean Squared Propagation (RMSprop) optimizer.

RESULTS

A convolutional graph trained on simulated data shows that synthetic data can be fed into a model. DL graph was trained with the batch size 32 and learning rate $lr = 0.001$ in 50 epochs. To keep track of overfitting, the model was validated on the validation set every epoch. Table I reports the performance of the trained model in the inference stage on the test set using the following metrics: Mean Absolute Error (MAE), MSE, and Root Mean Square Error (RMSE). For sake of a benchmark, the trained model was compared with the Y-Net [1] and ResNet [2] which were trained on a realistic dataset. The trained model of this work is called "SimResNet". As can be seen, SimResNet can learn total forces precisely without overfitting. Comparing the SimResNet with the Y-Net and ResNet, the obtained results are matched with the reported results. However, the MAE for SimResNet is slightly smaller than the other models. This can stem from the fact that in contrast to SimResNet, the output of Y-Net and ResNet are in a 3D and 2D force space respectively.

DISCUSSION

Through learning-from-simulation, this study proposes a deep learning approach for estimating tip force on steerable catheters. To determine the catheter's design parameters, FEM simulations were conducted. Next, the model is trained using the data extracted from simulation.

REFERENCES

- [1] P. Fekri, et al., "Y-net: A deep convolutional architecture for 3d estimation of contact forces in intracardiac catheters," *IEEE Robotics and Automation Letters*, vol. 7, no. 2, pp. 3592–3599, 2022.
- [2] ——, "A deep learning force estimator system for intracardiac catheters," in *2021 IEEE International Symposium on Medical Measurements and Applications (MeMeA)*, 2021, pp. 1–6.
- [3] H. Khodashenas, P. Fekri, M. Zadeh, and J. Dargahi, "A vision-based method for estimating contact forces in intracardiac catheters," in *2021 IEEE International Conference on Autonomous Systems (ICAS)*, 2021, pp. 1–7.

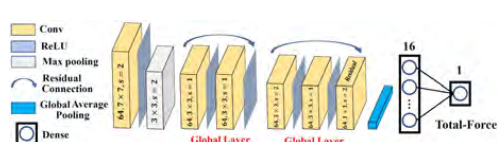


Fig. 4 Convolutional graph of the model inspired by the Y-Net [1].

DEBI: a new mechanical device for safer needle insertions

A. Aktas¹ and E. Franco¹

¹*Imperial College London, Mechanical Engineering Department, SW7 2AZ, UK*
a.aktas20@imperial.ac.uk

INTRODUCTION

Over 1 million core-needle breast biopsies are performed every year in the US alone [1], while gastrointestinal and prostate biopsies are estimated in similar numbers. The cost of core-needle breast biopsies ranges between \$500 for manual procedures to \$6,000 for image-guided procedures [2]. A retrospective study indicated that approximately 2.5% of breast biopsies fail [3]. Needle bending has been identified as a significant cause of error in biopsies and is particularly likely to occur at the insertion stage [2]. The associated risks include: i) biopsy of the wrong site leading to misdiagnosis; ii) puncture of sensitive areas in proximity of the insertion path; iii) repeated insertions, thus longer procedure duration and increased patient discomfort. Biopsy needles are also prone to buckling, which can damage the needle permanently. Common techniques for correcting needle bending in clinical settings include repeating the insertion (which can be time-consuming) or using a needle guide (which reduces the maximum insertion depth). In research, axial rotation is typically employed for steering bevel-tip needles, but it is less effective for needles with an axial-symmetric tip [4]. Additionally, straight insertions require continuous axial rotation, which can damage soft tissue due to the spinning of the bevel tip [5]. Alternative approaches employ steerable needles, which are not yet part of clinical practice [6].

We have developed a mechanical device that detects needle bending as soon as it occurs and that immediately reduces the insertion force thus helping to avoid deep insertions with deflected needles and the associated risks. Unlike existing solutions, our design does not require actuators or sensors hence it can be made MRI-safe, sterilisable or disposable. Finally, our device can be used with a variety of standard needles, including multi-bevel needles (e.g. diamond tip or conical tip).

MATERIALS AND METHODS

The proposed device resembles a syringe in that it consists of a piston, used to impart the insertion force, and a main body which houses the force-limiting mechanism and supports the needle (see Figure 1). The force-limiting mechanism consists of a spring-loaded relief valve connected to the needle base: when the needle bends, its base moves laterally and tilts the plunger of the relief valve. This reduces the compression of the o-ring mounted on the plunger; thus, the internal pressure

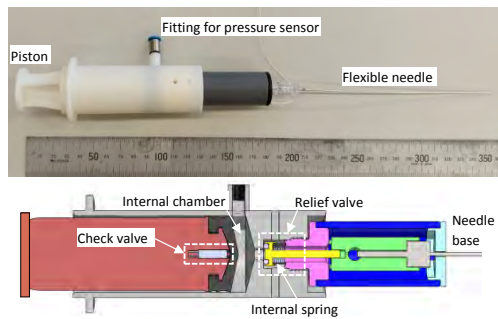


Fig. 1 Photo of the prototype, and section view of the CAD model highlighting the main components of the force-limiting mechanism.

generated by the piston drops, allowing the piston to advance towards the needle base. Consequently, the insertion force and the depth are automatically limited. A check valve is embedded in the piston to refill the internal chamber during retraction. We have manufactured a prototype measuring 172 mm in length and weighing 85 grams by employing standard 3D printing technologies. We have developed an automated test setup (see Figure 3) to assess the performance of the device with *in-vitro* experiments involving repeated needle insertions in a silicone rubber phantom representative of physiological tissues. The test setup consists of a double-acting plastic pneumatic cylinder (AC111-707-501, IPS Inc.) supplied with digital pressure regulators (Tecno Basic, Hoerbiger, Germany), while a linear encoder (EM1-300, US Digital) has been employed to measure the position of the piston. Each valve regulates the output pressure with an internal pressure sensor and a low-level control loop. A PID algorithm has been employed to control the position of the piston. The bending angle at the needle tip has been measured with an electromagnetic (EM) tracking system (Aurora, NDI Europe) by using an 18G coaxial needle (1.3 mm OD, 0.8 mm ID, 150 mm long) instrumented with an EM sensor (part number 610061, NDI Europe, RMS accuracy 0.2 degrees). The insertion force has been measured with a force sensor mounted on the piston (FSG15N1 A, Honeywell), while the pressure inside the force-limiting mechanism has been measured with an additional sensor

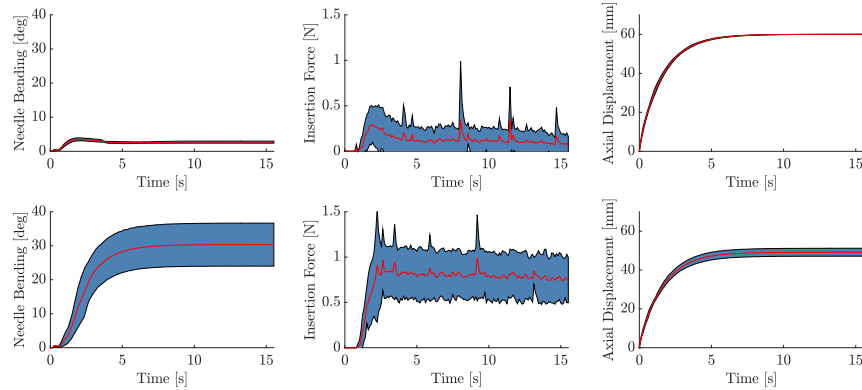


Fig. 2 Test results: Top row with force-limiting mechanism, Bottom row without force-limiting mechanism.

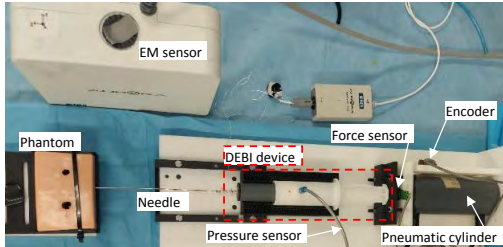


Fig. 3 Test setup for automated needle insertions.

(4525DO-DS3AS005GPF, Measurement Specialties). A micro-controller (mbed NXP LPC1768) communicates the pressure set-point to the proportional valves and collects the measurements from the linear encoder, the force sensor, and the pressure sensor. A Matlab script retrieves the sensor measurements using a serial link.

RESULTS

A set of needle insertions have been conducted with a silicone-rubber phantom (PlatSil GEL-10, Polytek), shore A = 10, representative of liver tissue [7], setting the needle perpendicular to the surface of the phantom. Each needle insertion has been repeated five times, and for each measurement we have computed the mean value (displayed in red) and the standard deviation (displayed in shaded blue) of axial displacement, bending angle, and insertion force. The test results (see Figure 2) show that the needle bending angle remains below 5°, while the insertion force remains below 0.5 N. The insertion speed is approximately 8 mm/s, which is representative of percutaneous interventions of the liver (see [8]). In comparison, removing the force-limiting mechanism yields needle bending angles above 30° and insertion forces above 1 N. Thus, the proposed mechanism reduces the needle bending by over 80%, which is similar to the results achieved with our controller [9] in automated closed-loop insertions.

DISCUSSION

The experimental results indicate that our device can effectively limit needle bending, thus reducing the associated risks. Since the device is completely mechanical (i.e., sensors have only been used for data collection), it can be produced in low-resource settings to suit various manual and robotic-assisted percutaneous procedures.

ACKNOWLEDGMENT

This work has been supported by the Hamlyn Accelerator for Surgical Innovation, HASI project DEBI. The work of Ayhan Aktas was also supported by the Republic of Türkiye.

REFERENCES

- [1] I. Jung, K. Han, M. J. Kim, H. J. Moon, J. H. Yoon, V. Y. Park, and E. K. Kim, "Annual trends in ultrasonography-guided 14-gauge core needle biopsy for breast lesions," *Korean Journal of Radiology*, vol. 21, no. 3, pp. 259–267, mar 2020.
- [2] K. P. Pritzker and H. J. Nieminen, "Needle biopsy adequacy in the era of precision medicine and value-based health care," *Archives of Pathology and Laboratory Medicine*, vol. 143, no. 11, pp. 1399–1415, nov 2019.
- [3] R. J. Jackman and F. A. Marzoni, "Needle-localized breast biopsy: Why do we fail?" *Radiology*, vol. 204, no. 3, pp. 677–684, 1997.
- [4] N. Abolhassani, R. V. Patel, and F. Ayazi, "Minimization of needle deflection in robot-assisted percutaneous therapy," *The International Journal of Medical Robotics and Computer Assisted Surgery*, vol. 3, no. 2, pp. 140–148, jun 2007.
- [5] C. L. Liu and Y. A. Huang, "Simultaneously Reducing Cutting Force and Tissue Damage in Needle Insertion with Rotation," *IEEE Transactions on Biomedical Engineering*, vol. 67, no. 11, pp. 3195–3202, nov 2020.
- [6] A. Donder and F. R. Y. Baena, "Kalman-Filter-Based, Dynamic 3-D Shape Reconstruction for Steerable Needles With Fiber Bragg Gratings in Multicore Fibers," *IEEE Transactions on Robotics*, pp. 1–14, dec 2021.
- [7] Y. C. Yoon, J. S. Lee, S. U. Park, J. H. Kwon, T. H. Hong, and D. G. Kim, "Quantitative assessment of liver fibrosis using shore durometer," *Annals of Surgical Treatment and Research*, vol. 93, no. 6, pp. 300–304, dec 2017.
- [8] D. J. van Gerwen, J. Dankelman, and J. J. van den Dobbelaer, "Needle-tissue interaction forces—a survey of experimental data," *Medical engineering & physics*, vol. 34, no. 6, pp. 665–80, 2012.
- [9] E. Franco, T. Brown, A. Astolfi, and F. Rodriguez y Baena, "Adaptive energy shaping control of robotic needle insertion," *Mechanism and Machine Theory*, vol. 155, p. 104060, jan 2021.

Valvuloplasty Balloon Catheter Sizing Approach for Calcified Aortic Valve with Different Annulus Ratios

J. Yao¹, G.M. Bosi¹, G. Burriesci^{1,2}, and H. Wurdemann¹

¹*Mechanical Engineering, University College London, UK*

²*Bioengineering at Ri.MED Foundation, Palermo, Italy*

junke.yao.19@ucl.ac.uk

INTRODUCTION

Transcatheter aortic valve implantation (TAVI) is regarded as the option of preference minimally invasive intervention to treat high-risk patients with aortic stenosis, which is a common heart valve disease characterized by the narrowing of the valve opening due to the thickening of the valve leaflets. During TAVI, a prosthetic aortic valve, replacing the diseased native valve with its function, is inserted and expanded by a balloon catheter if it is a balloon-expandable device. As a result, the correct size of the prosthetic device is vital due to its association with potential complications such as paravalvular regurgitation and aortic annulus rupture [1]. Pre-operative annulus size measurement based on imaging techniques is commonly applied before TAVI procedure including transthoracic echocardiography, transesophageal echocardiography and multi-detector computed tomography [2], [3]. However, these techniques face two major limitations: heavy dependence on the operator's experience and the influence of the optimum instant in the cardiac cycle for evaluation. In addition, the potential changes in the annular geometry caused by balloon aortic valvuloplasty, which uses a balloon catheter to dilate the calcified aortic leaflets as a bridge treatment to TAVI, are not considered. Therefore, intraoperative assessments based on valvuloplasty balloon catheters were introduced, which measure the annulus size by the balloon when it is inflated for dilatation [4]. They do, however, only provide limited compatibility for a limited number of devices. This study proposes an intra-operative method for measuring the aortic annulus that account for compliance and elliptical geometries using balloon internal pressure and volume data. The valvuloplasty balloon catheter from a commercially available source was used to obtain the intra-balloon pressure-volume curves by an inflation device. A characterized analytical model and a numerical model for balloon free-inflation were used to develop a sizing algorithm for estimating annulus dimensions.

MATERIALS AND METHODS

A. The compliant phantoms

For the purpose of validating the estimation method by balloon inflation, two types of idealized compliant

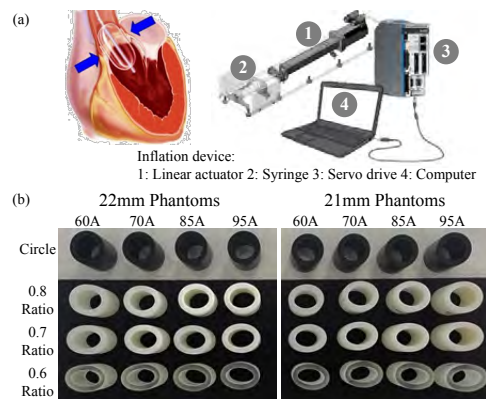


Fig. 1 (a) Balloon aortic valvuloplasty illustration and inflation device; (b) Aortic annulus phantoms.

aortic annulus phantoms were used: 8 circular cylinder phantoms (inner diameters of 21 and 22mm) and 24 elliptical cylinder phantoms (short diameter/long diameter as annulus ratio: 0.6, 0.7, and 0.8, two circumferences as the same value of 21 and 22mm diameter circles). The phantoms were produced by 3D printing with 5mm thickness and 40mm in length, whose shore hardness included 60A, 70A, 85A, and 95A as Fig. 1.

B. Experiment study

An Edwards 9350BC23 balloon catheter (Edwards Lifesciences, Irvine, USA) with a nominal diameter of 23mm and nominal volume of 21ml was used to dilate the phantoms. The balloon was connected to an inflation device, and a flow rate of 1ml/s was injected inside the balloon until the intra-balloon pressure reaches 4.5atm to avoid the balloon from bursting. The pressure and volume (p - v) data of the balloon during the inflation was recorded by the inflation device, imported into Matlab, and processed by an estimation algorithm.

C. Balloon numerical and analytical models

By comparing the p - v data of the free inflation and that of the inflation inside phantoms, the pressure value when the balloon starts to expand the phantoms could be figured out. Therefore, models of the balloon that use pressure

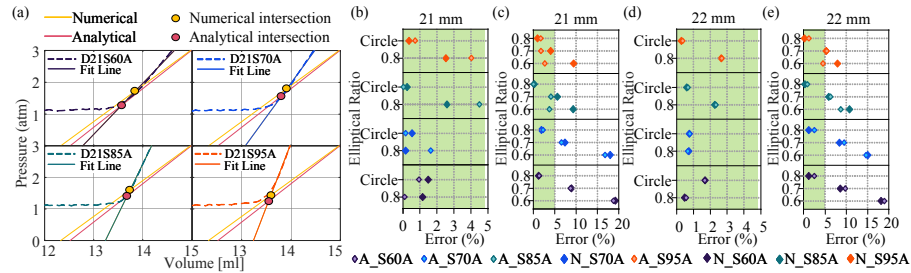


Fig. 2 Diameter estimation results. (a) Intersection points of fitting lines with analytical and numerical model lines; (b)-(e) Errors of diameter estimation: 21mm, 21mm for minor diameter, 22mm, 22mm for minor diameter.

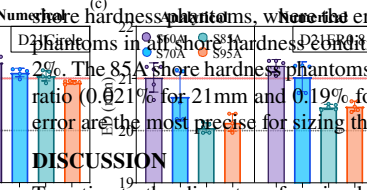
and volume to calculate the diameter of the balloon are necessary to be created. The numerical balloon model was created by a fitting regression of the diameter, applied pressure, and internal volume changes during the balloon inflation simulation. The equations of pressure-diameter data are $D_{stretched}(p) = 0.05p^2 + 0.45p + 20$. The analytical balloon model was based on defining the instantaneous balloon volumetric variation by the difference between the internal and external pressure during free inflation. And the diameter was calculated according to the transmural pressure of the balloon membrane as (2), where D_e is the estimated diameter and p_t is the transmural pressure.

D. Diameter estimation
When the balloon is fully in contact with the annulus, it later deforms by enlarging, with the compliance of the phantom influencing the pressure increment slope. The sizing algorithm is predicated on the idea that at the point where complete contact is almost made, the balloon's diameter will be equal to the annular diameter absent annulus deformation. Inferring the location in the acquired data where the pressure increment departs from the free inflation curve and estimating the corresponding balloon diameter using $D-p$ functions derived from balloon models allow for indirect sizing of the circular compliant annulus. Sizing for the short diameter of the elliptical compliant annulus can be achieved indirectly by determining the volume inside the balloon when the pressure increases from one atmosphere as the balloon begins to touch the narrow wall of the elliptical phantom.

RESULTS

The results of five tests with various elliptical ratios were averaged to produce the distinct $p-v$ curves for each phantom. When the balloon touches the phantom and the pressure increment deviates from the free inflation, the fitting lines for the extracted data with different shore hardness intersect. The analytical model and numerical model lines, allowing for the estimation of the circular diameter phantoms. One example of the phantoms for Numerical

the yellow intersection is used for estimating diameter by numerical model and the pink point is by the analytical model. The estimated diameter results by the numerical model are larger than the analytical model. Fig. 2(b) to (e) show the error of the estimations for different stiffness and

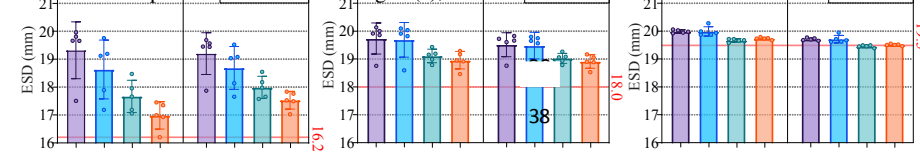


DISCUSSION

To estimate the diameter of a circular annulus and the smallest diameter of a non-circular annulus, an aortic annulus sizing approach based on the relationship between internal balloon pressure and volume was developed. The method was initially validated through experimental tests. The results demonstrate high accuracy for a variety of compliant circular phantoms and good accuracy for short-diameter estimation with stiffer elliptical (85A and 95A) or larger annular ratio (0.8) phantoms. The operator will receive helpful additional information from this precise diameter sizing to help them choose the right device size and to enhance the success of their post-implantation procedures. In order to test this sizing method in a more realistic environment, future studies could incorporate the actual shape of the aortic root, account for the influence of the physiological operating conditions, as well as investigate an improved approach for evaluating the material properties of the annulus.

REFERENCES

- [1] H. Möllmann *et al.*, "Complications of transcatheter aortic valve implantation (tavi): how to avoid and treat them," *Heart*, vol. 101, no. 11, pp. 1060–1065, 2015.
- [2] K. Blod *et al.*, "The impact of integration of a multidetector computed tomography annulus area sizing algorithm on outcomes of transcatheter aortic valve replacement: a prospective, multicenter, controlled trial," *Journal of the American College of Cardiology*, vol. 62, no. 5, pp. 431–438, 2013.
- [3] C. M. Otto *et al.*, "2020 ACC/AHA guideline for the management of patients with valvular heart disease: executive summary: a report of the american college of cardiology/american heart association joint committee on clinical practice guidelines," *Journal of the American College of Cardiology*, vol. 77, no. 4, pp. 450–500, 2021.
- [4] V. C. Babaliaros *et al.*, "Use of balloon aortic valvuloplasty to size the aortic annulus before implantation of a balloon-expandable transcatheter heart valve," *Journal of Cardiovascular Interventions*, vol. 3, no. 1, pp. 114–118, 2010.



Implementation of a Novel Handheld Endoscopic Operation Platform (EndoGRASP)

Chun Ping LAM¹, Ming Ho HO³, Shi Pan SIU³, Ka Chun LAU^{1, 3},
Yeung YAM^{1, 3}, Philip Wai Yan CHIU^{2, 3}

¹ Department of Mechanical and Automation Engineering; ² Department of Surgery,
Faculty of Medicine; ³ Multi-scale Medical Robotics Center,

The Chinese University of Hong Kong
cplam@link.cuhk.edu.hk, kclau@mrc-cuhk.com

INTRODUCTION

Flexible endoscopes are widely used due to their effective treatment of various conditions with minimal surgery. Existing ESD platform, such as Incisionless operation platform (IOP) [1] and ANUBIScope [2], while they may offer reliable support for endoscopic bending, they lack the ability to provide precise motorized motion or may potentially restrict the maneuverability of the platform in confined endoluminal environments. Another more advanced operation platform, namely EndoMaster [3], while providing excellent visualization of the surgical area due to its compact design, which allowed for easy docking and prevented interference from the working arms, however, its complex operational requirements, where the surgeon must control the console remotely and manipulate the robotic arms using hand controls, can be time-consuming and challenging for the surgeon to master. Over-the-Scope Clip (OTSC) [4] use a device that places clips over the endoscope to hold tissue before removal, but the effectiveness of these clips in securing the tissue is sometimes inadequate, resulting in incomplete tissue acquisition and suboptimal surgical outcomes. Existing operating systems face challenges such as limited mobility, insufficient tissue collection, complex setup, and high costs. EndoGRASP, a novel handheld endoscopic platform, addresses these issues with its flexible robotic overtube and actuation unit. Optimized for efficient endoscopic submucosal dissection, it enhances patient safety and ensures precise, motorized control of the endoscope and instruments.

MATERIALS AND METHODS

EndoGRASP is separated into two different parts, described as the overtube system portion and the integrated actuation unit portion. The overtube system consists of several components, including the Y-junction adapter used for the insertion of the endoscope, a cable gland and a coil sheath for connection and protection, tendon coils for transmitting actuation force to the overtube, and a biopsy channel tube for guiding the movement of the instrument.

The bending section of the overtube is mainly divided into two portions, namely active and supporting sections.

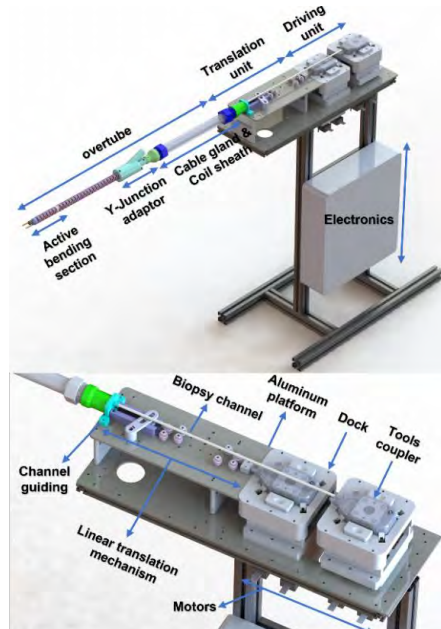


Fig. 1 CAD Model of EndoGRASP and the actuation unit

The active bending section is controlled by actuating four tendons, allowing for two degrees of freedom with planar bending. When inserting the robotic instrument, it is important to make sure it can smoothly pass through the continuum joint to reach the outlet. A biopsy channel tube is used as a guide, enabling the instrument to move easily from the proximal to the distal end of the overtube. When the overtube is actuated, it bends and stretches, increasing its length. To prevent restrictions in bending due to the non-stretchable biopsy tube, a biopsy channel stopper at the distal end of the overtube controls its movement. This design creates ample internal space for the biopsy channel to move even when the overtube is bent, ensuring that the non-stretchable tube does not limit the bending of the overtube. The stopper also secures the biopsy channel's position and prevents slippage while allowing for constant curvature bending.

The EndoGRASP actuation unit, shown in Fig. 1 and 2, includes key components for rapid overtube bending

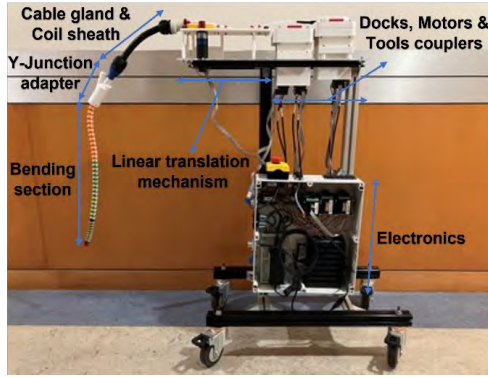


Fig. 2 Prototype of EndoGRASP

adjustments during surgery. It has a gearbox-equipped driving unit, tool coupler, linear translation mechanism, and motors. Two motors actuate the overtube, while four control the robotic gripper. Tendons connect to motor gears through tendon holders. The linear translation mechanism allows straight-ahead robotic instrument movement, and the aluminum platform with pink pulleys in Fig. 1 offers ample space for tool movement.

RESULTS

The endoscopic system's bending motion can be modeled using a polar coordinate system with four quadrants and a derived kinematic equation.

$$\Delta L_i = L - \left[\left(r \pm R_i \sin \left(\frac{\pi}{2} \pm (u_i - \Psi) \right) \right) * \theta \right], \quad (1)$$

Where ΔL_i is the change in length of tendon, L is the length of tendon before actuation, r is the bending radius, R_i is the minimum distance between tendons and the joint center, and u_i is the angle between the tendons and central axis of the joint. θ and Ψ are the bending angle and orientation, respectively. The bending angle of the overtube is precisely measured by employing optical sensors, which monitor the movement and orientation of the overtube throughout the procedure. This enhances control and optimizes the design for improved surgical outcomes. Figure 3 illustrates the constant curvature bending motion of the overtube at 45° and 90° with 0 orientation (the reference plane). Additionally, EndoGRASP achieves a 180-degree maximum bending angle and maintains a 50mm curvature while navigating tight spaces.

DISCUSSION

EndoGRASP represents a significant advancement in endoscopic surgery, offering unparalleled versatility and flexibility compared to existing ESD operation platforms. With the ability to bend at various angles, including the crucial retroflexion bend, EndoGRASP enables surgeons to provide therapy in hard-to-reach areas, such as the fundus portion of the gastrointestinal tract. This innovative platform is characterized by its unique overtube system, incorporating a biopsy channel stopper

that allows for constant curvature bending without limitations from non-stretchable biopsy tubes.

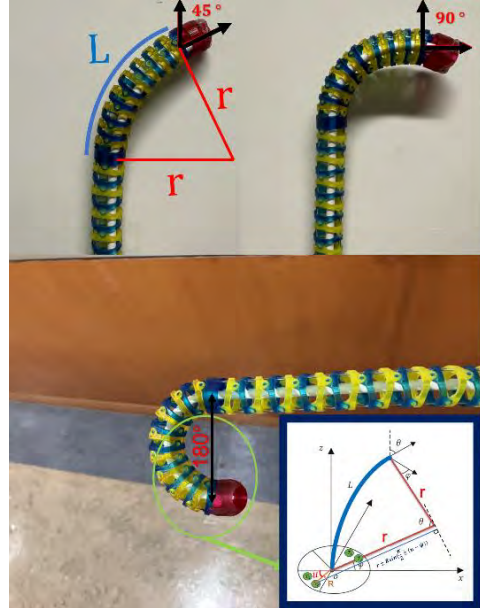


Fig. 3 Bending performance of EndoGRASP

The decoupling feature of EndoGRASP separates the movements of the endoscope, instrument, and overtube, giving surgeons greater control and precision during procedures. This state-of-the-art platform not only showcases its potential for a wide range of endoscopic surgeries but also highlights its applicability for various endoscopic procedures in the future. EndoGRASP's enhanced accessibility, precision, and adaptability make it a pioneering tool with the potential to transform endoscopic surgery and improve patient outcomes.

ACKNOWLEDGMENTS

This work is supported by InnoHK, HKSAR.

REFERENCES

- [1] Philip Wai-Yan, C., Hon Chi, Y., Ka Chun, L., & Yeung, Y., Techniques and Challenges with the Master-Slave System for Endoscopic Surgery, Innovative Endoscopic and Surgical Technology in the GI Tract (2021), 289-297.
- [2] Boškoski, I., & Costamagna, G., Endoscopy robotics: current and future applications. Digestive Endoscopy, 31(2) (2019), 119-124.
- [3] Chiu, P. W. Y., Ho, K. Y., & Phee, S. J., Colonic endoscopic submucosal dissection using a novel robotic system (with video), Gastrointestinal endoscopy, 93(5) (2021), 1172-1177.
- [4] Bartell, N., Bittner, K., Kaul, V., Kothari, T. H., & Kothari, S., Clinical efficacy of the over-the-scope clip device: A systematic review, World Journal of Gastroenterology, 26(24) (2020), 3495.

Magnetic Anchored and Cable Driven Endoscope for Minimally Invasive Surgery

Jixiu Li¹, Tao Zhang², Truman Cheng², Calvin Sze Hang Ng^{1,2},
 Philip Wai Yan Chiu^{1,2}, Zheng Li^{1,2}

¹*Department of Surgery, The Chinese University of Hong Kong,*

²*Multi-scale Medical Robotics Center (MRC), The Chinese University of Hong Kong*

*jxli@surgery.cuhk.edu.hk, tzhang@ieee.org, chengtruman@gmail.com,
 calvinng@surgery.cuhk.edu.hk, philipchiu@surgery.cuhk.edu.hk, lizheng@cuhk.edu.hk*

INTRODUCTION

Globally, the minimally invasive surgery (MIS) has been applied to more and more medical fields. MIS can provide many benefits for the patient, such as reduced pain, faster recovery, and better cosmesis [1]. But it also causes many challenges to the doctor and assistant during the long surgery. The most prominent problem is how to get the desired view through the narrow incision and the current solution is to insert a rigid endoscope into the surgical cavity of the patient. But this method will also bring about many problems and magnify the difficulty of the surgery. Firstly, the motion of the endoscope is limited by the incision especially when sharing the same port with other instruments, leading to the insufficient field of view (FOV) during the surgery. Also, the frequent collisions between the endoscope and other instruments will also interfere the adjustment of FOV. To address the above issues, the magnetic anchored and guided system (MAGS) is proposed [2]. Due to there is no rigid shaft and the endoscope is attached on the inner wall of the surgical cavity, the problems of port-crowding and instrument-fencing can be significantly alleviated, as shown in Fig.1. But how to arrange and control additional degrees of freedom (DOF) on MAGS to make it can cover the full FOV for surgeon is still a challenging problem. Here, we introduce the cable-driven mechanism to combine with the magnetic actuation method, providing a feasible solution for clinical application.

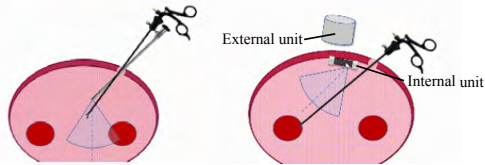


Fig. 1. The comparison between traditional endoscope and MAGS.

MATERIALS AND METHODS

This system mainly consists of two parts, the external unit and internal unit, as shown in Fig.2. The external unit contains one external permanent magnet (EPM) and its holding device (such as a robotic arm). The internal

unit is composed of one internal permanent magnet (IPM), one cable-driven mechanism, and a camera.

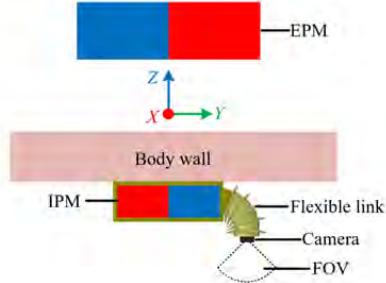


Fig.2. Overview of the whole system

As for the workflow of the system, firstly, the internal unit will be inserted into the patient body via the MIS incision and held to stick to inner wall of the surgical cavity by specific fixture device. Next, the external unit will be moved above the internal unit, the magnetic attractive force between the EPM and IPM can anchor the endoscope, and the fixture device can be released. Then the surgical assistant will move the external unit to actuate the inner endoscope translate to a desired position according to the demand of surgeon. During the surgery, the FOV from the endoscope can be adjusted by the pan motion of the IPM resulting from the rotation of the EPM and the tilt motion of the cable-driven mechanism to focus on the areas of concern for doctors. Finally, the internal unit will be moved to the vicinity of the MIS port and taken out when the surgery is finished.

The force analysis and motion description can be modeled with the help magnetic dipole theory [3]. In this system, the EPM and IPM can be considered as two magnetic dipoles regardless of volume approximately. Then the magnetic field strength generated by the EPM at the location of the IPM can be calculated:

$$B = \frac{\mu_0}{4\pi \|P_I - P_E\|^3} \left(\frac{3(P_I - P_E)(P_I - P_E)^T}{\|P_I - P_E\|^2} - I \right) M_E$$

where μ_0 is the vacuum permeability; P_I and P_E represent the position vector of the IPM and EPM; I is a 3×3 identity matrix; M_E indicates the 1×3 magnetic moment vector of the EPM.

Then, the force applied on the IPM can be obtained according to the magnetic field:

$$F = (M_I \cdot \nabla) B$$

which can be further expressed by:

$$F = \frac{3\mu_0}{4\pi \|r_{EI}\|^4} \left(M_I \hat{r}_{EI}^T + \hat{r}_{EI} M_I^T + \hat{r}_{EI} \cdot M_I (I - 5\hat{r}_{EI} \hat{r}_{EI}^T) \right) M_E$$

where r_{EI} represents the vector from the position of EPM to the position of IPM; M_I is the magnetic moment vector of the IPM.

The internal unit can be anchored against the inner wall of the body cavity when the force along Z-axis is bigger than the gravity of the internal unit. The movement of the external unit along the X-axis and Y-axis can produce the translational force to overcome the friction to actuate the translation of the internal unit.

According to the above equations, the anchoring force along Z-axis and the translation force along X-axis and Y-axis can be calculated.

As for the pan torque acting on the IPM, it can be formulated as:

$$T = M_I \times B$$

when the magnetic torque is larger than the friction torque, the internal unit begin to rotate along the Z-axis. The cable-driven mechanism is composed of serval disks and four attached cables. Control the tension of different cables can adjust the position and orientation of the camera fixed on the end of flexible link, as shown in Fig.3. The transformation matrix mapping from the base to the end can be expressed by [4]:

$$T = \begin{bmatrix} s_\phi^2 + c_\phi^2 c_\theta & c_\phi s_\phi (c_\theta - 1) & c_\phi s_\theta & c_\phi (1 - c_\theta) s / \theta \\ c_\phi s_\phi (c_\theta - 1) & c_\phi^2 + c_\theta s_\phi^2 & s_\phi s_\theta & s_\phi (1 - c_\theta) s / \theta \\ -c_\phi s_\theta & -s_\phi s_\theta & c_\theta & s_\theta s / \theta \\ 0 & 0 & 0 & 1 \end{bmatrix}$$

where θ and ϕ represent the two DOF of the flexible link and the symbol s and c indicate the \sin and \cos .

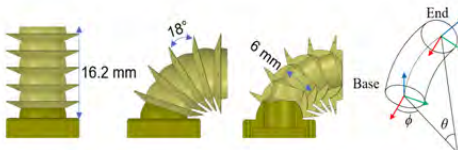


Fig.3 (a) The design and relevant parameters of the flexible link. (b) The motion and kinematics of the flexible link.

RESULTS

The parts of internal unit and external unit were 3D printed, both the EPM and IPM were magnetized with the strength of N52, and the camera attached on the end was from MISUMI, as shown in Fig.4. We set up the system with a simulated chest model, the result showed that we can anchor the internal unit stably and perform the translation and pan motion smoothly.

After testing the force and motion performance of the magnetic coupling, the experiment validating the DOF of the flexible was also conducted. Here, two pairs of

cables were used to control the flexible joint. And the result showed that the flexible link can achieve 90 degrees in two directions. The combination of the magnetic coupling and flexible link can provide sufficient FOV for the surgeon during the surgery.

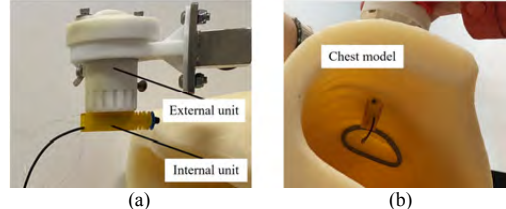


Fig.4 (a) Prototype of the external unit and internal unit. (b) Mockup with a simulated chest wall.

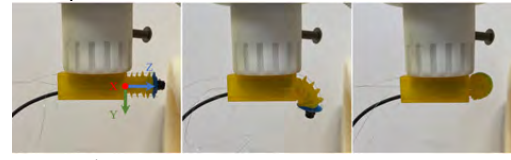


Fig.5 (a) The initial state of the flexible link. (b) Bending around X-axis. (c) Bending around Y-axis.

DISCUSSION

This article proposed a magnetic endoscope with a flexible link and preliminary experiments were conducted to validate the feasibility of the system. This endoscope can address the problem of port-crowding and instrument-fencing with traditional endoscopes and provide additional DOF to cover sufficient FOV for the surgeon in MIS. Of course, this system is still in a very preliminary stage, more experiments and tests need to be done to verify the accuracy of the modeling and the practicability in real clinical application. Especially, the interferences introduced by this endoscope (such as the influence from magnetic force and dangled tail on the operating instruments) need to be assessed by surgeons. In the future, we will integrate this system to a robotic arm and complete the actuation part for the flexible link. And the control algorithm will be developed to coordinate the motion of magnet and flexible link to realize the visual servoing task which can help doctors perform the surgery more conveniently.

REFERENCES

- [1] B. Jaffray, "Minimally invasive surgery," *Archives of disease in childhood*, vol. 90, no. 5, pp. 537–542, 2005.
- [2] J. Cadeddu, R. Fernandez, M. Desai, R. Bergs, C. Tracy, S.-J. Tang, P. Rao, M. Desai, and D. Scott, "Novel magnetically guided intraabdominal camera to facilitate laparoendoscopic single-site surgery: initial human experience," *Surgical endoscopy*, vol. 23, no. 8, pp. 1894–1899, 2009.
- [3] E.P.Furlani, Permanent magnet and electromechanical devices: materials, analysis, and applications. Academic press, 2001.
- [4] Z. Li and R. Du, "Design and analysis of a bio-inspired wire-driven multi-section flexible robot," *Int. J. Adv. Robot. Syst.*, vol. 10, no. 4, pp. 209:1–209:11, Apr. 2013.

SciKit-Surgery for Augmented Reality Surgery Research

Stephen Thompson¹, Miguel Xochicale¹, Thomas Dowrick¹, and Matthew J. Clarkson¹

¹*Wellcome EPSRC Centre for Interventional and Surgical Sciences, University College London*
s.thompson@ucl.ac.uk

INTRODUCTION

SciKit-Surgery provides open source libraries to support research and translation of applications for augmented reality in surgery [1]. This paper discusses recent developments in SciKit-Surgery and case studies using SciKit-SurgeryBARD to support research into visualisation and user interface design for augmented reality in surgery [2], [3].

The availability of high quality software tools for research and translation is a key enabler for scientific progress. Research into surgical robotics, image guided surgery, and augmented reality for surgery brings together many disciplines and depends on a strong engineering base to provide the tools that researchers need (e.g., hardware interfaces, data management, data processing, visualisation, and user interfaces). SciKit-Surgery was conceived as a more accessible replacement for existing toolkits written predominantly in C++. Experience has taught us that whilst implementations in C++ could be robust and offer optimised performance, the need to learn the language and the difficulties of maintaining cross platform compilation presented a higher a barrier of entry for most researchers. Whilst research software can be initially developed using short term research grants, the longer term sustainability of the software depends on other researchers being able to contribute to the software, both for maintenance and to introduce new features. For that to happen the software needs to be compact, written in a language that be easily interpreted by humans, and well documented. We conceived SciKit-Surgery to be a set of individual Python modules that could be used on their own by researchers to explore a specific topic or assembled into high quality applications that could be rapidly deployed to clinic to enable translation from bench to bedside.

MATERIALS AND METHODS

Python has grown to be the most used programming language for researchers¹. Python combines an accessible syntax with a massive ecosystem of user contributed modules to provide ready made tools for most research tasks. Perhaps most important are the package management tools that enable modules to be installed and maintained on many platforms. For this reason we chose Python and as the base platform to develop and distribute the SciKit-Surgery libraries.

¹[top-programming-languages-for-data-scientists-in-2022](#)

We made the key decision to keep our libraries highly modular. The intention is that each SciKit-Surgery library should do one thing and maintain orthogonality[4], so that modules could be combined into applications, without causing software conflicts. We developed a software template so that all SciKit-Surgery libraries share a familiar structure and continuous integration testing and deployment to PyPi is easily managed. The SciKit-Surgery organisation on GitHub creates a space where all libraries are collated and discussion and contribution is enabled.

Easily Swappable Hardware: SciKit-SurgeryCore sits at the centre of the ecosystem, defining data and message types common to all the SciKit-Surgery libraries. A key part of our work is developing hardware interfaces to talk to clinical and tracking hardware as this is a common stumbling block for researchers. SciKit-SurgeryCore defines an abstract API for all clinical hardware so that one tracking or imaging system can be easily substituted with another. Figure 1 gives an example of this, swapping an NDI tracking system with the open source ArUco tracking system [5].

For robotic surgery, we have demonstrated how our standard tracking interface can be used to create a ROS publisher node. We are also intending to develop tracking classes to get tracking data from robot kinematics, rather than relying on third party trackers.

RESULTS

SciKit-Surgery has grown rapidly since 2020 and is being used by researchers in image guided interventions globally. We are also seeing a steadily growing pool of contributors via GitHub. There are currently over 40 libraries listed on the SciKit-Surgery home page. We have found that it is the hardware interface libraries (SciKit-SurgeryNDITracker and SciKit-SurgeryBK) that have attracted the most external interest.

Within our own research group the use of SciKit-Surgery has had a transformational effect on our more junior research students (BSc and MSc). By carefully scoping research projects we can get junior researchers to contribute code and research outputs in short (3 months) projects.

SciKit-SurgeryBARD: Our current research on computer human interaction is built using SciKit-SurgeryBARD, the Basic Augmented Reality Demonstrator. BARD links together tracking libraries with visualisation using SciKit-SurgeryVTK and a

python-based user interface (PySide) to enable students to quickly test their own augmented reality systems. The majority of research into image guided surgery and augmented reality in surgery focuses on addressing the many technical challenges of image registration and tracking. We have been able to utilise SciKit-SurgeryBARD to perform rapid user studies examining the impact of visualisation design on depth perception [3] and on the occurrence of inattentional blindness [6] during augmented reality assisted surgery [2]. The lower part of Figure 1 shows an example from our inattentional blindness study, where the majority of our volunteers failed to notice the spider when performing a simulated surgical task. SciKit-SurgeryBARD enables the creation of lightweight applications using ArUco markers. For AR these are highly accurate as tracking and display use the same camera. This enables us to test different visualisation methods without worrying about tracking and registration accuracy.

Performance and Limitations: As a Python rather than a C++ library we are interested in the overall performance of the finished applications. We have observed that tasks such as instrument tracking and registration can be easily performed at the required frame rates ($\approx 30\text{fps}$). One limitation we have observed is with rendering. With semi opaque anatomy the performance of the underlying VTK libraries implemented in Python is significantly degraded in comparison previous work using C++ [7]. To compensate for this we have to reduce the number of vertices in our anatomical models. For overlay accuracy down to 1mm this is not problematic, and indeed may be beneficial in terms of simplifying the display for the surgeon. Work is ongoing to determine the impact and cause of the reduced rendering performance.

DISCUSSION

The SciKit-Surgery libraries provide an open source set of tools to support researchers in basic research through to translational clinical projects. By publicly hosting the libraries on GitHub and engaging with the research community, we aim to encourage direct contribution from users, so that the libraries last beyond the funding cycle for an individual project.

By creating a set of loosely coupled libraries we have been able to focus development effort on those libraries that have gathered the most interest both internally and externally. We currently have over 40 libraries listed on the SciKit-Surgery organisation page. Given our resources it would not be possible to maintain them all, but as they are all largely independent this has not proven to be a problem.

Work is ongoing to better understand what practices lead to the most sustainable software and to better embed these practices into our development.

ACKNOWLEDGEMENT AND COPYRIGHT

This research was funded in whole, or in part, by the Wellcome Trust [203145Z/16/Z]. For the purpose of Open Access, the author has applied a CC BY public

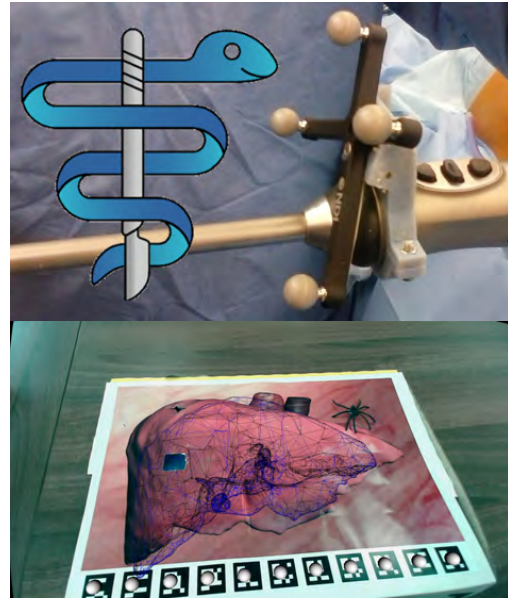


Fig. 1 Modular design is a key feature of SciKit-Surgery. Clinical hardware communicates through common interfaces defined in [SciKit-SurgeryCore](#) using Python's [Abstract Base Class](#) module. Modular design allows us to easily convert applications using clinical grade tracking hardware, [NDI Polaris](#) (at top), to applications suitable for visualisation and usability research beyond the lab, by utilising the open source [ArUco](#) library (at bottom) and vice-versa.

copyright licence to any Author Accepted Manuscript version arising from this submission.

REFERENCES

- [1] S. Thompson, T. Dowrick *et al.*, “Scikit-surgery: compact libraries for surgical navigation,” *International Journal of Computer Assisted Radiology and Surgery*, vol. 15, no. 7, pp. 1075–1084, Jul 2020. [Online]. Available: <https://doi.org/10.1007/s11548-020-02180-5>
- [2] C. Davis, “Enhanced surgeons: Understanding the design of augmented reality instructions for keyhole surgery,” in *Accepted for IEEE VR workshop XR Technologies for Healthcare and Wellbeing*.
- [3] A. Reissis, S. Yoo *et al.*, “The effect of luminance on depth perception in augmented reality guided laparoscopic surgery,” in *Medical Imaging 2023: Image-Guided Procedures, Robotic Interventions, and Modeling*, vol. 12466. SPIE, 2023, pp. 364–377.
- [4] A. Hunt and D. Thomas, *The Pragmatic Programmer: From Journeyman to Master*. USA: Addison-Wesley Longman Publishing Co., Inc., 2000.
- [5] S. Garrido-Jurado, R. Muñoz-Salinas *et al.*, “Generation of fiducial marker dictionaries using mixed integer linear programming,” *Pattern Recognition*, vol. 51, 10 2015.
- [6] A. S. Pandit, M. de Gouveia *et al.*, “Efficacy of a mindfulness-based intervention in ameliorating inattentional blindness amongst young neurosurgeons: A prospective, controlled pilot study,” *Frontiers in Surgery*, vol. 9, 2022. [Online]. Available: <https://www.frontiersin.org/article/10.3389/furg.2022.916228>
- [7] M. J. Clarkson, G. Zombori *et al.*, “The nifti software platform for image-guided interventions: platform overview and niftylink messaging,” *International journal of computer assisted radiology and surgery*, vol. 10, pp. 301–316, 2015.

Flexible Magnetic Soft Stent for Mobile Flow Diversion

Tianlu Wang and Metin Sitti

*Physical Intelligence Department, Max Planck Institute for Intelligent Systems
 {tianluwang, sitti}@is.mpg.de}*

INTRODUCTION

With the advantages in dimensions and exceptional locomotion capabilities, small-scale mobile robots have offered new opportunities for medical interventions in hard-to-reach regions, including the distal arteries in the circulatory systems. In this field, the wireless soft robots fabricated with compliant materials further provide unique adaptation capabilities and, thus, many exciting potential applications [1]. Although various locomotion abilities have been demonstrated and studied from the aspects of robot design, control strategies, and soft-bodied interactions [2], rare effective functions other than drug delivery have been properly incorporated into these robots for potential *in-vivo* utilities. Our group has recently developed a medical robotic system with a stent-shaped magnetic soft device (Stentbot) and the associated spatial magnetic actuation setup, which realized the on-demand local drug delivery and the flow diversion using a millimeter wireless robot design [3]. Its flexible locomotion capabilities have indicated its benefits of working as a mobile flow diverter if clinical migrations or misplacements happen when treating brain aneurysms using stent-like structures. However, this single-material development traded off the performance in locomotion abilities and the efficacy of flow diversion. For example, pure mesh-like structures ensure full body adaptation for the retrievable locomotion among the lumens with varying diameters, but the effectiveness of flow diversion is reduced since flow could go through the meshes freely. On the other hand, a full surface-sealed, hollow tube structure where all the gaps among meshes are filled could have a perfect flow diversion effect. However, the radial stiffness of the structure is notably increased, such that the shape adaptation capability is reduced. Therefore, there is a missing solution for the effective flow diverter with proper adaptation for the future treatments of brain aneurysms and other diseases, such as arteriovenous malformation.

MATERIALS AND METHODS

To address the challenge of simultaneously achieving effective adaptive locomotion and flow diversion, we proposed the concept of multi-material construction (**Fig. 1**). The device includes the magnetic composite part outside, which could be actively steered wirelessly for locomotion in the lumen, and the passive elastic part for flow diversion. A rotational and translational permanent

This work was funded by the Max Planck Society, European Research Council (ERC) Advanced Grant SoMMoR project with grant no: 834531, and ERC Proof of Concept Grant Stentbot (101100727).

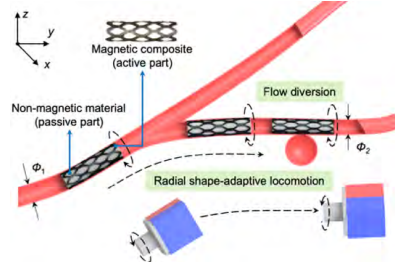


Fig. 1 Working principle of the mobile stent-shaped magnetic soft robot (Stentbot) with shape-adaptive locomotion and the function of flow diversion in vasculature. The rotational and translational permanent magnet enables robot locomotion. magnet, which was actuated by a 7-degrees-of-freedom (DoF) robotic arm (Panda, Franka Emika GmbH), provides the actuation. While the rotational magnetic torque changes the static friction to the kinetic one, the magnetic force pulls the robots to the desired location [3].

To accomplish the shape-adaptive locomotion in the lumen with varying diameters Φ_1 of around 1 – 1.5 mm, the overall normal force F_n from both parts applied to the complete device (**Fig. 2A**) should follow the relations:

$$F_{\text{mag}} + aF_{\text{drag}} + F_{\text{fric},\perp} \cos(\varphi) \geq F_{\text{fric},\parallel} \sin(\varphi), \quad (1)$$

$$T_{\text{mag}} \geq (F_{\text{fric},\parallel} \cos(\varphi) + F_{\text{fric},\perp} \sin(\varphi)) R_d, \quad (2)$$

where $F_{\text{fric},\perp} = \mu_{\perp} F_n$, $F_{\text{fric},\parallel} = \mu_{\parallel} F_n$, φ is the helix angle, which is 8°, R_d is the robot radius after radial deformation, μ_{\perp} and μ_{\parallel} are the CoF perpendicular to and parallel to the helix, respectively, F_{mag} and T_{mag} are the force and torque provided by the rotational and translational permanent magnet for actuation, and $a = 1$ or -1 indicates the cases when the robot moves with the flow or against the flow, respectively. Given the experimental conditions, materials, and designs, the maximum allowed F_n for each location could be acquired.

Second, to realize the effective flow diversion, the porosity of the mesh structure is ideally smaller than 70% [4]. The cell-shaped microstructure has been adopted for this purpose [5]. F_n could be estimated for each part,

$$F_n = \frac{6E_r I_b \Delta l_c}{l_b^3} \tan\left(\frac{2\pi}{n}\right) t, \quad (3)$$

where E_r is the Young's modulus of the structural material, I_b is the second moment of area for the cross-section of a single beam on the composing diamond-shaped cell, l_b is the length of the single beam, Δl_c is the change in distance of the two facing beams of the cell under deformation, n and t are the numbers of cells in the radial direction and axial direction, respectively. Polydimethylsiloxane (PDMS) and neodymium iron boron (NdFeB) magnetic microparticle composite were chosen for the active part, and parylene C was chosen for the passive part, given its feasibility of miniaturization and versatility in fabrication.

RESULTS

In the phantom fabricated by PDMS with the glycerol-water mixture as the blood simulant and a 5 cm-sized cubic permanent magnet for actuation, a robot with only the active part could be steered for retrievable shape-adaptive locomotion ($R_d = 0.75$ mm, length $l_r = 5$ mm, $E_r = 6.44$ MPa). F_n along with the deformation can be computed by Eq. 3. We first validated the model. Here, both finite element analyses (FEA, Abaqus 2019) and experiments by a mechanical tester were conducted (Instron 5942) (Fig. 2B). Then, using the above overall F_n as the threshold, we predicted F_n of the active and passive parts. Given the active part with $E_r = 5.00$ MPa, the maximum allowed F_n from the passive part could be computed (Fig. 2C).

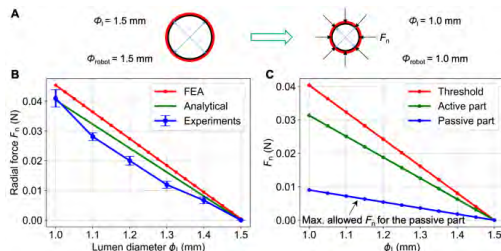


Fig. 2 Modeling of the shape adaptation in the lumen with varying diameters. (A) Cross-sectional view of the robot's shape adaptation. Normal force F_n appears given the radial deformation. (B) Validation of the analytical model. (C) Theoretical calculation of the maximum allowed F_n from the passive part.

For the first-generation prototype, we fabricated a robot with magnetic composite material as the active part and parylene C film as the passive part. The active part with an overall external dimension of 1.5 mm × 3 mm was fabricated using molding [3]. For the passive part, we used a commercial parylene C coater (SCS Labcotter® 2 (PDS 2010), Specialty Coating Systems, USA) to coat a 2-μm-thick parylene C on the acrylic board. Then, we used the laser to cut a piece of parylene C sheet (ProtoLaser U3, LPKF Laser & Electronics AG) with a dimension of around 5 mm × 1.5 mm × 3 mm, which was rolled and integrated into the active part. The robot could feasibly divert the blood simulant from flowing into a branch (flow speed: 10 cm/s), as shown in Fig. 3.

Based on the modeling for arteries, the threshold F_n and frictional force, when the robot enters the lumen with $\phi_l = 1$ mm, were estimated to be around 0.04 N and 0.003 N, respectively, in porcine arteries *ex vivo*. F_n here induces a compressive stress of around 5.0 kPa, smaller than the quantified threshold that ruptures the endothelial cell at around 12.4 kPa [6, 7]. Thus, this design can potentially enable safer interaction with endothelial cells.

DISCUSSION

While the multi-material constructions of Stentbot demonstrated the proof-of-concept flow diversion with the active and passive components, the design methodology and fabrication techniques need to be enhanced as the next step. First, the design should be

optimized for the desired locomotion and function, from the aspects of shape adaptation and effective porosity. For example, the effects of the shape and dimension of the cell structure for the two parts can be thoroughly investigated. Particularly, exploring proper pattern designs of the passive part could accomplish high versatility. Second, the selection of materials and fabrication methods must be reconsidered. Although parylene C has indicated the feasibility of miniaturization and biocompatibility [8], its 3D fabrication with encoded complex cell structures for shape adaptation needs to be investigated. Moreover, integrating soft polymers and plastic film into a single device is challenging. Alternative materials enabling the flexible fabrication of microscale mesh-like structures will be beneficial. More importantly, these materials must be both biocompatible and hemocompatible.

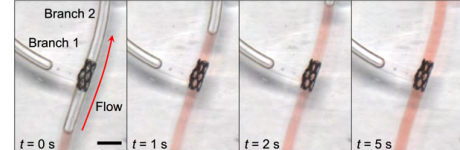


Fig. 3 Test of flow diversion. The device comprises the active magnetic composite part (outside: PDMS + NdFeB) and the passive part (inside: parylene C). The flow speed was set to 10 cm/s. Scale bar: 3 mm.

Finally, from the system aspect, the device's integration with the existing interventional paradigm using microcatheters could further facilitate clinical translation. For example, the robot could be integrated into a conventional medical catheter, navigated to hard-to-reach distal regions with the assistance of a guidewire, and released to locomote to the target for location-adjustable flow diversion.

REFERENCES

- [1] M. Sitti, "Miniature soft robots—road to the clinic," *Nat. Rev. Mater.*, vol. 3, no. 6, pp. 74–75, 2018.
- [2] W. Hu, G. Z. Lum, M. Mastrangeli, and M. Sitti, "Small-scale soft-bodied robot with multimodal locomotion," *Nature*, vol. 554, no. 7690, pp. 81–85, 2018.
- [3] T. Wang *et al.*, "Adaptive wireless millirobotic locomotion into distal vasculature," *Nat. Commun.*, vol. 13, no. 1, p. 4465, 2022/08/01 2022, doi: 10.1038/s41467-022-32059-9.
- [4] Y. Zhang, Y. Wang, E. Kao, L. Flórez-Valencia, and G. Courbebaisse, "Towards optimal flow diverter porosity for the treatment of intracranial aneurysm," *J. Biomech.*, vol. 82, pp. 20–27, 2019.
- [5] Y. Chen, C. Howe, Y. Lee, S. Cheon, W.-H. Yeo, and Y. Chun, "Microstructured thin film nitinol for a neurovascular flow-diverter," *Sci. Rep.*, vol. 6, no. 1, pp. 1–10, 2016.
- [6] D. Gonzalez-Rodriguez *et al.*, "Mechanical criterion for the rupture of a cell membrane under compression," *Biophys. J.*, vol. 111, no. 12, pp. 2711–2721, 2016.
- [7] E. Peeters, C. Oomens, C. Bouten, D. Bader, and F. Baaijens, "Mechanical and failure properties of single attached cells under compression," *J. Biomech.*, vol. 38, no. 8, pp. 1685–1693, 2005.
- [8] T. Y. Chang *et al.*, "Cell and protein compatibility of parylene-C surfaces," *Langmuir*, vol. 23, no. 23, pp. 11718–11725, 2007.

A novel stereoscopic thermal endoscope for tissue damage prevention

D. Scutelnic¹, G. De Rossi¹, N. Piccinelli¹, C. Daffara¹, S. Siracusano², and R. Muradore¹

¹*University of Verona* ²*University of L'Aquila*
giacomo.derossi@univr.it

INTRODUCTION

Multi-spectral imaging systems, namely thermal and visible spectrum imaging systems, are recently being employed successfully in multiple civilian applications, such as civil engineering, precision agriculture, and cultural heritage preservation [1], due to the more general availability of high-performing, compact sensors. The same success can not yet be appreciated in medical or surgical applications, with most examples of thermography in medicine being applied on the epidermis [2] or specialized applications with limited measurements [3]. Nevertheless, direct thermal tissue measurements could prove invaluable in laparoscopy and laparo-assisted robotic surgery, where bipolar electrocoagulation or ultrasonic energy are often used to achieve haemostasis to maximise a clear view of the surgical field. The temperatures exceed 45 °C where disruption in the neurovascular bundles (NVB) functions was observed *in vivo*, with protein denaturation and subsequent cellular death occurring between 57 °C and 65 °C [4]. Coagulation by thermal energy can be considered responsible for the damage to the NVB that are intimately located on the lateral, posterolateral and posterior surface of the prostate during nerve-sparing robotic-assisted radical prostatectomy (RARP) [5]. This damage can decrease the chance of a full recovery of physiological functions after the procedure, namely the erection and urinary continence, which is estimated to be at 50% [6]. For this reason, cautery-free procedures have been evaluated to reduce the amount of induced thermal damage by using clips [7], but they introduce risk of unintentional neural bundle dissection. We present a novel endoscope prototype for minimal invasive surgery: it integrates full stereoscopic vision with 3D-mapped, direct thermal measurements to evaluate the heat propagation over the surface target tissue during bipolar coagulation. The precise mapping of the multi-spectral images would allow clinicians to quickly assess the risk of damage to sensitive tissues intra-operatively.

MATERIALS AND METHODS

The stereoscopic visual-thermal endoscope is endowed with a pair of high-definition cameras (1920 × 1080 px, field-of-view (FOV) 65°) aligned with a compact thermal camera (160 × 120 px, 50° FOV) within a pivotable head to point towards the target, as illustrated in Figure 1. We



Fig. 1 Stereoscopic thermal endoscope prototype.

devised a novel calibration approach for the unique issues affecting target identification in thermal imaging, such as undesired reflections, contrast inversion issues, and time-changing, non-uniform size and shape of detectable markers due to heat diffusion. The occurrence of these effects negatively affect the identification precision of calibration targets for the camera array alignment when not properly accounted for. The novel algorithm performs two main additional steps compared to the standard visual calibration pipeline: it reconstructs the marker shape around the most representative identified points via pattern filling thanks to an intermediate homography estimation via a RANSAC-like optimization algorithm. This increases both the number of valid calibration patterns and the estimation precision of the centroids used in the camera parameters estimation. Figure 3 presents an overview of the steps of the algorithm and the result of a calibration on a 6 × 4 target board with circular markers 3 mm in diameter. The prototype is currently 20 mm in diameter; the miniaturization target for the final version is 15 mm, a limit currently imposed by the current thermal sensors technology. The design regarding the stereoscopic thermal endoscope and the calibration algorithm are covered by patents [8], [9].

RESULTS

The application of thermal imaging to endoscopy has been explored in a CO₂-rich environment over organic tissues with a thermal-only endoscope prototype [10], [11]. The study presented the disassociation between how the surgeon perceives thermal tissue damage, which currently solely relies on changing in visual appearance versus the actual measured surface temperatures that indicate the occurrence of cellular damage. As such, the main result of the proposed prototype camera array regards the quality of the visible-thermal calibration, which allows to pinpoint the temperature measurements

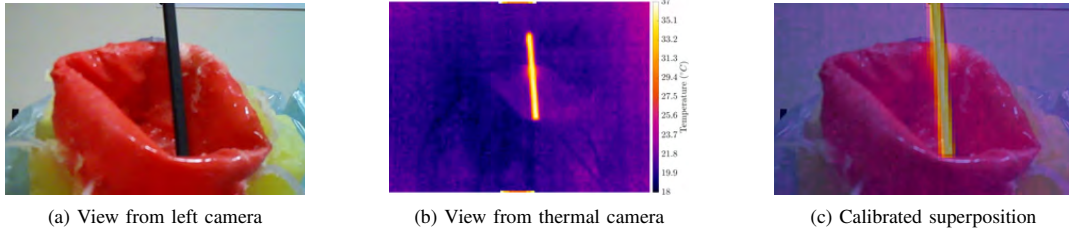


Fig. 2 Qualitative test on a bladder phantom @100 mm from the camera array to replicate the view of the surgeon in laparoscopy; the temperatures measured by the thermal camera (b) are mapped to colors with a custom color palette.

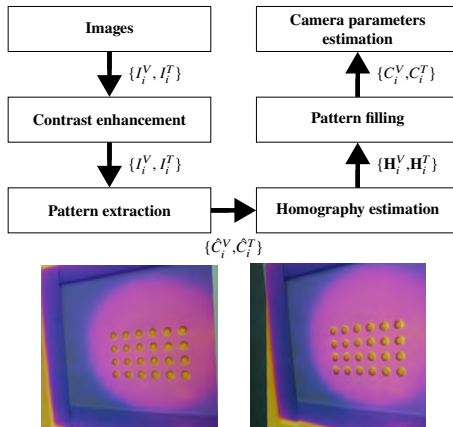


Fig. 3 Overview of the calibration algorithm with identified thermal markers mapped on left and right cameras

within the anatomical environment. This quality can be expressed with an estimated re-projection error of 0.24 px value between the visible stereo cameras and the thermal sensor. This translates in an average mismatch between the identified 3D point on the target and the correct thermal measurement of ≈ 0.5 mm@100 mm, given the relative camera array resolutions and FOVs. Figure 2 shows the result of a visible-thermal registration in the virtual space as a color blending: it demonstrates how the high-precision mapping between the visible camera scene and the temperature measurements leads to a precise identification of higher temperature spots in the simulated tissues due to the presence of the heated tool.

DISCUSSION

The combined stereo-thermal endoscope proposed in this work combines the traditional three-dimensional view usually available in robotic minimally access surgery (RMAS) with a superimposed temperature map to provide precise and critical measurements to the surgeon when needed and where needed. The novel capability provided by this endoscope could help improving the outcome of all the procedures involving electrocoagulation instruments (e.g., RARP) as the surgeon would be able to better estimate how much the energy discharged by

the electrocoagulation instrument spreads in the tissues, thus act accordingly to prevent excessive damage before physical alterations at cellular level occur. Furthermore, the system could provide tissue health estimation during renal enucleoresection and monitoring of vascularisation, which are currently performed by specialised vision systems via contrast agents, but that can be achieved by exploiting the temperature difference between organs and superficial vessels as measured by the thermal sensor. The image processing is being improved to include a thermal diffusion analysis to preemptively alert the surgeon before the energy discharge reaches any critical region.

ACKNOWLEDGEMENTS

This work has been funded by the *RoboIT* consortium under the supervision of *Pariter Partners*.

REFERENCES

- [1] C. Daffara, S. Parisotto, and D. Ambrosini, "Multipurpose, dual-mode imaging in the 3–5 μm range (mwir) for artwork diagnostics: A systematic approach," *Optics and Lasers in Engineering*, vol. 104, pp. 266–273, 2018.
- [2] P. Rajmanová, P. Nudzikova, and D. Vala, "Application and technology of thermal imagine camera in medicine," *IFAC-PapersOnLine*, vol. 48, no. 4, pp. 492–497, 2015, 13th IFAC and IEEE Conference on Programmable Devices and Embedded Systems.
- [3] M. Ohara *et al.*, "Developing thermal endoscope for endoscopic photothermal therapy for peritoneal dissemination," in *2020 IEEE/RSJ International Conference on Intelligent Robots and Systems (IROS)*, 2020, pp. 3040–3047.
- [4] I. I. Lantis JC *et al.*, "Comparison of coagulation modalities in surgery," *Journal of Laparoendoscopic & Advanced Surgical Techniques. Part A*, vol. 8, no. 6, pp. 381–394, Dec. 1998.
- [5] N. Mottet *et al.*, "EAU-EANM-ESTRO-ESUR-SIOG Guidelines on Prostate Cancer-2020 Update. Part 1: Screening, Diagnosis, and Local Treatment with Curative Intent," *European Urology*, vol. 79, no. 2, pp. 243–262, Feb. 2021.
- [6] S. A. Boorjian *et al.*, "A critical analysis of the long-term impact of radical prostatectomy on cancer control and function outcomes," *European Urology*, vol. 61, no. 4, pp. 664–675, Apr. 2012.
- [7] T. E. Ahlering *et al.*, "Feasibility study for robotic radical prostatectomy cauter-free neurovascular bundle preservation," *Urology*, vol. 65, no. 5, pp. 994–997, May 2005.
- [8] C. Daffara *et al.*, "Thermal endoscope for surgical applications," Italian Patent IT20190003347A1, 2019.
- [9] ———, "Thermal endoscope with three aligned optical windows," European Union Patent EP20159675.6, 2020, pending.
- [10] S. Siracusano *et al.*, "P199 - Experimental model of an artificial pneumoperitoneum to measure thermal energy spread during bipolar cauterizing," *European Urology Supplements*, vol. 17, no. 8, pp. 304–305, Sep. 2018.
- [11] D. Scutelnic *et al.*, "Thermal endoscope based on cost-effective lwir camera cores," *HardwareX*, vol. 11, p. e00300, 2022.

Augmented Reality-based Surgical Guidance for Anterior and Posterior Cruciate Ligament Reconstruction

Deokgi Jeung¹, Hyun-Joo Lee², Hee-June Kim², Jaesung Hong¹

¹*Department of Robotics and Mechatronics Engineering, DGIST,*

²*Department of Orthopaedic Surgery, School of Medicine, Kyungpook National University,
Kyungpook National University Hospital
jhong@dgist.ac.kr*

INTRODUCTION

Anterior and posterior cruciate ligament (ACL and PCL) reconstructions are common knee arthroscopic surgeries. ACL and PCL reconstruction have small incision sites, thus enabling fast recovery of the patient. However, an arthroscope provides a limited view due to the small size of the camera lens, and a small incision restricts the motion of surgical instruments. As a result, finding the exact bone drilling position that was preoperatively determined to connect a new ligament between the femur and tibia is challenging during surgery. A previous study verified that the complication ratio of ACL and PCL reconstruction is 9.0 % and 20.1 %, respectively, which are particularly high compared to other knee arthroscopic surgeries [1].

Augmented reality (AR)-based surgical guidance can assist in difficult ACL and PCL reconstruction. Hu et al. [2] proposed AR-based non-invasive drilling guidance for the femur in open knee surgery. To implement the non-invasive system, they performed the registration between the depth data of the femur obtained from RGBD sensors and the pre-scanned femur model. However, this method is suitable for open knee surgery and is not for arthroscopic surgeries such as ACL and PCL reconstruction. Recently, Chen et al. [3] introduced non-invasive AR for knee arthroscopy. However, to reflect knee movements occurring during surgery in AR, it is necessary to manually select four anatomical landmarks in the arthroscopic view. Manual selection is inconvenient and may be inconsistent, interfering with surgical procedures.

In this study, we propose a non-invasive AR-based surgical guidance for ACL and PCL reconstruction with compensation of the intraoperative knee movement. Unlike preoperative CT and MR, which are taken under the extension state, the knee is under the flexion state during surgery, which requires compensation for the knee movement. The proposed method estimates knee movement without direct bone exposure or manual intervention by exploring the correlation between the knee surface and the internal bones (femur and tibia) based on a finite element method. The proposed method can enhance the AR for knee arthroscopic procedures, leading to more accurate bone drilling for ACL or PCL reconstruction.

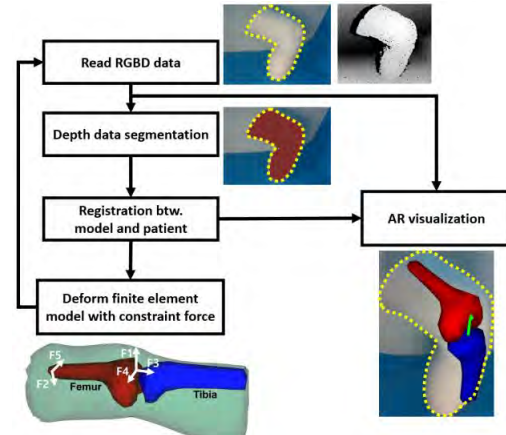


Fig. 1 Flowchart of the proposed AR-based surgical guidance.

MATERIALS AND METHODS

A. Correlation model between knee surface and bone

Fig. 1 shows the entire process of the proposed method. First, we defined individual finite element models for the knee surface, femur, and tibia (Fig. 2). For the femur and tibia, a tetrahedral co-rotational finite element was used to simulate a large displacement with accurately representing the shape of the bone. On the other hand, for the knee surface, the hexahedral finite element was used for its rounded shape and computational efficiency by adjusting the number of elements. In our study, we assumed that both knee surface and internal bones have isotropic elastic behavior. According to the previous study, Young's modulus of bones was set to 1000 MPa [4]. For the knee surface, Young's modulus was set empirically because it was a mixture of diverse soft tissues.

We introduced a mapping between finite element models [5] to make motions of internal bones according to the shape deformation of the knee surface. In each simulation loop, the hexahedron elements of the knee surface propagate displacement to corresponding internal tetrahedron nodes of bones. The forces generated due to the displacement of the tetrahedron node are inversely propagated to the hexahedron elements. A collision controlled between the femur and tibia was implemented to prevent overlapping the two models.

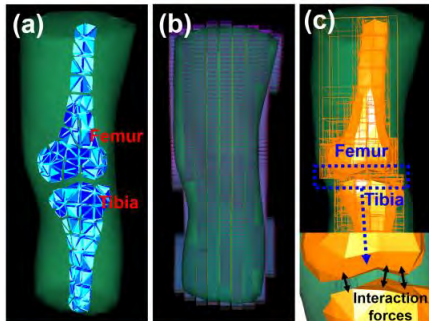


Fig. 2 (a) Tetrahedral finite element for femur and tibia. (b) Hexahedral finite element for knee surface. (c) Collision model and interaction forces between the femur and tibia

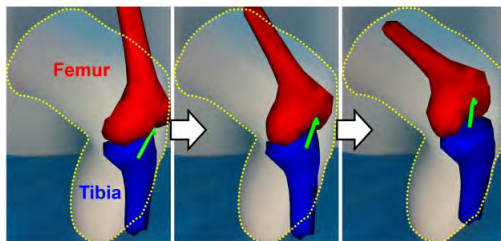


Fig. 3 AR visualization result. Green arrow represents the drilling guidance.

B. Registration and AR visualization

The proposed method repeats the processes as shown in Fig. 1 for each simulation loop to deform the correlation model and visualize AR in real time. First, the three-dimensional depth information of the knee surface is segmented from the entire data of the RGBD sensor using color and distance information. Next, the iterative closest points algorithm is used for the registration between the depth data of the knee surface and the correlation model. Based on the registration result, the magnitude and direction of the constraint forces (F_1 to F_5 in Fig. 1), which are required for the correlation model deformation, are updated. To apply consistent criteria for all patients' knee data, the direction of each constraint force is determined using the principal component analysis for the three-dimensional points constituting the femur. The point of application of the constraint forces is set to both ends of the femur. In the following simulation loop, if the registration accuracy between the depth data and the correlation model is improved, the magnitude of constraint forces is decreased, maintaining its direction. If the registration accuracy is reduced, the magnitude of constraint forces is increased, and the direction is reversed. F_1 and F_2 , which are constraint forces applying in the same direction along the knee flexion, take effect in entire simulation loops. The other constraint forces (F_3 , F_4 , and F_5) are applied alternately for every 30 simulation loops.

RESULTS

Extension and flexion state knee CT were photographed for the experiment. Extension state CT was used to

implement a correlation model between knee surface and internal bones. Flexion state CT was used to make knee phantom to evaluate the proposed method. The C++ programming language and SOFA framework [6] was used to simulate the deformation of the correlation model. The real surgical environment was simulated to determine the relative locations of the RGBD sensor and the knee phantom.

Fig. 3 shows the deformation of the correlation model and visualized AR over time. During knee deformation, the AR was updated to 10 frames per second (fps); after the deformation was completed, it was updated to 15 fps. The time consumed to complete the deformation was about 50 seconds. The shape of internal bones was not changed due to the high Young's modulus. The shape of the soft tissues around the bone is also not significantly deformed. Instead, the knee model was flexed with significant deformation of the joint between the femur and tibia. The target registration error of the internal bones measured between flexion state knee CT and the simulated correlation model was 7 mm, which is in an acceptable range for bone tunneling.

DISCUSSION

The proposed AR-based surgical guidance utilized the shape information of the knee surface to estimate the location of internal bones. The method is less invasive and easier to introduce than existing surgical guidance using invasive patient-attached markers. In addition, the proposed method does not require direct bone exposure or manual intervention for registration. The proposed system showed the effectiveness of AR overlay for internal bones. The evaluation of the bone drilling by using the proposed AR guidance remains as future work.

ACKNOWLEDGMENTS

This work was supported by the National Research Foundation of Korea (NRF) grant funded by the Korea government (MSIT) (No. 2020R1A2C2100012).

REFERENCES

- [1] Salzler MJ, Lin A, Miller CD, et al. Complications after arthroscopic knee surgery. Am J Sports Med 2014; 42(2):292–96.
- [2] Hu X, Liu H, Baena FRY. Markerless Navigation System for Orthopaedic Knee Surgery: A Proof of Concept Study. IEEE Access 2021; 9:64708–18.
- [3] Chen F, Cui X, Han B, et al. Augmented reality navigation for minimally invasive knee surgery using enhanced arthroscopy. Comput Methods Programs Biomed Elsevier BV 2021; 201:105952.
- [4] Sylvester AD, Kramer PA. Young's Modulus and Load Complexity: Modeling Their Effects on Proximal Femur Strain. Anat Rec 2018; 301(7):1189–202.
- [5] Peterlik I, Duriez C, Cotin S. Modeling and real-time simulation of a vascularized liver tissue. Med Image Comput Comput Assist Interv 2012; 15(Pt 1):50–57.
- [6] Faure F, Duriez C, Delingette H, et al. SOFA: A Multi-Model Framework for Interactive Physical Simulation. Stud Mechanobiol Tissue Eng Biomater 2012; 11(June):283–321.

Meshless Modelling for Heat-based Robotic Navigation of Radio Frequency Catheter Ablation

K. A. Mountris¹, R. Schilling², A. Casals³, and H. A. Wurdemann¹

¹*Mechanical Engineering Dept., University College London,*

²*Barts Heart Centre, St Bartholomew's Hospital,*

³*Research Center for Biomedical Engineering, Universitat Politècnica de Catalunya
k.mountris@ucl.ac.uk*

INTRODUCTION

Radio frequency catheter ablation (RFCA) of cardiac arrhythmia is commonly performed by navigating the catheter manually. Nevertheless, remote navigation techniques where catheter steering is performed using either a magnetic field or robotically are available. Clinical experience with these techniques demonstrated that higher contact forces can be achieved with robotic compared to magnetic field navigation [1]. This translates into more effective ablation lesions, but if excessive contact force is applied it may lead to higher risk of cardiac perforation [2]. However, the robotic navigation system is no longer commercially available and advancements have been stalled. To ensure high effectiveness and low complication risk in next-gen robotic navigation systems, tissue heat distribution should be taken into account. Computational models for heat distribution simulation predict lesion formation effectively [3]. However, their clinical application is limited since they have been developed for single-site ablation and numerical accuracy depends on the quality of mesh discretization. In this work, we propose a novel meshless model to simulate tissue heat distribution during robotic navigation assisted ablation. The model accounts for non-zero initial conditions and time dependent boundary conditions to simulate multi-site ablation. The meshless Fragile Points Method (FPM) is employed for the numerical solution of the model to ensure its suitability for clinical application, since FPM does not require the definition of a mesh [4], [5].

MATERIALS AND METHODS

In FPM, a domain of interest (Ω) is represented by a set of randomly distributed points which are enclosed in non-overlapping subdomains that partition Ω . Local discontinuous polynomials are used as trial functions. For a subdomain E_0 enclosing the point P_0 , the trial function u_h is given by:

$$u_h(x) = u_0 + (x - x_0) \cdot \nabla u \Big|_{P_0}, \quad x \in E_0 \quad (1)$$

where u_0 is the value of u_h at P_0 and x_0 the coordinates vector of P_0 . $\nabla u \Big|_{P_0}$ is estimated in terms of u_h values

at neighbor points of P_0 using Generalized Finite Differences [6]. Tissue heat distribution is then modelled by solving the bioheat Pennes equation:

$$\rho c(T) \frac{\partial T}{\partial t} - \nabla \cdot (k(T) \nabla T) = q \text{ in } \Omega \quad (2)$$

where ρ is density, $c(T)$ specific heat, t time, $k(T)$ thermal conductivity, T temperature. The heat source $q = \sigma(T) |\nabla \Phi|^2$ is produced by the RF current and is obtained by solving the electrical potential equation:

$$\nabla \cdot (\sigma(T) \nabla \Phi) = 0 \text{ in } \Omega \quad (3)$$

where $\sigma(T)$ is electrical conductivity and Φ electrical potential. Multi-site ablation is modelled using the temperature field from previously ablated sites as initial condition in Equation (2). Time-dependent Dirichlet conditions are employed in Equation (3) to account for the time interval between the start and end of the different ablations. Given the ablation starting time (t_s) at a given site, the time-dependent Dirichlet conditions are expressed as:

$$\Phi = \Phi_D u(t - t_s) \text{ in } \Gamma_D \quad (4)$$

where Γ_D is the Dirichlet boundary and $u(t - t_s)$ the step function:

$$u(t - t_s) = \begin{cases} 1 & \text{if } t \geq t_s \\ 0 & \text{if } t < t_s \end{cases} \quad (5)$$

An ablation protocol with two ablation sites $s1, s2$ of a 3D porcine ventricular tissue block with dimensions $40 \times 40 \times 20$ mm was considered. Density $\rho = 1076 \text{ kgm}^{-3}$, initial specific heat $c_0 = 3017 \text{ Jkg}^{-1}\text{K}$, initial thermal conductivity $k_0 = 0.518 \text{ Wm}^{-1}\text{K}$, and initial electrical conductivity $\sigma_0 = 0.54 \text{ Sm}^{-1}$ were used. Ablation sites were located at the top tissue surface at $s1 = (0, -1, 20) \text{ mm}$ and $s2 = (0, 1, 20) \text{ mm}$. Ablation time was $t_a = 30 \text{ s}$. Temperature $T = 37^\circ\text{C}$ was imposed as boundary condition. The surface of the catheter was held at $T = 22^\circ\text{C}$. Electrical potential at the bottom tissue surface was set $\Phi = 0\text{V}$ and $\Phi = 20\text{V}$ at the surface of the catheter. Simulations were performed with catheter indentation at perpendicular position and rotated around the x-axis by a 30° angle. To distinguish between the

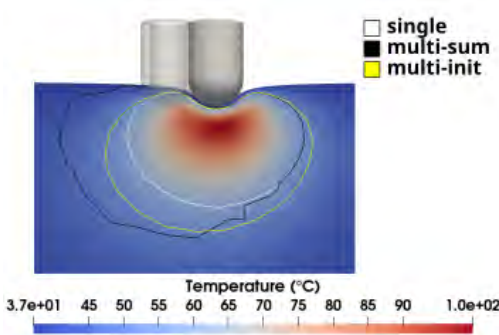


Fig. 1 $T \geq 50^\circ\text{C}$ isolines for single and multi-site ablation for perpendicular catheter indentation ($R_1 = 0^\circ$, $R_2 = 0^\circ$). The lesion in single ablation (white) is underestimated compared to multi-site with initial condition (yellow).

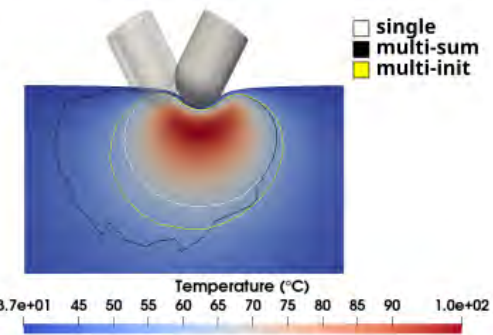


Fig. 2 $T \geq 50^\circ\text{C}$ isolines for single and multi-site ablation for indentation with angles $R_1 = 30^\circ$, $R_2 = -30^\circ$. Lesion underestimation in single-site ablation is observed.

different simulations we used the abbreviation $R_x = a^\circ$, where x denotes the ablation site and a° the catheter rotation angle. For instance, $R_{s1} = 0^\circ$, $R_{s2} = 0^\circ$ denotes the simulation where the catheter was perpendicularly indented at both sites. Similarly, $R_{s1} = 30^\circ$, $R_{s2} = -30^\circ$ denotes the simulation where the catheter was indented at an angle of 30° around x-axis at s1 and -30° around x-axis at s2. Indentation force was $F = 20\text{ g}$ in all simulations.

RESULTS

The ablation lesion at site s2 from single-site ablation simulation was compared with the lesion obtained from the proposed multi-site ablation simulation (multi-init). A comparison with summed single-site heat maps (multi-sum) was also performed. The region receiving $T \geq 50^\circ\text{C}$ was considered as lesion since tissue heat damage is permanent above 50°C . Lesion width (W), depth (D), and maximum temperature (T_{\max}) were computed to compare the heat maps obtained from the single, multi-init, and multi-sum simulations. Three different catheter rotation angles at s1, s2 were considered during simulations. These were namely ($R_{s1} = 0^\circ$, $R_{s2} = 0^\circ$), ($R_{s1} = 30^\circ$, $R_{s2} = 30^\circ$), and ($R_{s1} = 30^\circ$, $R_{s2} = -30^\circ$). Differences in the lesion characteristics between single and multi-init were up to 17.6% for W, 24.4% for D, and 6.1% for T_{\max} for ($R_{s1} = 0^\circ$, $R_{s2} = 0^\circ$) simulation. Similar results were demonstrated in simulations with different rotation angles. In Figures 1, 2 $T \geq 50^\circ\text{C}$ isolines are given for simulations with catheter rotation angles $R_{s1} = 0^\circ$, $R_{s2} = 0^\circ$ and $R_{s1} = 30^\circ$, $R_{s2} = -30^\circ$, respectively.

DISCUSSION

In this study, a novel meshless FPM computational model was proposed to simulate multi-site ablation for next-gen robotic navigation systems. Multi-site ablation simulation was performed using the temperature distribution from previous ablations as initial condition. Lesion characteristics were evaluated for single-site and multi-site simulations. It was found that lesion characteristics were

underestimated in single-site simulation. As shown in Figures 1 and 2, multi-init simulations predicted larger lesion compared to single-site simulations. While max temperature difference was in the range 5.7% - 6.1%, the lesion width was larger in multi-init heat maps by a range of 14.5% - 17.6%. and depth was larger in the range of 22.0% - 24.4%. Therefore, multi-site ablation simulation may assist in the formation of transmural lesions at lower tissue temperatures. The capacity of the presented computational model for meshless simulation of multi-site ablation has the potential to improve next-gen robotic navigation systems. Predicting heat maps while taking into account the heat accumulation from previous ablations could guide the robotic navigation system to deliver heat homogeneously to the area under treatment. Furthermore, since transmural lesions may be obtained for lower temperatures, the cardiac perforation risk due to excessive contact force could be reduced. Finally, since the proposed computational model is meshless it does not require a preprocessing step making its application in clinical robotic navigation systems straightforward.

REFERENCES

- [1] D. Steven, T. Rostock, H. Servatius *et al.*, “Robotic versus conventional ablation for common-type atrial flutter: a prospective randomized trial to evaluate the effectiveness of remote catheter navigation,” *Heart Rhythm*, vol. 5, 2008.
- [2] R. Bai, L. Di Biase, M. Valderrabano *et al.*, “Worldwide experience with the robotic navigation system in catheter ablation of atrial fibrillation: methodology, efficacy and safety,” *Journal of cardiovascular electrophysiology*, vol. 23, 2012.
- [3] A. Petras, M. Leoni, J. M. Guerra *et al.*, “A computational model of open-irrigated radiofrequency catheter ablation accounting for mechanical properties of the cardiac tissue,” *International journal for numerical methods in biomedical engineering*, vol. 35, 2019.
- [4] L. Dong, T. Yang, K. Wang, and S. N. Atluri, “A new fragile points method (fpm) in computational mechanics, based on the concepts of point stiffnesses and numerical flux corrections,” *Engineering Analysis with Boundary Elements*, vol. 107, 2019.
- [5] K. A. Mountris, L. Dong, Y. Guan *et al.*, “A meshless fragile points method for the solution of the monodomain model for cardiac electrophysiology simulation,” *Journal of Computational Science*, vol. 65, 2022.
- [6] T. Liszka and J. Orkisz, “The finite difference method at arbitrary irregular grids and its application in applied mechanics,” *Computers & Structures*, vol. 11, 1980.

Computer-based assessment of the operator's experience in obstetric ultrasound examination based on hand movements and applied forces

V. Penza¹, A. Santangelo¹, D. Paladini², and L. S. Mattos¹

¹Biomedical Robotics Lab, ADVR, Istituto Italiano di Tecnologia, Genoa, Italy

²UOC Medicina Fetale e Perinatale, Istituto Giannina Gaslini, IRCCS

veronica.penza@iit.it

INTRODUCTION

Obstetric ultrasound (US) is widely used in prenatal diagnosis to monitor the development and growth of the embryo or fetus and to detect congenital anomalies. The benefits offered by US in terms of timely diagnosis are extensive, but the quality of the examination is closely linked to the experience of the clinician [1]. Although proper training and assessment of acquired skills are considered of paramount importance in order to ensure a quality exam, there is no European standard establishing a training path with an objective assessment of operator's capabilities. In fact, the experience is often evaluated merely on the basis of the number of clinical tests performed. However, an operator with daily US examination experience may not perform as well as a true expert due to inadequate training [2].

Many studies have been conducted to assess hand gesture with the aim of establishing metrics to discriminate between experts and novice, which can also be used to study a specific training and objectively evaluate the acquired skills [3][4]. Inspired by these works, hand movement was also studied for fetal US on phantom [5] or in a virtual reality simulated scenario [6].

This paper presents a novel study for the objective assessment of the operator's experience in obstetric US examinations based on hand gestures and forces applied with the US probe on the abdomen, during real obstetric US examinations. A *Data Recording System* was designed to collect this information during US examinations performed by clinician with 3 different levels of experience (expert, intermediate and novice) on pregnant women at the 2nd trimester. The results presented here focus on assessing a set of metrics with the potential to provide an objective discrimination of the operator's level of experience. With respect to previous works, the novelty relies on validating the state-of-the-art discriminating metrics in a real scenario. Furthermore, this work includes as a novelty the measurement of the forces applied on the abdomen, which seems to be very relevant in the clinical practice.

This study was approved by the Regional Ethics Committee of Liguria (Italy) with the protocol number 379/2022 - DB id 12369.

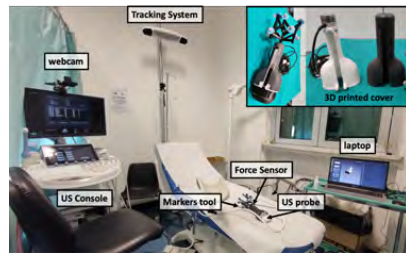


Fig. 1 An overview of *Data Recording System* and the experimental setup for the US examination.

MATERIALS AND METHODS

The data collected to characterize the operator's gesture while performing an obstetric US consists in:

- Roto-translational *US probe movement*;
- *Force/torque* exerted by the probe on the patient's abdomen;

A *Data Recording System* was designed to acquire this data during real US examinations (Fig. 1).

Data Recording System

The US device used in the experiments is the E10 (GE HealthCare Technologies Inc., USA) with a 1-5 MHz convex abdominal transducer.

The *US probe movement* is recorded using an Optical Tracking System (Polaris Vega ST, NDI Inc, Canada). A 3D printed cover was designed to place a tool of reflective markers on the US probe (Fig. 1). Considering the wide range of motion performed during the exam, a multi-faced markers tool with 5 perpendicular faces was designed to ensure robust US probe tracking. This was required because the tracking system tracks only one face on the tool at time, i.e. the one with the smallest angle between its normal and the tracking system. Furthermore, each face should have a unique geometry and respect the constraints presented in Tab. I.

Force/torque are measured through a force sensor placed on the US probe (Nano25, ATI Industrial Automation, USA). In order to measure only the contact forces between the US probe and the abdomen, the cover was designed with an inner layer physically detached from the

TABLE I Constraints for unique geometry marker tool

Unique Geometry Constraints	
Min nr of markers	3
Min segment length	50mm
Min segment lend diff	3.5mm
Min segment angle diff	2deg

outside layer in contact with the hand, transmitting all the interaction forces through the FT sensor, as shown in Fig. 1. The force/torque values are set to zero each time the system starts, which is performed keeping the probe in a fixed vertical position. Moreover, the force/torque are transformed to the contact point between the probe and the tissue, applying a transformation computed based on the system's CAD design.

The *Data Recording System* runs on Ubuntu, using ROS1 melodic. A Graphical User Interface (GUI) was developed to visualize the probe movement and the acquired force/torque data, which are time-stamped and recorded together with the start and end time of each experimental trial.

Experimental Protocol

We are currently conducting a prospective descriptive interventional study at the Istituto Giannina Gaslini, Italy. The preliminary results presented here involved 8 operators (subjects) with three different levels of experience: 1) 1 advanced (> 10 years of experience); 2) 3 intermediate (5 – 10 years of experience); 3) 5 novice (< 5 years of experience, postgraduates). The number of patients examined were 7. Both the subjects and the patients provided written informed consent.

After completing the routine exam and confirming normal fetal anatomy, the subject was asked to obtain a predefined set of standard scan planes related to the monitoring of fetal anatomy, as per indication of the SIEOG (Italian Society of Obstetric-Gynecological Ultrasound). The first trial was always performed by the expert operator, followed by an intermediate or beginner operator. No more than 2 tests per patient were performed to avoid significantly prolonging the US examination. The subject performing the test was required to save an image frame each time the required scan plane was reached. The test was considered valid if no gross fetal movements occurred between the examination of the 1st and 2nd operator.

RESULTS

A preliminary data evaluation is focused on the identification of a set of measures potentially able to discriminate the level of experience of the operator, based on literature and suggestions from expert clinicians. The measures selected were: (i) **total distance** traveled by the US probe; (ii) **average volume** of the US probe motion; (iii) **total time** of the trial execution; (iv) **average sequence time**, i.e. the average execution time to reach each sequence plane; (v) **max force**; (vi) **average force**; (vii) US probe dimensionless **jerk** [7].

A visual representation of the obtained results is shown in Fig. 2. The graph presents the seven objective metrics as

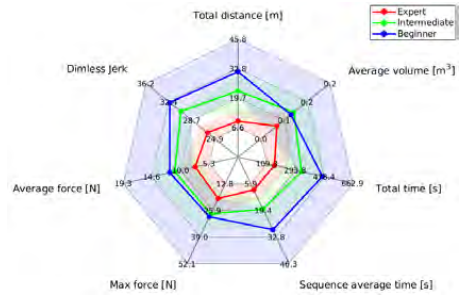


Fig. 2 Radar plot showing comparison of relevant measures between the 3 level of experience. The solid line represents the average value, and the shadowed area represents the minimum and maximum values.

a Radar Plot, which allows for an intuitive interpretation of the data. A clear difference between the data from the different operators can be seen.

DISCUSSION

This paper presented a data acquisition system and a set of objective metrics expected to allow a robust classification of the degree of experience of operators during real prenatal US examinations. The preliminary results already highlight differences between the level of experience of operators. Future work will include more patients and subjects to allow proper statistical analysis of the results. The most significant metrics will then be used by a Machine Learning-based classifier to automatically and objectively assess operator proficiency. In addition, we plan to investigate the use of Deep Learning methods to perform this classification without explicitly defining the assessment metrics, which could lead to a real-time proficiency assessment system.

REFERENCES

- E. Pajkrt, B. Mol, K. Boer, A. Drogstop, P. Bossuyt, and C. Bilardo, “Intra-and interoperator repeatability of the nuchal translucency measurement,” *Ultrasound in Obstetrics and Gynecology: The Official Journal of the International Society of Ultrasound in Obstetrics and Gynecology*, vol. 15, no. 4, pp. 297–301, 2000.
- M. G. Tolsgaard, “A multiple-perspective approach for the assessment and learning of ultrasound skills,” *Perspectives on medical education*, vol. 7, no. 3, pp. 211–213, 2018.
- V. Datta, S. Mackay, M. Mandalia, and A. Darzi, “The use of electromagnetic motion tracking analysis to objectively measure open surgical skill in the laboratory-based model,” *Journal of the American College of Surgeons*, vol. 193, no. 5, pp. 479–485, 2001.
- M. Uemura, M. Tomikawa, R. Kumashiro, T. Miao, R. Souzaki, S. Ieiri, K. Ohuchida, A. T. Lefor, and M. Hashizume, “Analysis of hand motion differentiates expert and novice surgeons,” *Journal of surgical research*, vol. 188, no. 1, pp. 8–13, 2014.
- B. P. Dromey, S. Ahmed, F. Vasconcelos, E. Mazomenos, Y. Kunpalin, S. Ourselin, J. Deprest, A. L. David, D. Stoyanov, and D. M. Peebles, “Dimensionless squared jerk: An objective differential to assess experienced and novice probe movement in obstetric ultrasound,” *Prenatal Diagnosis*, vol. 41, no. 2, pp. 271–277, 2021.
- M. Le Lous, F. Despinoy, M. Klein, E. Fustec, V. Lavoué, and P. Jannin, “Impact of physician expertise on probe trajectory during obstetric ultrasound: a quantitative approach for skill assessment,” *Simulation in Healthcare*, vol. 16, no. 1, pp. 67–72, 2021.
- B. Di Matteo, P. Angele, C. Lattermann, E. Kon *et al.*, “Innovative techniques to enhance musculoskeletal surgery outcomes,” 2018.

Dual Robot System for Autonomous Needle Insertion into Deep Vessels

Lorenzo Civati, Maria Koskinopoulou, Andrea Santangelo, and Leonardo S. Mattos

Biomedical Robotics Lab, Department of Advanced Robotics, Istituto Italiano di Tecnologia, Genoa, Italy

INTRODUCTION

Precise needle insertion is a key operation in many medical procedures such as peripheral catheterization, cardiac endovascular treatments, biopsy and treatment of tumours in soft tissues such as breast, prostate and abdomen [1]. Among them, Central Venous Access (CVA) is a routine procedure typically performed by experienced clinicians under ultrasound or x-ray guidance in a surgical room environment. CVA is most commonly conducted in three deep vein locations: the internal jugular vein, the subclavian vein, and the femoral vein.

During CVA, clinician should insert the needle while maintaining proper visualization of the target vessel (i.e. ultrasound-guided access). However, performing the detection and continuous visualization of the target vessel and simultaneously precisely controlling the needle insertion is not trivial. At the same time, complication rates during CVA range up to 15% (mechanical in 5-19% of patients; infectious in 5-26%; thrombotic in 2-26%) [2].

In this paper, we propose a dual robot system for autonomous needle insertion into deep vessels by enabling real-time visualization of the vein and adaptive trajectory planning to provide safe and quick interactions.

ROBOTIC NEEDLE INSERTION

The proposed dual robot system for autonomous needle insertion is composed by two Franka robots (Franka Emika GmbH, Germany): one to hold the ultrasound probe and one for the needle insertion robotic mechanism. For each robot a custom support was designed and manufactured as shown in Fig.1a-b. The needle insertion mechanism, called Cathbot, and its working protocol is based on the work presented in [3]. This system module exploits a venous entry detection system based on electrical impedance sensing (EBI) and the fact that different types of tissues present different electrical impedance values. A bipolar needle was used in this system and was electrically connected to the Cathbot control box. The ultrasound scanning and imaging was performed with a high-frequency ultrasound machine by GE Healthcare's Venue Go™ (USA) and a linear array ultrasound transducer (probe model: 12L-RS) with 5-13 MHz bandwidth. The work pipeline for the robotic needle insertion can be divided in sub-modules, as described below.

A. Autonomous Target Detection. The region of interest for CVA is defined by the user (e.g. leg, neck, etc.) and the target surface is detected by the robot using 3D vision and a color detection algorithm. For this purpose a D435i RealSense RGBD camera (Intel, USA) is mounted on the

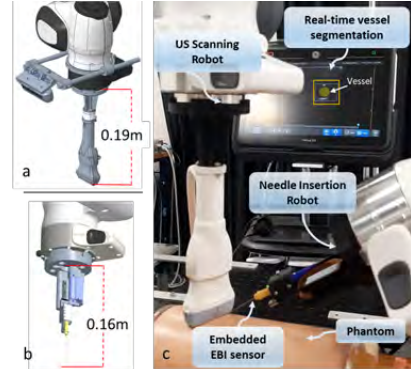


Fig. 1: a. Design model of the custom made ultrasound probe holder with the mounted RGBD camera; b. design model of the needle holder; and a system overview.

robot's end-effector as shown in Fig.1a. An OpenCV filtering in python is used to calculate the center of the phantom surface in the coordinate system of the camera. Then the depth map is aligned and the target's depth is projected to the camera space. An eye-in-hand calibration process is adopted in order to transfer the target's coordinates to the robot's coordinate system (marked as T_{calib} in Fig.2) using the Moveit-calibration package [4] in ROS Noetic. Finally, the target is successfully transferred to the robot's coordinate system and the ultrasound end effector is moved to the target position.

B. Ultrasound scanning and autonomous vessel segmentation. The robot tries to identify the optimal venous access location by autonomously scanning the target area. A robotic force control guarantees a good and consistent contact between the US transducer and the skin. In each position the US probe is tilted and slides on the skin while the US images are processed. To perform real time detection of deep vessels, a segmentation algorithm based on the well-known Mask Regional Convolutional Neural Network (Mask R-CNN) implementation [5] was used. The Mask R-CNN architecture includes a CNN backbone, a region proposal network, and a ROI Align layer. The training process was performed on a total of 1066 images (manually annotated) derived from a publicly available dataset [6], which were acquired using two different ultrasound devices (Ultrasonix and Toshiba). When the target vessel is detected, the US probe is oriented to center the vessels and acquire its image in the transverse plane.

C. Co-registration of the robotic arms. To control the two robots, namely Ultrasound Robot $\{R_{us}\}$ and Needle Robot $\{R_n\}$, in a common coordinate system, the rigid transformation $T_{K_{us}K_n}$ between the two robotic bases can be computed as: $T_{B_{us}B_n} = T_{BE_n} \cdot T_{EK_n} \cdot T_{BE_{us}} \cdot T_{EK_{us}}$, where T_{BE_n} and $T_{BE_{us}}$ denote the transformation between the base and the robot's end-effector for the needle and the ultrasound robot respectively, while T_{EK_n} and $T_{EK_{us}}$ stands for the relevant transformations between the robots' end-effectors and the end of the printed supports. For better understanding, Fig. 2c shows the named individual transformations graphically. To compute the transformation matrices T_{BE} , we follow the calibration procedure described in [7]. This co-registration of the robotic arms is used to compute the desired orientation and insertion depth to puncture the vessel in the defined target location. This information is sent to the Needle Robot to execute the needle insertion action [8].

D. EBI-guided needle insertion. The needle manipulation robot orients and moves the needle towards the target position while acquiring EBI measurements at the needle tip and obtaining updated target information from the vessel tracking module. Fine tuning of the insertion depth using an autonomous controller is performed to keep the needle aiming at the center of the vessel. A GUI is used to fine tune the controller parameters and provide functionalities to the user. The insertion stops once the blood is detected, completing the operation.

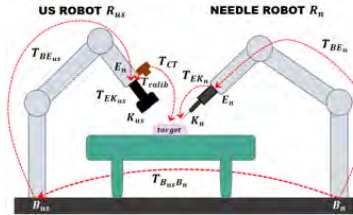


Fig. 2: Graphical sketch of the calibration process and depiction of the individual computed transformations.

SYSTEM INTEGRATION RESULTS

The assessment of the ultrasound vessel segmentation module was performed on 600 test images randomly selected from the dataset. Similarly to the training dataset, all test data images were coupled with labeling information containing ground truth information. The performance was assessed with the Intersection over Union between the segmented masks and the manually designed ground truth ones. The derived results are summarized in Table I where values for the *accuracy*, *precision*, *recall* and *F-score* metrics are given for three different IoU thresholds (0.2, 0.5 and 0.8). According to these results, the accuracy level of our Mask RCNN model ranges from 0.91 to 0.96, demonstrating a high overall performance.

The described experimental procedure is repeated 12 times, from 12 different starting points to 12 different scanning positions on top of the phantom (see Fig.3). The

TABLE I: Deep-vessel segmentation evaluation

Threshold	20%	50%	80%
Accuracy	0.96	0.94	0.91
Precision	0.98	0.98	0.97
Recall	0.99	0.96	0.94
F-score	0.98	0.97	0.95

mean 3D RMS error of the total 60 trials was measured as the difference between the insertion point on the skin (defined as a projection of the needle insertion trajectory computed based on information from the Ultrasound Robot) and the actual insertion point reached by the needle tip. This resulted in a positioning RMS error of 1.71mm ($\text{std } 0.52\text{mm}$), which can be considered as the accuracy of the system. In terms of the orientation during insertion, the mean rotation error measured was 4deg , while the mean insertion angle was 42deg with respect to the reference plane of the ultrasound transducer.

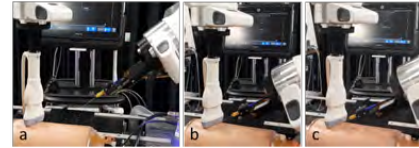


Fig. 3: Indicative snapshot from the performed experiments.

CONCLUSIONS

The developed dual robotic system successfully demonstrated autonomous central venous access on a realistic phantom model. This shows that real-time data from the hybrid sensing system based on ultrasound, bioimpedance, force and 3D vision could be effectively used by the intelligent control algorithms to enable accurate autonomous execution of this challenging medical procedure.

ACKNOWLEDGMENTS

This work is partially supported by BRACCO S.p.A.

REFERENCES

- [1] Z. Cheng, B. L. Davies, D. G. Caldwell, G. Barresi, Q. Xu, and L. S. Mattos, "A hand-held robotic device for peripheral intravenous catheterization," *Proc. of the Institution of Mechanical Engineers, vol. 231, no. 12, pp. 1165–1177, 2017.*
- [2] A. Leibowitz, A. Oren-Grinberg, and R. Matyal, "Ultrasound guidance for central venous access: Current evidence and clinical recommendations," *Intensive Care Medicine, vol. 35, no. 3, pp. 303–321, 2020.*
- [3] Z. Cheng, B. L. Davies, D. G. Caldwell, and L. S. Mattos, "A hand-held robot for precise and safe pive," *IEEE Robotics and Automation Letters, vol. 4, no. 2, pp. 655–661, 2019.*
- [4] "[https://github.com/ros-planning/moveit\\$Scalibration](https://github.com/ros-planning/moveit$Scalibration)."
- [5] W. Abdulla, "Mask r-cnn for object detection and instance segmentation on keras and tensorflow," <https://github.com/matterport/MaskRCNN>, 2017.
- [6] R. Benes, J. Karasek, R. Burget, and K. Riha, "Automatically designed machine vision system for the localization of cca transverse section in ultrasound images," 2013.
- [7] V. Penza, Z. Cheng, M. Koskinopoulou, A. Acemoglu, D. G. Caldwell, and L. S. Mattos, "Vision-guided autonomous robotic electrical bio-impedance scanning system for abnormal tissue detection," *IEEE TMRB, vol. 3, no. 4, pp. 866–877, 2021.*
- [8] M. Koskinopoulou, A. Acemoglu, and L. S. Mattos, "Dual robotic-arm collaborative system for autonomous venous access based on ultrasound scanning and bioimpedance sensing technology," *to be published in proc. ICRA 2023.*

Design of a Flexible Bone Drill Using a Hydraulic Pressure Wave

Esther P. de Kater¹, Tjalling G. Kaptijn¹, Aimée Sakes¹, Paul Breedveld¹

¹Department of Biomechanical Engineering, Delft University of Technology, Delft, The Netherlands

INTRODUCTION

Orthopaedic surgery focuses on the musculoskeletal system and often involves drilling through bone for fracture fixation, bone fusion, or tendon repair. Currently, straight rigid bone drills are utilized to create a tunnel through bone. Although these rigid bone drills are relatively easy to use, it would be advantageous to have a bone drill that can deflect to reach challenging areas, minimise damage to surrounding tissue or create better paths for the fixation of bone anchors or tendons. For instance, in spinal fusion surgery, the use of curved paths combined with novel bone anchors could potentially improve the fixation strength of the bone anchors compared to the currently used pedicle screws.

Currently, there are no commercial bone drills available that allow the surgeon to adjust the drilling trajectory during the intervention [1]. The design of steerable bone drills is challenging as the required flexibility to create a curved hole compromises the needed buckling resistance to advance the drill through hard material such as bone.

The flexible catheter designed by Sakes *et al.* was able to successfully transfer an impulse that could be used to hammer through calcification in blood vessels [2]. The catheter comprises a flexible fluid-filled tube that is used to transfer the impulse to the distal tip of the catheter to hammer through the occlusion. Although bone has different characteristics and the diameter of a drilled tunnel for pedicle screws (4 mm) is considerably different from the diameter of a catheter, the use of a hydraulic pressure wave could be beneficial, as the use of an impulse increases the buckling resistance while allowing the required bending for the drilling of curved tunnels. Furthermore, there are indications that the use of an impulse lowers the required penetration load due to the damping of the surrounding tissue which acts as a reaction force.

The goal of this study was, therefore, to investigate the use of a hydraulic pressure wave to hammer through bone in a flexible bone drill.

MATERIALS AND METHODS

In this study, two experiments were conducted to investigate: (1) the effect of hammer tip shape on the penetration rate and (2) the efficiency of impulse transmission through the fluid-filled tube both in a straight and curved configuration.

In Experiment 1, different hammer tip shapes all with a diameter of 4 mm were validated (Fig. 1a). The test facility (Fig. 1b) consisted of a hammer unit that was able to create an impulse via a spring-loaded

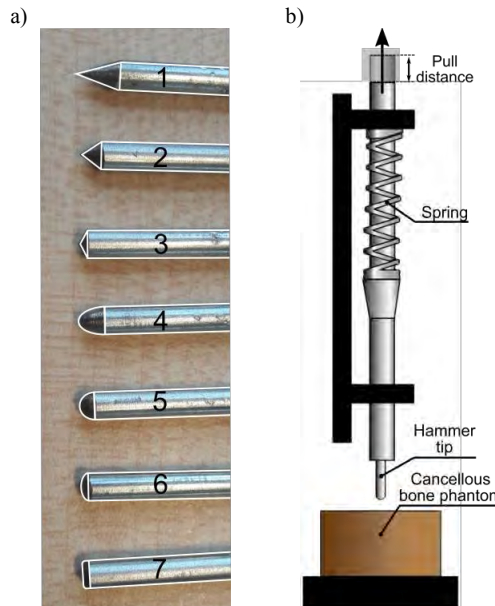


Fig. 1 The effect of tip shape on performance. a) Differently shaped hammer tips. b) Experimental facility Experiment 1.

mechanism. The impulse was transferred through the hammer tips to the cancellous bone phantom (polyurethane foam). Besides the hammer tip shape, the compression distance of the spring ($\text{Ø}22.0 \text{ mm}$, $k=1.99 \text{ N mm}^{-1}$) was varied to differ the generated impulse. The hammer tip was hammered five times into the bone phantom material. If there was no penetration visible the tip was hammered five more times. Based on the number of strokes and the measured penetration depth, the penetration rate [mm/stroke] could be determined. For Experiment 2, a bone drill comprising a handle and a flexible fluid-filled tube (Advanced Fluid Solutions, UK, $\text{Ø}4 \text{ mm L}=40 \text{ mm}$) with a hammer tip (Fig. 2a) was designed and manufactured. The spring ($\text{Ø}22.0 \text{ mm}$, $k=1.99 \text{ N mm}^{-1}$), located within the handle, is used to create an impulse that propagates through the flexible fluid-filled tube such that it encounters the hammer tip that is pushed into the bone (Fig. 2b). The prototype was manufactured using 3Dprinted parts (Envision TEC R5) and off the shelf springs, nuts and bolts. The distal end of the handle and the hammer tip were milled from stainless steel to minimise leakage of the fluid-filled tube. The hammer tip had an internal spring ($\text{Ø}2.5 \text{ mm}$, $k=1.4 \text{ N mm}^{-1}$) such that the tip would return to the initial position after a stroke to allow for continuous hammering.

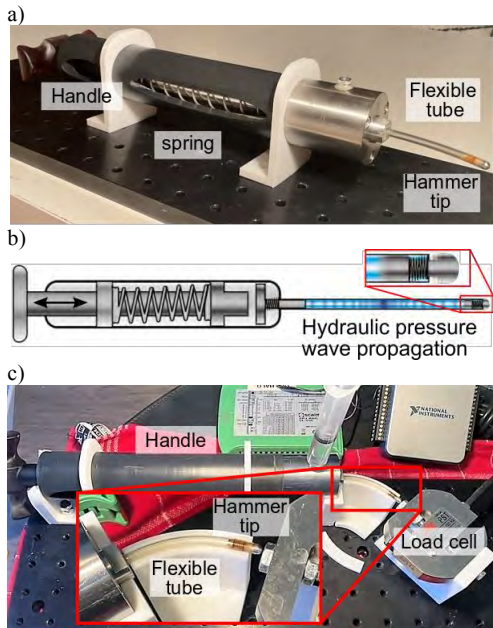


Fig. 2: Flexible bone drill. a) Drill prototype. b) Working principle of the drill. c) Experimental facility Experiment 2.

The impulse generated by the hammer tip was determined through the load cell (PST, 150 kg). The Experiment was conducted with the fluid-filled tube in a straight configuration and with the tube in a 45° and a 90° curve. Fig. 2c presents the experimental facility with the tube in a 45° curve.

RESULTS

Fig. 3 shows the results of Experiment 1. It can be observed that an increase in compression of the spring increases the penetration rate, as could be expected. Furthermore, the tip shape has a limited effect on the penetration rate, it must however be noted that using a blunt tip (Tip 3, 5, 6, and 7) resulted in a densely packed bone at the tip. Fig. 4 shows the results of Experiment 2. The impulse transferred from the tip of the drill decreases when there is a curve in the fluid-filled tube. Furthermore, the measured output impulse was substantially lower than the output impulse of 0.09 Ns that was achieved during Experiment 1.

DISCUSSION

In this study, the first steps are taken in the direction of a steerable bone drill that uses an impulse to advance through bone. The tip shape has a limited effect on the penetration rate but the accumulation of densely packed bone at the blunt tips could hamper drilling over a longer time. The presented drill design successfully transfers an impulse in a straight and curved orientation, but a curvature of the shaft does lower the efficiency of the impulse transfer. Furthermore, the efficiency of the impulse transfer is low which can partially be explained by the force required to compress the spring in the

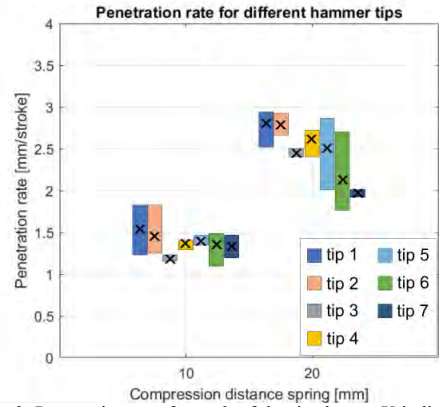


Fig. 3: Penetration rate for each of the tip shapes. X indicates the mean.

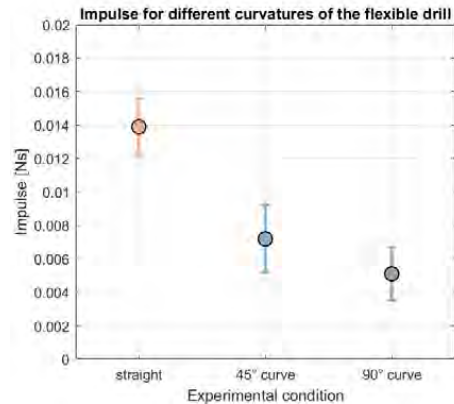


Fig. 4 Measured impulse with the flexible fluid-filled tube in a straight configuration and a 45° and 90° curve.

hammer tip, as part of the impulse is used to compress the spring and is thus not transferred to the cancellous bone. For future research, the hammer tip could be redesigned such that the spring is not required to bring the hammer tip to the initial position. Furthermore, the flexible section could be made steerable by adding steering cables. This would allow the surgeon to steer the drill and thus define the most optimal drilling direction.

The presented design for a flexible bone drill uses a hydraulic pressure wave to hammer through bone and shows promising results and is a first step in the direction of a steerable bone drill.

REFERENCES

- [1] A. Sendrowicz, M. Scali, C. Culmone, and P. Breedveld, ‘Surgical drilling of curved holes in bone—a patent review’, *Expert review of medical devices*, vol. 16, no. 4, pp. 287–298, 2019.
- [2] A. Sakes, T. Nicolai, J. Karapanagiotis, P. Breedveld, and J. W. Spronck, ‘Crossing Total Occlusions using a hydraulic pressure wave: a feasibility study’, *Biomedical Physics & Engineering Express*, vol. 4, no. 5, p. 055019, 2018.

Toward a Millimeter-Scale Tendon-Driven Continuum Wrist with Integrated Gripper for Microsurgical Applications

Alexandra Leavitt^{1,2}, Ryan Lam^{1,2}, Nichols Crawford Taylor^{1,2},
Daniel S. Drew^{1,3}, and Alan Kuntz^{1,2}

¹*Robotics Center, University of Utah,*

²*Kahlert School of Computing, University of Utah,*

³*Department of Electrical and Computer Engineering, University of Utah
alan.kuntz@utah.edu*

INTRODUCTION

Microsurgery, wherein surgeons operate on extremely small structures frequently visualized under a microscope, is a particularly impactful yet challenging form of surgery. Robot assisted microsurgery has the potential to improve surgical dexterity and enable precise operation on such small scales in ways not previously possible [1], [2]. Clinical applications of microsurgery include intraocular surgery, fetal surgery, otology, laryngeal surgery, neurosurgery, and urology.

Intraocular microsurgery is a particularly challenging domain [3], [4]. Challenges arise, in part, due to the lack of dexterity that is achievable with rigid instruments inserted through the eye. The insertion point introduces a remote center of motion (RCM) constraint that prevents control over a tool-tip's full pose (position and orientation) for conventional, straight instruments. Continuum robots based on concentric tubes [5], magnetic actuation [6], and tendon-actuated stacked disks [7], [8] have been proposed for intraocular microsurgery in order to overcome this constraint, but are frequently limited in their local curvatures—an important consideration in constrained spaces.

Inspired by these works, we present a new design for a millimeter-scale, dexterous wrist intended for microsurgery applications. The wrist is based on recent advances in tendon-driven continuum robot designs [9] and created via a state-of-the-art two-photon-polymerization (2PP) microfabrication technique. The 2PP 3D printing method enables our wrist to be constructed of flexible material, with complex internal geometries and critical features at the micron-scale (Fig. 1).

The wrist features a square cross section with side length of 1.25 mm and total length of 3.75 mm. The wrist is composed of a stacked rhombus shape, first proposed at macro scale by Childs et. al. [9]. This design intro-

This work was supported in part by the National Science Foundation under Award # 2133027. A. Leavitt and R. Lam were also supported in part by funding from the Undergraduate Research Opportunities Program at the University of Utah. We thank the groups of Dr. D. Caleb Rucker and Dr. Jake J. Abbott for valuable discussions.

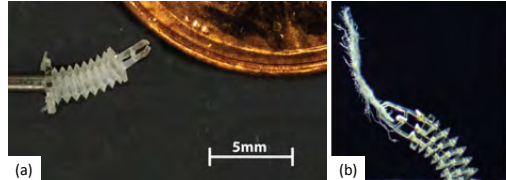


Fig. 1 (a) The robot presented in this work mounted on a stainless steel capillary tube shown next to the edge of a US 1 cent coin for scale. (b) The gripper enables the robot to manipulate loads while bending. Here, microfiber paper is used as a proxy for tissue.

duces torsional rigidity as a byproduct of its geometry. We leverage this design not for its torsional rigidity (although we envision that will aid modeling in future work), but rather due to the fact that the extruded nature of its geometry lends itself to 2PP sub-millimeter scale 3D printing. Building on this concept, we miniaturise the design and integrate a flexible gripper, bringing the total length to 5.47 mm. The wrist has three tendons routed down its length, spaced approximately evenly around the robot's circumference which, when actuated by small-scale linear actuators, enable bending in any plane. The gripper, designed to close upon loading due to the curvature at its simply supported ends, is actuated by a fourth tendon routed down the center of the robot. We evaluate the wrist and gripper by characterizing its bend-angle. We achieve >90 degrees bending in both axes. We demonstrate out of plane bending as well as the robot's ability to grip while actuated.

Our integrated gripper/tendon-driven continuum robot design and meso-scale assembly techniques have the potential to enable small-scale wrists with more dexterity than has been previously demonstrated. Such a wrist could improve surgeon capabilities during teleoperation with the potential to improve patient outcomes in a variety of surgical applications, including intraocular surgery.

MATERIALS AND METHODS

The backbone comprises repeat hollow rhombohedral unit cells (see Fig. 1), as in Childs et. al. [9]. Flexural bending



Fig. 2 Sequential images of the robot tracing a circular trajectory via coordinated actuation of the three tendons.

about each axis results from elastic deformations of the unit cells, which can be individually modeled as a parallel set of conjoined thin plates. The unit cells are torsionally stiff because of the relatively small thickness of the thin plate sections relative to their width and length. As a proof-of-concept, we designed a simple gripper which can be controlled by pulling a centrally-routed tendon (Fig. 1b). The tendon symmetrically bends the simply supported ends of the center plate, bringing the gripper jaws closer until they make contact.

The backbone and integrated gripper are fabricated using a 2PP printing process (Nanoscribe 3D Photonic Pro GT), enabling direct printing of three-dimensional structures with sub-micrometer resolution, using the semi-rigid IP-Q photoresin ($E \approx 5 \text{ GPa}$, $\nu \approx 0.35$).

Tendons (25 μm diameter tungsten) are manually threaded through the backbone channels. Two-part silver epoxy adhesive (MG Chemicals 8331D) is used for capping the tendons. Tendons are attached to linear actuators with 20 mm stroke and 18 N rated force (Actuonix PQ12-R). Minimum repeatable step size of the actuators was assessed experimentally to be approximately 100 μm .

RESULTS

We first qualitatively demonstrate out-of-plane bending for the robot. We actuate each of the three bending tendons in a coordinated fashion, causing the robot to bend in a 3D circular arc (see Fig. 2).

In Fig. 1b we show the gripper grasping a small piece of tissue paper, having externally actuated the gripper tendon and a bending tendon on the robot.

We next quantitatively characterize the robot's ability to bend in each of its orthogonal axes as a function of tendon displacement. In this experiment, we printed the backbone structure (without the gripper) with four bending tendons, located on the robot such that there were two tendons, antagonistically placed in both of the robot's primary axes. We placed the robot in front of a grid printed with 1mm x 1mm cells to optically measure bend angle through a stereo microscope.

For each of the two axes we actuated one of the bending tendons, measuring tendon displacement (via actuator encoders) and bend angle. We actuated the robot until the bend angle was 90 degrees or more. Note that this was an artificially imposed limit and the robot could be actuated further. We then released the tension on the tendon, measuring forward displacement of the actuator until we had returned to the initial displacement length. Next we actuated the appropriate antagonistic tendon to bend the robot in the opposite direction in plane repeating the measurements as described above. In Fig. 3 we show overlaid images of the robot bending in both directions for both axes, and include a hysteresis curve for each axis

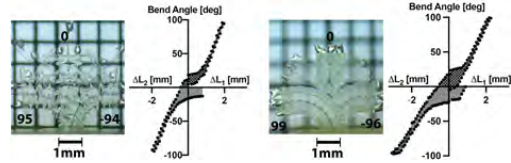


Fig. 3 Bend angles as a function of displacement in both primary axes. The robot exhibits ≥ 90 degree bending in both primary axes. The left figures show the robot as viewed from the front and the right figures show the robot as viewed from the right. Multiple bend angles are superimposed in each figure. We include hysteresis curves for bend angle as a function of tendon displacement.

quantifying bend angle to displacement. We achieve >90 degree bending in all four directions.

DISCUSSION

Our 2PP fabricated design demonstrates large bend angles (>90 degrees) in a small form factor (3.75 mm length). We demonstrate high curvature in the wrist with values between 2.1 and 2.3 mm radius of curvature. However, static friction in the tendon channels introduces significant hysteresis. Further, our current gripper couples slight amounts of axial compression into the jaw motion, a sub-optimal characteristic at these scales. In future work we intend to address these limitations and further reduce the scale of the device.

This work represents our first demonstration of 2PP fabricated wrists at these scales. We envision a large number of potential clinical uses for such a device. Our primary intended use case is to integrate our wrist with a teleoperated intraocular microsurgery robot.

REFERENCES

- [1] L. S. Mattos, D. G. Caldwell, G. Peretti, F. Mora, L. Guastini, and R. Cingolani, "Microsurgery robots: Addressing the needs of high-precision surgical interventions," *Swiss medical weekly*, no. 43, 2016.
- [2] D. Zhang, W. Si, W. Fan, Y. Guan, and C. Yang, "From Teleoperation to Autonomous Robot-assisted Microsurgery: A Survey," *Machine Intelligence Research*, vol. 19, no. 4, pp. 288–306, Aug. 2022.
- [3] E. Z. Ahranovich, N. Simaan, and K. M. Joos, "A Review of Robotic and OCT-Aided Systems for Vitreoretinal Surgery," *Advances in Therapy*, vol. 38, no. 5, pp. 2114–2129, May 2021.
- [4] I. Iordachita, M. D. De Smet, G. Naus, M. Mitsuishi, and C. N. Riviere, "Robotic Assistance for Intraocular Microsurgery: Challenges and Perspectives," *Proceedings of the IEEE*, vol. 110, no. 7, pp. 893–908, Jul. 2022.
- [5] F.-Y. Lin, C. Bergeles, and G.-Z. Yang, "Biometry-based concentric tubes robot for vitreoretinal surgery," in *2015 37th Annual International Conference of the IEEE Engineering in Medicine and Biology Society (EMBC)*. IEEE, 2015, pp. 5280–5284.
- [6] S. L. Charreyron, Q. Boehler, A. N. Danun, A. Mesot, M. Becker, and B. J. Nelson, "A Magnetically Navigated Microcannula for Sub-retinal Injections," *IEEE Transactions on Biomedical Engineering*, vol. 68, no. 1, pp. 119–129, Jan. 2021.
- [7] M. Jinno and I. Iordachita, "Improved Integrated Robotic Intraocular Snake: Analyses of the Kinematics and Drive Mechanism of the Dexterous Distal Unit," *Journal of Medical Robotics Research*, vol. 06, no. 01n02, p. 2140001, Mar. 2021.
- [8] ———, "Microgripper Using Flexible Wire Hinge for Robotic Intraocular Snake," in *2022 International Conference on Robotics and Automation (ICRA)*, May 2022, pp. 6218–6224.
- [9] J. A. Childs and C. Rucker, "Leveraging geometry to enable high-strength continuum robots," *Frontiers in Robotics and AI*, vol. 8, p. 629871, 2021.

Extracting Unusual Movements during Robotic Surgical Tasks: A Semi-Supervised Learning Approach

Yi Zheng¹ and Ann Majewicz-Fey^{1,2}

¹*Department of Mechanical Engineering, the University of Texas at Austin,*

²*Department of Surgery, the University of Texas Southwestern Medical Center*

yi.zheng@austin.utexas.edu

INTRODUCTION

Although modern features in surgical robots such as 3D vision, “wrist” instruments, tremor abolition, and motion scaling have greatly enhanced surgical dexterity, technical skill is a major challenge for surgeons and trainees. Surgeons who get constructive and real-time feedback can make more significant improvement in their performance [1].

Recent years, the research in automated surgical skill assessment has made considerable progress, however, the majority of surgical evaluation methods are post-operation analysis. Few studies introduced real-time surgical performance evaluations, for example, using Convolutional Neural Network [2], Codebook and Support Vector Machine [3], and Convolutional Neural Network - Long Short Term Memory [4]. One common limitation of these studies is data leakage during training which results in a higher estimate of model performance. Moreover, these studies cannot depict an intuitive representation of what actually differentiates expertise levels. In this study, we introduce a method to extract the unusual movements which are rarely seen in Experts and identify the types of the unusual movements. We believe detecting and correcting the unusual movements is an important aspect for surgeons to improve their skills.

MATERIALS AND METHODS

A. Dataset

The data is from our previous study [5]. 14 subjects performed 2 tasks (Ring and Rail, Suture Sponge) on a da Vinci Simulator. Each task was repeated 3 times. In this study, we focus on the motion data - linear acceleration (A_x, A_y, A_z) and angular velocity (G_x, G_y, G_z) of the left hand collected by an IMU. The IMU was mounted on the back of the left hand. Due to sensor failure and missing files, the data of 12 subjects including 3 Experts (EX, practicing robotic surgical faculty), 2 Fellows (FL, surgical fellows post residency), 3 Intermediates (IN, PGY-4 surgical residents), and 4 Novices (NO, medical students) is used in this study. For each trial, we downsample the data from 512 Hz to 30 Hz and use a sliding-window to organize the data into one-second frames. Each frame has a dimension of [30 Samples * 6 Features].

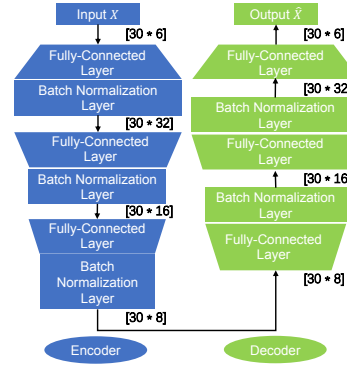


Fig. 1 Architecture of the Autoencoder.

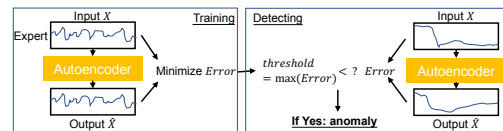


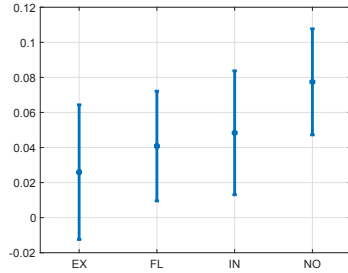
Fig. 2 Model training and anomaly detection.

B. Extracting Unusual Movements

To extract unusual movements, we adopt a method called “Anomaly Detection” which is used for identifying data points that deviate from normal patterns.

In this study, we treat the movements from EX as “normal” and identify the unusual movements which show large deviations from “normal” movements. Autoencoder is a popular tool for Anomaly Detection [6]. A simple Autoencoder which consists of Fully-connected layers and BatchNormalization layers is used (Fig. 1). Its Encoder takes input X - one-second frame of motion data. Its Decoder takes the compressed data from Encoder and reconstructs the data as output \hat{X} .

Our Autoencoder is trained by “normal” or EX movements (Fig. 2). It is a Semi-Supervised method which uses normal, labeled data to construct a model representing normal patterns. We use the largest reconstruction error during training as $threshold$. During detection, reconstruction errors smaller than $threshold$ mean ‘nor-

**Fig. 3** Average Error of the Unusual Movements.**TABLE I** Summary of statistical analysis (ANOVA).

Metrics	Significance	p-value
Number of Unusual Movements	NO > EX	0.0000
	NO > FL	0.0000
	NO > IN	0.0002
Average Error of the Unusual Movements	NO > EX	0.0000
	NO > FL	0.0165
	NO > IN	0.0373

mal” inputs, whereas reconstruction errors greater than *threshold* mean unusual inputs (anomalies) - the data patterns that Autoencoder has never seen from EX.

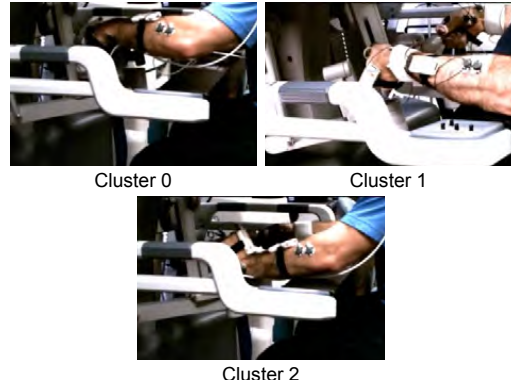
C. Identifying Unusual Movements

We extract the unusual movements, but we still don’t know what the unusual movements look like. To identify the types of unusual movements, we choose the K-Means clustering algorithm - an unsupervised learning algorithm that divides the data into different clusters in which data shares similar patterns.

RESULTS

For EX (subject: S1, S2, S4), we performed Leave-One-User-Out cross-validation to verify Experts’ performance. When the Autoencoder was trained by S1 and S2, S4 showed large reconstruction errors during detection. It is consistent with our reviewers’ rating that S4 received lowest scores among EX, even lower than FL and IN. Then we only considered the movements of S1 and S2 as “normal”. After training, the other subjects’ data was sent to the Autoencoder to make anomaly (unusual movement) detection based on the reconstruction error. For each trial, we calculated two metrics: Number of Unusual Movements, and Average Error of the Unusual Movements. NO showed significantly higher Numbers of Unusual Movements than EX, FL, and IN. NO also showed significantly higher Average Error of the Unusual Movements than EX, FL, and IN (Fig. 3 and Table. I). These significant differences indicate that NO had the worst performance in terms of Unusual Movement, thus validating our proposed method.

To identify the unusual movements, we first reviewed videos of extracted unusual movements. We selected the number of clusters $K = 3$, or the number of types of unusual movements based on observation. As preliminary results, we could see large wrist flexion in Cluster 0, large wrist deviation in Cluster 1, and large wrist extension in

**Fig. 4** Example images of unusual movements in different clusters.

Cluster 2 (Fig. 4). These kinds of movements were not observed in Experts data and should be corrected.

DISCUSSION

In this study, we used a semi-supervised learning method to extract unusual movements which didn’t follow the pattern from Experts. We identified the types of these unusual movements using clustering. The extracted movements can be used to train a model for real-time detection of unusual movements. We find that the use of the wrist is a good indicator of surgical expertise level.

One limitation of this work is choosing the number of clusters K . For example, in Cluster 2 (large wrist extension), the direction of the hand can point forward or to the right. In addition, the examples in Fig. 4 only show static poses, however, unusual movements also happen during transitions. We will find a better solution to identify the types of unusual movements and seek for methods to help surgeons avoid these behaviors.

REFERENCES

- [1] T. P. Grantcharov, S. Schulze, and V. B. Kristiansen, “The impact of objective assessment and constructive feedback on improvement of laparoscopic performance in the operating room,” *Surgical endoscopy*, vol. 21, no. 12, pp. 2240–2243, 2007.
- [2] Z. Wang and A. Majewicz Fey, “Deep learning with convolutional neural network for objective skill evaluation in robot-assisted surgery,” *International journal of computer assisted radiology and surgery*, vol. 13, no. 12, pp. 1959–1970, 2018.
- [3] M. Ershad, R. Rege, and A. Majewicz Fey, “Automatic and near real-time stylistic behavior assessment in robotic surgery,” *International journal of computer assisted radiology and surgery*, vol. 14, no. 4, pp. 635–643, 2019.
- [4] X. A. Nguyen, D. Ljubhar, M. Pacilli, R. M. Nataraja, and S. Chauhan, “Surgical skill levels: Classification and analysis using deep neural network model and motion signals,” *Computer methods and programs in biomedicine*, vol. 177, pp. 1–8, 2019.
- [5] M. Ershad, R. Rege, and A. Majewicz Fey, “Meaningful Assessment of Robotic Surgical Style using the Wisdom of Crowds,” *International Journal of Computer Assisted Radiology and Surgery*, vol. 13, pp. 1037–1048, 2018.
- [6] G. E. Hinton and R. R. Salakhutdinov, “Reducing the dimensionality of data with neural networks,” *science*, vol. 313, no. 5786, pp. 504–507, 2006.

Evolutionary Deep Learning using hybrid EEG-fNIRS-ECG Signals to Cognitive Workload Classification in Laparoscopic Surgeries

Adrian Rubio-Solis^{1,2}, Kaizhe Jin^{1,2}, Ravi Naik^{1,2}, and George Mylonas^{1,2}

¹ Department of Surgery and Cancer, Imperial College London, UK.

² Hamlyn Centre for Robotic Surgery, Imperial College London

arubioso, k.jin20, ravi.naik15, george.mylonas@imperial.ac.uk

INTRODUCTION

Deep learning classifiers have demonstrated their ability to provide robust accuracy for the treatment of combined signals including electroencephalography (EEG) and functional near infrared spectroscopy (fNIRS) [1], [2]. In this work, an evolutionary deep learning strategy is applied to classify different cognitive workload states that surgeons experience during laparoscopic surgery. The proposed learning strategy is applied to train an Evolutionary Multilayer Perceptron Neural Network (E-MLPNN), where multimodal raw data of EEG, fNIRS and Electrocardiogram (ECG) signals were collected and concatenated from a series of ten experiments using the back-end platform Multi-sensing AI Environment for Surgical Task & Role Optimisation (MAESTRO) as shown in Figure 1(a). Each experiment required surgical trainees to perform a simulated laparoscopic cholecystectomy (LCH), i.e. the removal of a gallbladder in a porcine model using a minimally invasive surgical technique as demonstrated in Figure 1(b). At each experiment, the level of Cognitive Workload (CWL) is assumed to increase as the mental activity increases during the surgical operation. As presented in Figure 1c, a number of tasks performed during the LCH were defined to measure the level of CWL.

MATERIALS AND METHODS

A. Data Collection and Processing

Ten surgical trainees were introduced to the laboratory and fitted with wearable sensors which were subsequently calibrated. As illustrated in Figure 2(a), a 4th order Butterworth low pass filter was applied to the signals, and Power Spectral Density was applied as the initial feature extraction of EEG signals [1]. A sampling frequency of 512Hz was used for all signals, where a sampling window of 1sec was used to create the final data set. fNIRS data were collected using the Artinis 24 × 11 system, (Brite, Artinis Medical Systems, Elst, The Netherlands, www.artinis.com), across 22 prefrontal cortex locations, while EEG signals were collected from a TMSi Mobita 32 channel system (TMSi, Mobita, EEG system , The Netherlands). A Shimmer wearable sensor was used to collect ECG data.

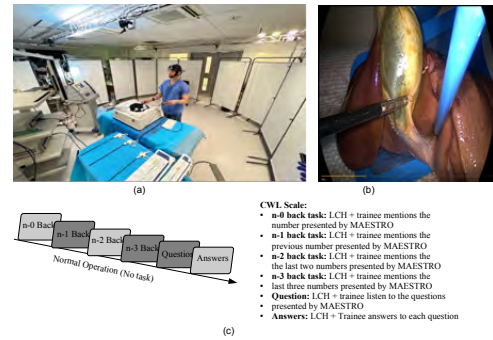


Fig. 1 (a) Surgical setup using MAESTRO, (b) Laparoscopic cholecystectomy, (b) Cognitive Workload (CWL) Scale defined for the experiments.

B. Proposed Evolutionary Deep Learning Strategy

As described in Figure 2(a), an iterative Evolutionary Deep Learning strategy based on a continuous genetic algorithm (GA) was applied to train a multilayer Perceptron neural network, termed E-MLPNN [3].

At each training iteration t , the parameters of the proposed E-MLPNN were updated in a 2 step fashion. Firstly, an unsupervised feature representation of the raw data was achieved and secondly, a supervised feature classification was subsequently performed. As detailed in Figure 2(b) [3], the output of each hidden layer in the E-MLPNN is represented as $\mathbf{H}_i = g(\mathbf{H}_{i-1} \cdot \beta_i)$. Where $\mathbf{H}_i = [h_1, \dots, h_K]$ is the output of the i th layer, $g(\cdot)$ is the activation function of each hidden unit and β_i is the output weight in the classification layer such as $i = 1, \dots, K$. The objective function for GA is [4]:

$$f_t = \left(\sum_{p=1}^P (\hat{y}_p - \hat{t}_p)^2 \right)^{1/2} \quad (1)$$

for a number of P training data points (\hat{y}_p, \hat{t}_p) , where \hat{y}_p and \hat{t}_p is the current and desired output respectively. The term β_{i-1} is computed by [3]:

$$\beta_{i-1} = \mathbf{H}_{i-1} \left(\frac{1}{\lambda} + \mathbf{H}_{i-1} \mathbf{H}_{i-1}^T \right)^{-1} \mathbf{T} \quad (2)$$

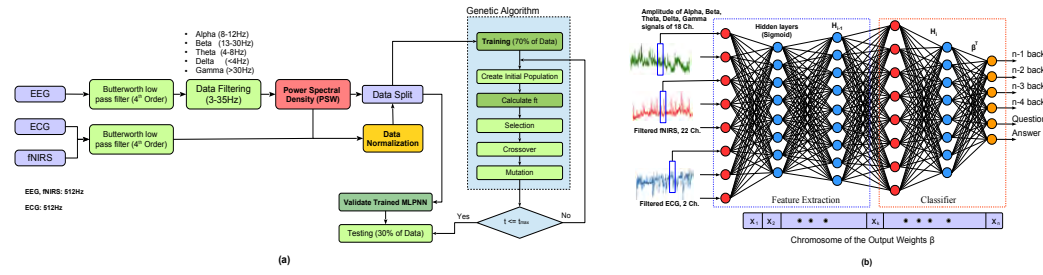


Fig. 2 (a) Flow diagram optimisation of a MLPNN using an GA whose raw input data is the concatenation of ECG, EEG, fNIRS data, (b) Multilayer Perceptron Neural Network used in this work.

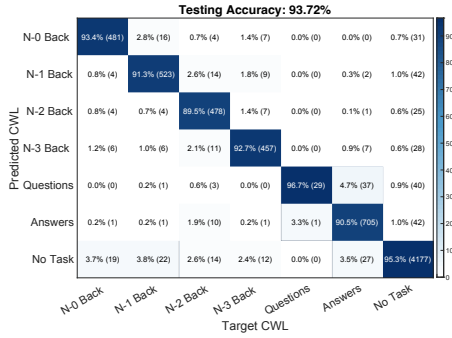


Fig. 3 Confusion matrix obtained for the validation of the ML-PNN (testing accuracy).

where λ is the regularisation term, the β_i weight is represented by a chromosome for the l th individual and it is optimised by a GA as shown in Figure 2(b). $\mathbf{T} = [t_1, \dots, t_P]^T$ is the desired task.

RESULTS

To cross-validate the proposed E-MLPNN, five experiments were performed. A final data set of 32769×24364 records was divided into two subsets, i.e. 70% for training and 30% for testing. Five other methods were also implemented to provide comparison to the proposed E-MLPNN method which included Random Forest + Support Vector Machine (RF + SVM) [3], RF + Principal Component Analysis (PCA), 1D-CNN [3], LSTM [2], and Multilayer Perceptron NN trained by using Extreme Learning Machine (MMLPNN) [3].

The experimental setup for the proposed E-MLPNN involves a mutation rate of 15%, a number of 8 individuals and max number of iterations $t_{max} = 50$. The neural structure of the E-MLPNN consists of [1300, 1100] hidden units. In Figure 3, the confusion matrix for testing the E-MLPNN is presented. Finally, in Table I, the average performance, training time and number of parameters for each model is shown.

TABLE I Average performance for five-cross-validation experiments using different machine learning techniques.

Model	CWL Classification (%)			
	Training	Testing	No. of Parameters	
	Avg.	time (s)	Avg.	
RF + SVM	82.7	920.1	79.9	327,128
RF + PCA	84.6	1233.4	81.2	4190
1D-CNN	99.9	1877.0	98.3	354,240
LSTM	99.9	1400.2	99.9	120,000
MLPNN	93.2	180.2	91.2	8400
E-MLPNN	95.7	620.9	93.7	8400

DISCUSSION

From our results, it can be observed from Figure 3 that the highest confusion for the estimation of CWL among all the participants is produced during the N-2 back task and the answer from clinicians to each question. It is also worth noting, a high rate of imbalanced data is present between the activities where there is assumed increase in the CWL (N backs task, questions and answers) and no task where the CWL is assumed to be normal. Finally, even though, the proposed E-MLPNN does not provide the highest accuracy, it produces one of the two highest trade-off between model performance and simplicity. By using GA to determine the parameters of an MLPNN, its model accuracy is improved for the classification of unseen data while model simplicity is preserved.

ACKNOWLEDGEMENTS

Funding. This project is funded by the EPSRC Transformative Healthcare Technologies grant EP/W004755/1.

REFERENCES

- [1] J. Cao, E. M. Garro, and Y. Zhao, "Eeg/fnirs based workload classification using functional brain connectivity and machine learning," *Sensors*, vol. 22, no. 19, p. 7623, 2022.
- [2] A. M. Chiarelli, P. Croce, A. Merla, and F. Zappasodi, "Deep learning for hybrid eeg-fnirs brain-computer interface: application to motor imagery classification," *Journal of neural engineering*, vol. 15, no. 3, p. 036028, 2018.
- [3] J. Tang, C. Deng, and G.-B. Huang, "Extreme learning machine for multilayer perceptron," *IEEE transactions on neural networks and learning systems*, vol. 27, no. 4, pp. 809–821, 2015.
- [4] O. E. David and I. Greental, "Genetic algorithms for evolving deep neural networks," in *Proceedings of the Companion Publication of the 2014 Annual Conference on Genetic and Evolutionary Computation*, 2014, pp. 1451–1452.

WaveLeNet: Transfer Neural Calibration for Embedded Sensing in Soft Robots

Navid Masoumi⁺¹, Negar Kazemipour⁺¹, Sarvin Ghiasi², Tannaz Torkaman¹, Amir Sayadi², Javad Dargahi¹, and Amir Hooshiar*²

¹Concordia University, Montreal, QC, Canada

²Surgical Robotics Centre, McGill University, Montreal, QC, Canada

⁺Equally contributed first authors *seyed.hooshiarahmedi@mail.mcgill.ca

INTRODUCTION

Soft robots have exhibited excellent compatibility with functional and physical requirements of intraluminal procedures such as bronchoscopy and cardiovascular intervention [1]. Despite their favourable mechanical compliance and scalable design, integrating miniature force and shape sensors on them is cumbersome [2]. Also, large mechanical deformation of such robots, i.e., flexures, may push traditional rigid sensors out of their linear range [3]. As an alternative approach, the authors have recently introduced a novel soft sensing method and soft embedded sensors for flexures that exhibited less than 10mN error in measuring external 3D tip forces on soft robots for bronchoscopy and cardiovascular applications [4], [5], [6]. Fig. 1(a –c) depict the conceptual design, the prototyped sensor developed in [5], and a representative interventional application. Their soft sensor was comprised of a gelatin-based matrix filled with graphite nano-particles that exhibited stable piezoresistivity under extremely large deformation. Despite its accuracy, the accuracy of the proposed sensor was adversely affected in noisy environments, e.g., operation rooms. The reason was that the rate-dependent features used in its neural calibration would amplify the peripheral noise which would diminish the accuracy. In this study, we have proposed and validated an alternative deep-learning-based method for calibration of the proposed soft sensor that is derivative-free thus does not amplify the peripheral noise and is versatile. Conceptually, the proposed calibration methods can be used to assemble an array of sensor readings for distributed sensing on soft robots. Our proposed method is based on generating a scalogram from the temporal-frequency content of the measured voltages using real-time wavelet transform and using transfer learning technique to infer rate-dependent and deformation-dependent features from the voltages' scalogram.

MATERIALS AND METHODS

As an alternative and derivative-free calibration method for the soft embedded sensor developed in [5], we investigated the utilization of a deep-learning-based calibration schema. Fig. 2(a) depicts the proposed calibration framework. To this end, first the scalograms Continuous Wavelet Transform (CWT) of two voltages V_1 and V_2 recorded during the sensor calibration were obtained

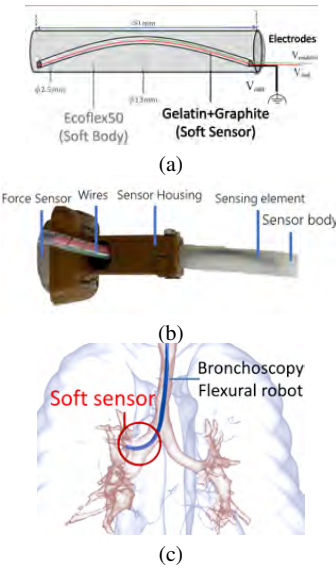


Fig. 1. (a) Conceptual design and (b) the prototyped soft flexure with embedded soft sensor [4], and (c) conceptual application of the proposed soft sensor.

using Matlab Signal Processing Toolbox. As shown in Fig. 2(a) scalograms were 2D images in red-green-blue (RGB) colorspace. More specifically, the Morse wavelet was employed to generate the CWTs. The CWT images were of 224×112 px size and were horizontally concatenated in the form of $[V_1 \ V_2]$ to form a 224×224 px input image for the transferred neural network. Also, we applied synchro-squeezing to the wavelet to improve the temporal resolution of the scalogram. A total of 70 pairs of CWT scalograms were obtained from the calibration dataset obtained in [5]. Considering the small size of the dataset and to perform accurate feature extraction on scalogram images, GoogLeNet (Alphabet Inc.) pre-trained network was used. It had a total of 22 layers (including convolutional and max-pooling). To perform force estimation (regression), the last layer of GoogLeNet (classifier) was replaced with eight fully-connected layers with 250,200,150,100,50,25,10, and 3 neurons with the rectified linear unit (ReLU) activation function. The restructured convolutional calibration model was denoted

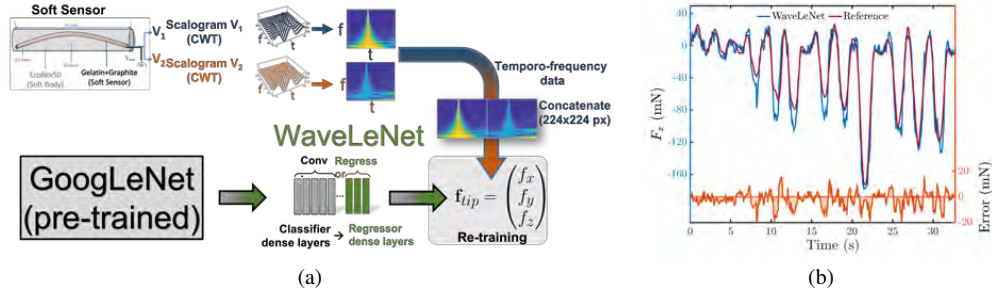


Fig. 2. (a) Dataflow-gram of the proposed transfer-learning-based calibration method, (b) representative performance of the proposed calibration.

as WaveLeNet in this study. For better accuracy, the training forces were normalized. In training, 'adam' optimizer with 20 epochs and goal function of mean-absolute error was used. The training was performed in Matlab Deep Learning Tool Box (Mathworks, MA, USA). The dataset was split (70:15:15 for train:validate:test).

RESULTS AND DISCUSSION

Fig. 2(b) shows a representative performance of the proposed calibration for unseen data for predicting tip force in x -direction, i.e. F_x . To assess the accuracy, maximum absolute error and mean absolute error between predicted force and ground truth (reference) were analyzed and compared with the previous rate-dependent calibration proposed in [5]. In addition, the minimum detectable force observed with WaveLeNet and that of [5] were compared. Table I summarizes the performance of WaveLeNet with the rate-dependent calibration proposed in [5]. The results showed that the MAE of the proposed network was less than 5% of full range (i.e., 160mN). Although the MAE over full range was larger than the previous rate-dependent calibration it was still below the 5% error level. Most importantly, we analyzed the error for small force ranges, where our previous rate-dependent calibration was most erroneous (due to noise amplification). The results showed that not only the proposed WaveLeNet calibration was more accurate than the rate-dependent calibration, but it was also more accurate compared to itself at full range. We believe the derivative-free nature of the WaveLeNet method has contributed to its superiority compared to rate-dependent calibration. Also, the more in-depth analysis showed that at force ranges $> 100\text{mN}$, the scalograms become quite bright and the temporal gradient of WaveLet scalograms diminishes. This might have contributed to lower accuracy in high forces.

CONCLUSION

In this study, we proposed a transfer learning-based calibration schema inherited from GoogLeNet for soft embedded sensing in soft robots. The proposed method was derivative-free and would capture temporal changes in electrical signals from the soft sensors by capturing image features in scalograms of wavelet transform. WaveLeNet, our derivative-free deep convolutional calibration

TABLE I
PERFORMANCE OF WAVELENET IN COMPARISON WITH REF. [5].

Force	MAE WaveLeNet (mN)	MAE [5] (mN)	MDF WaveLeNet (mN)	MDF [5] (mN)
F_x (full-range)	7.5	3.3	< 1	< 1
F_y (full-range)	7.1	2.6	< 1	< 1
F_z (full-range)	12	8.0	< 1	< 1
$F_x < 20\text{mN}$	3.3	12.0	< 1	< 1
$F_y < 20\text{mN}$	3.7	13.1	< 1	< 1
$F_z < 20\text{mN}$	5.4	14.4	< 1	< 1

MAE: Mean Absolute Error
MDF: Minimum Detectable Force

model, had comparable accuracy over the full range of our soft flexural sensor compared to a previously validated rate-dependent calibration. However, thanks to its derivative-free features, it improved the accuracy for small forces, i.e., $< 20\text{mN}$. The proposed sensor and derivative-free calibration facilitates utilization of the proposed sensor in soft robotic applications especially tactile grasping (with force feedback) and interventional soft robots (for intraluminal applications). The authors have demonstrated the applicability of the proposed sensor for bronchoscopy applications in [5].

REFERENCES

- [1] M. Cianchetti, C. Laschi, A. Menciassi, and P. Dario, "Biomedical applications of soft robotics," *Nature Reviews Materials*, vol. 3, no. 6, pp. 143–153, 2018.
- [2] A. Hooshiar, S. Najarian, and J. Dargahi, "Haptic telerobotic cardiovascular intervention: a review of approaches, methods, and future perspectives," *IEEE reviews in biomedical engineering*, vol. 13, pp. 32–50, 2019.
- [3] N. Bandari, J. Dargahi, and M. Packirisamy, "Tactile sensors for minimally invasive surgery: A review of the state-of-the-art, applications, and perspectives," *Ieee Access*, vol. 8, pp. 7682–7708, 2019.
- [4] T. Torkaman, M. Roshanfar, J. Dargahi, and A. Hooshiar, "Accurate embedded force sensor for soft robots with rate-dependent deep neural calibration," in *2022 IEEE International Symposium on Robotic and Sensors Environments (ROSE)*. IEEE, 2022, pp. 1–7.
- [5] T. Torkaman, M. Roshanfar, J. Dargahi, and A. Hooshiar, "Embedded six-dof force–torque sensor for soft robots with learning-based calibration," *IEEE Sensors Journal*, vol. 23, no. 4, pp. 4204–4215, 2023.
- [6] M. Roshanfar, S. Taki, A. Sayadi, R. Cecere, J. Dargahi, and A. Hooshiar, "Hyperelastic modeling and validation of hybrid-actuated soft robot with pressure-stiffening," *Micromachines*, vol. 14, no. 5, p. 900, 2023.

SimPS-Net: Simultaneous Pose & Segmentation Network of Surgical Tools

Spyridon Souapas¹, Anh Nguyen², Stephen G. Laws¹, Brian L. Davies¹, Ferdinando Rodriguez y Baena¹

I. INTRODUCTION

Image-based detection and localisation of surgical tools has received significant attention due to the development of relevant deep learning techniques, along with recent upgrades in computational capabilities. Although not as accurate as optical trackers [1], image-based methods are easy to deploy, and require no surgical tool redesign to accommodate trackable markers, which could be beneficial when it comes to cheaper, “off-the-shelf” tools, such as scalpels and scissors.

In the operating room however, these techniques suffer from drawbacks due to the presence of highly reflective or featureless materials, but also occlusions, such as smoke and blood. Furthermore, networks often utilise tool 3D models (e.g. CAD data), not only for the purpose of point correspondence, but also for pose regression. The aforementioned “off-the-shelf” tools are scarcely accompanied by such prior 3D structure data. Ultimately, in addition to the above hindrances, estimating 3D pose using a monocular camera setup, poses a challenge in itself due to the lack of depth information. Considering these limitations, we present SimPS-Net, a network capable of both detection and 3D pose estimation of standard surgical tools using a single RGB camera.

II. MATERIALS AND METHODS

A total of 4 tools, specifically a scalpel, a pair of scissors, a pair of forceps and an electric burr were employed for the experiments. The tools were recorded whilst operating on a cadaveric knee, with the background set up to best mimic actual operating room conditions.

¹Mechatronics in Medicine, Imperial College London, UK

²Department of Computer Science, University of Liverpool, UK

Both RGB images and the corresponding 3D pose of each observed tool in the frame were gathered. A RealSense D415 (Intel, USA) was utilised for image collection, while a ftk500 optical tracker (Atracsys, Switzerland) was employed for the localisation of the tools, which were mounted with fiducials for tracking purposes. With the two sensors extrinsically calibrated, 3D poses in the camera coordinate system were obtained, as explained in Equation 1:

$$\mathbf{p}_{\text{cam}} = [\mathbf{R}|\mathbf{t}] \mathbf{p}_{\mathbf{A}} \quad (1)$$

where \mathbf{p}_{cam} are the 3D coordinates of the tool tip in the camera frame, $[\mathbf{R}|\mathbf{t}]$ is the extrinsic calibration matrix, and $\mathbf{p}_{\mathbf{A}}$ are the tool 3D coordinates in the optical tracker frame. For visualisation of 3D poses in 2D images, both in training and testing, the camera intrinsic matrix, \mathbf{K} , was also incorporated.

The proposed network expands on the Mask-RCNN [2], a network used for semantic segmentation and classification, by introducing a third branch, capable of 3D pose regression, as demonstrated in Figure 1. Here, 3D pose \mathbf{p} is described by the combination of the position vector, \mathbf{x} , and the orientation vector, θ , the latter in the form of quaternions. Position and orientation are examined separately and then amalgamated in the pose loss function, shown in Equation 2. Constants α and β are used to address scale discrepancies between the vectors, and improve orientation results [3] respectively.

$$\mathcal{L} = \alpha \| \mathbf{x}_{\text{true}}, \mathbf{x}_{\text{pred}} \|_2 + \beta \| \theta_{\text{true}}, \theta_{\text{pred}} \|_2 \quad (2)$$

Overall, 5370 images were annotated, with 4027 images being used for training. Each image was semantically labelled, and was accompanied by a value for the observed 3D pose.

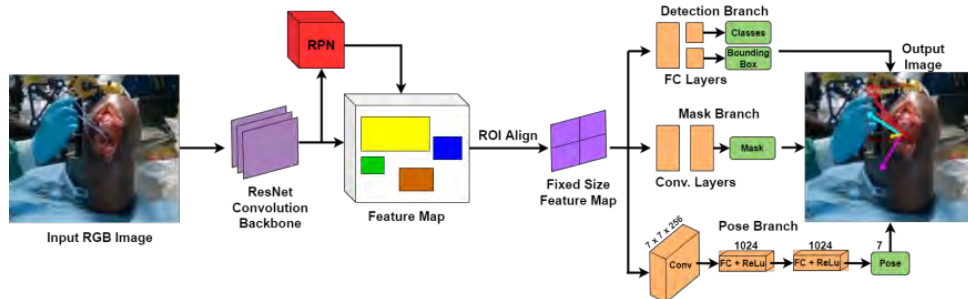


Figure 1: SimPS-Net Architecture

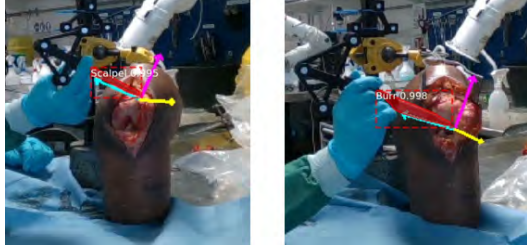


Figure 2: Inference Examples of Mask and Pose

III. RESULTS

Network evaluation was performed over 806 unseen images, with tool detection and 3D pose estimation being performed on each frame. This process was reiterated for various pose constant permutations, α and β . The optimal set was determined to be $\alpha = 700$ and $\beta = 300$.

Separate metrics for tool detection, position, and orientation were calculated during testing. The detection metrics of mean average precision (mAP) and mean DICE coefficient (mDICE) were independent of pose constant values, thus remaining constant across tests. The pose error, expressed in mm for position and degrees for orientation, was calculated as the average discrepancy between predicted and actual values along each coordinate axes separately. Each metric is listed in Table I, along with inference results of state-of-the-art networks which were trained and tested over the same novel dataset as SimPS-Net. As mentioned, 3D pose was projected to the 2D images using the intrinsic matrix. Therefore, examples of the predicted, projected poses, along with the predicted masks in a frame can be seen in Figure 2.

IV. DISCUSSION

Three networks, all capable of 3D pose estimation without prior 3D structure knowledge, were deployed for results comparison with SimPS-Net specifically PoseNet [3], ROPE [4], and GDR-Net [5]. Examining Table I, the proposed method demonstrates auspicious results across both position and orientation metrics. Each position error falls below the the results obtained by the compared networks. Regarding orientation errors, both pitch and yaw errors are comparable across all four networks. However, SimPS-Net presents more robust results for roll values. Combining this observation with the error noted in the depth axis, Z, it can be concluded that the network exhibits satisfactory performance for the intended purpose of 3D pose regression. Ultimately, SimPS-Net was found to have an average positional error of 5.5mm, with the average orientation error being 3.3°.

A limited number of techniques utilise an exclusively monocular setup to estimate the 3D pose of surgical tools, with most research focusing solely on 2D pose, thus expressing tool position in terms of pixels. Comparison with such methods, which are usually more robust, would provided limited insights, since they do not allow for 3D localisation of objects.

The proposed network exhibits a degree of versatility when compared with its counterparts. 3D pose estimation is performed without the use of prior 3D structure knowledge or initial shape assumptions for the objects being tracked, and the results overall outperform the state of the art results. Even though the reported values do not exceed the capabilities of optical trackers, this camera-based method enjoys a significant ease of deployment and minimal footprint in the operating room. Therefore, in cases where sub-millimeter accuracy is not necessary, such as robot path planning outside of the body, SimPS-Net could be an attractive option.

Despite the encouraging results, there are still some areas that need further improvements. Firstly, an occlusion handling mechanism should be integrated in the detection branch of the network, thus allowing it to compete with networks that focus exclusively on tool detection. In addition, hardware limitations restricted the novel dataset to images with single tools. Hence, a dataset expansion is needed to explore the pose errors with multiple tools observed in a frame. Ultimately, by utilising an improved GPU, a visual active constraint could be developed that involves the deployment of the network in real-time capabilities. This would result in the assimilation of SimPS-Net with a surgical robot pipeline, since the active constraint would ensure patient safety through its capacity for obstacle avoidance.

Table I: SimPS-Net Results Comparison against Literature

Source	PoseNet [3]	ROPE [4]	GDR-Net [5]	SimPSNet
mAP (%)	NA	56.8	58.5	62.9
mDICE (%)	NA	80.2	83.7	85
X (mm)	18.4 (11.6)	8.4 (3.5)	6.1 (5.2)	5.2 (4.5)
Y (mm)	18.6 (13.1)	11.4 (6.2)	5.0 (2.4)	4.0 (4.3)
Z (mm)	13.4 (9.2)	9.2 (5.2)	7.3 (3.4)	6.3 (6.0)
Pitch (deg)	2.3 (1.8)	3.2 (2.5)	2.6 (3.1)	2.4 (2.8)
Yaw (deg)	1.3 (1.0)	1.8 (2.1)	2.3 (2.6)	1.5 (1.5)
Roll (deg)	28.2 (28.2)	8.3 (16.2)	6.7 (10.7)	6.1 (37.3)

REFERENCES

- [1] David Bouget, Max Allan, Danail Stoyanov, and Pierre Jannin. Vision-based and marker-less surgical tool detection and tracking: a review of the literature. *Medical Image Analysis*, 35:633–654, 2017.
- [2] Kaiming He, Georgia Gkioxari, Piotr Dollár, and Ross Girshick. Mask R-CNN. *IEEE Transactions on Pattern Analysis and Machine Intelligence*, 42(2):386–397, 2017.
- [3] Alex Kendall, Matthew Grimes, and Roberto Cipolla. PoseNet: A convolutional network for real-time 6-dof camera relocalization. *Proceedings of the IEEE International Conference on Computer Vision*, pages 2938–2946, 2015.
- [4] Bo Chen, Tat Jun Chin, and Marius Klimavicius. Occlusion-Robust Object Pose Estimation with Holistic Representation. In *Proceedings - 2022 IEEE/CVF Winter Conference on Applications of Computer Vision, WACV 2022*, pages 2223–2233. Institute of Electrical and Electronics Engineers Inc., 2022.
- [5] Gu Wang, Fabian Manhardt, Federico Tombari, and Xiangyang Ji. GDR-Net: Geometry-Guided Direct Regression Network for Monocular 6D Object Pose Estimation. *Proceedings of the IEEE/CVF Conference on Computer Vision and Pattern Recognition (CVPR)*, pages 16611–16621, 2021.

Deep Imitation Learning for Automated Drop-In Gamma Probe Manipulation

Kaizhong Deng, Baoru Huang, and Daniel S. Elson

The Hamlyn Centre for Robotic Surgery, Imperial College London, London, UK
k.deng21@imperial.ac.uk

INTRODUCTION

Prostate cancer is one of the most common cancers in the UK, and Robotic-Assisted Surgery (RAS) has become a common method for prostate cancer surgery. Sentinel lymph node biopsy (SLNB) is an important component of prostate cancer surgery and provides accurate diagnostic evidence of disease extent.

A drop-in gamma probe, SENSEI, has been designed to improve the accuracy of sentinel lymph node detection in RAS. An example of its *in vivo* usage can be seen in Figure 1. It can distinguish cancerous tissue from normal tissue by detecting the radiation emitted from radiolabeled probes that have been injected into the body. A feasibility study has demonstrated that the drop-in gamma probe can provide accurate identification of positive nodes following the administration of technetium-99m nanocolloid [1].

However, relying on the live gamma level display and audible feedback from the console while the probe is scanned across the tissue surface is not an easy or intuitive way to identify hidden affected lymph nodes. This might affect the effectiveness of less experienced surgeons and latent hot spots may be overlooked. To address these issues, we propose a robotic scanning method to automatically and systematically examine an entire target area and locate the hot spots. In this study, we present a deep imitation training workflow based on simulation data for an end-to-end learning-based agent capable of systematically scanning target areas using visual input and the current robot state. The evaluation result shows that this approach is promising to automatically control the drop-in gamma probe.

MATERIALS AND METHODS

A. Building simulation environment

Surgical scene modelling: Surgical scene models are essential objects in the simulation. They should provide rich visual information both on texture and geometry to bring the simulated visual observation closer to reality. These were reconstructed using VisionBlender [2] to obtain a surface model from the SCARED dataset [3] which contains videos of laparoscopic surgery on the da Vinci robot. Keyframes from the dataset were reconstructed by VisionBlender to obtain a depth estimation map to generate a scene model. Subsequently, the created scene models were projected to a simplified mesh,

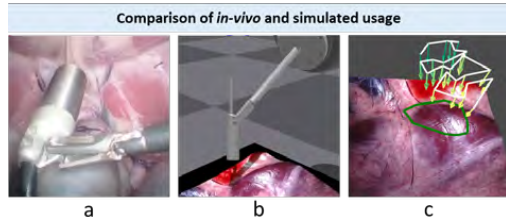


Fig. 1 Comparison of drop-in gamma probe usage: a) the use in an *in vivo* surgical view from laparoscope [4]; b) the use in the simulated surgical scene c) one example of generated scanning trajectory

resulting in a reduction of geometrical complexity while preserving a high-quality texture representation.

Robot system setup: The KUKA iiwa14 r820 (IIWA) robot and SENSEI drop-in gamma probe were adopted in this experiment. To mount the probe to IIWA, a customised probe holder was designed to hold the drop-in gamma probe and mount it to the flange of IIWA as shown in Figure 1 (b).

B. Demonstration data collection

Path generation: In this study, we proposed a workflow for the automatic generation of large quantities of demonstration data for use in the scanning task. To collect a dataset with diverse demonstrations, various target scanning areas were selected. The waypoints were chosen to follow the standard gamma probe manipulation with an approximate distance of 3 cm from the tissue and perpendicular to the surface. Therefore, the path generation workflow contained four steps: (1) generation of a 2D target scanning area by randomly sampling points from a Gaussian distribution and fitting a convex hull to the sampled points; (2) application of a grid-based coverage path planning algorithm as a deterministic policy to generate raster scanning paths; (3) projection of the planned waypoints onto the surgical scene to obtain the 3D position and normal direction of the tissue surface; and (4) offsetting and interpolating waypoints to acquire a smooth path that satisfied the distance and pose requirements.

Demonstration collection: The scanning process was simulated by Isaac Gym in the built environment. Isaac Gym can provide photo-realistic visual observations,

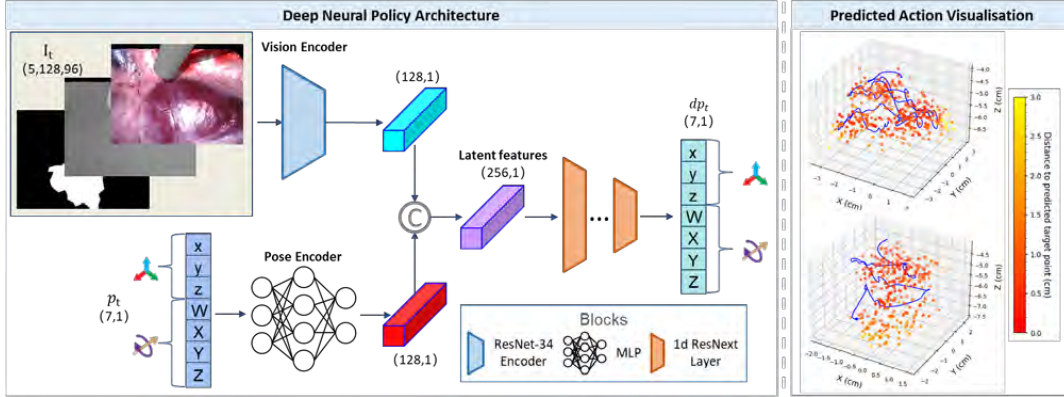


Fig. 2 Overview of the deep neural network policy and visualisation of predication action. Left) The main architecture or policy network consisted of pre-trained ResNet-34 as a vision encoder, a multilayer perceptron as a pose encoder, and 1-d ResNeXt layers as decoder to predict rotational and translational action. Right) Visualisation of predicted actions by showing the predicted next step position as the predicted action over the current position.

effectively minimizing the gap between simulation and reality. In the simulation experiment, a series of targeted waypoints were defined using a generated path, and the robot smoothly navigated to each of these points. The camera pose was varied depending on the location and area of the target scanning area to acquire sufficient diversity. The virtual RGBD camera captured RGB images and depth maps with a binary map representing the target scanning area. The end-effector trajectories in the camera coordinates were also recorded. In total, 250 demonstrations with different target areas from five varied surgical scenes were collected.

C. Imitation Learning

Imitation Learning is a supervised learning method that allows the agent to learn from expert demonstrations by observing and imitating the expert's action. In this task, the observation consisted of the current RGBD image I_t , a target area binary map M with identical size, and the current pose $p_t = \{x_t, y_t, z_t, W_t, X_t, Y_t, Z_t\}$ that included the Cartesian position and the orientation represented in a quaternion. The action was derived from N-step pose differences $dp_t^N = p_{t+N} - p_t$, where $N > 1$ was adopted to acquire steady action. The policy network, as shown in Figure 2, utilises an encoder-decoder architecture to predict action from observations. A hybrid loss function with the weighted sum of Huber loss, Negative Log-likelihood loss, and L2 norm loss, was used to train the network.

D. Experiments

Models were trained on an RTX 3060 graphics card for 200 epochs. The policy network was scaled up four times in experiments to maximize model performance. In the dataset, 120 demonstrations were used in training while 40 and 90 demonstrations were used for validation and evaluation. The network was evaluated by measuring the

distance error on $dp_t^N(x, y, z)$ and the direct angle error on $dp_t^N(W, X, Y, Z)$.

RESULTS

The proposed demonstration generation workflow can produce sufficient data for agent training. These demonstrations had an average trajectory length of $4.14 \pm 4.93 \text{ cm}$ and an average coverage area of $4.58 \pm 2.98 \text{ cm}^2$. The evaluation of the trained agent showed that the root mean square errors on each dimension of $dp_t^N(x, y, z)$ were 1.25 cm , 1.29 cm , and 1.24 cm with a mean distance error of $1.69 \pm 1.38 \text{ cm}$, and an error in direct rotational angle of $14.3 \pm 9.8^\circ$. Visualization of the predicted action points revealed that they were concentrated around the target ground truth trajectories.

DISCUSSION

In conclusion, the proposed training workflow could train an end-to-end vision-based gamma probe manipulation agent from the generated simulation data. The evaluation results demonstrated that it is promising to further improve the prediction accuracy of this framework and extend this method to a hardware setup. Future work includes evaluating the rollout of the agent and using Reinforcement Learning methods to further explore optimal control policy.

REFERENCES

- [1] I. G. T. Baeten *et al.*, “Feasibility of a drop-in γ -probe for radioguided sentinel lymph detection in early-stage cervical cancer,” *EJNMMI Research*, vol. 12, no. 1, jun 2022.
- [2] J. Cartuchero *et al.*, “VisionBlender: a tool to efficiently generate computer vision datasets for robotic surgery.” *Computer Methods in Biomechanics and Biomedical Engineering: Imaging & Visualization*, vol. 9, no. 4, pp. 331–338, dec 2020.
- [3] M. Allan *et al.*, “Stereo correspondence and reconstruction of endoscopic data challenge,” Jan. 2021.
- [4] B. Huang *et al.*, “Tracking and visualization of the sensing area for a tethered laparoscopic gamma probe,” *International Journal of Computer Assisted Radiology and Surgery*, vol. 15, pp. 1389–1397, 06 2020.

Enhancing Fluoroscopy-Guided Interventions: a Neural Network to Predict Vessel Deformation without Contrast Agents

François Lecomte¹, Valentina Scarponi¹, Pablo A. Alvarez¹, Juan M. Verde², Jean-Louis Dillenseger³, Eric Vibert⁴, and Stéphane Cotin¹

¹*Inria, CNRS, Univ Strasbourg, Strasbourg, France*

²*Department of Image-Guided Liver Interventions, IHU-Strasbourg, Strasbourg, France*

³*Univ Rennes, Inserm, LTSI - UMR 1099, Rennes, France*

⁴*AP-HP Hôpital Paul-Brousse, Centre Hépato-Biliaire, Villejuif, France*

francois.lecomte@inria.fr

INTRODUCTION

Image-guided procedures have experienced a rapid increase in popularity in recent years. The advancements in medical imaging technology have led to a shift in medical images from being used primarily for diagnosis to being a critical tool in theragnostic and therapeutic procedures. This shift has resulted in the emergence of new fields such as interventional radiology (IR), therapeutic endoscopy (TE), and minimally invasive image-guided surgery (IGS), with an increasing number of professionals adopting these techniques in their clinical practices due to improved outcomes [1]. One of the most widely used imaging methods in these procedures is X-ray-based imaging, including computed tomography (CT), 2D C-arm fluoroscopy, and cone-beam CT scans. These procedures typically require the use of contrast agents (CA) to visualize soft tissues with high definition and contrast. However, the use of CA presents several challenges, including the limited volumes that can be used and the toxicity of the agents when they are injected intravascularly [2]. The CA also follows the patient's hemodynamics, leading to transient visualization and asynchronous image guidance. In this paper, we aim to address the technical issues related to contrasted X-Ray images in image-guided therapy. We propose a deep learning approach that will allow for the visualization of vessels during image-guided procedures without the need for contrast agents, making these procedures safer, and more efficient, while providing real-time guidance.

MATERIALS AND METHODS

Before the intervention, a CT scan of the patient is acquired, vessels and other structures of interest are segmented and the planning of the intervention is performed. At this stage, the poses of both the C-arm and the patient are determined for the intervention. Then, at treatment time, the C-arm and the patient are positioned as per planning. However, due to breathing induced anatomical deformations, segmented vessels cannot be superposed to the fluoroscopic images. To compensate for these deformations, a non-rigid registration method is required.

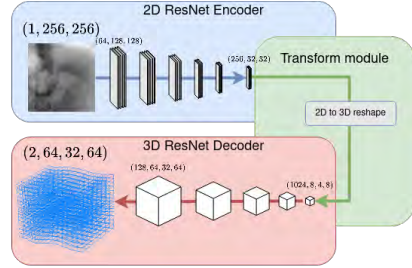


Fig. 1 Each block in the Encoder downscales the feature maps and increases their number by a factor of 2. In the Decoder, this is reversed. The last decoder layer transforms the 128 feature maps into a 2-channel 3D image.

Using the planning CT scan of the patient, we generate a dataset of Digitally Reconstructed Radiographs (DRRs) and displacement field pairs. This dataset is then used to train a neural network to recover a displacement field from a single fluoroscopic image. At the time of the intervention, the C-arm is adjusted to the planned pose, an X-ray image is acquired, and the network predicts in real-time the 3D deformation field which is used to warp the segmented structures to visually augment the fluoroscopy. Our fully convolutional network architecture is detailed in 1. Features are extracted from the 2D input image and then reshaped into 3D features. Finally, the 3D features are decoded into a 3D displacement field. This displacement field represents the non-rigid transform of the CT to the anatomy visible in the fluoroscopic image.

We assume that the deformations at the time of the intervention can be modeled as smooth and invertible displacement fields, preventing unrealistic deformations such as self intersection and excessive stretching or compression. To obtain such deformations, we model the displacement field as a sum of Gaussian Kernels. Specifically, the displacement field is integrated over $n = 100$ timesteps, while checking that smoothness and invertibility constraints are preserved after each timestep. The parameters of the Gaussian Kernels are randomized

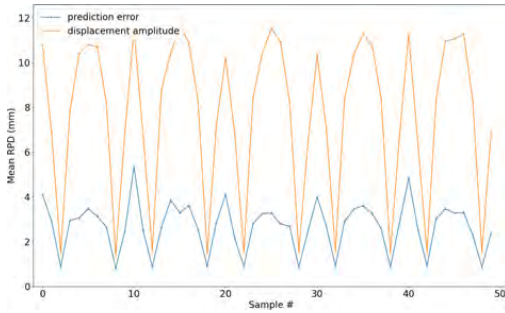


Fig. 2 The average RPD error of our method on the testing data against the average RPD displacement.

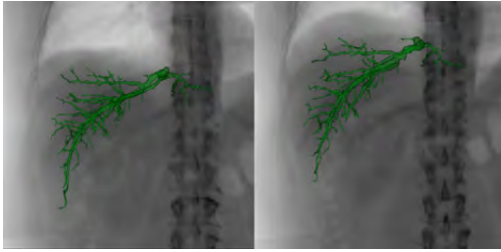


Fig. 3 Augmented DRR at full inspiration (left), and full expiration (right), with the predicted hepatic veins position.

at each step, following the principle of Domain Randomization. Using the DeepDRR framework [3], one DRR is generated for each deformation of the pre-operative CT.

RESULTS

A human liver CT obtained from a patient of the Paul Brousse hospital in Paris was used to generate a 10,000 sample dataset, split into 8,000 training samples and 2,000 validation samples. The maximum amplitude of deformation in the dataset was 22mm and 40mm in the LR direction and SI direction respectively.

The testing dataset was generated from the same 3D CT, this time using BSpline transforms tailored to mimic a breathing motion. Specifically, inhale and exhale phases and sliding motion of the organs against the bones were modeled. In this case, the maximum amplitude was 10mm and 25mm for the SI and LR directions. The dataset contains 5 inhale/exhale periods for a total of 50 samples. The accuracy of the network was measured via the reprojection distance (RPD) metric. Hepatic veins were deformed using the ground truth and the predicted displacement fields. The deformed mesh points were projected onto the image plane and the 2D RPD error was measured.

The mean RPD error on the testing dataset was 2.7 ± 1.9 mm while the mean RPD displacement was 7.7 ± 3.9 mm. Figure 4 shows the distribution of the error on the hepatic veins. Figure 3 shows an example of image augmentation by our method. A full video is available at <https://mimesis.inria.fr/project/augmented-fluoroscopy/>.

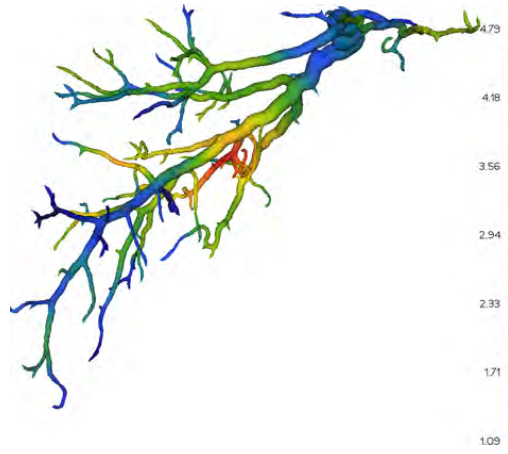


Fig. 4 The average RPD error in mm on the hepatic veins position on the testing dataset.

DISCUSSION

Even though the testing data were generated differently from the training data, the prediction of the network still reduced the error from 7.7 to 2.7mm. This validates our Domain Randomization approach, as the network learns to map a deformed fluoroscopy to a displacement field, and generalizes well on the testing data. This constitutes an advantage over other methods that might use a patient-specific motion prior obtained from a 4D-CT to train a neural network to predict deformations from a fluoroscopic image. A limitation arising from 2D fluoroscopy is that the displacement perpendicular to the image plane is not visible and thus cannot be predicted, but this is mitigated by the fact that the resulting out-of-plane error is also not visible on the augmented image.

ACKNOWLEDGEMENT

The authors would like to thank Simon Rouze, MD for his valuable inputs during the development of this method. This work was funded by the French national research agency ANR (VATSOP project). The work of Juan Verde was supported by French state funds managed within the “Plan Investissements d’Avenir” and by the ANR (reference ANR-10-IAHU-02).

REFERENCES

- [1] A. Epstein and al., “Impact of Minimally Invasive Surgery on Medical Spending and Employee Absenteeism,” *JAMA Surgery*, vol. 148, no. 7, pp. 641–647, 07 2013.
- [2] C. Mamoulakis and al., “Contrast-induced nephropathy: Basic concepts, pathophysiological implications and prevention strategies,” *Pharmacology Therapeutics*, vol. 180, pp. 99–112, 2017.
- [3] M. Unberath and al., “DeepDRR – A Catalyst for Machine Learning in Fluoroscopy-Guided Procedures,” *Lecture Notes in Computer Science*, vol. 11073, pp. 98–106, 2018.
- [4] N. Izumi and al., “Risk factors for distant recurrence of hepatocellular carcinoma in the liver after complete coagulation by microwave or radiofrequency ablation,” *Cancer*, vol. 91, pp. 949–956, 2001.
- [5] J. Tobin and al., “Domain randomization for transferring deep neural networks from simulation to the real world,” in *IROS*, 2017, pp. 23–30.

Comparison of denoising methods for synthetic low-field neurological MRI

Anthony O'Brien¹, Professor, Ferinando Rodriguez y Buena²

^{1,2}Imperial College London, London, United Kingdom

a.obrien22@imperial.ac.uk

INTRODUCTION

Over the past decade, the resurgence of low-field (LF) magnetic resonance imaging (MRI) sensor systems designed to operate up to 1 tesla range has proven well suited to inspire new solutions and design strategies to address frontline medical challenges where environmental factors are most extreme. Examples of successful low-field MRI devices in resource-limited environments include: (1) classification of infant hydrocephalus in Africa and (2) in remote small hospitals where the low-field scanner travels to the patient's bedside to observe volumetric changes in brain structure [1,2]. These low-field MRI design examples have been effective in leveraging MRI information in the setting where it is used with minimal available resources. In developing countries, access to high-field (HF) MRI is limited and requires support and infrastructure to be used. These lower-cost systems can potentially benefit from many developments that have occurred in higher fields, such as signal-to-noise dependence on static magnetic fields and hardware components (i.e., magnet, gradient coils, etc.) [3]. In addition, improvements in machine learning now provide superior noise reduction compared to traditional methods, resulting in improved performance with smaller size and lower power consumption. With improved access to medical imaging equipment, people around the world who cannot afford it due to the high cost of conventional MRIs will be able to obtain high-quality imaging data with improved contrast resolution and acquisition times.

SNR (signal-to-noise ratio) is an important measure of the quality of a signal in low-field MRI. The amount of useful information in a signal compared to background noise directly affects the effectiveness of a low-field scan [4]. The more relevant data that can be extracted from the images and the less interference or distortion from unwanted signals (e.g., electrical noise or other sources), the better the image quality, which can be enhanced by research and development of denoising and enhancement methods. In addition, any image classification system depends on the quality of the signal, so steps such as noise reduction can improve the overall performance of the system. Recently, improvements in block matching and 3D filtering (BM3D) have produced better results than standard methods such as median filters in reducing both random

and structured noise without introducing artifacts into the final image [5].

The study of denoising methods for low-field synthetic MRI datasets is a very underdeveloped area of research. By investigating the effects of denoising on image quality, the complexity and classification performance of machine learning architectures can be practically tested in diagnostic studies [4]. This study extends previous work through its unique consideration of the BM3D denoising method. The application of BM3D to low-field synthetic MRI datasets has not yet been published. With recent advances in the field, the BM3D method has been shown in other related studies to perform almost equivalently image denoising quality without the computational overhead of Deep Learning architectures [5].

MATERIALS AND METHODS

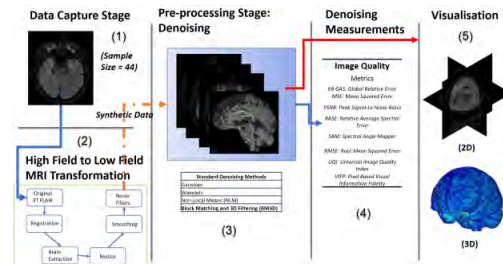


Fig. 1 A selection of key phases used to configure the experimental setup. Each phase, labelled 1 to 5, summarises key events: (1) data acquisition from HF MRI ($N=44$), (2) transformation of HF scans into synthetic low-field datasets, (3) standard denoising versus BM3D, (4) quantification of denoising method, and (5) 2D and 3D visualisation reconstruction.

A five-step process was used to determine the image quality of the synthetic datasets, as shown in Fig. 1. First, the HF MRI were collected from open source databases [6]. These datasets consisted of FLAIR images of individuals ($N=44$) used in related studies to detect Multiple Sclerosis. Second, a linear transformation of the HF scans into LF MRI datasets was performed as previously described [4]. Third, random noise was added to the medial slices of the converted LF and the original HF images. Fourth, the LF and HF slices were compared: quantifying the difference in image quality of the images. Finally, the

denoised synthesized LF images were reconstructed into 2D and 3D file for visualization. Image processing and linear transformation were performed in MATLAB 2022b. To compute the image quality metrics and BM3D, it was performed in Python 3.9 using the SciKit-Image library.

RESULTS

Table 1 provides a comparison of the standard noise reduction methods used in this study. It includes information on the type of method, its effectiveness in noise reduction, and the signal-to-noise ratio (SNR) values for each method. In addition, it shows how well BM3D performed compared to other methods when applied to low-field synthetic MRI data from forty-four subjects. The results suggest that BM3D could be an effective tool for providing sufficient noise reduction over a range of SNR values, which has implications for quantifying denoised synthetic results.

	BM3D		Gaussian		Wavelet (Daubechies 1)		NLM	
	Median	(\pm) SD	Median	(\pm) SD	Median	(\pm) SD	Median	(\pm) SD
ERGAS	20206.22266	2313.2	22895.55937	1735	19494.38715	2506.7	19307.26	2498.3
MSE	0.001808676	0.0006	0.005559388	0.0029	0.000946685	0.0003	0.000827	0.0003
PSNR	27.42677212	1.322	22.54975868	1.9387	30.23794392	1.5198	30.82361	1.461
RASE	5051.55665	578.3	5723.889842	433.74	4873.596789	626.69	4826.815	624.59
REF SAM	0.161909729	0.0226	0.290329757	0.027	0.115045054	0.028	0.107481	0.0262
RMSE	0.0425276	0.0066	0.074561182	0.0175	0.030768252	0.0053	0.028762	0.0046
UQI	0.303977622	0.0954	0.329486243	0.0941	0.309756622	0.0958	0.309703	0.0957
VIFP	0.761157224	0.0591	0.14890925	0.0245	0.992056496	0.0319	1.043759	0.0263

Table. 1 Effect of denoising methods on transformed low-field MRI data (N= 44). Data are expressed as median \pm standard deviation (SD). Comparison of image quality was performed using the following metrics: global relative error (ER GAS), mean square error (MSE), peak signal-to-noise ratio (PSNR), relative average spectral error (RASE), root mean square error (RMSE), universal image quality index (UQI), and pixel-based visual information fidelity (VIFP).

DISCUSSION

To our knowledge, the present study is the first comparative investigation of denoising methods for low-field synthetic MRI data and represents an important contribution to the development of LF portable scanners. Our study provides clear evidence that BM3D provides sufficient noise reduction effectiveness for image quality over a range of SNR values (see Table 1). This has implications for quantifying denoised synthetic results, but also suggests that the generated results could be used as input to a classification system when no other alternatives are available. Our results also support the growing evidence that low-field MRI systems can provide a cost-effective and accessible alternative to conventional higher-field scanners, while providing good data quality and high diagnostic value [7].

The study design and small sample size pose important limitations: (1) the sample was relatively small and included a limited number of pathologies, which is not be representative of the overall population and could lead to inaccurate conclusions from the data, (2)

alternative methods for denoising the synthetic MRI images were not used in this study, and (3) the transformation procedure used is relatively simple and does not account for potential field strengths, pulse sequences, or device-specific artifacts. However, this work is useful for experimenting with different configurations of medical devices from open-source imaging databases, which can provide insights and rationales for prospective studies and would allow researchers to test and validate new imaging devices without the need for costly clinical trials. Additionally, BM3D could be further refined with more advanced transformation methods of HF MRI and other noise reduction methods should be considered to improve image quality. Further research can be conducted to investigate alternative acquisition methods, transformations from those methods, and image reconstruction techniques for future low-field MRI systems.

REFERENCES

- [1] Harper, J., Mbabazi-Kabachelor, E., Mulando, R., Sheth, K. N., Yu, M., O’Riley, T., Cherukuri, V., Webb, A., Warf, B. C., Kulkarni, A., Monga, V., & Schiff, S. J. (2021). Quantifying the Utility of Low Resolution Brain Imaging: Treatment of Infant Hydrocephalus. MedRxiv.
- [2] Warf, B. C., Kulkarni, A. v, Sheth, K. N., Mulando, R., Yu, M., Mbabazi-Kabachelor, E., Harper, J. R., Webb, A. G., O’Reilly, T., Monga, V., Cherukuri, V., & Schiff, S. J. (2021). Assessing the Utility of Low Resolution Brain Imaging: Treatment of Infant Hydrocephalus. NeuroImage: Clinical.
- [3] Marques, J. P., Simonis, F. F. J., & Webb, A. G. (2019). Low-field MRI: An MR physics perspective. Journal of Magnetic Resonance Imaging, 49(6), 1528–1542.
- [4] Coffey, A. M., Truong, M. L., & Chekmenev, E. Y. (2013). Low-field MRI can be more sensitive than high-field MRI. Journal of Magnetic Resonance, 237, 169–174.
- [5] Makinen, Y., Azzari, L., & Foi, A. (2020). Collaborative Filtering of Correlated Noise: Exact Transform-Domain Variance for Improved Shrinkage and Patch Matching. IEEE Transactions on Image Processing, 29, 8339–8354.
- [4] Arnold, T. C., Baldassano, S. N., Litt, B., & Stein, J. M. (2021). Simulated Diagnostic Performance of Ultra-Low-Field MRI: Harnessing Open-Access Datasets to Evaluate Novel Devices. MedRxiv, 2021.07.02.21259789.
- [5] de Leeuw Den Bouter, M. L., Ippolito, G., O’reilly, T. P. A., Remis, R. F., van Gijzen, M. B., & Webb, & A. G. (123 C.E.). Deep learning-based single image super-resolution for low-field MR brain images.
- [6] Commowick, O., Kain, M., Casey, R., Ameli, R., Ferré, J. C., Kerbrat, A., Tourdias, T., Cervenansky, F., Camarasu-Pop, S., Glatard, T., Vukusic, S., Edan, G., Barillot, C., Dojat, M., & Cotton, F. (2021). Multiple sclerosis lesions segmentation from multiple experts: The MICCAI 2016 challenge dataset. NeuroImage, 244, 118589. Med Image Comput Comput Assist Interv. 2008;11(Pt 2):676-83.
- [7] Anoardo, E., & Rodriguez, G. G. (2023). New challenges and opportunities for low-field MRI. Journal of Magnetic Resonance Open, 14–15, 100086.

Learning Robotic Ultrasound through Coaching

Mythra V. Balakuntala¹, Deepak Raina¹, Juan Wachs², and Richard Voyles¹

¹School of Engineering Technology, Purdue University

²Industrial Engineering, Purdue University

{mbalakun, draina, rvoyles, jpwachs}@purdue.edu

INTRODUCTION

Medical imaging is an essential tool for diagnosing and monitoring various health conditions. Robotic remotization of such diagnostic medical procedures increases the safety of medical personnel and accessibility to the rural populace. However, ultrasound exams can be challenging and require skilled operators to obtain high-quality images. Automating such procedures requires programming robots to perform these dexterous medical skills. The programming constraint can be eliminated by leveraging human tutelage paradigms, enabling the robot to learn from observation and expert feedback. But, robots require massive libraries of demonstrations to learn effective policies using machine learning algorithms [1]. While such datasets are achievable for simple tasks, providing many demonstrations for contact-rich procedures such as ultrasound is not practical. This paper presents a novel method to learn complex contact-rich procedures by combining self-supervised practice with sparse expert feedback through coaching. The robotic ultrasound system (RUS) uses reinforcement learning (RL) to learn a policy for autonomous imaging of a urinary bladder phantom. Specifically, we use an off-policy soft actor-critic with a reward based on image quality assessed using a supervised convolutional neural network to learn the policy for ultrasound through practice. In addition to practice, experts provide online corrective feedback (coaching), which drives the robot to learn successful policies for ultrasound imaging.

MATERIALS AND METHODS

The proposed approach combines self-supervised practice through RL with online learning from expert feedback. First, the robot learns a policy to perform ultrasound purely using practice guided by an image quality metric. Next, expert users provide online feedback, which is used to update policy parameters to improve the execution, as shown in Figure 1.

A. Ultrasound Policy Learning

This section describes the reinforcement learning policy, which is learned based on an image quality reward. The robot model executes in a finite bounded horizon, with a Markov decision process \mathcal{M} , with state space \mathcal{S} and action space \mathcal{A} . For a horizon T , the state transitions

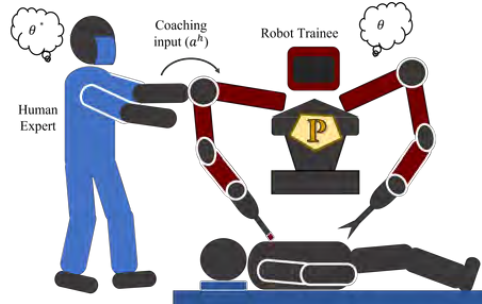


Fig. 1 The coaching framework to learn procedures

according to the dynamics $\mathcal{T} : \mathcal{S} \times \mathcal{A} \rightarrow \mathcal{S}$. A learning policy $\pi_\theta(a|s)$ represents the probability of taking action a given a state s , with parameters θ . The cumulative expected reward over horizon T is given by (1).

$$J(\pi) = \mathbb{E}_\pi \left[\sum_{t=1}^T \phi(s_t, a_t) \right] \quad (1)$$

We use an off-policy algorithm, Soft Actor-Critic (SAC) [2] to learn the policy. The algorithm maximizes the cumulative reward and entropy to learn the policy.

The action space A for the SAC agent is a combined force-position space. Specifically, the robot controls force along the z-axis (normal to the surface) and position in the XY plane. Thus, it localizes the feature and applies appropriate force to obtain good quality images. The state S that represents the state of the environment is defined based on the ultrasound image. We have adopted a image classification network from our previous work [3], which uses ResNet50 as base network with multi-scale and bi-linear pooling for fine-grained classification of image quality. This network encodes the image into a feature vector of size 2048, representing the system's current state. The reward for the SAC is based on the ultrasound image quality estimated using the same feature network used to generate the state. The image features are passed through a linear classifier layer which estimates a integer quality metric between 1-5. The reward is defined as shown in eq. (2).

$$r_t = 10(q_t == 5) + q_t/5 \quad (2)$$

where q_t is the integer quality of the image and the

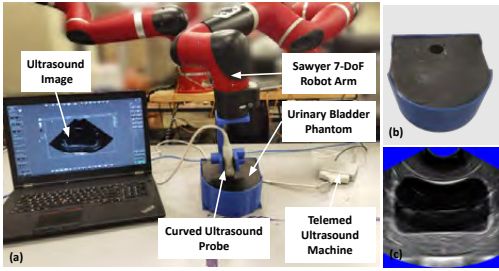


Fig. 2 (a) Robotic ultrasound system with probe attached to its end-effector (b) Urinary bladder phantom (c) Acquired ultrasound image from phantom

expression ($q_t == 5$) is 1 if quality is maximum and 0 otherwise. This image quality based reward guides the self-supervised learning of the ultrasound policy.

B. Coaching

The SAC agent learns the policy only guided by the image quality. While this leads to a partially successful policy, further tuning is required to learn effective policies for an autonomous ultrasound system. Additionally, poor image quality assessment and noise result in sub-optimal execution policies. To address this shortcoming, we propose leveraging expert feedback to improve performance. Figure 1 describes the interactive coaching method. The robot has learned a base policy whose parameters are θ . But, the human expert knows the actual desired policy whose parameters are represented as θ^* . However, the robot cannot obtain this knowledge directly as the true parameters are hidden. The robot can estimate these using observations of the human expert's corrective actions a^h . This system essentially is a partially observable Markov decision process (POMDP). However, solving a POMDP in higher dimensional spaces is intractable. Therefore, we propose to reduce this to an approximation using Kullback–Leibler (KL) divergence to update the policy. First, we approximate the true policy $\pi_{\theta^*}(a|s)$ using an approximate gaussian policy $\tilde{\pi}(a|s) : \mathcal{N}(\mu, \sigma)$. The parameters μ and σ are estimated using the set of coaching corrections a^h . Next, we update the policy $\pi_{\theta}(a|s)$ by minimizing the KL divergence loss,

$$\mathcal{L}_{KL} = \mathbf{D}_{KL}(\pi_{\theta}(a|s) || \tilde{\pi}(a|s))$$

This KL loss is combined with the policy loss of SAC, and the policy parameters θ are updated. The coaching corrections are separately stored in a “coach” replay memory, and the policy and critic network updates are performed by sampling from this coach replay buffer by optimizing for \mathcal{L}_{KL} . This essentially offsets the policy towards generating actions similar to expert in states where the corrections were provided.

RESULTS

We validate the proposed framework using the experimental setup shown in Fig. 2(a), which consists of 7-DOF sawyer robotic arm by Rethink Robotics, Germany and

ultrasound machine by Telemed Medical Systems, Italy. A Micro Convex MC10-5R10S-3 ultrasound probe is attached to robot's end-effector using a custom-designed gripper. The urinary bladder phantom has been used as shown in Fig. 2(b). The acquired ultrasound image shown in Fig. 2(c) is passed to the GPU laptop and whole system is connected via ROS. We executed 10 episodes of each RL policy with and without coaching feedback. Each episode has 10 steps. We compared the policy with and without coaching using the two metrics: (i) Number of high image quality regions sampled (ii) Average probe force error. We also compared the average reward for each episode across 10 steps as shown in Fig. 3.

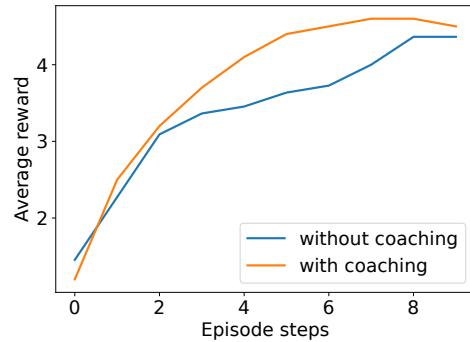


Fig. 3 (a) Comparison of average reward for RL policy with and without coaching feedback

TABLE I Quantitative Comparison of RL policy with and without coaching

Metrics	Without Coaching	With Coaching
High Image quality region	43/100	71/100
Avg. probe force error	6.06%	1.13%

DISCUSSION

The coaching of a RL policy for robotic ultrasound is a promising approach that can significantly improve the efficiency and accuracy of ultrasound image acquisition. The comparison of average rewards across 10 episodes has shown the increase in reward after 2 steps. The results in Table I have shown that coaching increases the sampling of high image quality sampling by 32.8% and decreases probe force error by 18%. Future research will focus on including the comprehensive probe control including its orientation.

REFERENCES

- [1] A. G. Billard, S. Calinon, and R. Dillmann, “Learning from humans,” *Springer handbook of robotics*, pp. 1995–2014, 2016.
- [2] T. Haarnoja, A. Zhou, P. Abbeel, and S. Levine, “Soft actor-critic: Off-policy maximum entropy deep reinforcement learning with a stochastic actor,” in *International conference on machine learning*. PMLR, 2018, pp. 1861–1870.
- [3] D. Raina, C. SH, R. Voyles, J. Wachs, and S. K. Saha, “Robotic sonographer: Autonomous robotic ultrasound using domain expertise in bayesian optimization,” in *2022 International Conference on Robotics and Automation (ICRA)*. IEEE, 2023.

Global versus local kinematic skills assessment on robotic assisted hysterectomies

A. Huaultmé¹, K. Nyangoh Timoh^{1,2}, V. Jan¹, S. Guerin^{1,2}, P. Jannin¹

¹Univ Rennes, INSERM, LTSI - UMR 1099, F35000, Rennes, France

²Department of Obstetrics and Gynecology, Rennes University Hospital, Rennes, France
arnaud.huaultme@univ-rennes1.fr

INTRODUCTION

Surgical skills assessment is a crucial step to help understanding surgical expertise and to provide technical knowledge to beginners. Scores, such as GOALS [1], have been designed to assess surgical skills. However, these scores are subjective and need experts to compute them.

With the advent of robotic surgery, it is possible to compute Automated Performance Metrics (APMs) based on the motion of robotic arms to assess surgical skills. Several studies have demonstrated statistically significant differences between APMs from different levels of expertise [2], [3]. The majority of these studies performed a global analysis, i.e., studying the surgical procedure or training task as a whole.

By using the Surgical Process Model (SPM) methodology [4], it is possible to describe the surgery at different levels of granularity and break it down into a sequence of elements. Riffaud et al. [5], decomposed Lumbar Disc herniation surgery by phases and demonstrated that the main expertise differences in terms of duration are due to specific phases or actions.

In this paper, we will combine SPM and APMs to study global and local kinematic skills during robotic-assisted hysterectomies.

MATERIALS AND METHODS

Data – Fifty-two robotic-assisted laparoscopic hysterectomies (RALH) performed on the Da Vinci SI (Intuitive®) robotic system have been acquired between June 2020 and September 2021 thanks to the DVLogger. Thirty-six surgeries have been performed by 5 expert surgeons (more than 35 RALH at inclusion) and 16 surgeries by 3 intermediate surgeons (less than 20 RALH). For each case, we recorded the surgical video (25Hz) and the kinematic data (50Hz). The kinematic data contains the position (x, y, z) and the Euler angles for each of the left and right robotic arms.

Data annotation – Each surgical sequence has been annotated following the SPM methodology at phase granularity by one gynecologic resident thanks to the surgical video. Height phases have been defined: “surgical approaches”, “exhibition”, “adnexal dissection left”, “adnexal dissection right”, “anterior dissection”, “dissection of the uterine pedicles”, “resection” and “restoration of the operating site”. According to our clinical partner, the most difficult phases are the “adnexal dissection left” and the “dissection of the uterine pedicles”. The complexity of the first one is due to the

uterus preventing direct access of arm 2 (right-hand) to the left adnexa for right-handed people. The second is due to the high risk of adverse events such as blood loss or ureteral injury.

Data synchronization – We used the timestamp information provided by the DVLogger and the SPM description to synchronize the kinematic data with the video.

Extraction of global and local kinematics – In the surgical environment, the endoscope is connected during the instrument preparation made by the scrub nurse. This generally happens few minutes before the beginning of surgery. Even if kinematics and video are synchronized, to only study the robotic movement during the surgery, we have to take into account the real duration of surgery. For that, we extracted the kinematic data thanks to the SPMs which are synchronized with videos. The global kinematic sequences are the kinematic data for the complete duration of the surgeries, and the local kinematic sequences are the ones for each phase.

APMs extractions – For each global and local kinematic sequence, we extracted 16 APMs. These APMs are the average velocity ($m.s^{-1}$), the average acceleration ($m.s^{-2}$), the average jerk ($m.s^{-3}$), the smoothness ($m.s^{-4}$) [6], the trajectory length (m), the working volume (m^3) and the economy (m^2) for each robotic arm independently (14 APMs). We also computed the duration (s) and the bimanual dexterity (2 APMs).

Statistical analysis – The Shapiro-Wilk test was used to test the normality of the data for each feature for each local kinematic sequence. In all cases, the feature distribution was non-normal. A Wilcoxon-Mann-Whitney test was performed to ensure that the differences were significant between the sequences of the experts and those of the intermediates ($p < 0.05$).

RESULTS

The Table 1 summarizes the statistically significant APMs for each phase and robotic arms. On the global kinematic analysis, only 4 APMs were statistically different between experts and intermediate (p -value <0.05): average velocity, average jerk for each arm. For the local kinematic analysis, all phases, except “surgical approaches” and “exposition”, have at least one statistically significant feature. Of the 16 APMs, 15 of them are significant for at least one phase with a p -value <0.05 , and 4 of them with a p -value <0.001 .

Phases	Arm 1 (Left)	Arm 2 (Right)	Both arms
All surgery (global)	2	Velocity Jerk	2
Adnexal dissection left		1	Smoothness
Adnexal dissection right	1	Path length	4
Anterior dissection	4	Velocity* Path length Volume Economy	3
Dissection of the uterine pedicles		2	Jerk Volume
Resection	2	Acceleration* Jerk	2
Restoration of the operating site	1	Smoothness	4
			1
			Duration*

Table 1 Statistically significant APMs by phases and robotic arms. All APMs have a p-value <0.005, the APMs with a star (*) have a p-value <0.001.

For the “adnexal dissection left”, the smoothness is statistically different for robotic arm 2 ($p=0.039$, Fig 1.a). Experts have a lower value than intermediate, i.e., more smooth motion ($48.81\pm22.50 \text{ m.s}^{-3}$ vs. $74.22\pm32.25 \text{ m.s}^{-3}$).

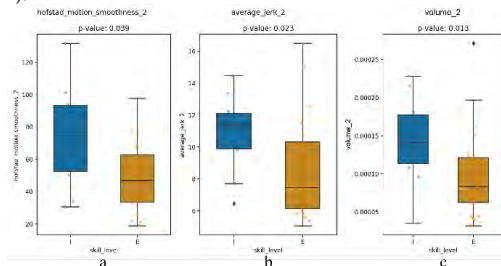


Figure 1: Boxplot for the right robotic arm of “adnexal dissection left” for the motion smoothness (a), of the “dissection of the uterine pedicles” for the jerk (b), and the working volume (c) of experts (E) vs. intermediates (I) surgeons.

For the second complex phase, “dissection of the uterine pedicles”, the jerk and the working volume were statistically different for robotic arm 2 ($p=0.023$, Fig 1.b & $p=0.013$, Fig 1.c). Experts had a jerk of $8.54\pm3.03 \text{ m.s}^{-3}$ and a working volume of $95.46\pm54.32 \text{ cm}^3$, whereas intermediates had respectively $10.86\pm2.44 \text{ m.s}^{-3}$ and $144.35\pm57.29 \text{ cm}^3$.

DISCUSSION

This study analyzed kinematic data coming from surgical routine to analyze expertise whereas most similar previous studies relied on simulated procedures. Additionally, our local analysis based on SPM methodology gives more information than a global one. While the significant differences were only in acceleration and jerks at the global levels, the local analysis allows us to better understand the specificity of each surgical phase. In the case of “adnexal dissection left”, the uterus blocks the movement of the right tool

(arm 2), leading to less smooth motion for intermediates. One tip to counter this would be to improve mobilization of the uterus with the uterine manipulator.

The main limitation of this paper is the focus on phases to perform the local analysis. Make a focus on a finer granularity would allow better understanding. For example, the “dissection of the uterine pedicles” phase is split into two different steps relative to the laterality of the pedicles. It is possible that the uterus has also an impact on the robotic arm motion. Future works will focus on this point.

REFERENCES

- [1] M. C. Vassiliou *et al.*, “A global assessment tool for evaluation of intraoperative laparoscopic skills,” *Am J Surg*, vol. 190, no. 1, Jul. 2005, doi: 10.1016/J.AMSURG.2005.04.004.
- [2] S. Guerin, A. Huault, V. Lavoue, P. Jannin, and K. Nyangoh Timoh, “Review of automated performance metrics to assess surgical technical skills in robot-assisted laparoscopy,” *Surg Endosc*, vol. 36, no. 2, Feb. 2022, doi: 10.1007/s00464-021-08792-5.
- [3] A. J. Hung *et al.*, “Experts vs super-experts: differences in automated performance metrics and clinical outcomes for robot-assisted radical prostatectomy,” *BJU Int*, vol. 123, no. 5, May 2019, doi: 10.1111/BJU.14599.
- [4] F. Lalys and P. Jannin, “Surgical process modelling: a review,” *Int J Comput Assist Radiol Surg*, vol. 9, no. 3, Nov. 2013, doi: 10.1007/s11548-013-0940-5.
- [5] L. Riffaud *et al.*, “Recording of Surgical Processes: A Study Comparing Senior and Junior Neurosurgeons During Lumbar Disc Herniation Surgery,” *Operative Neurosurgery*, vol. 67, Jul. 2010, doi: 10.1227/NEU.0b013e3181f741d7.
- [6] E. F. Hofstad, C. Väpenstad, M. K. Chmarr, T. Langø, E. Kuhry, and R. Mårvik, “A study of psychomotor skills in minimally invasive surgery: What differentiates expert and nonexpert performance,” *Surg Endosc*, vol. 27, no. 3, Oct. 2013, doi: 10.1007/S00464-012-2524-9.

Using LOR Syringe Probes as a Method to Reduce Errors in Epidural Analgesia – a Robotic Simulation Study

N. Davidor¹, Y. Binyamin², T. Hayuni², and I. Nisky¹

¹*Department of Biomedical Engineering, Ben-Gurion University of the Negev*

²*Department of Anesthesiology, Soroka Medical Center*

nitsanti@post.bgu.ac.il

INTRODUCTION

In epidural analgesia, anesthetics are injected into the epidural space, to block signals from traveling through nerve fibres in the spinal cord or near it. To do so, the anesthesiologist inserts a Touhy needle into the patient's skin and uses it to proceed to the epidural space, while using the haptic feedback received from a "loss of resistance" (LOR) syringe [1] to sense the environment stiffness and identify loss of resistance from potential spaces. The two most common errors or complications of epidural analgesia are failed epidurals (FE) – halting the needle insertion in a superficial location, which will cause no pain relief – and accidental dural punctures (ADP), leading in most of the cases to post dural puncture headache (PDPH).

The task of identifying the epidural space correctly and stopping the needle insertion while in it is challenging mechanically, and requires extensive training [2]. Hence, robotic simulation is an attractive method to help optimize skill acquisition [3]. Another advantage of robotic simulation is the ability to record kinematic information throughout the procedure, to evaluate users' performance and strategy. In this study, we used a bimanual robotic simulator that we developed in previous work [3] to analyze the effect of LOR probing strategies on procedure outcomes.

MATERIALS AND METHODS

Our experimental setup was comprised of a haptic bimanual simulator (Fig. 1) described in details in [3]. The simulator emulates the forces applied on the Touhy needle and the LOR syringe throughout the procedure (Fig. 2a), and allows for patient weight variability and recording kinematic data.

23 anesthesiologists of different levels of experience participated in two experiments. The first experiment ($N_1 = 15$) included three familiarization trials, in which there was a constant patient body mass, followed by 12 test trials that involved three different patient body masses (55, 85 and 115 kg). The second experiment ($N_2 = 8$) included only the test trials. To eliminate differences in familiarization between the two experiments, we used only the final nine trials of experiment two for our analyses.



Fig. 1 The experimental setup: a haptic bimanual simulator for epidural analgesia. One haptic device is connected to a Touhy needle and the other is mounted by an LOR syringe.

To obtain LOR syringe probes, we subtracted the trajectory of the haptic device that was connected to the Touhy needle from the trajectory of the haptic device that was mounted by the LOR syringe. We then took the peaks of the adjusted trajectory and enumerated them.

To examine if there were differences in probing amounts between different outcome trials, we plotted the mean number of probes performed in successful trials as a function of the mean number of probes performed in unsuccessful trials. This analysis is impossible for participants who had success rates of 0% or 100%, and hence they were excluded from this analysis ($N_{ex.} = 4$). In addition, we used the two-sided Wilcoxon signed rank test to compare between mean number of probes in successful and unsuccessful trials – this is because our data did not distribute normally.

To further delve into probing differences between different outcome trials, we examined the mean number of probes performed in each layer in the epidural region, in successful and unsuccessful trials. To avoid bias that is rooted in the layer thickness, we normalized the mean number of probes in each layer by dividing it by the layer thickness. This part of the study is exploratory, and hence we chose not to perform statistical analysis for testing hypotheses, and instead use this part of the analysis as preliminary investigation for a future hypothesis driven study.

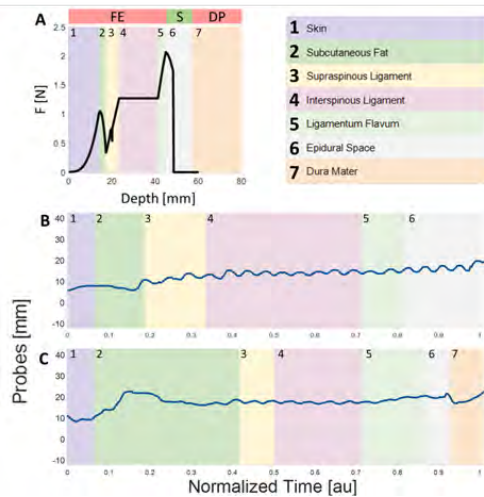


Fig. 2 Exerted forces and probes in two example trials. (A) Forces exerted by the haptic devices as a function of needle insertion depth. (B)-(C) The trajectories of the LOR syringe haptic devices as a function of the normalized time in a successful trial (B) and an unsuccessful trial (C). The different background colors and numbering in all panels represent the layers in the epidural region.

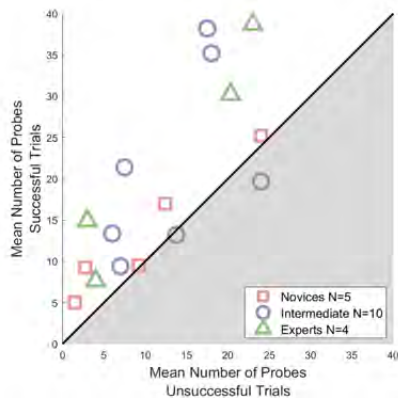


Fig. 3 The mean number of probes observed in unsuccessful trials as a function of the mean number of probes observed in successful trials. Each symbol represents one participant, and the different marker types and colors refer to the participant level.

RESULTS

We present examples of probes in two trials (Fig. 2): a successful trial, and a dural puncture. Consistently with the trend observed in most of the participants and trials, more probes were performed in the successful trial. Studying the number of probes performed in successful trials against number of probes in unsuccessful trials (Fig. 3) demonstrates that most participants were above the line

of equality, indicating that they performed more probes in successful trials, compared to unsuccessful trials (two-sided Wilcoxon signed rank test yielded $p = 0.0018$). This result was not affected by participant level. Examining the locations of probes within the epidural region (Fig. 4) revealed that more probes were performed in successful trials compared to unsuccessful trials in all layers, and the most prominent differences were observed in the three layers preceding the epidural space.

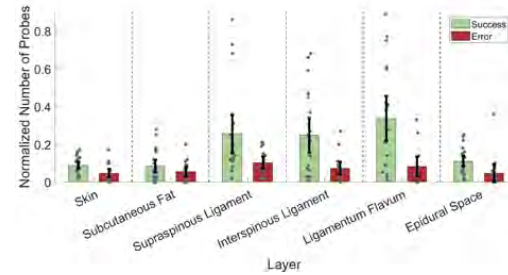


Fig. 4 Mean normalized number of probes per trial corresponding to layer in epidural region. Green bars represent successful trials and red bars represent unsuccessful trials. Dashed black vertical lines represent the separation between the different layers in the epidural region. The gray points represent the mean number of probes performed by each participant in the relevant layer, and the black bars represent the non-parametric mean 95% confidence intervals.

DISCUSSION

We used a haptic bimanual simulator to evaluate the effect of probing with the LOR syringe on procedure outcomes in epidural analgesia. We found that the majority of participants probed more in successful trials compared to unsuccessful trials. Furthermore, we demonstrated that this difference is more prominent in the three layers preceding the epidural space. These results indicate that a more extensive use of the LOR syringe (and more specifically, when approaching the epidural space) can assist in reducing errors in epidural analgesia. We argue that these findings may be useful in training anesthesia residents (when training in the virtual environment or the real one): instructing novices to focus on probing in relevant locations may enhance learning and produce better procedure outcomes.

REFERENCES

- [1] A. M. P. Dogliotti, "Research and Clinical Observations on Spinal Anesthesia: With Special Reference to the Peridural Technique," *Anesthesia & Analgesia*, vol. 12, no. 2, pp. 59–65, Apr. 1933.
- [2] C. Konrad, G. Schüpfer, M. Wielisbach, and H. Gerber, "Learning manual skills in anesthesiology: Is there a recommended number of cases for anesthetic procedures?" *Anesth Analg*, vol. 86, no. 3, pp. 635–639, Mar. 1998.
- [3] N. Davidor, Y. Binyamin, T. Hayuni, and I. Nisky, "Design and validation of a bimanual haptic epidural needle insertion simulator," 2023. [Online]. Available: <https://arxiv.org/abs/2301.11036>

Design of an ex-vivo experimental setup for spine surgery based on in-vivo identification of respiration-induced spine movement

E. Saghbiny^{1,2}, S. Vafadar¹, A. Harlé¹, and G. Morel¹

¹Sorbonne University, CNRS UMR 7222, INSERM U1150, ISIR, Paris, France.

²Armand-Trousseau Hospital, Paris, France.

INTRODUCTION

In spine surgery, e.g., pedicle screw placement, patients are in the prone position, anesthetized, and breath using respirators. Respiration-induced spine movements may interfere with the operation. For evaluating spine surgery robotic systems [1] without resorting to in-vivo experiments, it is necessary to provide a setup that realistically reproduces the spine movement in a lab.

The literature is not very rich in documenting such a movement. Most of the time, only the range of motion of one or two vertebrae is provided. Glossop et al. [2] measured this respiration-induced motion for two human lumbar vertebrae (L3 and L4) to be 1.3 mm using optical markers screwed to the spinous process. The same authors [3] measured the respiration-induced motion, using the same techniques, for three pig lumbar vertebrae (L3-L5) under ventilation that ranged from 0.8-1.1 mm. In a more recent study, Liu et al. [4] measured this motion on different levels of vertebrae – cervical (C1), thoracic (T7), and lumbar spine (L4) – using optical markers placed on the patient's skin. Mean \pm 2SD motions were 1.3 ± 0.7 mm, 2.3 ± 1.6 mm, and 1.6 ± 0.7 mm.

In this study, we measure respiration-induced spine movements (T6-L5) in an open-spine surgery on a pig. A mechanical probe mounted on a force-controlled medical robotic arm is used for measurements. Then, we propose an ex-vivo experimental setup that could implement the measured motions to emulate the respiration-induced movement.

MATERIALS AND METHODS

The in-vivo experimental setup consisted of a KUKA LBR Med 7 robotic arm. A mechanical probe (a 2 mm diameter ruby ball attached to a 1.5 mm diameter rod) was mounted on the robot's end-effector, which have a high bandwidth force feedback. The protocol, approved by the relevant ethical committee, consisted in operating on a pig to reproduce the conditions of the operating room.

The experiment was performed on a 40 Kg female pig (*Sus scrofa domesticus*). A preoperative CT scan of the spine was recorded. The 3D reconstruction of the spine was generated with RadiAnt DICOM Viewer. The entire surgical procedure was performed under general anesthesia. The volume of the inhaled gas is imposed by a

respirator with a controllable frequency. The respiration rate was fixed at 10 breathing cycles per minute (period = 6 sec). We performed a posterior surgical approach to expose the spine from the fifth thoracic vertebra to the sacrum. At the end of this step, the spinous process, lamina, articular and transverse process were exposed for each vertebra.

For each vertebra, the surgeon placed the probe on the left articular process, the spinous process, and the right articular process successively. The robot was set to co-manipulation mode, such that the surgeon could manually move the robot to the desired position. Once the probe was in contact with the bone surface, we put the robot in the force control mode applying a force of 1 N, helping keep contact with the bone without sliding, while following the breathing movement. At each step, we recorded the respiration-induced spine movement for 30 seconds, i.e., 5 breathing cycles. The robot's joint positions were recorded and converted to Cartesian coordinates at the tip of the mechanical probe. The coordinates were finally obtained with respect to the coordinate system attached to the spine (see Fig. 2B). The measured spine movements at different levels were synchronized by cross-correlation between the signals. For each vertebra, we computed the centroid of the three measured points (left and right articular and spinous process).

RESULTS

As shown in Fig. 1, the range of motion (Mean \pm 2SD) along the Z-axis (vertical, $3 \text{ mm} \pm 1.4 \text{ mm}$) is the most significant compared to the X- and Y-axis ($0.4 \pm 0.3 \text{ mm}$ and $0.3 \pm 0.2 \text{ mm}$, respectively). Such a variation between vertebrae suggests that a spine mock-up (or an ex-vivo spine sample) animated by a global rigid motion would not reproduce accurately, in the lab, the vertebrae movements observed in the operating room (OR).

Focusing now on the lumbar spine only, we can observe a more regular variation of motion range, from 2.2 mm (L5) to 3.7 mm (L1). An approximation of the Z displacement for each vertebra can be given by a Fourier series:

$$\Delta_z = a_0 + \sum_{i=1}^2 a_i \cos i\omega t + \sum_{i=1}^2 b_i \sin i\omega t ,$$

where $\omega = 2\pi/6 \approx 1.05$ and the best fitted a_i and b_i values are given for the different vertebrae in Table I.

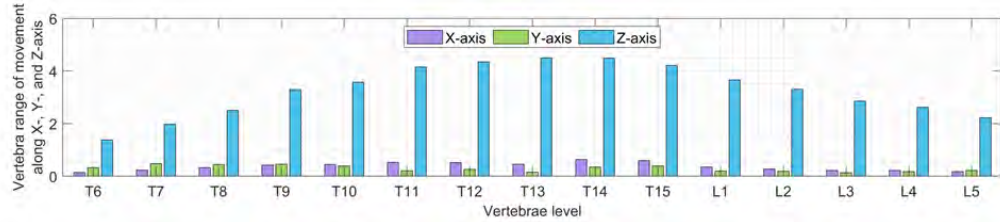


Fig. 1 Range of motion for the vertebrae T6 - L5 along X-, Y-, and Z-axis (mm). See location shown in Fig. 2B

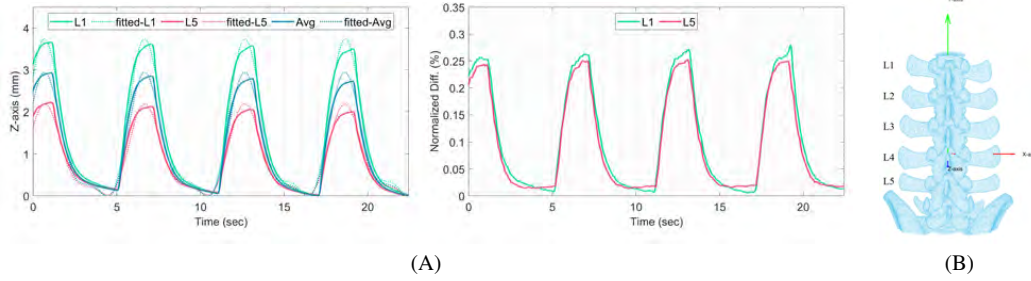


Fig. 2 (A) Range of motion for the lumbar vertebrae. (B) 3D reconstructed lumbar vertebrae

We thus suggest several different options to animate either a rigid spine mock-up that can be 3D-printed from a spine CT-Scan, or an ex-vivo pig spine sample that can be acquired at a butcher shop, as in Fig. 3:

(I) Using a simple 1-DoF (degree of freedom) translation device, that can not be dynamically programmed and can only be parameterized by the shape of a rotating cam, one can use the parameters for the average movement (last column). The average resulting difference, compared to the real movement, would therefore be limited to ≈ 1 mm (25% normalized difference). (II) Using a fully programmable animating device, like the robot used in Fig 3, one can adapt the programmed movement for each vertebra using the values given in the column.

attached to the thoracic cage, resulting in less movement, while the lower thoracic spine (T11-T15) has floating ribs, allowing for a higher range of movement (> 4 mm). The study results can be applied to create ex-vivo experimental setups that mimic the in-vivo experimental conditions.

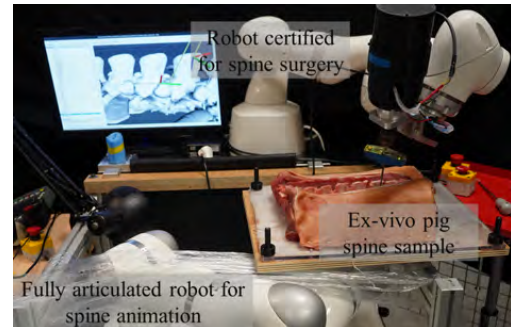


Fig. 3 An ex-vivo experimental setup

TABLE I Parameters of the movement along Z-axis (mm)

	L1	L2	L3	L4	L5	Avg
a_0	1.41	1.25	1.09	0.99	0.85	1.11
a_1	1.23	1.09	0.95	0.82	0.68	0.95
b_1	1.24	1.12	0.98	0.86	0.74	0.99
a_2	0.18	0.15	0.14	0.11	0.09	0.13
b_2	0.57	0.51	0.44	0.39	0.32	0.44
$rmsd$	0.15	0.14	0.12	0.12	0.11	0.13

DISCUSSION

This study showed a movement of 2.2 mm to 3.7 mm in the lumbar spine. This study reports higher ranges compared to the literature, possibly due to different experimental conditions. For example, a previous study [3] was conducted on a dead pig while this experiment was conducted on a live pig. The thoracic spine has a higher movement range than the lumbar spine because it is located above the lungs. The upper thoracic spine is

REFERENCES

- [1] S. H. Farber, M. A. Pacult, J. Godzik, C. T. Walker, J. D. Turner, R. W. Porter, and J. S. Uribe, "Robotics in spine surgery: a technical overview and review of key concepts," *Frontiers in Surgery*, vol. 8, p. 578674, 2021.
- [2] N. Glossop and R. Hu, "Assessment of vertebral body motion during spine surgery," *Spine*, vol. 22, no. 8, pp. 903–909, 1997.
- [3] ———, "Effects of tracking adjacent vertebral bodies during image guided pedicle screw surgery," in *CVRMed-MRCAS'97*. Springer, 2005, pp. 531–540.
- [4] Y. Liu, C. Zeng, M. Fan, L. Hu, C. Ma, and W. Tian, "Assessment of respiration-induced vertebral motion in prone-positioned patients during general anaesthesia," *The International Journal of Medical Robotics and Computer Assisted Surgery*, vol. 12, no. 2, pp. 214–218, 2016.

Towards a robotic minimally invasive surgery assessment and augmentation platform for visual-haptic acuity development

Sergio Machaca¹ and Jeremy D. Brown¹

¹*Department of Mechanical Engineering, Johns Hopkins University
smachac2@jh.edu*

INTRODUCTION

Up to half of the technical errors made by surgical trainees result from improper tool forces on tissue [1]. This skill inadequacy is exacerbated in robotic minimally invasive surgery (RMIS) due to the perpetual technical barriers prohibiting robust haptic (touch) sensations in clinical RMIS systems. Expert RMIS surgeons have developed a unique skill, termed visual-haptic acuity, that enables them to visually estimate the absent haptic sensations [2]. RMIS experts have developed this visual-haptic acuity through years of repeated surgical practice, on real patient tissue. For current RMIS trainees, limitations on working hours and caseloads severely constrain practice with real patient tissue [3]. Given that skill gained in virtual reality simulation does not always transfer to the real world [4], there is a critical need for a focus on visual-haptic acuity development. Previous research has shown that supplemental haptic feedback provided during simulation-based RMIS training helps surgical trainees to reduce their applied forces when completing RMIS training tasks [5], and that this effect is sustained even when haptic feedback is removed [6]. In addition, supplemental haptic feedback has demonstrated the potential to help RMIS trainees increase accuracy (reduce applied forces) while also increasing speed (reducing task completion time) during RMIS training [7]. Unfortunately, the benefits of supplemental haptic feedback have not been demonstrated beyond basic simulated training environments. Additionally, we lack validated objective methods for specifically assessing an RMIS trainee's ability to visually estimate haptic sensations when operating on real patient tissue. In light of this need, we are developing a modular data acquisition and multimodality haptic feedback system (as shown in Figure 1) to catalyze visual-haptic acuity development for novice RMIS trainees. The system is capable of simultaneous acquisition of multiple timestamped data streams from sensors internal and external to the RMIS platform and simultaneous feedback of various haptic cues in different rendering modalities. In our prior work [8], we demonstrated the efficacy of this system using an Intuitive da Vinci Si clinical robot. Here, we expand on this prior work to better understand how this system may be used for objective assessment

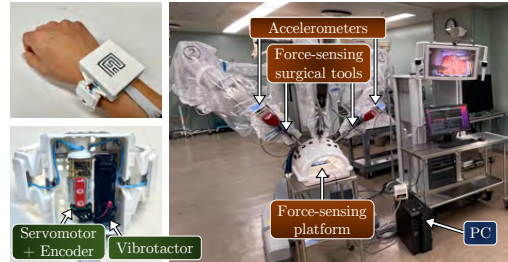


Fig. 1 Experimental setup featuring tactile actuators, da Vinci Si, external sensors, and PC.

of visual-haptic acuity during RMIS training, and real-time haptic feedback based on these assessments. We recorded surgical interactions between sensorized da Vinci instruments and an ex vivo porcine bowel as an intermediate and expert surgeon completed a simulated bowel running and knot tying task. Results highlight the difference in various kinetic metrics between intermediate and expert performance. When coupled to our haptic feedback devices, these measures can be used to both assess and augment tissue handling skill during training, which we envision will catalyze visual-haptic acuity development.

MATERIALS AND METHODS

One experienced robotic surgeon (>50 robotic cases on human patients) and one certified surgical educator (intermediate skill level) were recruited for the experiment. Participants performed one trial each of two RMIS training tasks on an ex-vivo porcine bowel with a da Vinci Si robot: 1) bowel running task and 2) three extracorporeal single throws of a square knot. Both participants provided informed consent according to a protocol (IRB00205668) approved by the Johns Hopkins University Institutional Review Board. The experiment lasted approximately 15 minutes and participants were compensated \$10 for their participation.

As shown in Figure 1, the da Vinci Si was augmented with our ROS-based haptic feedback and data acquisition framework for measuring instrument forces and vibrations, as well as the forces applied to the tissue. Two Endowrist Large Needle Drivers, sensorized with trans-

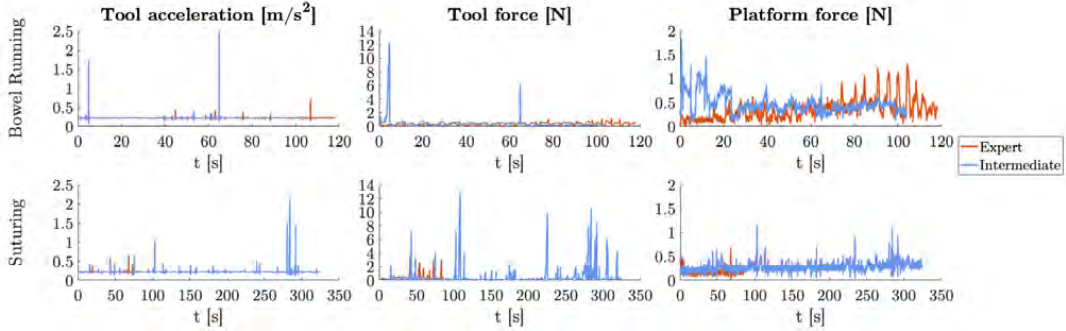


Fig. 2 Sample of kinetic signals captured by data collection system.

ducer film (Forcen Inc., Canada), provided measurements of the mid-air forces (e.g., when pulling a suture). An instrumented platform containing an ATI Mini40 SI-40-2 F/T transducer provided measures of the forces applied to the surgical task materials by the instruments. Finally, two Arduino Nano RP2040 Connect microcontrollers mounted to the top of the left and right da Vinci tool arms measured the contact accelerations created by the instruments and the motion kinematics of the arm. All signals were published to individual ROS topics, timestamped, and recorded to rosbags, as detailed in [8], using a PC (Dell Inc. Precision 5820) with an internal PCIe Sensoray 826 data acquisition board. Our data collection system is also capable of measuring kinematic streams and recording stereoscopic video from the da Vinci Research API. For this manuscript, however, we will focus on the data recorded from our external sensors. Tool accelerations, tool forces, and platform forces are reported as the average measurement from both tools.

RESULTS

All average applied forces were lower for the expert surgeon than the intermediate surgeon. Tool accelerations were the same for both participants in both tasks. The task completion time was lower for the intermediate surgeon than the expert surgeon in the bowel running task, but much higher than the expert surgeon in the suturing task. Figure 2 shows a sample of real-time kinetic signals collected during a trial, including tool forces, tool accelerations, and platform forces.

DISCUSSION

The results clearly show disparities in skill level between intermediate and expert skill level surgeons. While our expert surgeon produced less average force overall on the porcine bowel in both tasks, the intermediate surgeon completed the bowel running task faster. Here, the expert surgeon was likely more careful in performing the task at the cost of task completion time. Conversely, the intermediate surgeon completed the suturing task much slower than the expert surgeon, possibly because of the increased complexity and difficulty of suturing compared

to bowel running. Finally, the average tool accelerations were likely the same across both participants and tasks because the participants both had a baseline level of surgical experience that precluded them from producing clearly different magnitudes of vibration with the tools, as might be the case when comparing against the performance of a surgical novice.

Improving the tissue handling skill of novice and intermediate surgeons to the level of expert surgeons will require a focus on developing their ability to visually estimate the haptic cues generated by their tool-tissue interactions (i.e., visual-haptic acuity). The data generated by our system will be vital for both assessing a trainee's visual haptic acuity as well as understanding the best way to augment it.

REFERENCES

- [1] B. Tang, G. B. Hanna, and A. Cuschieri, "Analysis of errors enacted by surgical trainees during skills training courses," *Surgery*, vol. 138, no. 1, pp. 14–20, 2005.
- [2] M. E. Hagen, J. J. Meehan, I. Inan, and P. Morel, "Visual clues act as a substitute for haptic feedback in robotic surgery," *Surgical Endoscopy and Other Interventional Techniques*, vol. 22, no. 6, pp. 1505–1508, 2008.
- [3] C. B. Barden, M. C. Specht, M. D. McCarter, J. M. Daly, and T. J. Fahey, "Effects of limited work hours on surgical training," *Journal of the American College of Surgeons*, vol. 195, no. 4, pp. 531–538, 2002.
- [4] G. Caccianiga, A. Mariani, E. De Momi, G. Cantarero, and J. D. Brown, "An Evaluation of Inanimate and Virtual Reality Training for Psychomotor Skill Development in Robot-Assisted Minimally Invasive Surgery," *IEEE Transactions on Medical Robotics and Bionics*, vol. 2, no. 2, pp. 118–129, 2020.
- [5] C. R. Wagner, N. Stylopoulos, P. G. Jackson, and R. D. Howe, "The benefit of force feedback in surgery: Examination of blunt dissection," *Presence: Teleoperators and Virtual Environments*, vol. 16, no. 3, pp. 252–262, 2007.
- [6] J. D. Brown, J. N. Fernandez, S. P. Cohen, and K. J. Kuchenbecker, "A wrist-squeezing force-feedback system for robotic surgery training," *2017 IEEE World Haptics Conference*, pp. 107–112.
- [7] S. Machaca, E. Cao, A. Chi, G. Adrales, K. J. Kuchenbecker, and J. D. Brown, "Wrist-Squeezing Force Feedback Improves Accuracy and Speed in Robotic Surgery Training," *2022 IEEE International Conference on Biomedical Robotics and Biomechatronics*, pp. 1–8.
- [8] S. Machaca, Z. Karachiwalla, N. D. Riazat, and J. D. Brown, "Towards a ROS-based Modular Multi-Modality Haptic Feedback System for Robotic Minimally Invasive Surgery Training Assessments," *2022 IEEE International Symposium on Medical Robotics*.

/ 01234356 */+,- */ / 1 /Y1 0Y101# 31 1 +647./ ROBO*0" , 45 , 356/H0123435 <-
10.31256/HSMR2023.45

Integrating a Real-time Surgical Robot Dynamic Simulator with 3D Slicer*

Hongyi Fan, Manish Sahu, Peter Kazanzides, Russell H. Taylor, Adnan Munawar

*Laboratory for Computational Sensing and Robotics (LCSR), Johns Hopkins University,
Baltimore, MD, USA
hfan15@jhu.edu*

1 INTRODUCTION

Background Medical robotics, particularly image-guided robotic systems, have revolutionized the surgical field by improving precision and accuracy. 3D Slicer(1), an open-source platform, has become a crucial tool in this field as it allows for visualization, processing, and registration of 2D and 3D medical imaging data, making it an essential component in current research in robotic intervention(2) (3). However, there is a missing component in 3D Slicer - a native physics engine for simulating the interaction of a robot with the anatomy. AMBF(4), an open-source software, was designed to address this issue by simulating the kinematics, dynamics, and interaction of complex surgical robots. By integrating 3D Slicer and AMBF using Robot Operating System (ROS), we can empower researchers to utilize both the extensive capabilities of 3D Slicer for visualization, processing, and registration of medical imaging data, and the physics-based constraint of AMBF for simulating the interaction of a robot with the anatomy. By combining these two platforms, researchers will have a comprehensive tool to study and develop projects in medical robotics, ultimately contributing to the advancement of the field.

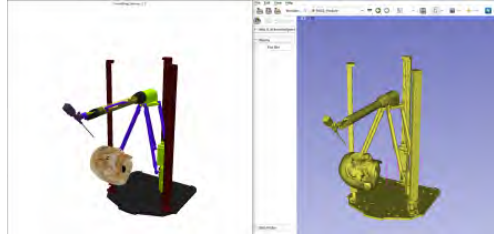


Figure 1: Simulated robotic sinus endoscopy in AMBF (left), and real-time synchronized scene in 3D Slicer (right). The physics interaction between the robot and the anatomy in AMBF will be reflected in 3D Slicer.

*https://github.com/LCSR-CIIS/3D-Slicer_ROS_Module_with_AMBF

Related Works Connolly et. al (5) have developed a module for 3D Slicer that can load a robot model in Universal Robot Description Format (URDF) and update it using ROS2 communication pipeline. Our work builds on their work but uses the original ROS platform which is still widely used in the robotics community. Additionally, our work extends the previous research by connecting 3D Slicer with the powerful dynamics simulator AMBF. This allows for more realistic simulations and testing for medical robotics research.

2 METHODS

Dependencies 1) 3D Slicer built from source, as the extension was developed within the 3D Slicer platform and a ROS node was incorporated to achieve the desired outcome. 2) ROS noetic, along with its standard packages, as the ROS communication infrastructure was used for the transmission of data between the various components. 3) AMBF and the plugin designed for the task, built from source. The AMBF plugin was utilized to construct the robot simulation and update the robot state within the 3D Slicer environment. It is important to note that these dependencies must be satisfied in order to successfully replicate the results presented in this article.

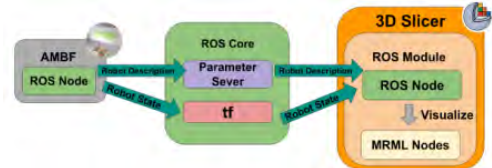


Figure 2: Higher level structure of ROS Module connected with AMBF Simulator

Robot Description Compared to Connolly et al., our project supports both URDF and a custom message structure that includes the rigid body name and mesh file path. This adaptation was necessary for the AMBF

/01234356 // /1Y 0Y101 1 20453/0123435

simulator, which handles relative poses of the rigid bodies at a lower level, and allows direct queries of the poses of rigid bodies. At the initialization stage, the simulator writes a custom message to the ROS parameter server, which our 3D Slicer extension subsequently parses to load the robot's rigid bodies.

Robot State The 3D Slicer ROS module utilizes the ROS Transformation package¹ (`tf`) to obtain the robot's state. Our AMBF simulator plugin updates each rigid body's position through `tf`, allowing the 3D Slicer's ROS module to query each rigid body's transformation in relation to the world frame and update the corresponding models within the Medical Reality Modeling Language (MRML) scene.

Synchronization In order to synchronize the 3D Slicer with the simulator, a Qt timer was implemented in the ROS module of the 3D Slicer. With a rate of 200 Hz, it triggers the 3D Slicer to spin the ROS node and update the MRML scene's robot model. This method avoids the additional computational costs of a ROS timer and eliminates the need for an extra synchronization method according to Connolly et al.

3 RESULTS

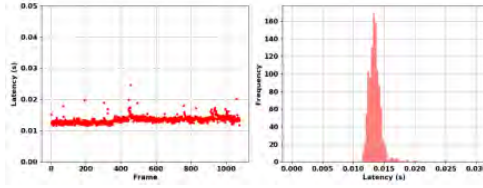


Figure 3: Latency analysis over 1078 frames

Latency Evaluation For evaluating the performance of the system, the Galen Surgical Robot model comprising 25 rigid bodies and a skull model was loaded into AMBF. The 3D Slicer ROS module was designed to update at a maximum frequency of 200Hz. The evaluation consisted of actuating the robot within AMBF, and for each update, the time difference between the timestamp of the first rigid body's `tf` transformations and the timestamp at the completion of the robot model update in 3D Slicer was recorded. We have **Mean:13.64ms**, **Median:13.40ms**, **std:4.37ms**. Since average delays in `tf` are less than 1 ms, we conclude that the source of delay is mainly from robot model updates in 3D Slicer. The statistics show that delay of the ROS module is stable at around 13ms.

Compatibility Similar to (5), the 3D Slicer ROS module is compatible with all ROS simulators as long as the simulator uses URDF for robot description and `tf` for robot state updates (e.g. RViz). In addition, the module

is specifically modified to adapt to the AMBF simulator which uses a custom message for robot description instead of URDF.

4 DISCUSSION & CONCLUSION

In this study, a ROS module for 3D Slicer was developed, incorporating a ROS node. The module has the capability to extract URDFs from the ROS parameter server, load meshes for each link, and recreate the robot within the 3D Slicer scene. The module also demonstrates real-time synchronization of robot motion when used in conjunction with simulators such as RViz. Furthermore, it has been optimized to work with AMBF, by reading the mesh file path for each link from the parameter server and updating the robot's motion based on the rigid body poses in the AMBF simulator. In conclusion, the developed ROS module serves as a crucial link between 3D Slicer and simulators, allowing for real-time synchronization of robot motion. This represents a practical contribution to the field of robotic intervention research and development that use 3D Slicer and simulators.

Future work For future work, we plan to extend our current implementation by developing a function that imports volumetric anatomy from the 3D Slicer to the AMBF simulator. This would allow us to reflect the physics interaction between the anatomy and surgical drill back to the 3D Slicer interface. The surgeons are more accustomed to the 3D Slicer interface because they can create target entry and exit points much more intuitively with 3D Slicer than with AMBF. Such workflow with 3D Slicer and AMBF can be used for interactive planning for hard tissue surgeries.

REFERENCES

- [1] S. Pieper, M. Halle, and R. Kikinis, "3d slicer," in *2004 2nd IEEE international symposium on biomedical imaging: nano to macro (IEEE Cat No. 04EX821)*, pp. 632–635, IEEE, 2004.
- [2] C. He, K. Olds, I. Iordachita, and R. Taylor, "A new ent microsurgery robot: error analysis and implementation," in *2013 IEEE International Conference on Robotics and Automation*, pp. 1221–1227, IEEE, 2013.
- [3] B. Mitchell, J. Koo, I. Iordachita, P. Kazanzides, A. Kapoor, J. Handa, G. Hager, and R. Taylor, "Development and application of a new steady-hand manipulator for retinal surgery," in *Proceedings 2007 IEEE International Conference on Robotics and Automation*, pp. 623–629, IEEE, 2007.
- [4] A. Munawar and S. F. Gregory, "An asynchronous multi-body simulation framework for real-time dynamics, haptics and learning with application to surgical robots," *IROS*, Nov 2019.
- [5] L. Connolly *et al.*, "Bridging 3D Slicer and ROS2 for image-guided robotic interventions," *Sensors*, vol. 22, 14 5336, Jul 2022.

¹<http://wiki.ros.org/tf>

A Soft Continuum Robot with Multi-Modal Shape and Contact Force Sensing for Minimally Invasive Surgery

Max McCandless, Frank Juliá Wise, and Sheila Russo

College of Engineering, Boston University
mdm1024@bu.edu, russos@bu.edu

INTRODUCTION

Minimally invasive surgery (MIS), e.g., interventional endoscopy and single-incision laparoscopy, has paved the way toward increased patient safety, fewer postoperative complications, and shorter recovery times [1]. The inherent compliant nature of soft robots makes them suitable for addressing current limitations in MIS, such as the lack of dexterity of rigid robotic devices; however, soft robots often lack adequate shape and contact sensing which makes them difficult to control [2], [3]. The future of laparoscopic surgical tools is moving toward flexible and soft robotic solutions for safer interaction with human tissue [4]. However, newly developed technologies lack effective embedded sensing [5]. This work presents a fully soft robot combining *i*) a soft optical sensorized multi-modal gripper for tip tracking and contact force sensing with *ii*) a multi-directional bending module with integrated 3D shape sensing (Fig. 1, a-b). The gripper embeds two soft pneumatic actuators to deploy the jaws, two soft pneumatic actuators to control grasping, and two fully soft optical waveguide sensors (WG) (one in each jaw) with tuned roughness to monitor both actuator tip positions and subsequent contact force on an object.

MATERIALS AND METHODS

A. Design and Fabrication: The 125 mm long, 36 mm diameter robot module and 50 mm long, 25 mm diameter gripper are fabricated using 3D printed and machined aluminum (Al) molds. Fig. 1, b shows a cross sectional view of the embedded soft optical sensor paths and highlights the roughened WG tip. We tune the response of the WGs by altering the roughness (R) of the Al molds used to fabricate them via laser micromachining. These selectively anisotropic WGs are then used to develop 3D shape sensing with a distinctly bidirectional sensor response (optical gain and optical loss in either opposite direction). The WGs consist of an optical cladding layer made with Mold Star™ 30, with refractive index $n_2 = 1.40$, and a core of Norland Optical Adhesive 73, with $n_1 = 1.56$. Light is coupled through a 1 mm diameter plastic optical fiber to emit (LED) and collect (phototransistor) the signals through the "U" shaped soft WG paths. The output power change through a sensor (P) is determined from the WG output in its base (undeformed) state (I_0) and the current measured signal (I) as: $P = 10\log_{10}(I_0/I)$, where $P > 0$ corresponds to

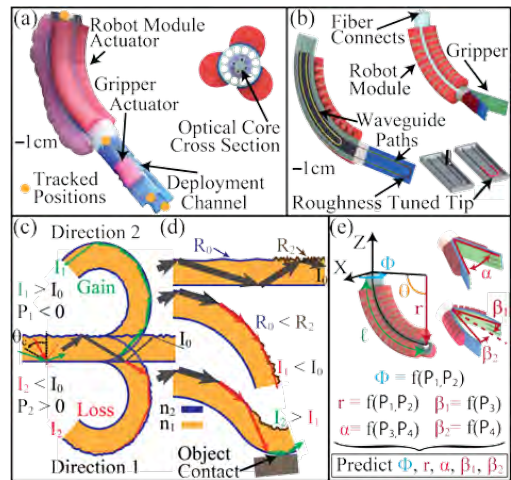


Fig. 1 Soft robot overview: a) design and tracked positions, b) fabrication, c-d) sensor physics, and e) control strategy diagrams showing mapping function parameter definitions.

optical loss and $P < 0$ corresponds to an increase in light intensity or optical gain. Upon bending, light reflecting off of the smoother side (Direction 2) creates optical gain and the rougher side (Direction 1) creates optical loss (Fig. 1, c). Three soft pneumatic actuators are integrated to steer the robot module in all directions, and constant curvature modeling is used for mapping the WG responses to the tracked positions in the workspace (Fig. 1, a). Light intensity increases due to an applied contact force on the end of a roughened sensor tip, which causes bending in the opposite direction (Fig. 1, d, bottom).

B. Experiments: Fig. 1, e, shows CAD diagrams of the shape sensing module and gripper defining the constant curvature variables (r and ϕ) and deployment (α) and bending (β_1 and β_2) gripper angles. To develop functions to track the predicted positions, the continuum robot was calibrated using an Aurora electromagnetic (EM) tracker, an Instron testing machine, and a DAQ to collect the WG output power changes of the robot module (P_1 and P_2) and gripper (P_3 and P_4) as well as the gripper actuator pressure at known positions. To validate our robot functionality in a simulated surgical scenario, we built a laparoscopic simulator. A graphical user interface (GUI) was developed in MATLAB to output the real-time shape sensing and

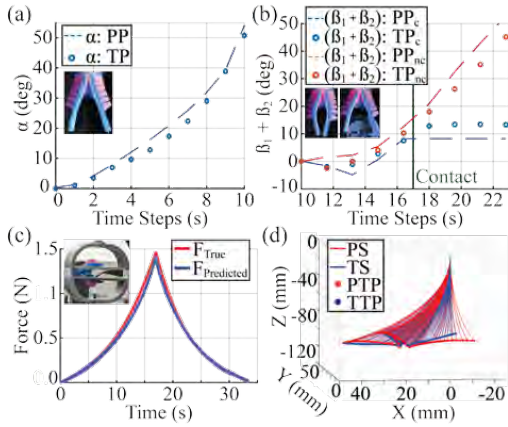


Fig. 2 Validation experiments. a-b) Comparison of predicted (PP) and true positions (TP) of the multi-modal gripper deployment and bending shape sensing with contact (c) and without contact (_{nc}). c) Force prediction accuracy test at 21 mm thickness (average difference 8.9%). d) Comparison of the predicted tip position (PTP) and shape (PS) of the robot module compared to the true tip position (TTP) and shape (TS).

contact force prediction of the system.

RESULTS

A. Shape Sensing and Contact Force Accuracy Validation: The accuracy of the calibration of the gripper deployment, bending, and contact recognition was tested and the gripper predicted and true positions are compared at subsequent steps of deployment (Fig. 2, a) and bending (Fig. 2, b) both with and without subsequent contact. The contact recognition capabilities of a single multi-modal tuned WG is validated by showing the predicted bending angle remaining constant after contact. Then, the accuracy of the force prediction of the soft gripper was tested between thicknesses of 10 mm to 21 mm to demonstrate the capability of picking up different sized objects (Fig. 2, c). Further, the shape sensing module is oriented throughout its workspace and the predicted position and shape of the module are compared to the true position of the EM tracker. The entire 3D projection of the tip position of the robot module compared to the true tip position had an average error of 3.4 mm (Fig. 2, d).

B. Peg Transfer Task: Our in-vitro test shows the ability of the robot to move in a mock laparoscopic environment and complete a peg transfer test with full shape sensing and contact force prediction relayed via the GUI. The results of the test are shown in Fig. 3 wherein the shape of the robot is tracked accurately from its base state configuration (Fig. 3, a) through moving to an object (Fig. 3, b), grasping it with force monitoring (Fig. 3, c), and releasing it in another position (Fig. 3, d-e).

DISCUSSION

Our roughness tuning fabrication approach for multi-modal soft optical sensors allows for embedding more intelligence into soft robots without requiring many sensors and can improve closed loop control of soft robots. We have shown that our soft robot can predict force

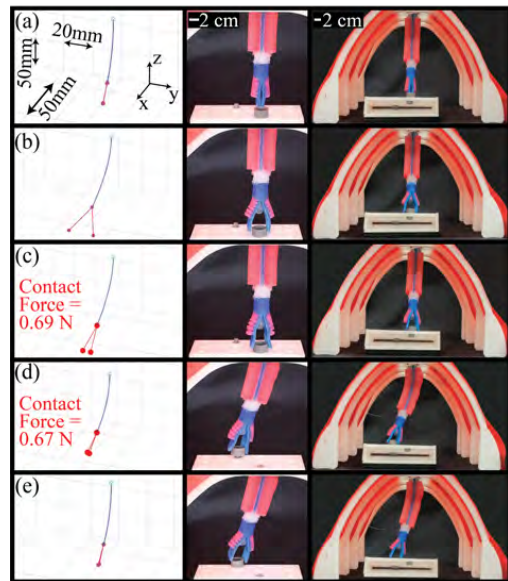


Fig. 3 Shape sensing and contact force prediction during laparoscopic peg transfer test moving from the a) base configuration to b) object position and deploying the gripper, c) grasping an object with force prediction, d) moving an object to the next peg, and e) releasing the object and returning to deployment state.

interactions with objects of varying sizes and monitor shape with minimal embedded sensors. Ultimately, this technology moves toward making MIS procedures easier for the surgeon and safer for the patient. The robot was able to demonstrate its ability to perform a peg transfer task in a mock laparoscopic environment while providing real-time shape sensing and contact force prediction to the surgeon via a GUI. Future works will focus on miniaturizing the system to fit within ports common to single-site laparoscopic procedures (i.e., 25 mm) and performing *ex-vivo* and *in-vivo* validation experiments.

ACKNOWLEDGEMENTS

Research reported in this publication was supported by the National Institute of Biomedical Imaging and Bioengineering of the NIH (award R21EB029154). The content is solely the responsibility of the authors and does not necessarily represent the official views of the NIH.

REFERENCES

- [1] S. A. Antoniou, G. A. Antoniou, A. I. Antoniou, and F. A. Grandérath, "Past, present, and future of minimally invasive abdominal surgery," *Journal of the Society of Laparoendoscopic Surgeons*, vol. 19, no. 3, 7 2015.
- [2] M. Runciman, A. Darzi, and G. P. Mylonas, "Soft Robotics in Minimally Invasive Surgery," *Soft Robotics*, 3 2019.
- [3] A. B. Dawood, J. Fras, F. Aljaber, Y. Mintz, A. Arezzo, H. Godaba, and K. Althoefer, "Fusing dexterity and perception for soft robot-assisted minimally invasive surgery: What we learnt from stiff-flop," *Applied Sciences (Switzerland)*, vol. 11, no. 14, 7 2021.
- [4] K. Kawashima, T. Kanno, and K. Tadano, "Robots in laparoscopic surgery: current and future status," *BMC Biomedical Engineering*, vol. 1, no. 1, 12 2019.
- [5] G. Rateni, M. Cianchetti, G. Ciuti, A. Menciassi, and C. Laschi, "Design and development of a soft robotic gripper for manipulation in minimally invasive surgery: a proof of concept," *Mecanica*, vol. 50, no. 11, pp. 2855–2863, 8 2015.

Soft artificial bladder with volume monitoring capabilities

Federica Semproni, Veronica Iacovacci, Sabina Maglio, Simone Onorati, Michele Ibrahimi, Arianna Menciassi

The BioRobotics Institute, Scuola Superiore Sant'Anna, Pisa, Italy
federica.semproni@santannapisa.it

INTRODUCTION

Urinary bladder cancer is the tenth most common cancer in the world with an incidence of approximately 550,000 new cases each year [1]. Non-muscle invasive tumors are locally removed with trans urethral resection or chemotherapy, while invasive tumors (30% of cases) are generally treated with the surgical removal of the entire bladder and the urethra (radical cystectomy) to avoid recurrence [2]. Following cystectomy, uretero-cutaneostomy (i.e., urine drainage from the kidneys to an external container) or neobladder reconstruction with autologous intestine are possible solutions. Although they are standard clinical procedures, they present several complications including possible onset of infections, rupture of the neobladder, tumor recurrence, as well as low patient's quality of life [3].

This scenario motivates the development of alternative solutions to restore bladder functions, i.e., urinary continence and controlled micturition. Over the years, researchers moved towards the development of fully implantable bioartificial [4] and artificial [5] bladder systems. Considering the Valsalva maneuver (i.e., abdominal torsion) as a possible voiding strategy, two functions are crucial for a complete bladder system: urine collection and fullness sensitivity. In this regard, some preliminary sensing systems have been proposed in literature. However, the solutions are closely related to specific and not bio-inspired geometries [5] or suitable only for small animals [6].

In this framework, we propose a novel biorobotic organ composed of a soft hexagonal-shaped artificial bladder (AB) coupled to a resistive textile sensors-based volume monitoring apparatus. The foldable structure of the AB together with the small thickness and flexibility of the embedded sensors make the system compact and suitable for implantation. The design and fabrication processes are here shown together with a preliminary validation of the sensorized AB.

MATERIALS AND METHODS

System Overview

The proposed system (Figure 1a) is designed to be implanted in the abdomen following radical cystectomy to replace the urinary bladder. The main module is a latex AB sized to accommodate up to 250 ml of urine (volume of the first physiological need to void [3]). The urine produced by the kidneys enters the AB through two latex inlets, to be connected to the native ureters, and it is expelled through a fluidic outlet replacing the urethra. The bladder is shaped as a hexagonal polygon, inspired

by origami, to occupy a little volume when empty, and to assume a shape similar to the natural bladder when full (i.e., spherical).

The prototyping material makes the AB walls non-stretchable, thus facilitating sensors integration. Only four walls of the AB can controllably fold to reach the closed configuration. To replace the lost proprioception system that allows to perceive the bladder fullness state, a textile sensing system has been integrated. The sensors are placed on the four foldable walls (two sensors each to follow both the cranial -near the ureters- and caudal -near the urethra- shape variations) to monitor the degree of closure/opening of the folds.

The complete system includes an implantable electronic unit to be surgically lodged in a subcutaneous pouch. To date, the electronic unit is replaced by bench-test electronics based on Arduino Mega.

Artificial Bladder Fabrication

The bladder prototype is obtained through simple fabrication steps (Figure 1b): i) twice dipping of a 3D-printed mold of the AB core (designed in SolidWorks) into an uncured latex reservoir followed by air curing (~4 hours); ii) positioning of semi-rigid acetate components (obtained by laser cutting) with bio-adhesive tape on AB walls as reinforcement; iii) twice dipping into an uncured latex container followed by air curing (~4 hours); iv) removal of the internal mold by making an incision, subsequently closed with additional latex pouring.

Sensing system

The volume monitoring system exploits the geometric features of the prototype and the unstretchability of the selected material. It is based on thin textile sensors, whose resistance changes according to their stretching. In the selected position, the extreme sides of the sensors are moved away from each other, thus stretching the central part of the sensor, as a consequence of the AB folds displacement during filling (Figure 1c). The eight rectangular sensors (10 mm x 25 mm) are obtained by laser cutting from a fabric of conductive material (Medtex P130, Shieldex). The extreme sides of the sensors (10 mm x 10 mm) are anchored to conductive wires and attached to the AB walls. The central and active area of each sensor is free to be stretched in the range 0-50% during the opening of the folds (Figure 1c). In fact, this range features a linear increase in output voltage of the sensors with their progressive lengthening. Each sensor was conditioned with a Wheatstone bridge.

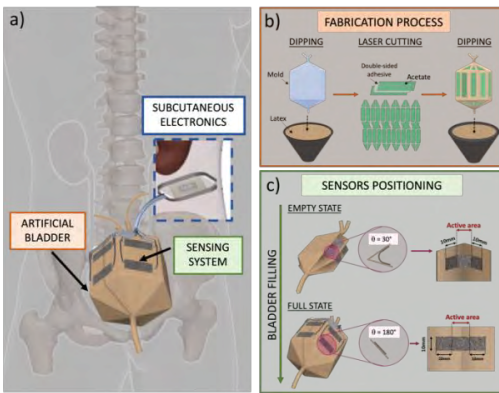


Figure 1: a) Overview of the system composed of the AB, the sensing system and the electronics; b) manufacturing process of the AB; c) positioning of the sensors on the AB.

Volume monitoring algorithm

By exploiting geometric considerations in the hexagonal-shaped prototype, the volume estimation algorithm is based on a 3D reconstruction (implemented in Matlab) of the bladder itself. Starting from the output voltage of each sensor, the percentage of elongation of the central part is derived (based on previous sensor calibration), and the opening angle of each fold (both in cranial and caudal positions) is estimated. The AB volume is obtained as the sum of a prism and two pyramids placed at the top and bottom ends. Positioning the origin of the Cartesian axes at the center of the AB, the relative positions of each edge of the polygon at the base of the prism and the pyramids are obtained starting from the opening angles of the AB folds.

In vitro validation

To evaluate the functioning of the system, filling tests (0–250 ml range) are performed by injecting water in the prototype with a motorized syringe pump (Figure 2a). At each timepoint, the output voltage of each sensor is read by an Arduino Mega and sent to a custom Labview interface. The data are subsequently imported in Matlab for volume reconstruction. The filling volume estimated by the algorithm ($V_{\text{estimated}}$) is compared with the volume injected by the syringe (V_{injected}) to observe the estimation errors made by the system. Three filling cycles are performed by positioning the prototype horizontally on the bench.

RESULTS

Figure 2b shows the relationship between V_{injected} and $V_{\text{estimated}}$. Although the algorithm is able to monitor the bladder filling, there is a tendency to underestimate the urine volume. For filling volumes below 25 ml high estimation errors are observed. However, in the filling range 25–250 ml an average estimation error of 24.55 ± 20 ml is obtained. When the bladder reaches its maximum capacity (250 ml), the algorithm estimates a maximum volume of 225.28 ml.

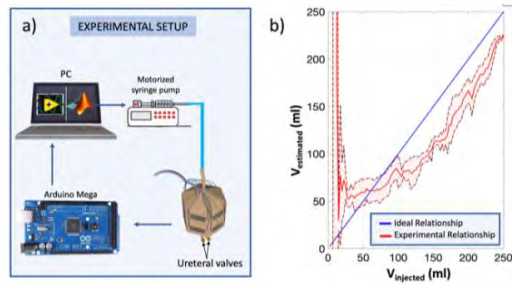


Figure 2: a) Experimental setup for the in vitro validation of the system; b) experimental (red) and ideal (blue) relation between the injected and the estimated volume.

DISCUSSION

This study reports the design of a novel implantable urinary bladder characterized by an origami-inspired hexagonal shape to enable opening/closing during filling and emptying bladder phases. The AB is combined with a sensing system for volume monitoring based on flexible and thin sensors embedded in the bladder structure. An ad-hoc algorithm exploits the output voltage values of the sensors to estimate the degree of opening of each bladder fold and reconstruct the 3D shape of the bladder. The preliminary validation of the prototype showed good performances of the system, with a tendency to underestimate the filling volumes.

The choice of a biocompatible soft material, as well as the design of miniaturized electronics will allow the authors to pave the way towards a fully implantable AB system.

ACKNOWLEDGMENT

This work was supported by INAIL, the Italian National Institute for Insurance against Work-related Injuries (non-commercial entity), within the PR19-CR-P2 BioSUP (BIOonic Solutions for Urinary impaired People) project framework.

REFERENCES

- [1] A. Richters, K. K. H. Aben, and L. A. L. M. Kiemeney, ‘The global burden of urinary bladder cancer: an update’, *World J Urol*, vol. 38, no. 8, pp. 1895–1904, Aug. 2020.
- [2] K. C. DeGeorge, H. R. Holt, and S. C. Hodges, ‘Bladder Cancer: Diagnosis and Treatment’, *Am Fam Physician*, vol. 96, no. 8, pp. 507–514, Oct. 2017.
- [3] F. Semproni, V. Iacovacci, and A. Menciassi, ‘Bladder Monitoring Systems: State of the Art and Future Perspectives’, *IEEE Access*, vol. 10, pp. 125626–125651, 2022.
- [4] A. Atala, ‘Tissue engineering of human bladder’, *British Medical Bulletin*, vol. 97, no. 1, pp. 81–104, Mar. 2011.
- [5] S. Pane, T. Mazzocchi, V. Iacovacci, L. Ricotti, and A. Menciassi, ‘Smart Implantable Artificial Bladder: An Integrated Design for Organ Replacement’, *IEEE Trans Biomed Eng*, vol. 68, no. 7, pp. 2088–2097, Jul. 2021.
- [6] A. D. Mickle *et al.*, ‘A wireless closed-loop system for optogenetic peripheral neuromodulation’, *Nature*, vol. 565, no. 7739, Art. no. 7739, Jan. 2019.

A Fluidic Actuated Soft Robot for Improving Bronchoscopic Biopsy

D. Van Lewen¹, T. Janke¹, H. Lee¹, R. Austin¹, E. Billatos², and S. Russo¹

¹*College of Engineering, Boston University*

²*School of Medicine, Boston University,
danielvl@bu.edu, russos@bu.edu*

INTRODUCTION

Lung cancer has long been one of the deadliest forms of cancer in large part due to the difficulty in diagnosis when at its earlier stages [1]. Because of their large diameter (i.e., ≈ 6 mm) preventing them from navigating in the peripheral lung, traditional bronchoscopes used in minimally invasive biopsy encounter difficulty when trying to reach smaller, deep-seated lesions [2]. Robotic solutions have been developed to address these limitations in surgical navigation. Commercial robotic bronchoscopy systems, like the Auris Monarch™ and Intuitive Ion™, consist of tendon-actuated continuum robots which focus on navigation and biopsy deeper into the lung periphery [3]. Soft robots present a promising alternative to these commercial robotic systems due to their scalability, inherent flexibility, and potential for safer interactions with biological tissue, making them well-suited for procedures in the peripheral lung [4]. Furthermore, the materials used in soft robotics are generally more economical and allow seamless integration of soft robotic actuation and sensing mechanisms. Exploration of various actuation methods, such as magnetic and fluidic, have demonstrated navigation capabilities in hard-to-reach areas of the lung and the ability to integrate useful tools, such as needles and cameras [5], [6]. However, with miniaturization, the ability of soft robots to transmit forces and interact with the surrounding biological tissue diminishes.

We propose a 3.5 mm diameter soft robot with embedded degrees of freedom (DOFs) for tip steering, tip stabilization, and needle deployment for tissue biopsy in bronchoscopy procedures (Fig. 1). Via soft actuators embedded in its continuum body, the robot can navigate through the lung branches to the target lesion and anchor itself within an anatomical channel. After anchoring, a needle may be deployed from the robot tip using an origami-inspired soft actuator to puncture the target lesion and take a biopsy. The fluidic actuated DOFs embedded in the proposed robot seek to reach deeper into the lungs, actively increase force transmission at the millimeter scale, and distally control the biopsy needle laying the framework for enhanced surgical capabilities in minimally invasive bronchoscopy procedures.

MATERIALS AND METHODS

The continuum body, seen in Fig. 2A, holds two actuation chambers, one off-center along its axis for steering and

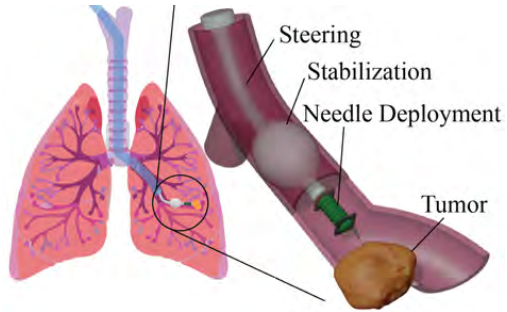


Fig. 1 The fluidic actuated soft robot with steering, stabilization, and needle deployment DOFs to take a lung biopsy.

one circumferential around its tip for stabilization via radial expansion. The tip needle deployment DOF of the robot consists of a 3 mm diameter bellows actuator with a mounted needle, as shown in Fig. 2B. The robot is fabricated using a series of molding processes for the continuum body and a heat-pressure based method for the needle deployment DOF. The base of the continuum body, made of DragonSkin 10, is molded with the axial chamber and base of the circumferential chamber. The stabilization membrane is subsequently molded using Ecoflex 00-30 to promote the radial expansion of the stabilization DOF, as seen in Fig. 2C. The axial chamber, shown pressurized in Fig. 2D, is sealed at the tip of the continuum body to complete the steering DOF. The needle deployment DOF is fabricated by the heat-pressure induced bonding of thermoplastic elastomer (TPE) (Stretchlon 200, Fiber-Glast USA) and masking of fluidic chambers via PTFE films. Each layer of TPE and PTFE is laser cut with a circular pattern and layered such that the resulting bellows are connected in series, as seen in Fig. 2B. The resulting actuator is fitted with stainless steel plates to mount a biopsy needle and fixed to the robot tip using Sil-Poxy adhesive.

RESULTS

To characterize the increase in force transmission due to stabilization, the robot was fixed in a 6 mm diameter tube and a displacement of 2 mm was applied to its tip with an ATI Nano17 force sensor. Force was measured over three repetitions for when there was no stabilization and with stabilization deployed. Force characterization of the stabilization DOF found that the effective stiffness of the

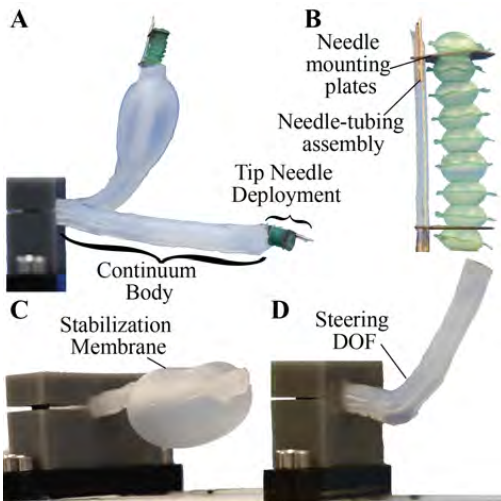


Fig. 2 A) Continuum body DOFs and needle deployment DOF in actuated and unactuated states. B) Bellows actuator for needle deployment. C) Pressurized stabilization membrane and (D) steering DOF on the continuum body.

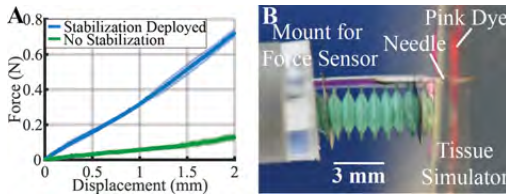


Fig. 3 Force characterization of (A) the stabilization DOF and (B) puncture with the needle deployment DOF.

tip increased by 5×, as seen in the results in Fig. 3A.

To verify the force transmission to the needle, the needle deployment DOF was mounted to the Nano17 force sensor ≈6 mm away from a tissue simulator made of 10% by weight gelatin (Knox Gelatin) and pressurized with air to 100 kPa to puncture (Fig. 3B). Two separate speeds were used to measure force. The slower speed pressurized the mechanism in 5 kPa steps up to 100 kPa over 60 seconds. The faster speed pressurized the mechanism immediately to 100 kPa within 1.75 seconds. Both speeds yielded similar results with the average recorded force necessary to puncture being 0.06 N. The measured result aligns with the previously determined force to puncture lung tissue of 0.088 N [6]. Puncture of the tissue simulator was visually confirmed by injecting pink dye, as seen in Fig. 3B.

An *in-vitro* test was performed by imitating a bronchoscopic biopsy procedure. The soft robot was inserted into a 3D printed lung model (Elastic 50A, Formlabs, USA) to demonstrate the intended surgical workflow of steering to the target (Fig. 4, A-B), stabilizing within the branch (Fig. 4, C), and deploying a needle into the tissue simulator (Fig. 4, D). Pink dye was again injected into the tissue simulator at the end of the lung model for visual confirmation of biopsy. The continuum body was dyed green for clear visualization within the lung model.

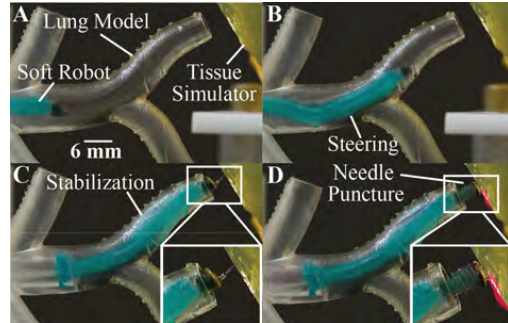


Fig. 4 In-vitro demonstrations for the fully assembled soft robot in a 3D printed lung model.

DISCUSSION

This study demonstrates the potential to give surgeon's greater control over their tools in interventional bronchoscopy by integrating multiple distal DOFs into a mm-scale soft robot. The robot actively increases tip forces during biopsy and distally controls a biopsy needle. At a 3.5 mm diameter, the robot can reach deep into the lungs with the advantages over commercial bronchoscopy systems being high flexibility, safer tissue interactions, and a needle that initiates puncture from the tip. Further, the robot can achieve these advantages due to the ability to actively increase stiffness by 5×. It uses this greater stiffness to transmit the measured 0.06 N force through the needle from its tip rather than through the body of the bronchoscope as is done in current biopsy procedures. The proposed robot can successfully steer, stabilize, and puncture within our mock anatomical setup demonstrating its ability to operate in a similarly scaled environment. Future work will also focus on ex-vivo and in-vivo animal experiments to validate the robot on biological tissue.

ACKNOWLEDGEMENTS

This work was supported by the Department of Education, GAANN Award P200A210041 and by the National Center for Advancing Translational Sciences, National Institutes of Health, through BU-CTSI Grant Number 1UL1TR001430. Its contents are solely the responsibility of the authors and do not necessarily represent the official views of the NIH.

REFERENCES

- [1] R. L. Siegel, K. D. Miller, H. E. Fuchs, and A. Jemal, "Cancer statistics, 2022," *CA: A Cancer Journal for Clinicians*, vol. 72, pp. 7–33, 1 2022.
- [2] T. J. Paradis, J. Dixon, and B. H. Tieu, "The role of bronchoscopy in the diagnosis of airway disease," *Journal of Thoracic Disease*, vol. 8, p. 3826, 2016.
- [3] A. J. Kent, K. A. Byrnes, and S. H. Chang, "State of the art: Robotic bronchoscopy," *Seminars in Thoracic and Cardiovascular Surgery*, vol. 32, pp. 1030–1035, 12 2020.
- [4] M. Runciman, A. Darzi, and G. P. Mylonas, "Soft robotics in minimally invasive surgery," *Soft Robotics*, vol. 6, pp. 423–443, 8 2019.
- [5] G. Pittiglio, P. Lloyd, T. da Veiga, O. Onaizah, C. Pompili, J. H. Chandler, and P. Valdastri, "Patient-specific magnetic catheters for atraumatic autonomous endoscopy," *Soft Robotics*, 3 2022.
- [6] M. McCandless, A. Perry, N. DiFilippo, A. Carroll, E. Billatos, and S. Russo, "A soft robot for peripheral lung cancer diagnosis and therapy," *Soft Robotics*, vol. 9, pp. 754–766, 8 2022.

Soft Robotic Pneumatic Actuators Assist Diaphragmatic Dysfunction in a Respiratory Simulator

D. Quevedo-Moreno¹, J. Tagoe¹, E.T. Roche^{1,2*}

¹ Department of Mechanical Engineering, Massachusetts Institute of Technology

² Institute for Medical Engineering and Science, Massachusetts Institute of Technology

*etr@mit.edu

INTRODUCTION

The diaphragm is a critical muscle for the respiratory system, responsible for up to 70% of the inspiration effort. Phrenic nerve trauma or neuromuscular disease can generate severe diaphragm dysfunction that ultimately leads to respiratory failure [1]. The current treatment for patients with severe diaphragm dysfunction is permanent airway tethering to mechanical ventilation, which greatly impacts patient's quality of life and autonomy by hindering activities like speech, swallowing, and mobility. Soft robots are ideal to assist in complex biological functions like the contraction of the diaphragm. Diaphragmatic mechanical assistance using implantable soft robots has shown promising results in restoring respiratory function [2]. However, the design of the soft robotic actuator can be optimized to effectively assist the diaphragm. Here, we present a soft robotic pneumatic actuator that inverts its curvature to efficiently displace the diaphragm and assist in the inspiratory effort, restoring physiological thoracic and abdominal pressurization levels. Moreover, we show how the respiratory simulator can replicate clinically relevant pleural pressure (P_{pl}) and abdominal pressure (P_{ab}), demonstrating its potential as a platform to validate this technology.

MATERIALS AND METHODS

The soft robotic actuators used in this work are composed of a thermoplastic polyurethane (TPU) and an inextensible nylon woven fabric. By increasing pressurization, the TPU stretches, while the fabric acts as the strain-limiting component, constraining linear expansion and generating bending motion. If both ends of the actuator are constrained vertically then a displacement (Δd) at the middle of the actuator is generated (Fig. 1 A). To determine how much displacement the actuator is generating, when it is pressurized, a finite element model was developed and validated experimentally (Fig. 1 B).

A modified version of a respiratory simulator, described in [3], is used as a benchtop model to replicate the motion and function of the diaphragm. Tendon are attached to an elastomeric diaphragm-like layer and pulled-down with the rotation of a DC motor (GB37-150, Pololu Corp.). High fidelity motion of the diaphragm is achieved by using positional closed-loop control of the motor.

The elastomeric diaphragm divides two acrylic airtight chambers that represent the thoracic and abdominal

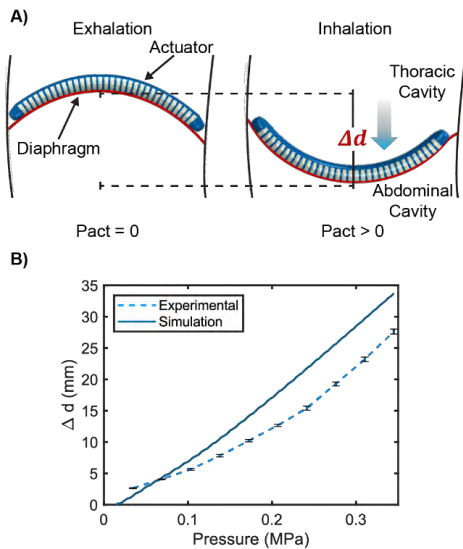


Fig. 1 Soft robotic pneumatic actuator for diaphragmatic assistance. A) Schematic of the soft robotic pneumatic actuators assisting the diaphragm. P_{act} denotes the input pressure to the actuator. At exhalation (left), the actuator input pressure is zero. B) Displacement (Δd) over different pressurization levels (P_{act}) for finite element simulation (solid line) and experimental validation (dashed line), error bars are mean +/- standard deviation.

cavities (Fig. 2). The cavities are instrumented with pressure transducers (PRESS-S-000, PendoTech) and pressures are recorded using a PowerLab System. Diaphragm dysfunction is simulated by reducing the rotational displacement of the motor by 50%, with 100% being the baseline. Rotational displacement for baseline condition is manually adjusted to replicate physiologic pleural pressure (P_{pl}) ranges from -3 to -5 cmH₂O [3]. Transdiaphragmatic pressure (P_{di}) is a metric for diaphragmatic function and is expressed as the difference between the abdominal pressure and the pleural pressure ($P_{di} = P_{ab} - P_{pl}$) [4]. The assisted condition is simulated by pressurizing the soft actuators while maintaining the dysfunction condition (50% of rotational displacement). The pneumatic soft actuators are pressurized using a custom electropneumatic control system previously described in [2]. The nominal peak pressure for the input waveform was 0.35 MPa. A respiratory rate of 12 breaths

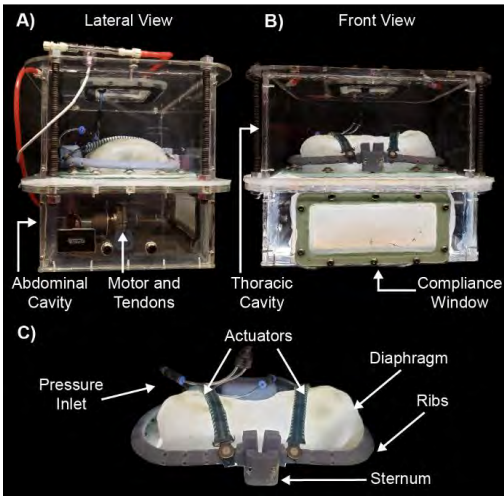


Fig. 2 Respiratory Simulator. A) Lateral view of the respiratory simulator. B) Front view of the simulator. C) Close-up view to the diaphragm section.

per minute is simulated for 10 consecutive respiratory cycles for each condition (baseline, dysfunction and assisted). One-way ANOVA and Tukey's Honestly Significant Difference (HSD) were used to evaluate significance between conditions.

RESULTS

The respiratory simulator presented in this work is able to replicate clinically relevant respiratory pressure waveforms for baseline and dysfunction conditions (Fig. 3). Baseline average P_{di} is 6.22cmH₂O, for diaphragmatic dysfunction, P_{di} is reduced to an average of 3.78cmH₂O. In the assisted condition, the soft robotic actuator is capable of restoring or even augmenting P_{di} from the dysfunction condition to an average of 7.19 cmH₂O (Fig. 4).

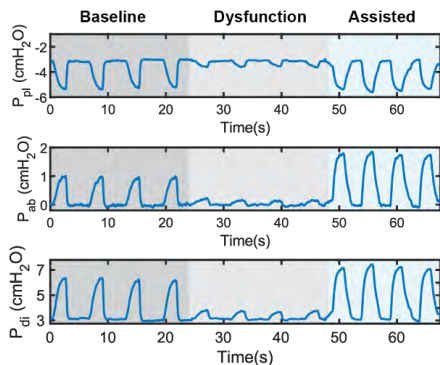


Fig. 3 Respiratory Pressure Waveforms. Representative Pleural pressure (P_{pl}), abdominal pressure (P_{ab}) and transdiaphragmatic pressure (P_{di}) waveforms for baseline (dark grey), dysfunction (light grey) and assisted (light blue).

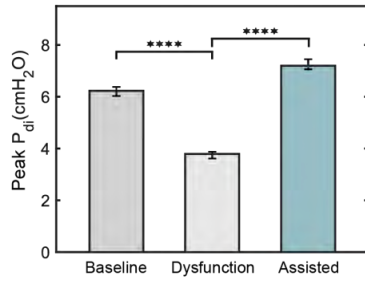


Fig. 4 Peak Transdiaphragmatic Pressures. Ten consecutive respiratory cycles for each condition. **** denotes $p<0.0001$. Error bars are +/- maximum and minimum peak values.

DISCUSSION

The results indicate that the simulator can be used to: 1) replicate diaphragmatic function and physiological pressurization levels; 2) simulate diaphragmatic dysfunction by changing the rotational displacement generated by the motor; and 3) mimic the effect of diaphragmatic mechanical assistance. Moreover, the soft robotic pneumatic actuators are able to produce substantial augmentation of the transdiaphragmatic pressure from the dysfunction condition, showing their capability to assist diaphragmatic dysfunction.

Future work includes evaluation of the diaphragmatic displacement as well as the actuators' performance for different abdominal compliances. Moreover, additional characterization of the positioning and durability of the actuators is required to further optimize the performance of the mechanical assistance. For the soft robotic system, future work involves synchronized actuation and closed-loop feedback control of the actuator.

ACKNOWLEDGEMENTS

This work was supported by the grant R21-EB02841401A1 from the National Institutes of Health (NIH) National Institute of Biomedical Imaging and Bioengineering (NIBIB).

REFERENCES

- [1] D. O. Hutchinson and K. Whyte, "Neuromuscular disease and respiratory failure," *Practical Neurology*, vol. 8, no. 4, pp. 229–237, Aug. 2008. doi: 10.1136/pn.2008.152611.
- [2] L. Hu *et al.*, "An implantable soft robotic ventilator augments inspiration in a pig model of respiratory insufficiency," *Nat Biomed Eng*, 2022, doi: 10.1038/s41551-022-00971-6.
- [3] M. A. Horvath *et al.*, "An organosynthetic soft robotic respiratory simulator," *APL Bioeng*, vol. 4, no. 2, 2020, doi: 10.1063/1.5140760.
- [4] L. Brochard, "Transdiaphragmatic Pressure," in *Pulmonary Function in Mechanically Ventilated Patients*, S. Benito and A. Net, Eds. Berlin, Heidelberg: Springer Berlin Heidelberg, 1991, pp. 52–61. doi: 10.1007/978-3-642-84209-2_5.

Computational Predictive Model for Full Body Controlled Soft Continuum Magnetic Robots under Hybrid Actuation

Kiana Abolfathi¹, James H. Chandler², Keyoumars Ashkan³, Luca Citi¹, Pietro Valdastri² and Ali Kafash Hoshiar¹

¹School of Computer Science and Electronic Engineering, University of Essex, Colchester, UK

²STORM Lab, Institute of Autonomous Systems and Sensing, School of Electronic and Electrical Engineering, University of Leeds, Leeds, UK

³Department of Neurosurgery, King's College Hospital, London, UK

a.kafashhoshiar@essex.ac.uk

INTRODUCTION

In recent years, medical microrobots have emerged as a non-invasive solution to many medical interventions [1, 2]. Soft continuum magnetic robots (SCMRs), a class of soft robots, were introduced as a promising method for endovascular intervention [1]. The small scale, adaptability, flexibility, and high controllability of SCMRs made them well suited for the clinical applications.

The SCMRs originally introduced for endovascular intervention [1, 3], however, utilised rigid permanent magnets within their structure, increasing the risk of vascular trauma during deployment. Therefore, fully soft continuum magnetic robots (FSCMRs), made of magneto-responsive soft material, were introduced to improve their clinical implementation [4].

Imparting a lengthwise magnetisation profile into FSCMRs, full body shape forming is possible under application of homogeneous magnetic fields, improving conformation to anatomical structures. Shapes have been predicted for homogeneous electromagnet (EM) generated fields using computational models [5], and through permanent magnet (PM) actuation with mathematical models [6]. However, the whole-body modelling of FSCMRs under actuation via combinations of PM- and EM-generated fields has not been explored.

The presented study introduces a computational model to capture FSCMR shape-forming via independent and

simultaneous PM (up to two) and EM actuation. The accuracy of this model is validated with the experimental data.

EXPERIMENT SETUP

The experimental setup consists of three main parts (shown in Fig. 1): (1) an EM external magnetic field generator (MFG100 system), two robotic arms (DoBot Magician), camera (Basler, puA1280-54um) and a computer for monitoring; (2) FSCMRs with a diameter of 600 μm and length of 25 mm; and (3) a 3D-printed 120 mm square test bed and FSCMR holder, arranged to align its centre with the centre of FSCMR and the EM field generator, and 3D-printed holders to host the PMs and attach to the robotic arms.

SIMULATION

COMSOL Multiphysics (V. 6) software was used for computational modelling of the FSCMR within inhomogeneous magnetic fields, using the mechanical properties introduced in [5]. Simulated magnetic fields were produced to match three distinct actuation scenarios: (i) one PM; (ii) two PMs; and (iii) hybrid system consisting of one PM and the EM system. For each scenario a range of actuation parameters were tested, varying the PM position and direction, and EM field magnitude and direction.

VERIFICATION

The experimental range bounded the PM movement from 20 mm to 45 mm (x direction) with 5 mm steps and from -45 to 45 (y direction) with 5 mm steps and covered the three scenarios introduced above. Each scenario and parameter combination were simulated using the computational model and replicated experimentally, with the FSCMR in an aqueous environment. Image processing (MATLAB, MathWorks, USA) was used to extract FSCMR shapes from the experimental and computational data for comparison. To assess the

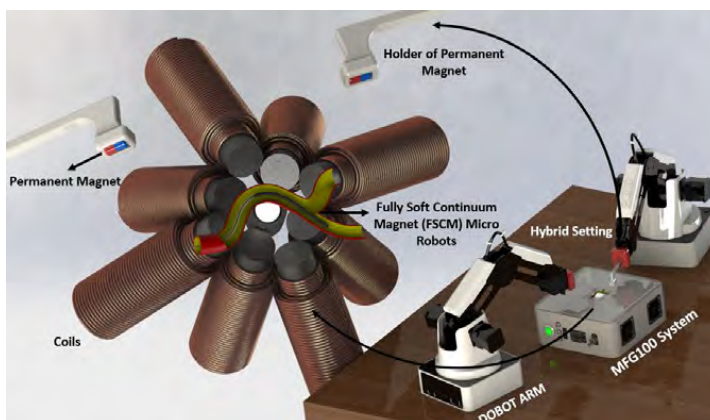


Fig. 1: Conceptual figure of the systems for full body control of the FSCMs.

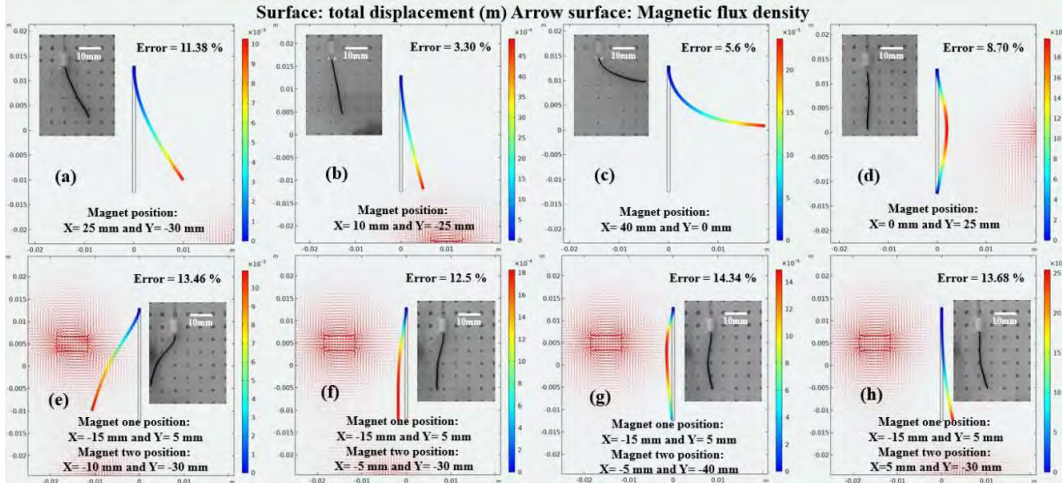


Fig. 2: Simulation and experimental shapes of the FSCMRs in different conditions. The tip position error of FSCMs between experiment and simulation are showed in each image. (a), (b), and (c) One PM with a pull effect; (d) one PM with a pull effect and electromagnet with a magnitude of 3 mT; (e), (f), (g), and (h) two PMs with a pull and push effect.

suitability and accuracy of the proposed numerical platform, two parameters were considered: (1) the shape classification of the FSCMR, and (2) the tip position of the FSCMR. Shape classification was evaluated based on attainment (through polynomial fitting) of one of eight independent shape categories, identified from the range of experimental data (as illustrated in Fig. 2). Tip position accuracy was calculated as 89.63 % ($e = \frac{r_{exp} - r_{sim}}{r_{exp}}$, where index exp and sim indicate experiment and sin shows the simulation results, and r is the tip vector of the FCSMs that is $\sqrt{x^2 - y^2}$).

Fig. 2 shows comparisons for eight body shape categories, with tip deformation errors ranging from 3.3% to 14.34%. In scenario one (one PM), 20 permanent magnet positions were studied, resulting in 85% similarity in shape classification with a 5.34% tip position deviation. In scenario two (two PMs), 15 different positions with three different effects were tested, resulting in 82.5% shape similarity with an 11.61% tip position deviation. In the hybrid (PM-EM) implementations, shape classification had similar results in all cases, with an average tip position deviation of 12%. Although the error level in predicting the tip position of the soft robot may seem high in some cases, it is considered an acceptable error since it does not result in any physical contact between the robot's tip and the boundary of the vessel.

DISCUSSION AND CONCLUSION

A computational model has been proposed in this academic paper for predicting the shape of a soft robot under different actuation scenarios using the COMSOL software. The accuracy of the platform has been assessed through experimental data, and the results indicate that the model has an acceptable accuracy in predicting the shapes and tip positions of FSCMRs under a hybrid

actuation system. Although there were some discrepancies between the predicted and experimental data, the errors were deemed acceptable as they did not result in collisions with the vessel wall. Overall, the proposed computational model can be used as a predictive tool for designing or guiding soft magnetic robots under more versatile hybrid actuation scenarios, while preventing them from contacting hypothetical boundary constraints.

REFERENCES

- [1] S. Jeon *et al.*, "A magnetically controlled soft microrobot steering a guidewire in a three-dimensional phantom vascular network," *Soft robotics*, vol. 6, no. 1, pp. 54-68, 2019.
- [2] A. Moghanizadeh, H. Khaksar, and A. Hoshiar, "A novel non-invasive intervention for removing occlusions from shunts using an abrading magnetic microswarm," *IEEE Transactions on Biomedical Engineering*, 2022.
- [3] A. Kafash Hoshiar, S. Jeon, K. Kim, S. Lee, J.-y. Kim, and H. Choi, "Steering algorithm for a flexible microrobot to enhance guidewire control in a coronary angioplasty application," *Micromachines*, vol. 9, no. 12, p. 617, 2018.
- [4] Y. Kim, G. A. Parada, S. Liu, and X. Zhao, "Ferromagnetic soft continuum robots," *Science Robotics*, vol. 4, no. 33, p. eaax7329, 2019.
- [5] P. Lloyd *et al.*, "A learnt approach for the design of magnetically actuated shape forming soft tentacle robots," *IEEE Robotics and Automation Letters*, vol. 5, no. 3, pp. 3937-3944, 2020.
- [6] G. Pittiglio *et al.*, "Patient-specific magnetic catheters for atraumatic autonomous endoscopy," *Soft Robotics*, vol. 9, no. 6, pp. 1120-1133, 2022.

A Soft Laparoscopic Grasper for Retraction of the Small Intestine

L. Kinnicutt¹, J. Lee¹, J. Oden¹, L.T. Gaeta¹, S.K. Carroll¹, A. Rathi¹,
Z.H. Lim¹, M. Lee¹, C. Orakwue¹, K.J. McDonald¹, D. Hess², T. Ranzani¹

¹ Boston University College of Engineering, Boston, MA, USA

²Boston Medical Center, Boston, MA, USA

lkinni@bu.edu, tranzani@bu.edu

INTRODUCTION

Laparoscopy can improve outcomes and patient recovery times compared to open surgery. However, the minimally-invasive nature of these procedures deprives clinicians of tactile feedback which, when coupled with pinching graspers that deliver high-stress concentrations, increases the likelihood of inflicting iatrogenic trauma upon tissues, especially the small intestine [1]–[4].

Retraction of the small intestine is often necessary to visualize and access nearby tissues [5], [6]. Commercially-available devices rely on passive structures to hold intestinal segments and do not embed compliance [7]. Prior research on surgical retractors has focused on granular jamming [5], pneumatic balloons [6], and either cable-driven [8] or vacuum [9] graspers. However, these devices are challenging to integrate into surgical workflows, require auxiliary instruments, and do not provide feedback regarding tissue interaction forces.

We introduce a laparoscopic grasper capable of passing through an 18 mm trocar, expanding to a controllable width once inside the abdominal cavity, and safely enveloping the small intestine to enable retraction. Upon entry into the abdominal cavity, the grasper establishes an initial hold on a target intestinal segment by pulling vacuum through the suction unit on its distal tip (Fig. 1[a]); this functionality helps the surgeon isolate the target intestinal segment from surrounding bundles. Once a preliminary suction hold has been established, the grasper envelopes the intestine by inflating a pair of pneumatic fiber-reinforced soft actuators (FRSAs) (Fig. 1[b]–[c]), whose separation can be modulated up to 40 mm using a miniaturized scissor lift mechanism (MSLM). This approach distributes the force necessary to grasp and hold the intestine over a large surface area (i.e., the whole surface of the FRSAs) rather than concentrating it in a small region, allowing safe, robust grasps even on dilated intestinal segments. Inflation of the FRSAs and suction are controlled using two buttons (Fig. 1 [d]). The horizontal position of the FRSAs and the separation between them are independently actuated via two linear motors, which the surgeon controls using a rocker switch and trigger, respectively (Fig. 1 [d]). Each actuator is equipped with two soft sensors to interpret 3D interaction forces via a machine learning algorithm.

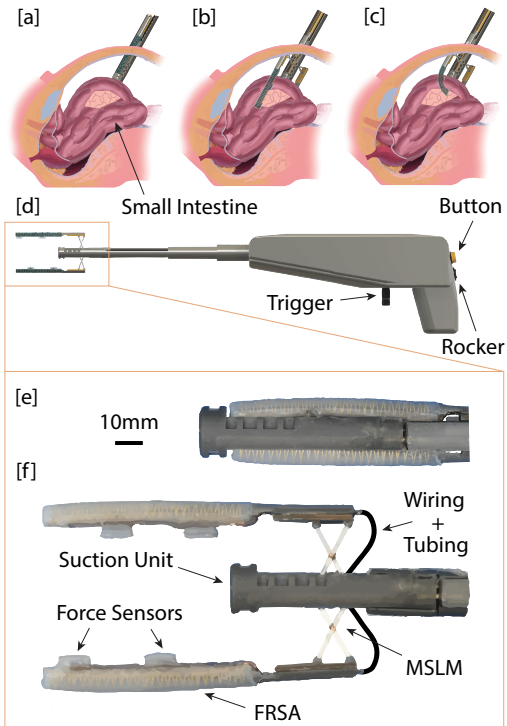


Fig. 1 [a] Activation of suction, [b] deployment of FRSAs, and [c] envelopment of intestine. [d] Complete grasper in [e] closed and [f] deployed configurations.

MATERIALS AND METHODS

The FRSAs are fabricated using Dragonskin 20 (Smooth-On), and are 70 mm in length with a semicircular cross-section of diameter 8 mm. The FRSAs are biased to perform a bending motion when pressurized due to a strain-limiting layer of Muslin fabric and Kevlar fiber wrappings (McMaster-Carr). One end is sealed with additional Dragonskin 20, and a custom pneumatic interface composed of Grey v4 Resin (Formlabs) is partially inserted into the open end for structural rigidity.

The FRSA are deployed via the MSLM, which can adjust the separation of the actuators anywhere between the closed configuration (Fig. 1[e]) and 40 mm (Fig. 1[f]), sufficient to envelop both healthy and pathologically dilated segments of the small intestine [10].

Each FRSA is equipped with a pair of soft magnetometric sensors (see Fig. 1[f]) to monitor tissue-tool interaction forces during grasping. The soft force sensors consist of a triple-axis magnetometer (Melexis) and a 1.6 mm diameter, 0.8 mm thick N52 NdFeB magnet (K&J Magnetics) embedded in Ecoflex 00-50 (Smooth-On). The sensors transduce a 3D force input into a nonlinear, coupled 3D magnetic field vector output. A TensorFlow dense neural network (DNN) with three hidden layers was used to interpret sensor calibration data, given its simplicity, accuracy, and microcontroller compatibility. Electrical signals are routed using a printed circuit board (PCB) that conforms to the FRSA curvature. This flexible PCB consists of alternating layers of spin-coated Ecoflex 00-10 silicone (Smooth-On) and 500 μm -thick laser-cut copper traces (McMaster-Carr).

The stroke of the FRSA was determined using an electromagnetic tracking system (Northern Digital Inc., Aurora), and the forces generated at their tips were obtained via a blocked force test using a NANO17 6-axis force transducer (ATI Industrial Automation Inc.). The soft sensors were calibrated using the NANO17 and a U5e Universal Robot, and the ability of the grasper end-effector to hold a tissue sample was assessed using standard weights and an explanted porcine small intestine.

RESULTS

Results of the FRSA stroke and force tests are reported in Fig. 2[a-b]. The FRSA bend with radius ≈ 22 mm, and exert >2.5 N at their tip. When pressurized to 250 kPa, the grasper end-effector can hold 500 g (Fig. 2[c]), and retract an explanted porcine small intestine (Fig. 2[d]). The DNN uses an 80% training - 20% validation data split and 100 epochs to interpret soft sensor calibration data; the forces recorded by the NANO17 are plotted against the DNN-predicted values in (Fig. 2[e]-[g]). The maximum mean absolute error was found to be 0.16 N in a normal force range of 0–10 N and a shear force range of 0–2 N.

DISCUSSION

We introduce a laparoscopic grasper capable of retracting the small intestine via atraumatic envelopment. The utilization of inherently compliant FRSA, accompanied by a deployable MSLM and an array of soft sensors capable of transducing 3D forces, enable the proposed device to manipulate intestinal segments safely. Future work will focus on *in-vitro* testing using abdominal phantoms and evaluating grasping of simulated dilated intestines.

ACKNOWLEDGMENTS

The work was supported by the DoE GAANN Award P200A210041 and the NCATS, NIH, Boston University CTSI Grant Number 1UL1TR001430. Its contents are solely the responsibility of the authors and do not necessarily represent the official views of the NIH.

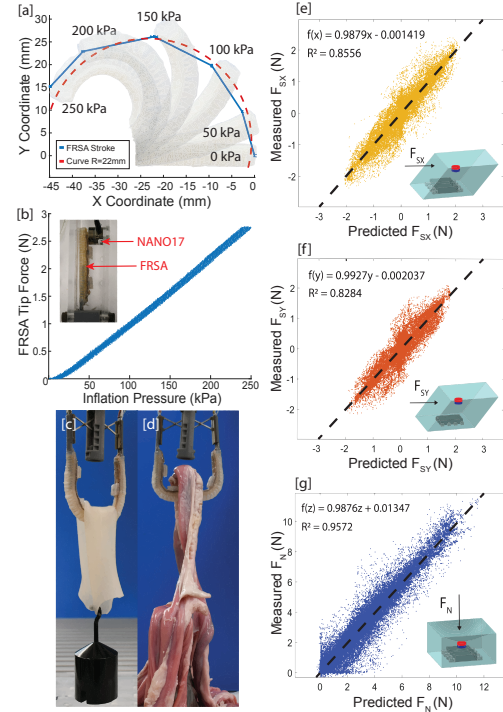


Fig. 2 Plots of FRSA tip [a] position and [b] force during inflation. [c] Grasper holding 500 g silicone tube and [d] explanted porcine small intestine. Measured vs DNN-predicted [e] X shear (F_{SX}), [f] Y shear (F_{SY}), and [g] normal (F_N) forces applied to sensors, with best fit lines.

REFERENCES

- [1] S. De *et al.*, “Assessment of tissue damage due to mechanical stresses,” *Int J Rob Res*, vol. 26, no. 11-12, pp. 1159–1171, 2007.
- [2] A. F. Khan *et al.*, “Defining the relationship between compressive stress and tissue trauma during laparoscopic surgery using human large intestine,” *IEEE J. Transl. Eng. Health Med.*, vol. 7, pp. 1–8, 2019.
- [3] E. Heijndijk *et al.*, “Inter-and intraindividual variabilities of perforation forces of human and pig bowel tissue,” *Surg. Endosc.*, vol. 17, pp. 1923–1926, 2003.
- [4] M. Van der Voort *et al.*, “Bowel injury as a complication of laparoscopy,” *Br J Surg*, vol. 91, no. 10, pp. 1253–1258, 2004.
- [5] A. Cavallo *et al.*, “A soft retraction system for surgery based on ferromagnetic materials and granular jamming,” *Soft Robot.*, vol. 6, no. 2, pp. 161–173, 2019.
- [6] C. O’Shea *et al.*, “Design, development and evaluation of an inflatable retractor for atraumatic retraction in laparoscopic colectomy,” *Ann Biomed Eng*, vol. 42, pp. 1942–1951, 2014.
- [7] N. Ladwa *et al.*, “Retraction techniques in laparoscopic colorectal surgery: a literature-based review,” *Colorectal Dis*, vol. 15, no. 8, pp. 936–943, 2013.
- [8] J. Gafford *et al.*, “Shape deposition manufacturing of a soft, atraumatic, and deployable surgical grasper,” *Journal of Mechanisms and Robotics*, vol. 7, no. 2, p. 021006, 2015.
- [9] D. Vonck *et al.*, “Vacuum grasping as a manipulation technique for minimally invasive surgery,” *Surg. Endosc.*, vol. 24, pp. 2418–2423, 2010.
- [10] S. Jacobs *et al.*, “Small bowel faeces sign in patients without small bowel obstruction,” *Clin Radiol*, vol. 62, no. 4, pp. 353–357, 2007.

A Pop-Up Soft Robot Driven by Hydraulic Folded Actuators for Minimally Invasive Surgery

Jianlin Yang¹, Mark Runciman², James Avery², Zhijun Sun¹, George Mylonas²

¹*State Key Laboratory of Mechanics and Control of Mechanical Structures,*

Nanjing University of Aeronautics and Astronautics, Nanjing, China,

²*Hamlyn Centre, Imperial College London, London, UK*

yangjianlin@nuaa.edu.cn

INTRODUCTION

The incidence rate of colorectal cancer ranks third among all cancers, which is a serious threat to human health [1]. Endoscopic submucosal dissection (ESD) is an effective endoscopic surgical method for early gastric and colorectal cancers [2]. However, ESD is a procedure with high technical requirements, which brings a higher risk of complications and requires long training for clinicians [3].

Robots are expected to simplify ESD procedures and reduce training time. But there is no standard flexible robotic endoscope at present. Soft robots can potentially offer better adaptability and safer interaction with the environment. As such, they hold great potential in solving the technical challenges of the current minimally invasive surgery (MIS), which are difficult to be solved by rigid robots.

Here we demonstrate an inflatable robot which is largely made of flexible plastic film. In the deflated state, it is easy to collapse, fold and roll into a small size, promising easier delivery by a carrier endoscope to the proximal colon. After reaching the target site, the robot is inflated and the surgery is performed. This work is based on the inflatable Cyclops robot [4][5]. However, small folded hydraulic actuators are used to replace the contraction-based pouch actuators used in [5], which have a larger size. The anchor points of the cables with planar layout replace the spatial layout in [4], which reduces the axial size of the robot, allowing it to pass through the colon bends more easily. Folded actuators made of an airbag are flexible and adaptable [6]. The actuator volume is very small under deflated condition, but it can achieve large deformation after inflation. The proposed actuator uses a folded chamber to pull the cable to produce a large displacement without the need of displacement amplification mechanisms. In the deflated state, the length of soft scaffold of the robot is about 65mm, and the overall size of the robot is 100mm × 6mm × 20mm. In the state of inflation, the soft scaffold deploys into a hexagonal prism with a length of 55mm, and the bottom side length of the prism is 30mm. The tip workspace of the robot can reach 40mm in all three directions of the local coordinate system.

MATERIALS AND METHODS

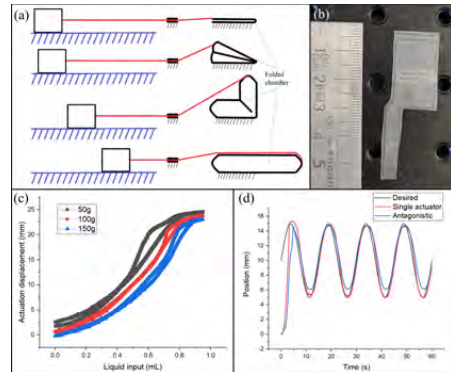


Fig. 1 Test of the hydraulic folded actuator. (a) Working principle of the folded actuator. (b) An actuator manufactured by laser welding. (c) Relationship between liquid input in the actuator and actuation displacement under different payloads. (d) Single actuator control and antagonistic control results.

Figure 1(a) shows the working principle of the actuator. Initially shown is a folded chamber with no liquid or gas in it. One end of the chamber is connected to a cable through a small hole, which then connects to a slider. When the chamber is inflated, the folded chamber will deploy and pull the slider to move. When the chamber is fully deployed, the displacement of the slider is nearly equal to the length of the chamber. Figure 1(b) shows a fabricated actuator, which is made of plastic film laser welded as shown in [4]. The length of the inflatable part of the actuator is 25mm and the width is 15mm. Due to the incompressibility of liquid, a hydraulic actuator can be open-loop controlled. Here we use tape water as hydraulic media. The cable is connected to a slider with a retroreflective marker. The cable displacement is measured by tracking the position of the marker. Figure 1(c) shows the relationship between the cable displacement and the liquid input in the actuator. To make the cable reciprocate, weights are hung on the cable via a pulley. The displacement of the actuator almost reaches the length of the chamber. When the

actuator is in a large displacement, the hysteresis decreases as the payload increases. This is because when the payload is small, the chamber has a certain stiffness. Even if it is not completely filled with liquid, it still has some stiffness and is not easily folded. The mathematical expression of the plot is obtained by curve fitting, which can be used for position control of the actuator. Figure 1(d) shows the position tracking results of a single actuator and of a pair of actuators in antagonistic mode. When the payload is 100g, the tracking accuracy for single actuator is high. In this case, the accuracy may decrease if the payload is unknown. In the antagonistic mode, the cable tension between two actuators is unknown, so tracking accuracy decreases.

RESULTS

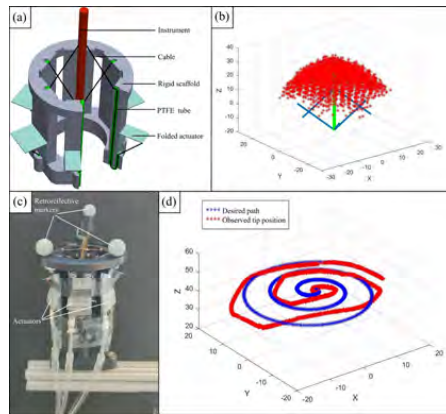


Fig. 2 6-cable parallel robot test. (a) 3-D model of the robot (actuators mounted outside). (b) Workspace of the robot. (c) Path scanning experiment setup. (d) Result of path scanning experiment.

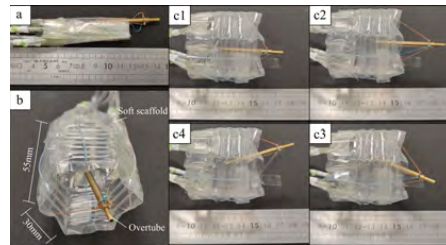


Fig. 3 Deployment and use of the pop-up robot. (a) Robot in folded state. (b) Front view of the deployed robot (actuators mounted inside). (c1-c4) Side view of the deployed robot. The overtube has different poses.

Figure 2(a) shows a parallel robot driven by 6 cables, including a rigid scaffold, six proposed actuators and a cylindrical instrument. The cables are connected to the instrument through PTFE tubes in the rigid scaffold.

Figure 2(b) shows the workspace of the robot, in which the cable displacement limit is considered. Figure 2(c) shows the test setup. Three retroreflective markers are fixed on the scaffold and one marker is fixed at the tip of instrument. Positions of the markers are tracked by an optical motion tracking system. Figure 2(d) shows the result of scanning a spatial spiral path.

A robot with a soft inflatable scaffold was also built. The folded actuators were welded inside the soft scaffold which was previously developed in [4]. This robot version is a monolithic device as the scaffold and actuators are included in a single piece. Figures 3(a) and (b) show the folded and unfolded states of the robot. In the folded state, the deflated robot is folded and rolled around the instrument. Figures 3(c1-c4) show different poses of the actuated instrument.

DISCUSSION

The proposed robot can realize 5-DOF motion of the Cyclops robot in [4]. This means that the pitch and yaw angle of the instrument can be adjusted when its tip is fixed on a certain position. In the soft robot system, 6 folded hydraulic actuators are mounted in a confined space, but they do not collide with each other when working as the actuators are small enough. This robot is going to be used in phantom studies. Being a cable-driven parallel robot, antagonistic actuation is required, which somewhat reduces the achieved open-loop tracking precision. This is due to cable friction and variable cable tension. The second reason may be that the two folded parts of the chamber do not perform the ideal movement when folding and unfolding as shown in figure 1(a). For example, the crease sometimes does not appear in the desired position. In future work, in-built sensors can be applied to help measure or estimate the cable tension to improve the actuator and robot control accuracy.

REFERENCES

- [1] F. Bray, et al., "Global cancer statistics 2018: GLOBOCAN estimates of incidence and mortality worldwide for 36 cancers in 185 countries," *Cancer J. Clin.*, vol. 68, pp. 394–424, 2018.
- [2] T. Oyama, et al., "Endoscopic submucosal dissection of early esophageal cancer," *Clin. Gastroenterol. Hepatol.*, vol. 3, no. 7, pp. S67–S70, 2005.
- [3] A. Y. B. Teoh, et al., "Difficulties and outcomes in starting endoscopic submucosal dissection," *Surgical Endosc.*, vol. 24, no. 5, pp. 1049–1054, 2010.
- [4] M. Runciman, J. Avery, M. Zhao, A. Darzi, and G. P. Mylonas, "Deployable, Variable Stiffness, Cable Driven Robot for Minimally Invasive Surgery," *Frontiers in Robotics and AI*, vol. 6, 2020.
- [5] M. Runciman, J. Avery, A. Darzi, and G. Mylonas, "Open Loop Position Control of Soft Hydraulic Actuators for Minimally Invasive Surgery," *Applied Sciences*, vol. 11, no. 16, 2021.
- [6] C. T. O'Neill, C. M. McCann, C. J. Hohimer, K. Bertoldi, and C. J. Walsh, "Unfolding Textile-Based Pneumatic Actuators for Wearable Applications," *Soft Robotics*, pp. 163–172, 2022.

Development of an Untethered Inflatable Capsule Robot for Stricture Dilation - a Preliminary Study

K. Esendag¹, M. E. McAlindon², S. Miyashita^{1,3,4}, and D. D. Damian^{1,3,4}

¹*Automatic Control and Systems Engineering Department, University of Sheffield, UK*

²*Royal Hallamshire Hospital, Sheffield Teaching Hospitals NHS Foundation Trust, UK*

³*Insigneo Institute for in silico Medicine, University of Sheffield, UK*

⁴*Sheffield Robotics, University of Sheffield, UK*

kesendag1@sheffield.ac.uk, d.damian@sheffield.ac.uk

INTRODUCTION

Capsule robots have the potential to provide untethered access to the gastrointestinal tract and perform simple tasks that could reduce invasiveness and provide a better alternative method of access than an endoscopy or colonoscopy. Current state-of-the-art for capsule robots already fulfil the need for inspection, but there is a gap that exists between the capabilities of current capsule robots when compared with those of endoscopic surgical robots [1]. For example, strictures occurring throughout the gastrointestinal tract due to inflammation or Crohn's disease needs a source of pressure to break the strained organ and unblock the stenosis. Additionally, access to the distal parts of the small intestine remains difficult even for Endoscopic Balloon Dilation (EBD). A capsule robot with an actuator that can provide volumetric expansion could fulfil both of these needs, i.e., opening the lumen at a stricture site, anchoring for surgical procedures in difficult-to-access GI areas. This paper presents a capsule robot prototype, of 14 mm diameter and 28 mm length, with a soft internal actuator capable of providing wireless volumetric expansion as seen in Fig. 1. The inflation of the capsule is based on the chemical reaction between NaHCO_3 and $\text{C}_6\text{H}_8\text{O}_7$, which releases carbon dioxide (CO_2) gas. The inflation of the internal actuator is wirelessly controlled through magnetic induction which generates thermal energy. The capsule also deflates over time due to the CO_2 being slowly reabsorbed into water as carbonic acid (H_2CO_3). Mechanisms that can provide wireless expansion, such as using a wireless electronic module with a pump to inflate and deflate a balloon, using liquid-to-gas transition of chemicals as the source of expansion, or using chemical reactions that release gas as a source of pressure have been previously presented [2]–[4]. However, the method of actuation should not require operating at temperatures that can cause permanent tissue damage [5]. In the current work the generated thermal energy is below limits of hyperthermia [5].

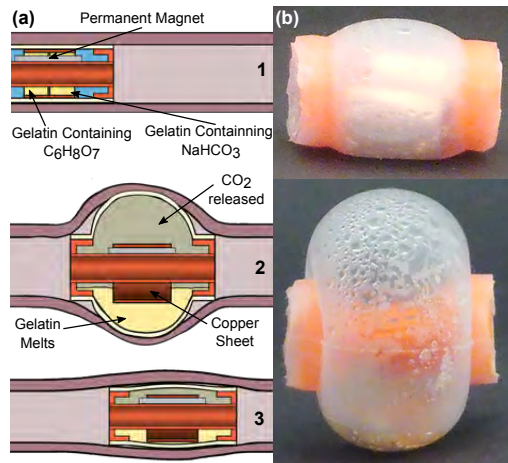


Fig. 1 (a) Drawings showing a cross-section view of the robotic capsule dilating a section of the intestine and then deflating. (b) Images of the capsule before and after inflation.

The chemicals and the dissolution medium used are all safe for ingestion, making them suitable for gastrointestinal applications, and the capsule design provides a novel and promising alternative for ballooning operations without using electronics or a battery.

MATERIALS AND METHODS

The capsule has a rigid hollow core which is encapsulated by a soft membrane. The rigid core, made of PLA, limits the longitudinal expansion of the soft membrane so that the capsule only expands radially against the walls of the intestine. The hollow structure of the capsule allows the passage of food through the GI lumen. A neodymium magnet of $12.7 \times 3.2 \times 1.5$ mm length, width and height respectively, is attached on the rigid body for navigation. The reactants are stored separately in solid rings of gelatin,

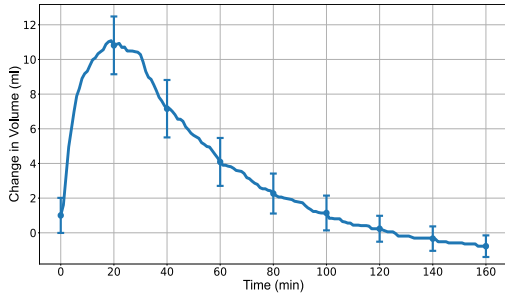


Fig. 2 Expansion and deflation of the capsule showcased over 160 minutes, with 30 minutes of heating time at the start. The plot shows the mean expansion of 5 trials with standard deviation.

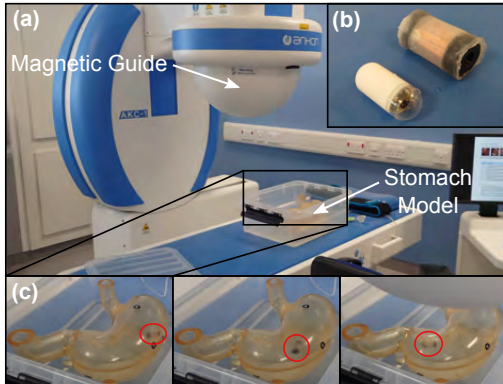


Fig. 3 (a) The capsule navigation was tested with an Ankon AKC-1. (b) Ankon's imaging capsule (left) next to our capsule robot (right). (c) Close-up of the capsule being navigated through a stomach model used for training (sequence from left to right).

acting as the dissolution medium which ensures that they do not mix without thermal input. For the fabrication of citric acid gelatin rings, 170 mg of gelatin, 384 mg of water, and 92 mg of $C_6H_8O_7$ were used. For bicarbonate gelatin rings 102 mg of gelatin, 460 mg of water, and 110 mg of $NaHCO_3$ were used. The capsule is filled with 2 ml. A 0.1 mm thick copper sheet is wrapped around the rings which acts as the thermal energy receiving medium. The magnetic fields are provided by a low power induction system producing 5 mT magnetic field alternating at 27 kHz, which heats up the copper sheet inside the capsule [6]. The soft membrane that forms the ballooning body that interfaces with the tissue is made out of Ecoflex 00-30 (Smooth On Inc.).

The inflation and deflation capacity of the capsule was tested on a benchtop setup in which the capsule was submerged in a beaker of warm water starting at 36 °C. Inflation was measured using video tracking the water displaced in the beaker over time, and the temperature was monitored using a thermocouple.

RESULTS

The dilation profile of the capsule, measured across five trials, is shown in Fig. 2. The heat was applied in the first 30 minutes of the experiment, where the temperature outside the capsule, and in the proximity of its expanding walls, reached a maximum of 42.5 °C, which is below the limits of cell hyperthermia [5]. The actuation pattern shows a repeatable behavior of the inflation mechanism, with a maximum standard deviation of 1.67 and minimum of 0.62. The largest deviation in volume from the trends shown in Fig. 2 is at 20 minutes when the capsule reaches its maximum volume ranging from 9.14 to 12.46 ml. From the footage of one of the trials, the axial diameter at its maximum point has increased from 14 mm to 22.5 mm, which corresponds to a %66 increase. The navigation of the capsule was tested successfully using the lab-built electromagnetic coil [6], as well as with an Ankon AKC-1 inside a stomach model. Here we show the latter performance, as shown in Fig. 3 [7].

DISCUSSION

In this paper, an untethered inflatable capsule robot was presented for stricture dilation or tissue anchoring. The design and control of the capsule can be deemed safe for in vivo applications given that: the method used for internal actuation has low risk of harming the patient, the chemicals the actuation is based on is safe for ingestion in the case of a burst, and the capsule has shown repeatable actuation behavior across trials. A limitation of the current actuation approach is that the current chemical reaction is not reversible, thus the inflation cannot be repeated. Future work will look at controlling the inflation/deflation capability of the capsule to fit within the typical duration of a dilation procedure used for the Chron's disease, by regulating the reactants dosage and the heat input. Further miniaturisation is also envisaged as a next step.

REFERENCES

- [1] M. F. Hale, R. Sidhu, and M. E. McAlindon, "Capsule endoscopy: current practice and future directions," *World journal of gastroenterology*, vol. 20, no. 24, pp. 7752–7759, Jun 2014.
- [2] L. Yan, T. Wang, D. Liu, J. Peng, Z. Jiao, and C.-Y. Chen, "Capsule robot for obesity treatment with wireless powering and communication," *IEEE Transactions on Industrial Electronics*, vol. 62, no. 2, pp. 1125–1133, 2015.
- [3] S. M. Mirvakili, D. Sim, I. W. Hunter, and R. Langer, "Actuation of untethered pneumatic artificial muscles and soft robots using magnetically induced liquid-to-gas phase transitions," *Science Robotics*, vol. 5, no. 41, 2020.
- [4] M. Adami and A. Seibel, "On-board pneumatic pressure generation methods for soft robotics applications," *Actuators*, vol. 8, no. 1, 2019.
- [5] A. E. Deatsch and B. A. Evans, "Heating efficiency in magnetic nanoparticle hyperthermia," *Journal of Magnetism and Magnetic Materials*, vol. 354, pp. 163–172, 2014.
- [6] J. Liu, X. Chen, Q. Lahondes, K. Esenadag, D. Damian, and S. Miyashita, "Origami robot self-folding by magnetic induction," in *2022 IEEE/RSJ International Conference on Intelligent Robots and Systems (IROS)*, 2022, pp. 2519–2525.
- [7] H.-L. Ching, M. F. Hale, and M. E. McAlindon, "Current and future role of magnetically assisted gastric capsule endoscopy in the upper gastrointestinal tract," *Therapeutic Advances in Gastroenterology*, vol. 9, no. 3, pp. 313–321, 2016.

Proof of Concept of a Novel Growing Soft Robot for Colonoscopy

C. Tutcu¹, S. K. Talas¹, O. Kocaturk², N. Tozun³, and E. Samur^{1*}

¹*Department of Mechanical Engineering, Bogazici University, Turkey*

²*Institute of Biomedical Engineering, Bogazici University, Turkey*

³*Department of Gastroenterology, Acibadem Mehmet Ali Aydinlar University, Turkey*

*evren.samur@boun.edu.tr

INTRODUCTION

Colonoscopy is considered to be the gold standard for the detection of colorectal polyps and other colonic disease. In this study, a novel growing soft-continuum robot is presented as a proof of concept for a potential colonoscopy application. Compared to the state-of-the-art systems such as the ColonoSight system [1] using an inflated balloon attached over the colonoscope shaft, or Neoguide [2] actuated via electromechanical actuators, the proposed architecture utilizes the advantage of pneumatic propulsion as well as allowing control in three degrees of freedom. The growing robot concept pushes the end effector from the tip and prevents loss in propulsion force at the tip that results a lower mechanical forcing on the colon. Since the actuation is performed pneumatically and controlled via electromechanical interface, there is no need for users to apply high forces for pushing/pulling to progress and maneuver the robot.

MATERIALS AND METHODS

The robotic system is first introduced in the literature by Altinsoy et al. for a possible medical application [3]. The system actuated via three pressurized tubes that are connected to a pinch roller mechanism that generates propulsion force [4]. Three actuation mechanisms located circumferentially on the end effector that allows robot to follow 3-dimensional paths similar to the colon geometry. The robotic colonoscopy system is separated into two modules as the *in-vivo* section that is to be inserted into the colon including the end effector and colonoscope shaft named as the robot body (Fig. 1), and the *in-vitro* section named as the control hub including the servo motors, spools, and valves. Models are developed as a force model of the actuation mechanism, and continuum robot kinematics and statics in order to design particular features of the robot such as pinch roller dimensions, and to be used in the robot control [5]. A prototype of the robotic system is manufactured as a proof of concept (Dia: 40 mm) which has scale-up dimensions of a conventional colonoscope (Dia: 15 mm). Reaction force between the robot body and a maze wall is measured on the test setup shown in Fig. 2. The maze diameter is selected such that the ratio of maze diameter to robot shaft diameter is similar to the ratio

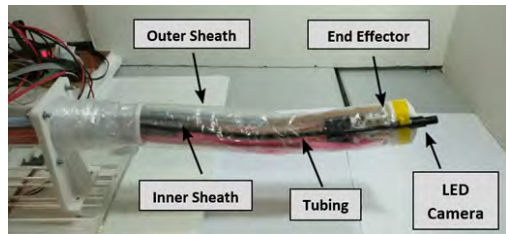


Fig. 1 *In-vivo* section of the proposed robotic system and its main features.

of a conventional colonoscope and the sigmoid colon diameters. The maze is attached to a platform that is allowed to slide in y, and z directions via marble spheres placed under the platform. A load cell (ATI Nano 17 force/torque sensor) that has capability to measure forces and moments in 6 degrees of freedom is attached to the right edge of the platform. As the robot progressed through the maze, reaction forces in three directions are measured, and the resultant reaction force is calculated.

RESULTS

The reaction force between the robot body and the maze wall is measured as the robot advances to the goal point at the end of the maze (see Fig. 3). Peaks on the plot is numbered based on the change in anchoring point of the body and end effector-wall contact points shown in

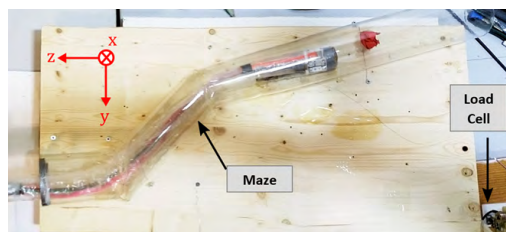


Fig. 2 Test setup for wall reaction measurement. Top view of the test setup. Reaction forces are measured with the 6-DOF load sensor located at the right bottom corner.

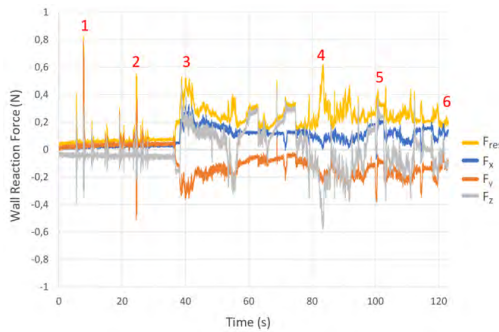


Fig. 3 Reaction force measurements through the motion of robot in the maze.

Fig. 4. Maximum reaction force is measured as 0.82 N at point 1 which is at the entrance of the maze. Reaction forces vary with the change in contact points and generates a continuous contact force starting from point 3 with an average value of 0.35 N. The average speed of the robot is calculated as 5.5 mm/s.

DISCUSSION

The system presented in this study provides improved locomotion for a possible colonoscopy application as a growing type soft robot. As the major difference from the conventional colonoscopy, propulsion is applied from the tip that facilitates more stable locomotion and low reaction forces. The maximum wall reaction force during the conventional colonoscopy is measured as 16.1 N by Korman et al. [6] while the minimum perforation force is reported by Johnson et al. is 14.08 ± 2.18 N [7]. The proposed robotic system has considerably low wall reaction force (0.87 N maximum, 0.35 N continuous) when compared to the minimum perforation limit that is proved for the safe operation. The proposed system has second to best average speed with 5.5 mm/s comparing to the caecal intubation speeds of similar systems reported as 2.8 mm/s for Invendoscope [8], and 5.7 mm/s for Aer-O-Scope [9]. Navigation capability of the robot is proved with the experiments for essential maneuvers required for colonoscopy and given in detail by Talas et al. [10]. The control interface used in this study is an off-the-shelf haptic device (Omega 6, Force Dimension) that is used for medical applications.

The proposed robotic approach is addressing the future colonoscopy competencies by mitigating patient pain and discomfort, reducing operation related complications, and improve colonoscopist ergonomics during operation. In addition to these competencies, the proposed system has potential to have a disposable body since the costly electromechanic actuators and steering systems are placed at the *in-vitro* section. A disposable colonoscope body has advantage of removing the infection risk that may be a strong criterion for preferring the system. Future works will be to add a force sensor to measure tip reactions in order to generate haptic feedback, and to validate the

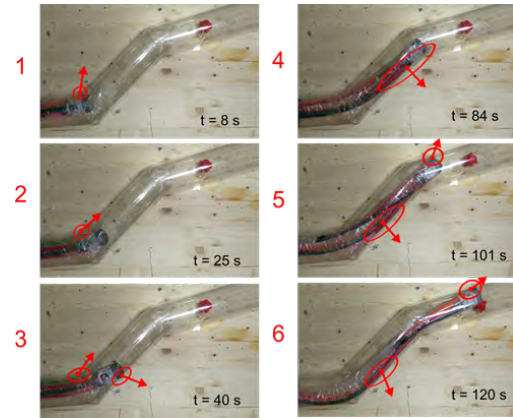


Fig. 4 Captions from the motion that correlates with peaks in the force measurements.

concept at the real scale using medical colon models or conducting pre-clinical experiments.

ACKNOWLEDGEMENT

This project is supported by the Scientific and Technological Research Council of Turkey (TUBITAK 115E717).

REFERENCES

- [1] M. Shike, Z. Fireman, R. Eliakim, O. Segol, A. Sloyer, L. B. Cohen, S. Goldfarb-Albak, and A. Repici, "Sightline colonoscopy system for a disposable, power-assisted, non-fiber-optic colonoscopy," *Gastrointestinal Endoscopy*, vol. 68, no. 4, pp. 701–710, 2008.
- [2] A. Eickhoff and et al., "Computer-assisted colonoscopy (the neoguide endoscopy system): Results of the first human clinical trial ("pace study")," *The American journal of gastroenterology*, vol. 102, pp. 261–6, 03 2007.
- [3] T. Altinsoy, B. A. Baydere, S. K. Talas, O. M. Erkan, C. Tutcu, and E. Samur, "Design of an Extensible Colonoscopy Robot," in *Hamlyn Symposium on Medical Robotics*, 2018, pp. 25–26.
- [4] B. A. Baydere, S. K. Talas, and E. Samur, "A novel highly-extensible 2-dof pneumatic actuator for soft robotic applications," *Sensors and Actuators A: Physical*, vol. 281, pp. 84–94, 2018.
- [5] C. Tutcu, B. A. Baydere, S. K. Talas, and E. Samur, "Quasi-static modeling of a novel growing soft-continuum robot," *The International Journal of Robotics Research*, vol. 40, no. 1, pp. 86–98, 2021.
- [6] L. Y. Korman, V. Egorov, S. Tsuryupa, B. Corbin, M. Anderson, N. Sarvazyan, and A. Sarvazyan, "Characterization of forces applied by endoscopists during colonoscopy by using a wireless colonoscopy force monitor," *Gastrointestinal Endoscopy*, vol. 71, no. 2, pp. 327–334, 2010.
- [7] S. Johnson and et al., "How much force is required to perforate a colon during colonoscopy? an experimental study," *Journal of the Mechanical Behavior of Biomedical Materials*, vol. 91, pp. 139–148, 2019.
- [8] T. Rösch, A. Adler, H. Pohl, E. Wettschureck, M. Koch, B. Wiedenmann, and N. Hoepffner, "A motor-driven single-use colonoscope controlled with a hand-held device: a feasibility study in volunteers," *Gastrointestinal Endoscopy*, vol. 67, no. 7, pp. 1139–1146, 2008.
- [9] B. Vučelic, D. Rex, R. Pulanic, J. Pfefer, I. Hrštic, B. Levin, Z. Halpern, and N. Arber, "The aer-o-scope: Proof of concept of a pneumatic, skill-independent, self-propelling, self-navigating colonoscope," *Gastroenterology*, vol. 130, pp. 672–7, 04 2006.
- [10] S. K. Talas, B. A. Baydere, T. Altinsoy, C. Tutcu, and E. Samur, "Design and development of a growing pneumatic soft robot," *Soft Robotics*, vol. 7, pp. 521–533, 2020.

Scalable and Spatially Selective Actuation of Living Microrobots

N. Mirkhani, T. Gwisai, M. Christiansen, S. Schuerle

ETH Zurich, D-HEST

simone.schuerle@hest.ethz.ch

INTRODUCTION

In drug delivery, one key challenge is to minimize off-target accumulation in healthy regions, which can lead to toxicity or other associated complications. To address this challenge, drug delivery platforms can be designed either to localize the accumulation of active compounds to the target site or to selectively activate the portion that arrives in the targeted tissue. In the case of living bacterial therapeutics or bacteria-based biohybrid microrobots, bacteria can be equipped with onboard sensing, aiding their preferred accumulation in target regions such as tumors [1]. Nevertheless, robust tumor colonization by bacteria is still limited by low administrable doses and biological barriers that permit only a small portion to reach a target site after intravenous administration.

Therefore, strategies that provide a means to target external energy to bacteria in a spatially selective manner can offer a much-needed element for enhanced targeting of living therapeutics [2]. Magnetotactic bacteria (MTB) are a group of bacteria noted for their intrinsic responsiveness to magnetic fields, and have been investigated as a drug carriers and potential living therapeutics. We previously demonstrated the possibility for enhancing tumor colonization using a scalable magnetic torque-based control approach employing a homogenous rotational magnetic field [3]. Here, we increase the spatial selectivity of this technique by employing a magnetostatic selection field that suppresses off target torque-based actuation.

MATERIALS AND METHODS

Mammalian and bacterial cell culture

Human breast cancer cells (MCF-7) were cultured in high glucose Dulbecco's Modified Eagle's Medium (DMEM, ThermoFischer) supplemented with 10% FBS and 1% P/S. Ultralow adhesion plates (InSphere) were utilized to form tumor spheroids from MCF-7 cell line. Seeding density of 10,000 cells/well in 50 μ L of growth media was used in 96 well plates. The well plates were centrifuged at 500 \times g for 10 min followed by incubation at 37 °C with 5% CO₂. Size of the tumor spheroids reached ~400 μ m after 3 days. DNA staining with Hoechst 33342 at a final concentration of 5 μ g/mL in media was performed before the experiment for one hour at 37°C. To stain the bacteria and be able to track subsequent generations, 2 μ L of the far-red proliferative dye was added to 1 mL of bacteria suspension at 5 \times 10⁸

cells/mL. Following 20 min of agitation on a shaker while protected from light, the dye was deactivated using 100 μ L of DMEM for 10 min. The bacteria were spun down and resuspended in 1 mL DMEM for the actuation experiments.

Experimental setup

For the application of a homogenous RMF, an 8-coil magnetic micromanipulation setup integrated in an inverted microscope (MFG-100-I, Magnebotix AG) was used. A static gating magnetic field was superimposed by introducing permanent magnets in the experimental chambers made from PDMS and consisting of a target well in the center and four off-target wells in the North, South, West and East (see more details of setup in [3]). Wells were rinsed with ethanol, air dried, and then exposed to UV for an hour for sterilization. A field of 20 mT and 14 Hz was applied for 1 hour, after which the spheroids were collected from the wells, washed thoroughly with media, and then incubated in well plates at 37 °C and 5% CO₂ for 24 hours.

Imaging and readout

Spheroids were transferred into the PDMS rings after 24 hours and imaged with taking 200 μ m high z-stacks in 10 μ m intervals. To quantify the accumulation of bacteria in tumor spheroids, ROI was defined as the outer edge of the spheroid in binarized z-projected image in the DAPI channel. Far-red signal was then integrated throughout the resulting ROI at all planes to measure the fluorescence intensity which is correlated with the number of bacteria colonizing the spheroid.

RESULTS AND DISCUSSION

Here, we report on a method for tumor targeted, spatially selective controlling of magnetically responsive living microrobots, specifically the bacterium MTB, using a combination of a magnetostatic and rotating magnetic field. To test the method, we use MCF-7 to form spheroids about 400 μ m in diameter, which are placed in five different (target in center and off wells with MTB suspensions within a workspace of 1.5 cm x 1.5 cm (**Fig. 1**).

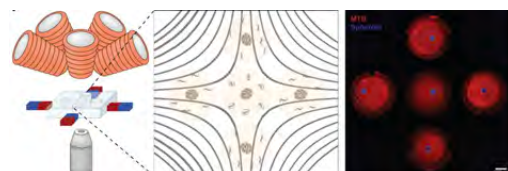


Fig. 1 Sketch of setup, wells with spheroids (blue), MTB (red)

To ensure that the MTB are properly controlled by the magnetostatic selection field, we measure their translational velocity in response to a 12 mT rotating magnetic field at 14 Hz and a gating field from small magnets. We find that this combination of fields suppresses torque-driven motion of the MTB. We also test a stronger magnetostatic field and find that it improves the suppression of off-target movement but reduces the extent of actuation within the target well due to higher overall suppression.

Because the spheroids present additional barriers to successful penetration by the MTB, we expose the samples to an RMF of 20 mT at 14 Hz for one hour to account for the added resistance of the cancer cells. A sweeping RMF was applied where the rotation vector is sweeping through a full sphere of 360°C and compared to a constant RMF where the rotation vector remains its pose.

The results of the experiment presented in **Figure 2** show that exposing the spheroids to RMF leads to a 2.3 fold increase in accumulation of stained bacteria compared to the control. Additionally, MTB colonization of the target spheroids is not affected by the magnetostatic selection field, resulting in an approximately 3-fold increase in accumulation compared to the control. However, at off-target sites, a significantly lower accumulation is observed in the presence of a superimposed gating field, which is due to field gradients being prevalent in the

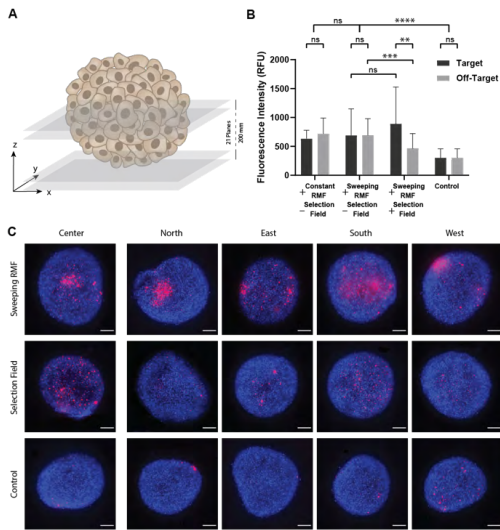


Fig. 2 Selective accumulation of the bacteria in the target spheroid. A) Schematic of a spheroid and the focal planes used for confocal imaging and quantification. B) Accumulation of bacteria in tumor spheroids at different locations under various actuation schemes. C) Confocal microscopy images of the spheroids exposed to different actuation conditions.

miniaturized system. Although stronger static fields lead to complete suppression of off-target transport, the associated field gradients cause forces that act against transport to the target. However, this effect is less relevant in larger targeting areas with lower field gradients. The proposed control strategy's scalability and selectivity make it an essential step towards the clinical translation of magnetically based delivery strategies.

Accordingly, we used the gained insights to design a larger scale setup for selective magnetic actuation in mice, as illustrated in **Figure 3**. The static gating field is produced with a partial “magic sphere” [4] and a DC coil is integrated to move the zero field point radially, thereby allowing to adjusting the target position.

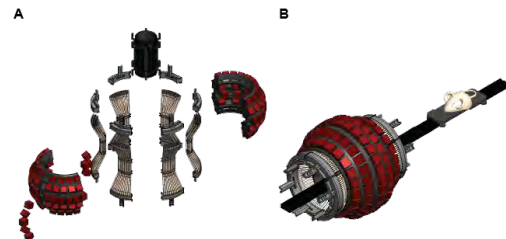


Fig. 3 Schematics of the final assembly of the animal scale selection field setup. The setup consists of an array of permanent magnets as the outer most layer, an AC coil in the center, and a DC coil in between. A) Exploded view of the assembled prototype. B) Envisioned track and slider for mouse positioning inside the setup.

CONCLUSION

We demonstrate that spatially selective actuation of living microrobots is feasible in 3D tumor models through the addition of a static gating magnetic field, effectively suppressing actuation in off target regions. Based on these results, a prototype for *in vivo* studies has been proposed which is currently tested. We suggest that using efficient torque-based actuation under selection fields at human scales could pave the way for development of practical magnetically assisted delivery strategies in clinical applications.

REFERENCES

- [1] Zhou, Shabin, et al. "Tumour-targeting bacteria engineered to fight cancer." *Nature Reviews Cancer* 18.12 (2018): 727-743.
- [2] Mirkhani, Nima, Tinotenda Gwisai, and Simone Schuerle. "Engineering Cell-Based Systems for Smart Cancer Therapy." *Advanced Intelligent Systems* 4.1 (2022): 2100134.
- [3] Gwisai, Tinotenda, et al. "Magnetic torque-driven living microrobots for increased tumor infiltration." *Science Robotics* 7.71 (2022): eab0665.
- [4] H. A. Leupold, A. Tilak, E. Potenziani, Permanent magnet spheres: Design, construction, and application. *J. Appl. Phys.* 87, 4730–4734 (2000).

Real-Time Cognitive Workload States Recognition from Ultra Short-Term ECG Signals on Trainee Surgeons Using 1D Convolutional Neural Networks

Kaizhe Jin^{*1,2}, Ravi Naik^{*1,2}, Adrian Rubio-Solis^{1,2}, and George Mylonas^{1,2}

¹ Department of Surgery and Cancer, Imperial College London, UK.

² Hamlyn Centre for Robotic Surgery, Imperial College London

k.jin20@imperial.ac.uk

INTRODUCTION

Surgery is a mentally demanding task that is focused on patient safety and requires the precise execution of motor control and decision making in a timely manner. Episodes of high Cognitive Workload (CWL) induced by stressors or distractions have been shown to lead to inferior performance potentially compromising patient safety [1]. We have proposed a promising CWL assessment platform utilising a wide range of physiological sensors [2]. However, there are some disadvantages associated with a complex multimodal sensing design, including high device cost, long set up time and the discomfort caused by wearing multiple wearable sensors for long periods during surgery. To address this problem, the proposed one-dimensional convolutional neural network (1D-CNN) model discussed here, offers an alternative solution to recognising CWL states, achieving satisfactory performance (91.3% accuracy) with the use of a wireless ECG sensor alone, showing great potential for widespread deployment in the operating room (OR).

MATERIALS AND METHODS

A. Experiment Protocol

Twenty surgical trainees were asked to undertake laparoscopic peg transfer (LPT) from the FLS curriculum, whilst undertaking a cognitive task (N-back test) of varying difficulty. The N-back test is a task used in cognitive neuroscience to measure working memory. Participants performed a control task with no N-back task as well as an N0, N1 and N2-back task in randomised order. To measure the objective CWL, all surgical trainees were equipped with eye-tracking glasses (Pupil Core, Pupil Labs, Berlin) and ECG sensors (Shimmer3 ECG unit, Shimmer Sensing Inc., Netherlands) while undertaking the above task. Subjective workload measures were recorded using a questionnaire called the Surgery Task Load Index (SURG-TLX), a validated tool used in surgery to measure CWL. Figure 1 shows a participant wearing an ECG sensor and eye tracker performing the proposed experiment in the simulated OR at St. Mary's Hospital.



Fig. 1 A participant wearing an ECG sensor and eye tracker performing the proposed experiment in the simulated OR at St. Mary's Hospital.

B. ECG Data Modelling

One-dimensional Convolutional Neural Networks demonstrate state-of-the-art performance in signal modelling applications including EEG signals, communications, health monitoring, anomaly detection, and motor fault detection [3]. In this study, a 1D-CNN was employed to recognise real-time cognitive workload states from ultra-short-term ECG signals (780 milliseconds) of trainee surgeons. To be more specific, a multi-class classifier was implemented to recognise low, moderate, and high cognitive workload states, corresponding to the introduction of N0, N1, and N2, respectively while the LPT task was undertaken in the background. Figure 2 represents the 1D-CNN structure utilised in this multiclass classification model.

Three channels of raw ECG signals were first calibrated into millivolts and then filtered by 5th order high-pass Butterworth filter with a cut-off frequency of 0.5 Hz. Each cleaned raw ECG signal was segmented by a sliding window of 400 samples with a stride equal to 50 samples. Then, three corresponding ECG segments were concatenated horizontally, forming a 1200×1 feature vector. A total number of 53,304 instances were generated from 19 subjects (1 subject was rejected due to signal drop-off). Two identical 1D convolutional layers each defined 90 kernels of size 7, where Tanh was used as the activation. A max pooling layer of size 3 was utilised to reduce the complexity of the output and

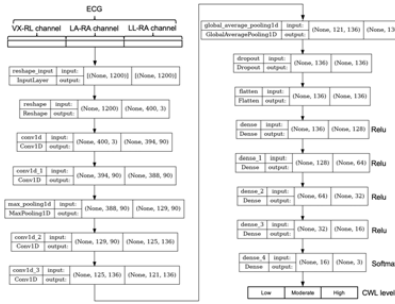


Fig. 2 The 1D-CNN structure utilised in the multiclass classification model.

prevent overfitting of the data. Another two identical 1D convolutional layers follow in order to learn higher-level features, where each defined 136 kernels of size 5. A global average pooling layer was used to further avoid overfitting by taking the average of 121 weights output in the fourth 1D convolutional layer. The dropout layer with a 0.2 rate was applied to make the model less sensitive to the small variation in the training data. Finally, the fully connected layers with softmax activation output the three values, representing the probability for each of the three classes, including low CWL (N0), moderate CWL (N1), and high CWL (N2).

RESULTS

To provide an unbiased evaluation of the model, 53,304 instances were split into training, validation, and test datasets with a ratio of 8:1:1. The k-fold cross validation is not implemented since instances from each class are identically distributed. The model was trained for 80 epochs with a batch size of 20. The confusion matrix shown in Figure 3 presents the accuracy of the 1D-CNN model for multiclass classification on the validation dataset (92.1%) and test dataset (91.3%). The Macro average precision, recall, and f1-score of test dataset are 0.914, 0.914, and 0.913 respectively. In summary, the 1D-CNN model can successfully identify low, moderate, and high cognitive workload states with 91.3% accuracy based on only 780 ms of ECG signal.

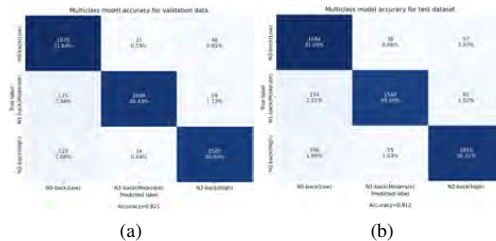


Fig. 3 Confusion matrices present the accuracy of the 1D-CNN model for multiclass classification on the (a) validation dataset (92.1%) and (b) test dataset (91.3%).

As presented in Table I, the 1D-CNN model significantly

TABLE I A comparison of classification accuracy between different deep learning architectures.

Model	ECG channels used	Classification accuracy (%)	
		Validation	Test
NN	1 channel	57.33	49.02
NN	3 channels	55.24	48.62
1D-CNN	1 channel	87.92	84.23
1D-CNN	3 channels	92.12	91.26
LSTM	1 channel	85.72	83.69
LSTM	3 channels	89.26	87.53

outperforms the NN and LSTM models. Indeed, in contrast to the NN model which needs a hand-crafting feature extraction process, the proposed 1D-CNN model inherits the ability of deep learning strategies to perform a feature extraction process as part of its inner decision mechanism. The LSTM model shows promising results since it can capture long-term and short-term information in the ECG signal [4]. Consequently, the bi-directional LSTM is expected to achieve better results since it can utilise bidirectional data dependence. Moreover, the model based on the combination of 1D-CNN and LSTM is also under investigation, and the results will be updated in the next version of the manuscript.

DISCUSSION

In this study, the modelling of the single modality ECG demonstrates promising preliminary results. The 780ms sliding window spans all essential characteristics of the ECG signal, including the P, Q, R, S, and T waveforms. Furthermore, applying 1D-CNN to three ECG channels, including Vx-RL, LA-RA, and LL-RA channels, fully utilises the CWL-related ECG morphological information and further improves classification accuracy.

In contrast to the studies assessing CWL when only performing a single task, the proposed model identifies the change of CWL levels resulting from a secondary task, the N back task in this case. This setup mimics the mechanics of real-world scenarios in the OR, contributing to forming a reliable CWL assessment approach in the OR in order to objectively measure and optimise the cognitive resource allocation of the surgeon. The proposed 1D-CNN allows this with the use of a single wearable sensor. Further work will evaluate the use of this system in a clinical setting.

Funding: This project is funded by the EPSRC Transformative Healthcare Technologies grant EP/W004755/1.

REFERENCES

- [1] A. T. Meneghetti, G. Pachev, B. Zheng, O. N. Panton, and K. Qayumi, "Objective assessment of laparoscopic skills: dual-task approach," *Surgical innovation*, vol. 19, no. 4, pp. 452–459, 2012.
- [2] K. Jin, A. Rubio-Solis, R. Naik, T. Onyeogulu, A. Islam, S. Khan, I. Teeti, J. Kinross, D. R. Leff, F. Cuzzolin, *et al.*, "Identification of cognitive workload during surgical tasks with multimodal deep learning," *arXiv preprint arXiv:2209.06208*, 2022.
- [3] C.-C. Chen, Z. Liu, G. Yang, C.-C. Wu, and Q. Ye, "An improved fault diagnosis using 1d-convolutional neural network model," *Electronics*, vol. 10, no. 1, p. 59, 2020.
- [4] U. E. Manawadu, T. Kawano, S. Murata, M. Kamezaki, J. Muramatsu, and S. Sugano, "Multiclass classification of driver perceived workload using long short-term memory based recurrent neural network," in *2018 IEEE Intelligent Vehicles Symposium (IV)*, 2018, pp. 1–6.

Priority-Based Shared Control for Peg Transfer Task

Z. J. Hu¹, L. Chen¹, Y. Huang², E. Burdet², and F. Rodriguez y Baena¹

¹*Department of Mechanical Engineering, Imperial College London,*

²*Department of Bioengineering, Imperial College London*

jacopo.hu20@imperial.ac.uk

INTRODUCTION

Supervisory methods in shared control allow a dynamic adjustment of the level of autonomy in a surgical robot based on the current task demands and the capabilities of the human operator. Several benchmarks [1] are available to evaluate the performance of these controllers, however the operator can struggle with the task due to inexperience or limited environmental information.

In this paper, we propose an admittance control strategy based on guidance priority adaptation to enable a human operator to assume a supervisory role during one-handed peg transfer task (Figure 1). We implement an epsilon-greedy maximum entropy inverse reinforcement learning (EG MaxEnt IRL) [2] algorithm to enable an agent to control the surgical tool in a virtual environment while the human supervises the procedure. We successfully implement the proposed method and observe that the supervisory method can be further improved with a cooperative control, specifically a segmented control.

MATERIALS AND METHODS

A. Agent in the Environment

We use a modified SurRoL environment [2][3] integrated with an Omega 7 (Force Dimension) to control in real-time a da Vinci Research Kit (dVRK) simulator. The virtual environment is the same one on which we train the agent in order to avoid any issue caused by the transition sim-to-sim or sim-to-real.

The human motion and strategies are transferred from an expert human operator to a dVRK using an EG MaxEnt IRL algorithm. The model is generated as in [2] and it enables to train an intelligent agent that can collaborate with the human operator during the procedure.

B. Shared Control with Guidance Priority Adaptation

By allocating the same control priority at the start of the task, the human and the robot can work as partners. This allows the robot to perform its assigned task without scaling, which will later occur during the negotiation of the control authority after the switching point. [4] uses force and deviation distance to achieve guidance priority adaptation, but the human needs to apply a relatively large force to get involved in decision-making when the end-effector follows the robot's desired trajectory. Using our proposed method, the agent can conduct the task without external aid; if any correction is needed, the

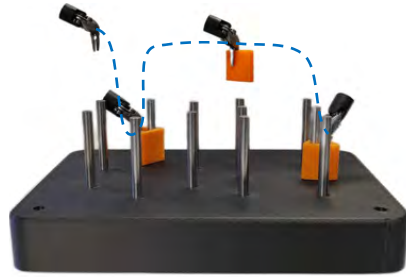


Fig. 1 Typical trajectory of the surgical tool during the peg transfer task scenario. The authority over the surgical tool is negotiated between the autonomous agent and the human operator through a supervisory control.

human can get involved in the task with partial priority. The shared control strategy that switches control priority is defined as:

$$\Delta x(t) = (1 + k_\alpha)\Delta x_h(t) + (1 - k_\alpha)\Delta x_a(t) \quad (1)$$

where $\Delta x_h(t)$ is the deviation of the controller's end position, $\Delta x_a(t)$ is the deviation of the agent's input. The parameter k_α is the relative coefficient that achieves guidance priority adaptation, which is defined by:

$$k_\alpha = \begin{cases} 0, & D \leq D_{min} \\ \frac{1}{2}(1 - \cos \frac{\pi(D-D_{min})}{D_{max}-D_{min}}), & D_{min} < D \leq D_{max} \\ 1, & D_{max} < D \end{cases} \quad (2)$$

where D is the distance between the autonomous agent pattern and end-effector position in one time step, while D_{min} and D_{max} are the minimal and maximal interference distance, respectively (Figure 2).

The guidance priority is determined by the deviation distance of the robot's end-effector and the path generated by the agent. While the deviation distance is less than the minimal interference distance D_{min} , slight trembling will not affect the agent's task. When the deviation distance increases, the control priority is gradually transferred to the human. While if the deviation distance is larger than the threshold of maximal interference distance D_{max} , the human receives all control priority.

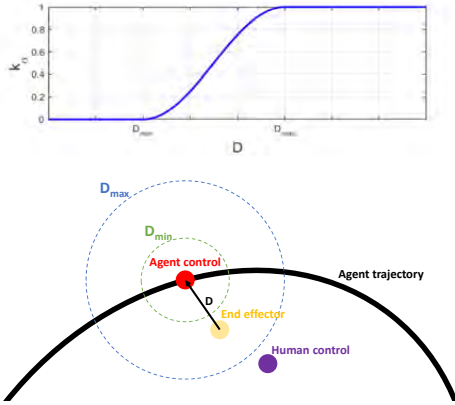


Fig. 2 Proposed guidance priority adaptation. The magnitude of the relative coefficient used for guidance priority adaptation changes according to the distance D generated by the human operator.

RESULTS

We conducted a short study with three participants without experience using the dVRK exclusively to evaluate the viability and performance of the shared control, hence no statistical analysis was performed. The experiments were approved by the Research Ethics committee of Imperial College London (21IC7042). At the start of the experiment, the subjects were briefed on the supervisory task and the general trajectories, and were asked to intervene if they perceived the agent's behaviour to be incorrect. It is important to notice that the agent was capable of successfully completing the task with human intervention as no noise was introduced in environment. As the subjects were not made aware of their inputs in the controller during the first trial stems from their mistrusts of the agent's abilities and limited perception based solely on visual feedback. Therefore only recorded the subjects' first trial, as the participant would eventually learn that their input was not necessary for the agent to complete the task. The objective of recording was to understand at which points during task the operators feel more compelled to intervene desire to obtain more control. With the results obtained the control authority can then later be better tailored to human behaviour. Figure 3 illustrates the input command obtained from the first trial of one of the participants, which reveals that, interestingly, the participant had a tendency to input during moments of near-collision in the task, specifically during the actions of grasping and lifting the peg, and in the process of placing it down. Similar results were obtained for the other subjects.

DISCUSSION

With the guidance priority adaptation we allowed the human operator to monitor the performance and intervene if necessary. The results obtained in Figure 3 indicate that the human operator feels more compelled to intervene

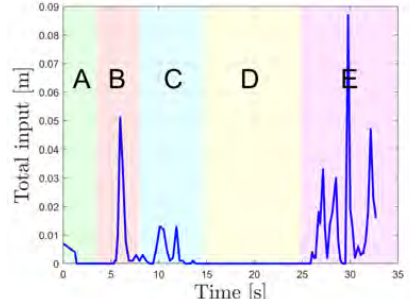


Fig. 3 Human operator command input during supervised peg transfer. (A) Robot arm hovering over target block. (B) Hand approaching target block. (C) Block picked up and lifted. (D) Robot arm hovering towards target peg. (E) Block inserted through the peg and placed down.

during contact points of the peg transfer task. This can be attributed to the human's perception of danger during contacts, limited vision of the environment, and to the limitations of EG MaxEnt IRL to perform natural human movements.

Currently, we are working at the integration of the guidance priority adaptation with a collaborative control framework as in [2] in order to allow more freedom and control to the human during critical stages of the task. With this approach, the agent and human control negotiation is tailored to the operator, according to the results we obtained in Figure 3, but the human operator can still intervene at any time to provide input or take control of the robot. The segmentation of the proposed



Fig. 4 Segmented guidance priority adaptation tailored to the operator behaviour during peg transfer.

REFERENCES

- [1] H.-C. Hur, D. Arden, L. E. Dodge, B. Zheng, and H. A. Ricciotti, "Fundamentals of laparoscopic surgery: a surgical skills assessment tool in gynecology," *Journal of the Society of Laparoendoscopic Surgeons*, vol. 15, no. 1, p. 21, 2011.
- [2] Z. J. Hu, Z. Wang, Y. Huang, A. Sena, F. Rodriguez y Beaana, and E. Burdet, "Towards human-robot collaborative surgery: Trajectory and strategy learning in bimanual peg transfer," *Submitted*.
- [3] J. Xu, B. Li, B. Lu, Y.-H. Liu, Q. Dou, and P.-A. Heng, "Surrol: An open-source reinforcement learning centered and dvrk compatible platform for surgical robot learning," in *IEEE/RSJ International Conference on Intelligent Robots and Systems (IROS)*, 2021, pp. 1821–1828.
- [4] H. Ren, Z. Li, Q. Wu, and D. Wu, "Guidance priority adaptation in human-robot shared control," in *IEEE International Conference on Mechatronics and Automation (ICMA)*, 2022, pp. 1634–1639.

Incident Angle Study for Designing an Endoscopic Tool for Intraoperative Brain Tumor Detection

K. K. Yamamoto¹, T. J. Zachem¹, W. Ross², and P. J. Codd^{1,2}

¹*Department of Mechanical Engineering and Materials Science, Duke University*

²*Department of Neurosurgery, Duke University School of Medicine*

kent.yamamoto@duke.edu

INTRODUCTION

Surgery is one of the most prevalent methods of controlling and eradicating tumor growth in the human body, with a projection of 45 million surgical procedures per year by 2030 [1]. In brain tumor resection surgeries, pre-operative images used for the detection and localization of the cancer regions become less reliable throughout surgery when used intraoperatively due to the brain moving during the procedure, referred to as brain shift. To solve the brain shift problem, intraoperative MRI (iMRI) has been used, but it is costly, time intensive, and only available at the most advanced care facilities [2]. Intraoperative fluorescence-guided methods, both exogenous (introducing foreign fluorophore molecules into the body) and endogenous (utilizing innate fluorophores within the body), have been investigated as an alternative to iMRI to circumvent the brain shift problem.

This paper introduces the proposed design, shown in Fig. 1(a), of an endoscopic tool for intraoperative brain tumor detection incorporating a laser-based endogenous fluorescence method previously explored by [3], called TumorID, depicted in Fig. 1(b). The device has also been deployed on ex-vivo pituitary adenoma tissue by [4] for intraoperative pituitary adenoma identification and subtype classification. This study explores whether a non-perpendicular angle of incidence (AoI) will significantly affect the emitted spectral data. With a better understanding of the relationship between AoI and collected spectra, the results can help shed light on the potential steering modality (optical [5] or fiber [6]) and end-effector movement profile for the proposed optics-based endoscopic tool.

MATERIALS AND METHODS

The experimental setup, Fig. 2(a), consisted of TumorID and its components, in addition to a spectrally-tuned gellan gum phantom model. The objective of the study was to scan the phantom model at different incident angles to observe the effects, if any, in the emitted spectral data.

A. TumorID

The TumorID, a non-contact tumor detection device completed in previous work by [3], leveraged the fact that NADH and FAD are endogenous fluorophores to

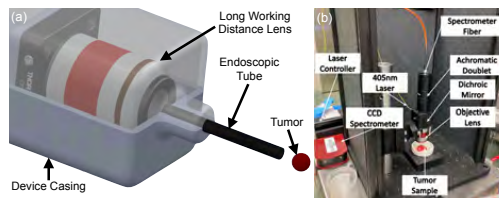


Fig. 1 a) Proposed endoscopic tumor detection device. b) Current TumorID setup scanning a tumor sample.

classify tissue type based on spectral signatures. The spectral signatures between tumor and healthy tissue differed due to the Warburg Effect, resulting in different concentrations in healthy and tumor cells due to differing metabolic properties. The system used a 405 nm laser diode (Thorlabs, NJ, USA) to irradiate the tissue. The emitted light was guided through a collimating lens to a dichroic mirror, then focused on the sample through an objective lens.

The TumorID was attached to a NEMA 17 hybrid stepper motor (Moon's, Shanghai, China) using a standard optical post for rigid attachment, as shown in Fig. 2(b). The stepper motor was controlled using a microcontroller (Elegoo, Shenzhen, China) and motor controller (SparkFun Electronics, CO, USA). The motor controller was powered by an external power supply at 11V. Spectral data were collected by a Thorlabs CCS200 spectrometer (Thorlabs, NJ, USA).

B. Phantom Model

Two gellan-gum phantom models with varying geometries (a flat plate and a spherical tumor representing a pituitary tumor) were prepared using NADH and FAD to mimic the spectral properties of tumors. The concentrations and volumes of both NADH and FAD were used from previous work on creating tumor-mimicking phantom models [7]. The phantom solution was cured in both a flat and convex mold that was 3D printed (UltiMaker S3, Utrecht, Netherlands). The cured phantoms were then placed in their respective fixtures, with the convex fixture representing a pituitary tumor's geometry during an endonasal approach. Both flat and convex phantoms are shown in the experimental setup in Fig. 2(c) and Fig. 2(d), respectively.

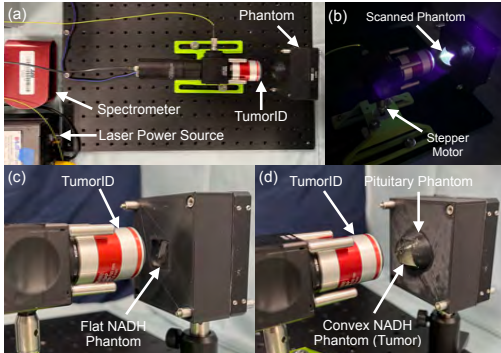


Fig. 2 (a) Experimental setup for TumorID AoI study. (b) TumorID mounted on a stepper motor, scanning the convex phantom. (c) Flat phantom (control) prepared for angle of incidence study. (d) Convex phantom (representing a pituitary tumor) fixed in skull base phantom frame.

C. Experimental Design

The rotating TumorID was placed 17 mm, the objective lens' working distance, from the phantom at an incident angle of 90°. To initiate the experiment, the TumorID was placed at the edge of the phantom boundary, then swept clockwise in increments of 1.8° to collect a spectral signal at each incident angle (18° in both directions with respect to an AoI of 0°).

The procedure was executed on both the flat phantom and the curved phantom in triplicates. The Area Under the Curve (AUC) of each spectrum was calculated as a metric to observe whether the spectral signal significantly changed at each incident angle for both phantoms. After spectral collection, the data was normalized individually with respect to the largest intensity value greater than 450 nm [4]. 450 nm was selected as the cutoff for normalization due to the transmittance behavior of the dichroic mirror. After max normalization, the data was smoothed by convolving with a window size of two. The AUC was calculated by conducting trapezoidal integration of the normalized signal from 450 nm to 750 nm. For clarity of presentation, AUC for each phantom model was normalized via max normalization.

RESULTS

The spectra at each AoI were recorded for both the flat and convex phantom, the latter shown in Fig. 3(a). Each line represented the spectra observed at an incident angle. Spectra collected at each incident angle resulted in the emission peaks for NADH and FAD [3], found at 460 nm and 525 nm, respectively. Fig. 3(b) showed the relationship between normalized AUC values and incident angle for both the flat and convex phantoms. The AUC values within 95% of the max value resided within $\pm 18^\circ$ from the zero position for the flat phantoms, decreasing as AoI increases. The AUC values calculated for the convex phantom showed a similar trend, but the values within 95% of the max value were present in a smaller region ($\pm 14^\circ$). The mean AUC for the flat phantom was $0.98 \pm$

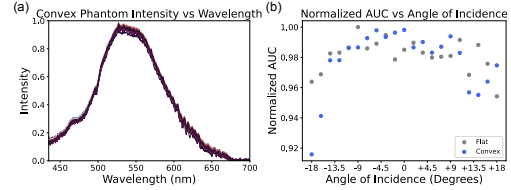


Fig. 3 (a) Spectral responses of the convex phantom at each incident angle, $n = 21$. (b) Average normalized AUC values at tested AoI.

DISCUSSION

A study on a non-contact tumor identification device, the TumorID, was conducted to investigate the effect of AoI on spectral response. The data collected for both a flat and convex scanning surface showed that although there was a change in spectra intensity at various AoI's, there was negligible difference in the spectral signature at the 460 nm and 525 nm wavelengths, where NADH and FAD emissions were present. The AUC values calculated were all within an average of 0.98 and a standard deviation of 0.02, indicating that the change in spectra intensity due to AoI was also very minimal after normalization. These findings helped consider that the end-effector of the proposed endoscopic device may not need to be perpendicular to the scanning surface continuously. Future work will include integrating TumorID into a handheld device, conducting an AoI study with a longer working-distance lens, and designing and implementing a compact steering method for bidirectional optics toward minimally invasive intraoperative tumor detection.

REFERENCES

- [1] O. Alatriste *et al.*, "Global cancer surgery: Delivering safe, affordable, and timely cancer surgery," *The Lancet Oncology*, vol. 16, pp. 1193–1224, 09 2015.
- [2] M. S. Eljamal and S. O. Mahboob, "The effectiveness and cost-effectiveness of intraoperative imaging in high-grade glioma resection; a comparative review of intraoperative ala, fluorescein, ultrasound and mri," *Photodiagnosis and Photodynamic Therapy*, vol. 16, pp. 35–43, 12 2016.
- [3] M. B. Tucker *et al.*, "Creation of a non-contact, automated brain tumor detection device for use in brain tumor resection," *SPIE*, 11225, International Society for Optics and Photonics. SPIE, 2020, p. 112250C.
- [4] T. J. Zachem *et al.*, "Intraoperative ex vivo pituitary adenoma subtype classification using noncontact laser fluorescence spectroscopy," *Journal of Neurological Surgery Part B: Skull Base*, vol. 84, no. S 01, p. P116, 2023.
- [5] P. A. York, R. Peña, D. Kent, and R. J. Wood, "Microrobotic laser steering for minimally invasive surgery," *Science Robotics*, vol. 6, no. 50, p. eabd5476, 2021.
- [6] D. V. A. Nguyen *et al.*, "A hybrid concentric tube robot for cholesteatoma laser surgery," *IEEE Robotics and Automation Letters*, vol. 7, no. 1, pp. 462–469, 2022.
- [7] M. B. Tucker *et al.*, "Creation of an optically tunable, solid tissue phantom for use in cancer detection," in *Clinical and Translational Neurophotonics 2018*, S. J. Madsen and V. X. D. Yang, Eds., vol. 10480, International Society for Optics and Photonics. SPIE, 2018, p. 104800H.

Comparative usability study of human-computer interfaces for 3D model manipulation in surgical augmented reality applications

A. Neri^{1,2}, V. Penza¹, and L. S. Mattos¹

¹Biomedical Robotics Lab, ADVR, Istituto Italiano di Tecnologia, Genoa, Italy

²Department of Informatics, Bioengineering, Robotics, System Engineering,
(DIBRIS) University of Genoa, Italy.
alberto.neri@iit.it

INTRODUCTION

Augmented reality (AR) is becoming essential in several surgical specialities [1]. Fusing patient-specific preoperative information, typically 3D models extracted from CT scans or MRI, on the real-time surgical images allows the surgeon to have detailed information on the anatomical structure of the surgical target intraoperatively. As stated in [2] and [3], an AR system's first step consists of an initial rigid registration of the 3D models on the surgical image. Most of the approaches are manual or semi-automatic. While the latter exploits physical landmarks on the tissue or 3D surface features, the manual approach requires Human-Computer Interfaces (HCI) to manipulate the models. The choice of the HCI is fundamental to develop an easy-to-use application with a short learning curve. In fact, the way the manual registration is performed can impact the users' physical and mental stress, influencing their final performances.

This paper presents a human-centred usability study that aims to evaluate two modern HCI devices commonly proposed for 3D model manipulation in surgical augmented reality applications, i.e., the SpaceMouse® and UltraLeap®. Accordingly, a software interface was developed to allow the manipulation of 3D models in a minimally invasive partial nephrectomy scenario. Subjects were asked to perform a rigid manual registration of a kidney's 3D model on the image of the real kidney. Quantitative and qualitative evaluation was performed to assess the cognitive and physical load imposed on the operators, which can support an informed selection of HCI to maximize system usability and operator performance. These trials were performed under study protocol 229/2019 - ID 4621, approved by the Regional Ethics Committee of Liguria (Italy).

MATERIALS AND METHODS

An AR system was developed to overlay, on the surgical image, the 2D projection of patient-specific 3D organ models, as shown in Fig. 1. The system takes as input (i) a set of patient-specific 3D models and (ii) the commands from two different HCI, the SpaceMouse® (3Dconnexion,

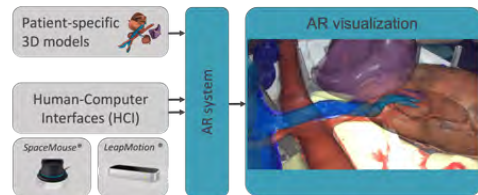


Fig. 1 Overview of the AR system architecture and the HCI used to perform the manual registration.

Germany) and the UltraLeap® (LeapMotion, USA). These HCI are used to perform the rigid manual registration between a 3D model and the corresponding real organ on the surgical image.

The AR visualization consists of a virtual environment with a virtual camera configured to behave like an endoscope. In fact, its projection matrix is set equal to the matrix of the undistorted camera. The *position*, *focal point* and *view up* axis of the virtual camera are set to visualize the 3D organ models located in the origin of the virtual environment. The endoscope image is represented behind the 3D models by mapping the undistorted surgical image on a plane parallel to the camera. The transparency of the 3D models can be changed to visualize the surgical image behind them.

Two different HCI, SpaceMouse® and UltraLeap®, were selected to control 6 DOF of a virtual 3D model to be overlaid on the surgical images. The UltraLeap® control is implemented by detecting the finger pinch with a strength over a threshold $P_{strength} > 0.9$. While the pinch is detected, the hand palm centre rotation and translation increments are used to transform the models with respect to the camera frame. The SpaceMouse® control is implemented by applying the translation and twist offset as the model's velocity with respect to the camera frame. A scale factor is added in both HCI to facilitate a precise model manipulation.

Experimental Protocol

The experiments included 13 subjects without experience in 3D object manipulation. Each experimental session

consisted of two trials, where the task was respectively and randomly performed with the SpaceMouse® or the UltraLeap®. The task consists in accurately aligning the 3D model of the left kidney with the real video image of the corresponding kidney phantom, with the 3D virtual model always located at the scene centre as suggested by Bergström et al. [4]. For each trial, the user was asked to perform the same task on 3 different images of the kidney phantom in a different position and orientation. The sequence of images was the same for both trials. At the beginning of each trial, the user had 5 to 10 minutes to familiarize him/herself with the manipulation HCI. After each trial, the user was asked to compile the SURG-TLX survey [5]. The task was considered completed when the user was satisfied with the achieved alignment. Quantitative measures consisted of: (i) intersection over union (IOU), computed between the real kidney mask (GT) and the 3D model projection mask, to evaluate the alignment accuracy for each task, (ii) task execution time. Qualitative information is extracted from the survey answers describing each interface's perceived workload.

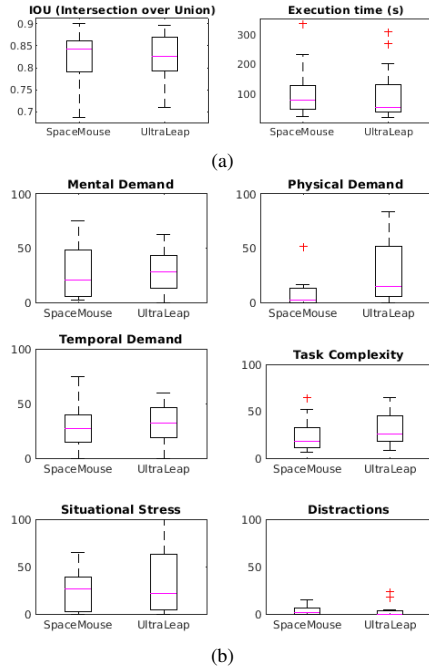


Fig. 2 (a) IOU and execution time box plots. (b) Box plots of the six dimensions in the SURG-TLX survey.

RESULTS

Fig. 2a shows the results related to IOU and execution time for the 2 HCI. The SpaceMouse® median IOU (0,84) is slightly better than the UltraLeap® one (0,82), while the latter holds a lower median execution time (55s) against the 81s of the first. Since the number of samples was not high enough, the data could not be analysed as a normal

distribution; consequently, a non-parametric statistical test was used (Wilcoxon rank sum test) to evaluate any significant difference between the data. For both IOU ($p = 0,77$) and execution time ($p = 0,19$), no significant differences have been found. It is noteworthy that for each task executed with the second interface, whatever it is, the execution time decreases, and the IOU obtained increases. This could mean that the learning curve of manipulating a 3D object has a very steep initial slope. Figure 2b presents the result of the surveys. All the dimensions, except for Physical Demands, have equivalent median values, and their Wilcoxon rank sum test does not show any difference. This indicates that the users found these dimensions comparable with both interfaces. The case of Physical Demands requires more attention; with a p-value of 0,068, it is barely over the threshold; collecting more data could lead to a significant difference between the 2 HCI, where the UltraLeap® results in more physically demanding.

DISCUSSION

In general, inexperienced users managed to complete the task with a good IOU (>0,8) and in less than 1min and 30s in both cases; this suggests that the two interfaces are natively intuitive and suitable to perform this task. Some users were very critical of UltraLeap®, finding it challenging to complete the task with it. This was because the position with the arm raised was uncomfortable for them, and they had problems with the control algorithm. On the other side, the majority stated that they felt more in control with the SpaceMouse®, which could explain why they decided to invest more time in it, feeling they could get better alignment. Considering that the choice of the interface turns out to be user-dependent, in this study the SpaceMouse® comes out as a slightly better option. The following steps will be to improve the UltraLeap® control algorithm to find better hand gestures to manipulate the objects. In the future, UltraLeap® has the potential to be the most intuitive solution since it grants complete freedom of hand movements, exactly like when we manipulate something in everyday life.

REFERENCES

- [1] J. W. Yoon, R. E. Chen, E. J. Kim, O. O. Akinduro, P. Kerecoudis, P. K. Han, P. Si, W. D. Freeman, R. J. Diaz, R. J. Komotar et al., "Augmented reality for the surgeon: systematic review," *The International Journal of Medical Robotics and Computer Assisted Surgery*, vol. 14, no. 4, p. e1914, 2018.
- [2] S. Bernhardt, S. A. Nicolau, L. Soler, and C. Doignon, "The status of augmented reality in laparoscopic surgery as of 2016," *Medical image analysis*, vol. 37, pp. 66–90, 2017.
- [3] T. Collins, D. Pizarro, S. Gasparini, N. Bourdel, P. Chauvet, M. Canis, L. Calvet, and A. Bartoli, "Augmented reality guided laparoscopic surgery of the uterus," *IEEE Transactions on Medical Imaging*, vol. 40, no. 1, pp. 371–380, 2021.
- [4] J. Bergström, T.-S. Dalsgaard, J. Alexander, and K. Hornbæk, "How to evaluate object selection and manipulation in vr? guidelines from 20 years of studies," in *proceedings of the 2021 CHI conference on human factors in computing systems*, 2021, pp. 1–20.
- [5] M. R. Wilson, J. M. Poolton, N. Malhotra, K. Ngo, E. Bright, and R. S. Masters, "Development and validation of a surgical workload measure: the surgery task load index (surg-tlx)," *World journal of surgery*, vol. 35, pp. 1961–1969, 2011.

Area-Based Total Length Estimation for Position Control in Soft Growing Robots

Korn Borvorntajanya¹, Shen Treratanakulchai², Enrico Franco¹, and
 Ferdinando Rodriguez y Baena¹

¹*Department of Mechanical Engineering, Imperial College London,*

²*Department of Biomedical Engineering, Mahidol University*

k.borvorntajanya22@imperial.ac.uk

INTRODUCTION

Recently, the use of eversion-based movement in robotics has gained popularity. Eversion mechanisms enable objects to turn inside out, similar to flipping a sock, allowing them to move through narrow spaces without making direct force on the environment. This type of movement can be used for medical devices such as catheters and endoscopes [1]. For instance, an autonomous colonoscope must navigate through tight and curved spaces in the colon. Eversion movement is a suitable solution that allows the colonoscope to move more safely. Furthermore, the implementation of feedback control enhances the accuracy and efficiency of the examination process.

The total length of the eversion portion (L) is typically controlled by a reel mechanism [2]. The reel mechanism consists of a spool wrapped tightly with plastic tubing connected to a motor. The system calculates the total length by counting the number of motor rotations. However, the diameter of the reel mechanism varies depending on the layers of material around the roller, making it difficult to calculate the total length from the standard roller model [3], [4].

This paper introduces a method for calculating the total length of the everted portion based on area. The model was validated using an optical tracking camera and compared with four other methods for calculating the total length in roller mechanisms.

MATERIALS AND METHODS

The plastic layflat tubing on the roll is assumed to be in the shape of an Archimedean spiral rather than a logarithmic spiral and has a uniform thickness (h). One end of the plastic tubing is glued to the spool. At a specific rotation angle, the tubing's end comes into contact with the portion of the wrapped layflat tube. This point forms the tangent to the cylinder, marking the final point of contact with the cylinder as shown in Figure 1. The following layers of the wrapped sheet consist of a cylindrical section around the spool and a flat section between the layers.

The entire radius of the spool (R) with the inner radius (r) is calculated by $R = r + kh$, where k is the number of

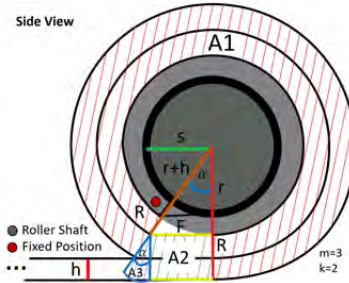


Fig. 1 Diagram of area based calculation for reel mechanisms: Light gray area is the inner radius(r), Dark gray represents the rotating shaft (s)

rotations. The inner radius is denoted by $r = (m - k)h + s$, where m is the total number of layers around the shaft, s is the radius of the spool. The flat section's length (yellow line), denoted as F , between the glued end and the second layer is calculated as $F = \sqrt{(r + h)^2 - r^2} = \sqrt{(2r + h)h}$. The angle (α) between red line and orange line in the Figure 1 is calculated using Equation 1.

$$\alpha = \arccos \frac{r}{r + h} \quad (1)$$

The area of entire roll is divided into three parts (A_1, A_2, A_3) [5], where A_1 represents the cylindrical section of the roller, A_2 refers to the rectangular area of the roller, and A_3 represents the sector between the layers as follow:

$$\begin{aligned} A_1 &= \left(\pi - \frac{\alpha}{2}\right) (R^2 - r^2) \\ A_2 &= (R - r - h)\sqrt{(2r + h)h}. \\ A_3 &= \frac{\alpha}{2}(R - r - h)^2 \end{aligned} \quad (2)$$

The total length (L) is calculated by dividing the total area by the thickness of the sheet, as

$$\begin{aligned} L &= \frac{1}{h} (A_1 + A_2 + A_3) \\ &= k(R + r)\pi + (k - 1)\sqrt{(2r + h)h} \\ &\quad - \left(k(r + h) - \frac{h}{2}\right) \arccos \frac{r}{r + h} \end{aligned} \quad (3)$$

The reel mechanism was equipped with a DYNAMIXEL motor (MX-24), controlled through USB communication using a U2D2 device. The Matlab script was utilized to control the rotation times by extended position control mode. The robot's tip was with a passive optical marker. An optical tracking camera (fusionTrack 500, Atracsys) was employed to provide the system with feedback on the tip's coordinates, as depicted in Figure 2b. The Cartesian coordinates of the marker were recorded at each step $k = (1, 2, \dots, 10)$. The plastic tubing ($h = 0.13\text{mm}$) was wrapped around the shaft ($r = 7.7\text{mm}$) in total of 15 layers ($m = 15$). The experiment was repeated 5 times ($n = 5$) with different rolls of tubing. Additionally, the pressure in the experiment was set to 0.5 bar, which is below the maximum bearing pressure of the plastic tubing. The experiment was repeated five times to calculate the standard deviation of the results.

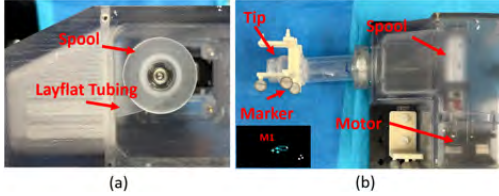


Fig. 2 Soft Growing Robot: a) Side view of the robot with a spool and layflat tubing, b) Top view of the robot with marker at the tip of the robot.

RESULTS

The 3D Euclidean distance between the starting and stopping points at each step was calculated as follow:

$$D = \sqrt{(x_k - x_s)^2 + (y_k - y_s)^2 + (z_k - z_s)^2} \quad (4)$$

where k is stopping positions and s denotes the starting position at $n = 0$. The results were plotted and compared to the calculations from four different models, including the proposed method, the common roll model [4], the Archimedean spiral model, and Dehghani's method [3], as shown in Figure 3. Additionally, the position at the tip (x^*) of evertting structure is equal to the total length divided by 2 as $x^* = \frac{L}{2}$. The root mean square error (RMSe) between the total length from the calculations and Euclidean distance from the experiment are in Table I. The maximum standard deviation in the experiment across multiple samples was approximately 2.1585 mm, significantly lower than the step commands.

DISCUSSION

The proposed method was found to yield the best prediction, with a maximum RMSe of approximately 2.534 mm in estimating the tip position (x^*). Compared to Dehghani's model [3], the proposed approach was, on average, 2 times more accurate ($k > 1$) in RMSe. In general, the maximum difference in RMSe between the proposed method and the other approaches was approximately 1.5% of the total length. Considering

k	Mean $\pm SD$	Proposed	Roll	Spiral	Dehghani
1	31.284 \pm 1.967	0.898	1.172	5.157	0.559
2	62.958 \pm 1.471	1.381	3.142	8.293	2.121
3	94.103 \pm 0.821	1.575	4.992	10.731	3.562
4	124.077 \pm 0.688	2.123	6.079	13.115	4.649
5	153.372 \pm 0.687	2.534	6.895	14.954	4.649
6	182.684 \pm 1.377	2.110	8.137	15.550	5.482
7	210.941 \pm 1.227	1.925	8.733	15.975	5.671
8	238.070 \pm 1.589	2.051	8.608	16.304	5.137
9	265.247 \pm 2.158	1.313	8.940	15.360	5.060
10	290.067 \pm 1.973	2.112	7.324	15.546	3.035

TABLE I The Mean and SD Euclidean distance (D) of tip position at number of rotation (k) from Different Samples ($n = 5$) and Comparison of Root Mean Squared Error (mm) in Total Length between the Experiment and Models.

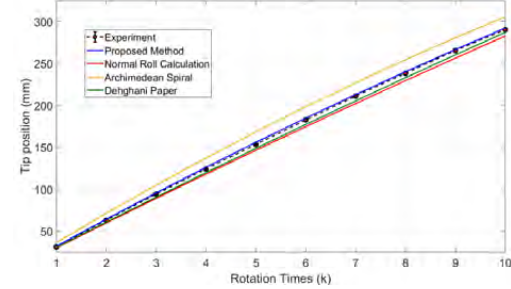


Fig. 3 The tip position (mm) of the evertting portion from the 4 different models and Euclidean distance at each step (k), as obtained from the experiment.

a typical colonoscopy with a length of 170 cm, the difference in RMSe corresponds to 2.55 cm, which is much larger than the size of a small polyp. Additionally, this difference was attributed to the thickness of the plastic tubing used (0.13 mm), which did not result in significant differences between the models. The design of the side chambers for steering in the growing structure can lead to an increase in the overall thickness of the tubes, thereby enhancing the disparities between the models. As a result, the approach has the potential to significantly improve the accuracy of endoscopic interventions that employ a soft-growing (evertting) device.

REFERENCES

- P. Berhet-Rayne, S. M. H. Sadati, G. Petrou, N. Patel, S. Giannarou, D. R. Leff, and C. Bergeles, "MAMMOBOT: A Miniature Steerable Soft Growing Robot for Early Breast Cancer Detection," *IEEE Robotics and Automation Letters*, vol. 6, no. 3, pp. 5056–5063, 2021.
- L. H. Blumenschein, M. M. Coad, D. A. Haggerty, A. M. Okamura, and E. W. Hawkes, "Design, Modeling, Control, and Application of Evertting Vine Robots," 11 2020.
- H. Dehghani, C. R. Welch, A. Pourghodrat, C. A. Nelson, D. Oleynikov, P. Dasgupta, and B. S. Terry, "Design and preliminary evaluation of a self-steering, pneumatically driven colonoscopy robot," *Journal of Medical Engineering and Technology*, vol. 41, no. 3, pp. 223–236, 4 2017.
- M. M. Coad, L. H. Blumenschein, S. Cutler, J. A. Reyna Zepeda, N. D. Naclerio, H. El-Hussieny, U. Mehmood, J. H. Ryu, E. W. Hawkes, and A. M. Okamura, "Vine Robots: Design, Teleoperation, and Deployment for Navigation and Exploration," *IEEE Robotics and Automation Magazine*, vol. 27, no. 3, pp. 120–132, 9 2020.
- K. David, "Calculating the length of the paper on a toilet paper roll," 1 2016. [Online]. Available: <https://math.stackexchange.com/questions/1633704/calculating-the-length-of-the-paper-on-a-toilet-paper-roll>

A Novel Handheld Robotic System for Endoscopic Neurosurgery: A Cadaver Pilot Study

Emmanouil Dimitrakakis¹, George Dwyer¹, Nicola Newall^{1,2}, Danyal Z. Khan^{1,2},
Hani J. Marcus^{1,2}, and Danail Stoyanov¹

INTRODUCTION

Neurosurgery has always been in need of adapting new technologies. Endoscopic Endonasal Transsphenoidal Surgery (EETS), a common minimally invasive neurosurgical technique, is especially in the need of innovation. This approach is performed via an anterior sphenoidotomy and aims at the removal of sellar and parasellar lesions with the use of an endoscope and rigid instruments [1]. Although a promising alternative to open brain-surgery, it comes with its limitations, namely the lack of instrument articulation and the constrained operative space of the nasal channel [2].

This work presents a novel handheld robotic instrument for endoscopic neurosurgery. The system is comprised of a series of articulated spherical-joint tendon-driven 3mm end-effectors, paired with an ergonomically designed handheld controller which does not require the shaft to be resting against a trocar-port. This first-of-its-kind robotic instrument for neurosurgery was evaluated during a cadaver pilot study with preliminary results suggesting feasibility within a clinical context.

MATERIALS AND METHODS

The handheld robotic system can be seen in Fig. 1. It consists of an ergonomically designed handheld controller with a joystick-and-trigger interface, and a series of 3mm detachable end-effectors. It is cabled to connect the controller to the control box, and weighs 247g.

A. Interchangeable end-effectors

The robotic end-effector located at the distal end of the handheld robotic instrument advances preliminary development [3] to incorporate an overall diameter of 3mm and a 2 DoF tendon-driven spherical joint that allows movement in the pitch and yaw axes around a rolling surface. The roll axis motion can be compensated by the surgeon's hand movement. To cover a larger set of neurosurgical instruments, and since the end-effector can be easily detached and re-attached to the handheld controller, we amended the grasper end-effector design to enhance other standard instruments with robotic articulation. Namely, these instrument end-effectors were a ring-curette, a spatula dissector, and an endoscope. The alternative end-effectors are found in Fig. 2.

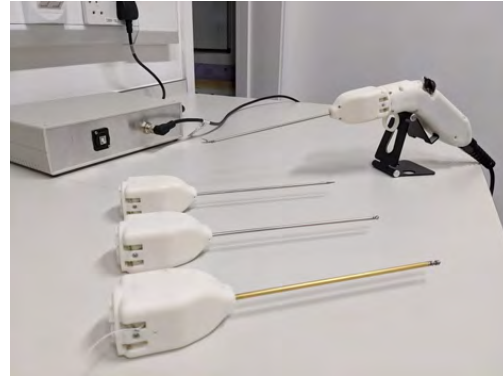


Fig. 1 The handheld robotic instrument deploying a grasping tool, alongside three alternative articulated tools; a flat dissector, a ring-curette, and an endoscope.

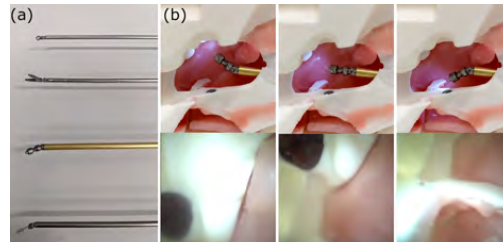


Fig. 2 (a) (Top to bottom) The articulated end-effectors, namely the ring-curette, the grasper, the endoscope, and the spatula dissector, and (b) The endoscope inside a pituitary anatomy phantom at three different angles, alongside the accompanying views from the camera.

B. Ergonomic handheld controller

To control the end-effector, we aimed to build a handheld controller that would be ergonomically designed to not cause the surgeon strain or fatigue, while also being easy to use and associated with small learning curves. The handle with the shaft should maintain a 45° angle to avoid wrist-strain when maintaining it, and to make the control instinctively easy to adopt, the thumb should control the robot-joints, and the index-finger should operate the robotic gripper. After our concept design was preliminarily validated in previous work [4], [5], we incorporated motors and electronics to turn it into

¹Wellcome/EPSRC Centre for Surgical and Interventional Sciences (WEISS), University College London (UCL), London, UK

²National Hospital for Neurology and Neurosurgery, London, UK
e.dimitrakakis@ucl.ac.uk

a fully-functional handheld robotic controller.

C. Experimental evaluation: Cadaver pilot study

The scope of this pre-clinical study was exploratory, relying on qualitative surgeon feedback to investigate the feasibility, robustness, and durability of the robotic device. The novel instruments that were brought into the operating theatre for this study are found in Fig. 3. Standard equipment consisted of a 0° neuroendoscope accompanied with its tele-pack stack (Karl Storz SE & Co. KG, Tuttlingen, Germany), and an endoscopic pituitary instrument set (B.Braun Melsungen, Germany).



Fig. 3 The robotic instruments that were tested during the cadaver pilot study. Left to right: control box, handheld controller, and articulated tools.

One expert neurosurgeon, one intermediate, and four novices were recruited to evaluate the robotic instrument on a single cadaver. The EETS including the durotomy was performed pre-task, followed by the introduction of the robotic instrument. The participants explored the pituitary fossa with the robot and interacted with soft tissue and bony structures. Then, the expert and intermediate neurosurgeons tried the robotic endoscope, both with and without the guidance of the standard rigid endoscope.

RESULTS

Fig. 4 presents the robotic tools used in the cadaveric specimen. To qualitatively evaluate the feasibility of the device, feedback regarding the dexterity, force delivery, structural integrity of the robotic device, and user experience was obtained through a post-task questionnaire.

The questions and surgeon replies are presented in Table I. Further minor comments included that while the participants were satisfied with the robot articulation when each DoF was actuated individually, the movement felt constrained when the end-effector was moving diagonally when both DoF were actuated. Finally, regarding the concurrent usage of an articulated instrument and articulated endoscope, the takeaway was that depth perception of the articulated visual elements is challenging and that the best usage of such a device would most likely be alongside a standard endoscope.

DISCUSSION

In this work, we presented a novel handheld robotic system for endoscopic neurosurgery, with an ergonomically

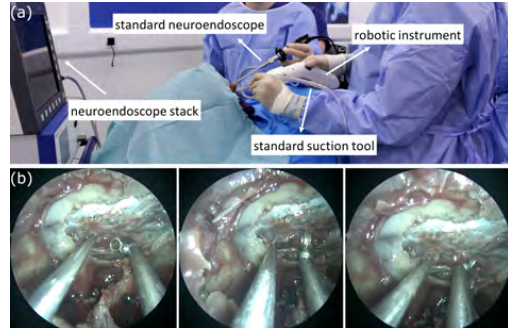


Fig. 4 (a) The surgical setup with the introduction of the novel robotic instrument, and (b) (left to right) A standard suction tool and the robotic curette in different poses interacting with soft tissue.

TABLE I The post-cadaver study questionnaire, and the surgeon replies

Question	Yes	No
Does the robot maintain its pose when pressing against soft and bony tissue?	6	0
Does the robot allow for precise movements?	0	6
Does the robot allow for increased dexterity?	6	0
Does the robot apply sufficient forces when already articulated?	6	0
Does the robot apply sufficient forces while in motion?	0	6
Is the robot easy to use?	6	0
Is the robot comfortable to use?	6	0

designed handheld controller, and a series of 3mm tendon-driven spherical joint robotic end-effectors. The robotic system was tested during a cadaver pilot study where its feasibility was investigated and its limitations, namely the control methodology and force-delivery capabilities, were identified. Encouraging, however, results on workspace exploration, dexterity, structural integrity, and ease-of-use, suggested clinical relevance and set the pace for in-vivo clinical validation and surgical adoption.

REFERENCES

- [1] P. Cappabianca, L. M. Cavallo, and E. De Divitiis, "Endoscopic endonasal transsphenoidal surgery," *Neurosurgery*, vol. 55, no. 4, pp. 933–941, 2004.
- [2] H. J. Marcus, T. P. Cundy, A. Hughes-Hallett, G.-Z. Yang, A. Darzi, and D. Nandi, "Endoscopic and keyhole endoscope-assisted neurosurgical approaches: a qualitative survey on technical challenges and technological solutions," *British journal of neurosurgery*, vol. 28, no. 5, pp. 606–610, 2014.
- [3] E. Dimitrakakis, G. Dwyer, L. Lindenroth, P. Giataganas, N. L. Dorward, H. J. Marcus, and D. Stoyanov, "A spherical joint robotic end-effector for the expanded endoscopic endonasal approach," *Journal of Medical Robotics Research*, vol. 5, no. 03n04, p. 2150002, 2020.
- [4] E. Dimitrakakis, L. Lindenroth, G. Dwyer, H. Aylmore, N. L. Dorward, H. J. Marcus, and D. Stoyanov, "An intuitive surgical handle design for robotic neurosurgery," *International Journal of Computer Assisted Radiology and Surgery*, pp. 1–9, 2021.
- [5] E. Dimitrakakis, H. Aylmore, L. Lindenroth, G. Dwyer, J. Carmichael, D. Z. Khan, N. L. Dorward, H. J. Marcus, and D. Stoyanov, "Robotic handle prototypes for endoscopic endonasal skull base surgery: Pre-clinical randomised controlled trial of performance and ergonomics," *Annals of biomedical engineering*, vol. 50, no. 5, pp. 549–563, 2022.

Developing a customisable inflatable rectal obturator

A. Niknam Maleki¹, M.S. Runciman¹, A.J. Thompson¹, J. Murray², G. Mylonas¹

¹The Hamlyn Centre, Department of Surgery and Cancer, Imperial College London, London, UK

²The Institute of Cancer Research and the Royal Marsden NHS Foundation Trust, Department of Radiotherapy and Imaging, London, UK
aryan.niknam-maleki17@imperial.ac.uk

INTRODUCTION

Rectal obturators like ProSpare and endorectal balloons (ERB) may reduce prostate motion during prostate radiotherapy, improving dosimetry of the target volume and surrounding healthy tissue [1-3]. ERBs are inflatable and well-tolerated, but an accumulation of gas proximal to the device can decrease its efficacy in reducing prostate motion [4]. ProSpare's angled shape allows it to "lock in" at the anorectal angle and is made of high-impact ABS to reduce prostate motion. However, initial data from the POPS trial (NCT02978014) has shown 7/19 (37%) of patients could not insert ProSpare at their initial attempt, possibly because of the anal sphincter not stretching enough to accommodate the device. To address this issue, we present a deployable or inflatable device that becomes rigid and angled like ProSpare upon deployment, aiming to improve outcomes by reducing motion during prostate radiotherapy, while achieving good tolerance for nearly all patients. Laser welding was used to create inflatable chambers, forming ridges that provide rigidity once inflated [5]. Here, we report initial designs and validations of rigidity.

MATERIALS AND METHODS

The device was made using a custom plastic laser welding system developed at the Hamlyn Centre, St Mary's Hospital [5]. The plastic sheets used were triple laminate: 30/60/30 µm PE/PET/PE. Following welding, laser cutting was done using a Beamo (FLUX Europe) laser cutter and Beam studio software. The edges of the flat sheet were soldered together at 160°C to create the 3D shape. Two designs were explored: a dual-truncated prism, a three-sided and four-sided design is shown in Figure 1, and a reinforced actuator design, shown in Figure 2. The first reinforced actuator design (Figure 2, left) includes a channel (8 mm) in which a Tygon tube (length 75 mm; outer diameter 4 mm) was inserted to cause bending in the opposite direction. The horizontal welds on the face with the tube were replaced with vertical welds, and the tube channel was removed. All designs were created in SolidWorks (Dassault Systèmes), had cut-out patterns with a cut-out distance of 1.5 mm and crosses to help with alignment during the transfer from laser welding to laser cutting. Devices were tested for inflatability, rigidity, and bursting by

inflating them using a pneumatic compressor to 50 kPa (gauge pressure) and incrementing the pressure by 50 kPa at a time. Radial stiffness (force/displacement) was obtained by compressing the devices between two surfaces and measuring the force applied with a force sensor (Nano 17, ATI Automation, USA) and displacement with a digital calliper. Radial stiffness was obtained for four trials of the device on the right of Figure 2.

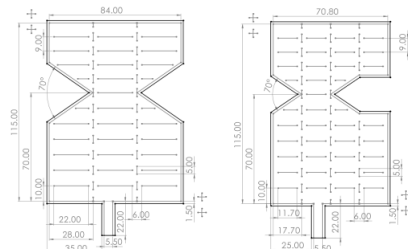


Fig. 1 Design and dimensions of a three-sided (Left) and four-sided (Right) dual-truncated prism.

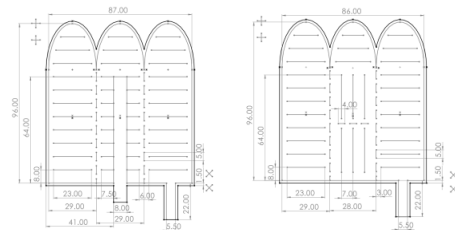


Fig. 2 Left: The initial design of a reinforced device with a channel for an inextensible tube and horizontal chambers. Right: Current design with 7 mm vertical chambers and a split of horizontal welds but no channel for a tube.

At low displacements and forces, the device's bend caused force measurements to fluctuate in the same measurement. Instead of gradually increasing compression, devices were compressed as much as possible and then moved back 1 mm at a time. Leakage under pressure was tested by inflating the device with water with a 50 ml syringe, on top of a dry paper towel, and examining the paper towel for leakage. The width and angles of the devices were measured using a digital calliper and rounded to the nearest millimetre. Minimum widths in the AP and LR direction of the

uninflated, ‘folded’ device and maximum dimensions of the inflated, deployed device were measured to obtain an expansion ratio by volume.

RESULTS

For the dual truncated design, the 3-sided device could not be folded into a straight device so a 4-sided one was created, which could be folded. However, the deployment of the 4-sided device would push against the posterior anal wall before locking in the anorectal angle (Figure 3). As highlighted in Figure 4, the first reinforced actuator design did not bend the device as intended, but in the new design with vertical chambers, the tube was no longer necessary to induce the bend. Figure 4 right, shows a pelvic cone-beam CT scan, highlighting the discrepancy in angles between this device and ProSpare, at 20° and 70°, respectively.



Fig. 3 Four-sided dual-truncated prism device when deflated and folded and then expanding to form its final 3D shape.



Fig. 4 From left to right: The inflated 3D shape of the first design containing an embedded inextensible tube; the inflated 3D shape of the latest design with vertical welds and no tube; Vertical chambers on the anterior face of the device providing rigidity on that face; The latest design of inflatable design superimposed on ProSpare on CBCT comparing the angle of the bend in each device and its relation to the anorectum.

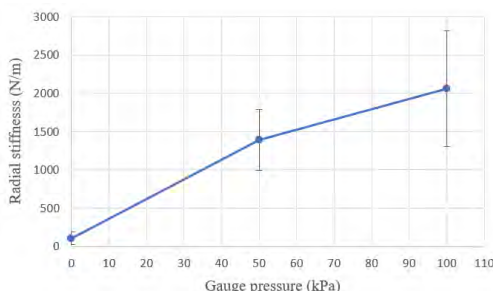


Fig. 5 Radial stiffness of the device with the latest design against gauge pressure. Means \pm standard deviations from 8 measurements. Internal welds failed at 150 kPa.

While deflated, the device was folded axially three times to reduce the dimensions down to 3 mm by 17 mm with a length of 96 mm. Once inflated, the device reached a width by depth of 25 mm by 30 mm, with the length remaining at 96 mm, which resulted in an expansion ratio of 14.7 by volume. Figure 5 shows the radial stiffness increased as the pressure of the pneumatic compressor increased. Internal welds burst at 150 kPa, but the soldered edges did not fail. Water did not leak from the main body but did leak from the tubing connected to the syringe.

DISCUSSION

A novel device capable of inflating to a rigid, angled form has been successfully designed and fabricated using laser welding. This represents the first instance of laser welding used to create a rectal obturator for use in prostate radiotherapy. The device's fully compressible, uninflated form should allow easy insertion past the anal sphincter, and then deployment to its final angled shape. However, the angle of the device needs to be increased to match the anorectal angle. This could be achieved by removing material at the bend to prevent obstruction of the bending action. Additionally, a customisable device could potentially improve positional reproducibility in the superior-inferior axis, which is a limitation of ProSpare. The device's rigidity has been validated, as the radial stiffness increased with increased pressure. Future work will compare its rigidity to that of ProSpare and ERB. Further development will include adding an introducer for insertion, continuous tubing to prevent water leakage, embedding fiducial markers to allow for image-guided radiotherapy, and testing with water/saline for burst safety and minimizing scatter.

REFERENCES

- [1] Smeenk RJ, Teh BS, Butler EB, van Lin, Emile N. J. Th, Kaanders JHAM. Is there a role for endorectal balloons in prostate radiotherapy? A systematic review. *Radiotherapy and oncology*. 2010; 95 (3): 277-282. 10.1016/j.radonc.2010.04.016.
- [2] Murray J, McNair H, Alexander E, O'Shea T, Thomas K, Nill S, et al. B90: ProSpare, a rectal obturator reduces intrafraction target motion in prostate cancer radiotherapy. *Abstracts from the NCRI Cancer Conference, 2015*.
- [3] Murray JR, Gulliford S, Alexander EJ, Menair H, Dearnaley DP. P028 The effect of ProSpare, a rectal obturator on anorectal doses in prostate radiotherapy. *European urology supplements: official journal of the European Association of Urology*. 2014; 13 (5): 119. 10.1016/S1569-9056(14)61253-7.
- [4] Wang KK, Vapiwala N, Bui V, Deville C, Plastaras JP, Bar-Ad V, et al. The impact of stool and gas volume on intrafraction prostate motion in patients undergoing radiotherapy with daily endorectal balloon. *Radiotherapy and oncology*. 2014; 112 (1): 89-94. 10.1016/j.radonc.2014.05.008.
- [5] Runciman M, Avery J, Zhao M, Darzi A, Mylonas GP. Deployable, Variable Stiffness, Cable Driven Robot for Minimally Invasive Surgery. *Frontiers in Robotics and AI*. 2019; 6 141. 10.3389/frobt.2019.00141

Feasibility of Mobile Application for Surgical Robot Teleoperation

Akhil Deo¹, Peter Kazanzides¹

¹Laboratory for Computational Sensing and Robotics, Johns Hopkins University

{adeo1, pkaz}@jhu.edu

INTRODUCTION

In recent years, robotic surgery has gained popularity due to its numerous advantages, including greater control and access for surgeons, shorter recovery times, and lower levels of pain for patients [1]. However, surgical robot systems require extensive training for surgeons to master their use. Simulation-based training has become a component of surgical education [2], providing a safe environment for trainees to acquire and refine their skills. However, most existing training platforms require bulky and expensive control consoles, which limits their availability and convenience. The development of a low-cost and easily deployed control console can address these limitations, thereby potentially enhancing the effectiveness of robotic surgery training. A system that satisfies these criteria can also enable medical robotics research in low-resource environments, where cost and accessibility are the most significant impediments to research. This paper describes the creation and evaluation of an iPhone application for these purposes.

MATERIALS AND METHODS

da Vinci Research Kit (dVRK)

The dVRK is an open-source system, currently available at about 40 institutions worldwide, that is used to control retired da Vinci surgical systems for research purposes [3]. It empowers researchers to control the position and orientation of two remote Patient Side Manipulators (PSMs), using two Master Tool Manipulators (MTMs). An external MTMR (Right) is shown in Fig. 1.



Fig. 1 External MTMR for direct vision during user study.

Mobile Application

The mobile app is built with Swift and Objective C and is designed for most recent iPhones, including the iPhone X, 11, 12, 13, and their related models. The application attempts to emulate the functions of an MTMR or MTML by using the ARKit library for visual-inertial odometry. As shown in Fig. 2, this allows the app to use visual

odometry and data from the phone's inertial measurement unit (IMU) to track the position and orientation of the phone at a frequency of 60 Hz.

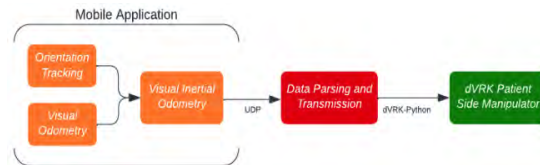


Fig. 2 Overview of the process enabling robot teleoperation with mobile app.

The app can also influence the PSM instrument jaw via buttons that increment and decrement the jaw value, as well as freeze both the position and orientation of the robot with the “clutch” button, which is displayed in Fig. 3. The clutch button is similar to the clutch foot pedal on the MTM; however, since the phone does not have motorized mechanical parts like the MTM, there is no method to enforce absolute orientation. Thus, the mobile application allows for relative orientation, meaning that the phone orientation generally will not directly correspond to the PSM instrument orientation.

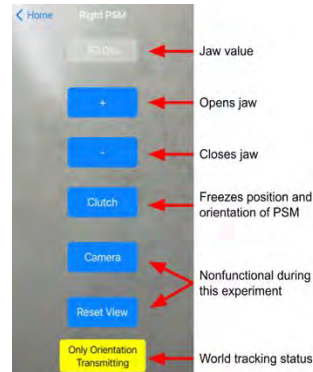


Fig. 3 PSM control screen and description of functions.

A different screen of the app enables users to enter an IP address so that data can be sent to the system operating the dVRK. The script that reads incoming packets on the dVRK computer parses the data from the iPhone and sends the appropriate instructions to the PSM using the dVRK Python package.

Instrumented Training Platform

Although our motivating use cases include simulated patient-side environments, we performed experiments with a physical PSM and ring rollercoaster training task

(see Fig. 4) to guarantee a realistic evaluation. A custom-made electrical circuit detects contact between the surgical instrument, and thus the metal ring, and the wire. This structure is based on the experimental setup first presented by Brown et al. [4], except we will not be using a force sensor.

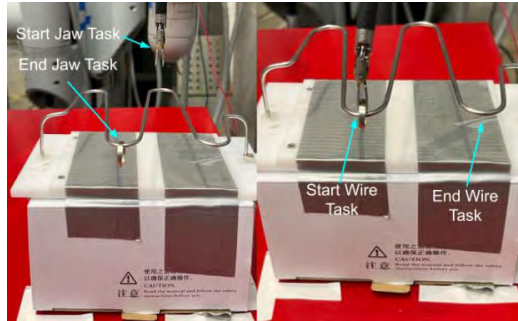


Fig. 4. Left: Start & end points for jaw task. Right: Start & end points for wire task.

Experiment Protocol

We recruited 16 novice participants (7 male, 9 female) between the ages of 18 – 24 from the adult population of Johns Hopkins University. All participants were consented according to a protocol approved by the Johns Hopkins Homewood Institutional Review Board (#HIRB00000701). Each of the following tasks was conducted in the same order for each human subject. Participants were introduced to the mobile application and instructed on controlling the PSM (instrumented with Maryland Bipolar Forceps) using this input device. Participants were given a few training tests and 3 minutes to practice further. Participants were instructed to complete the task three times. The process was repeated with the external MTMR.

The experiment is split into the jaw task and the wire task. The jaw task, shown in Fig. 4-Left, occurs first and involves grabbing and lifting the ring in as few attempts as possible. Then, the wire task begins. Participants are instructed to move the ring to the end position referenced in Fig. 4-Right while minimizing the number of times the ring and the wire collide.

RESULTS

Of the 48 trials conducted with the phone application and the 48 trials with the MTMR, one from each set of trials was removed due to experimenter error (not starting data collection). Table 1 shows the completion times of the jaw and wire tasks. Though the jaw task only took about 28% longer using the phone ($p = 0.488$), the wire task took over 125% longer to complete using the mobile application than the MTMR ($p = 7.05 * 10^{-6}$).

Table 1. Completion times for the jaw and wire tasks, in format mean \pm standard deviation

	Jaw Task (s)	Wire Task (s)
Phone	24.2 ± 14.1	85.9 ± 41.1
MTMR	18.8 ± 27.4	38.1 ± 32.7

Though the MTMR seems superior at first glance, Tables 2 and 3 show that users were more accurate when controlling the PSM with the iPhone application. The average number of attempts necessary to grab the ring was about 9% lower when using the phone ($p = 0.232$), and the average non-collision was about 7.6% lower than the MTMR ($p = 4.86 * 10^{-6}$). When participants were using the phone application, it appears that they prioritized accuracy, even if the tasks would take significantly longer.

Table 2. Number of attempts to initially hold the ring, in format mean \pm standard deviation

Phone	1.46 ± 0.798
MTMR	1.60 ± 1.20

Table 3. Non-collision percentage for the wire task, in format mean \pm standard deviation

Phone	49.9 ± 24.0
MTMR	54.0 ± 31.1

DISCUSSION

From the results, it is apparent that to achieve better accuracy by using the phone, participants had to take a significantly longer time to complete the tasks. Though this indicates that this app cannot be deployed in a time-sensitive environment, we believe it still has merit as a low-cost and readily available input device for surgical robotic training, as well as for facilitating medical robotics research in low-resource settings. It is also worth noting that the iPhone application has a frequency of 60 Hz , which is significantly lower than the MTMR (500 Hz), and therefore a target for improvement. Future work should include integration of a low-cost and compact stereo visualization system, such as a head-mounted display (HMD), to replicate the full functionality of a surgical control console.

ACKNOWLEDGEMENTS

We thank Anton Deguet for aiding with the dVRK system integration.

REFERENCES

- [1] G. Guthart, J. K. Salisbury Jr, “The Intuitive™ telesurgery system: Overview and application,” in IEEE Intl. Conf. on Robotics and Auto. (ICRA), 2000, pp. 618–621.
- [2] S. Azadi, I. C. Green, A. Arnold, M. Truong, J. Potts, and M. A. Martino, “Robotic surgery: The impact of simulation and other innovative platforms on performance and training,” Journal of Minimally Invasive Gynecology, vol. 28, no. 3, pp. 490–495, 2021.
- [3] P. Kazanzides, Z. Chen, A. Deguet, G. S. Fischer, R. H. Taylor, and S. P. DiMaio, “An open-source research kit for the da Vinci(R) surgical system,” in IEEE Intl. Conf. on Robotics and Automation (ICRA), 2014, pp. 6434–6439.
- [4] J. D. Brown, J. N. Fernandez, S. P. Cohen, and K. J. Kuchenbecker, “A wrist-squeezing force-feedback system for robotic surgery training,” in Proceedings of the IEEE World Haptics Conference (WHC), Furstenfeldbruck (Munich), Germany, 2017, pp. 107–112.

An application of SlicerROS2: Haptic latency evaluation for virtual fixture guidance in breast conserving surgery

L. Connolly¹, A. Deguet², T. Ungi¹, A. Kumar², A. Lasso¹, K. Sunderland¹,
P. Kazanzides², A. Krieger², J. Tokuda³, S. Leonard², G. Fichtinger¹,
P. Mousavi¹, R.H. Taylor²

¹Queen's University, CAD ²Johns Hopkins University, USA,

³Brigham and Women's Hospital, USA

INTRODUCTION

Breast conserving surgery (BCS) is a surgical intervention for breast cancer where the surgeon resects the primary tumor and preserves the surrounding healthy tissue. These procedures have a high failure rate because it is often difficult to localize breast tumor boundaries intraoperatively. Emerging surgical robotic technology demonstrates promise for addressing such challenges. Hand-over-hand control is a design concept that involves cooperative handling of a surgical instrument by the surgeon and a robot. These systems can be used to reduce hand-tremor, improve dexterity, and implement virtual guidance [1]. One way to do this is with a virtual fixture (VF) which is a computer-generated constraint that is communicated from robotic devices to human operators via force and position signals [2]. A forbidden region VF can be used to enforce a safety region or “no-go zone” that can prevent the operator from damaging delicate or critical anatomy. In this paper, we use an Omni Bundle robot (formerly known as a Phantom Omni) to introduce haptic feedback in BCS. In doing so, we demonstrate a new and simplified approach to implementing a VF using open-source software tools such as 3D Slicer and robot operating system (ROS). We also make use of an existing surgical navigation platform that is used for BCS and describe how to deploy this system to encourage adaptation to other clinical applications.

MATERIALS AND METHODS

The goal of this system is to extend an existing surgical navigation platform for BCS to incorporate haptic feedback in the form of a virtual fixture. A positive margin is created during BCS procedures when the surgeon’s cautery device breaches the tumor, therefore we hypothesize that using the tumor boundary as a forbidden region will help prevent this action.

Image guidance and navigation: This robotic system is a direct extension of the NaviKnife platform which was designed to provide additional navigation in BCS [3]. Traditionally in BCS procedures, a radiologist guides a needle through the tumor before the surgery begins for localization. The NaviKnife system uses electromagnetic (EM) navigation to track this needle relative to the surgeon’s instruments. The platform is comprised of an EM tracker, an ultrasound probe, an electrocautery, and a navigation computer. These tools are all deployed using

the open-source medical imaging software 3D Slicer (www.Slicer.org) and PLUS toolkit (plustoolkit.github.io). A scripted 3D Slicer module is used to complete the NaviKnife workflow, which involves imaging the breast to identify the tumor boundaries around the localization needle. This boundary is identified by placing points on the ultrasound image. The convex hull of these points is then used as a 3D model of the tumor in Slicer. This model is tracked by an EM sensor on the needle (Fig 1.1).

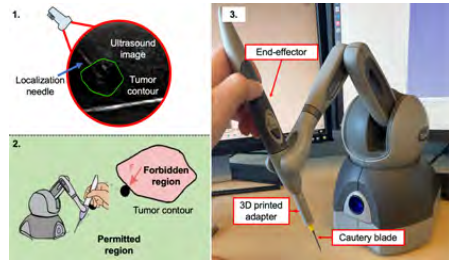


Fig. 1: (1): Tumor contour is identified in ultrasound image. (2): Forbidden region VF implemented around the tumor contour. (3): Modified Omni Bundle robot with electrocautery blade.

The distance between the tip of the surgeon’s cautery and the tumor is then displayed in real time by tracking the localization needle that is inserted into the tumor relative to the cautery. To visualize the distance between the surgeon’s tool and the tumor, a module called “Breach-Warning” available in the SlicerIGT extension is used. This module computes the distance between the tracked tumor model and the tip of the surgeon’s cautery. On its own, the NaviKnife platform provides the surgeon with visual navigation feedback but is still heavily reliant on freehand guidance. Therefore, incorporating robotics has the potential to address this limitation.

Cooperative control: To extend the NaviKnife platform to support a virtual fixture, we incorporate a cooperative robotic device called the Omni Bundle robot (Quanser, Markham, ON, Canada). The end-effector (EE) of the device is modified using a 3D printed adapter to hold the blade of an electrocautery (Fig 1.3). The Omni Bundle device is interfaced with ROS2 using the CISST-SAW libraries (github.com/jhu saw/sawSensablePhantom) and further integrated with 3D Slicer using SlicerROS2 [4]. An admittance type VF is deployed using the cartesian position controller that is available in

sawSensablePhantom, and the aforementioned BreachWarning module. Approximately every 13 ± 18 ms, the distance between the tip of the robot and the tumor model is evaluated. If a collision is detected (ie. the tip of the robot is in anywhere in the tumor), a cartesian position control signal (in the form of a ROS topic) is sent to the Omni Bundle to stay in the current position. This signal corresponds to a position signal for a low-level PID controller and acts like “glue” or friction to help the surgeon identify the tumor boundary. When a collision is not detected, a null force is sent to release the device (Fig 1.2).

Initial experimental evaluation: We evaluate the latency of the applied haptic feedback loop using a 3D tumor model that was extracted from a NaviKnife clinical recording. We consider this model to be a “virtual tumor”. The “virtual tumor” is registered roughly to the center of the workspace in front of the Omni bundle rendering. Users are then asked to move the handle of the Omni bundle freely within the device workspace for 30 seconds without looking at the visualization. As they move through the workspace, we ask them to stop and indicate when they feel force feedback being applied to the handle. When they make this indication, we place a fiducial at the current robot tip position (based on the manipulator’s internal tracking).

RESULTS

Integration: Hardware for the NaviKnife system is interfaced with 3D Slicer using the PLUS toolkit. Although 3D Slicer is cross-platform, PLUS is only supported on Windows 10 and 11 whereas ROS is most commonly used on Linux machines. To address this operating system incompatibility, a peer-to-peer network between a Windows and Linux computer is setup using the OpenIGTLINK interface in 3D Slicer [5] (Fig 2). The Linux device hosts the ROS interface for the Omni Bundle and the NaviKnife display.

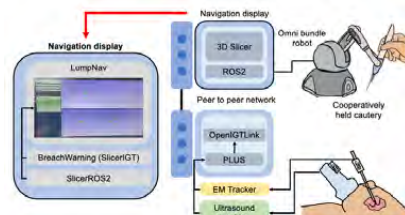


Fig. 2: Software and hardware implementation.

Customization: To implement this VF system in BCS, a scripted 3D Slicer module was written to complement the original SlicerROS2 module. The core logic of this module consists of only 11 lines of python code. This additional code involves instantiating a subscriber and publisher to the cartesian position of the EE of the Omni, as well as a publisher to the servo in the Omni handle. If a collision is detected, the cartesian position of the handle is retrieved from the subscriber and published to the EE. Otherwise, a null wrench is sent to the servo in the Omni bundle handle.

Haptic latency evaluation: Figure 3 demonstrates the results of our haptic latency evaluation for one user. This user indicated that they felt force feedback a total of 10 times, therefore 10 fiducials were added to the scene and all of these fiducials were inside the tumor. We performed the same experiment with 4 users in total, 3 of them only placed fiducials inside of the tumor. One user placed 2 fiducials (out of 5) outside of the tumor. These two fiducials were only 2.0 and 3.4 mm from the surface of the tumor and were likely caused by slight movement of the device between when the user reported haptic feedback and when the fiducial was placed in the scene.

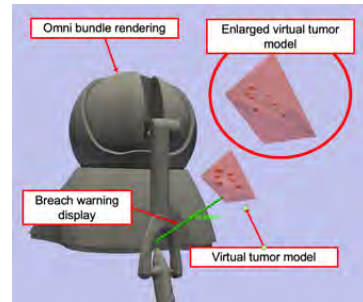


Fig. 3: Screenshot from virtual tumor experiment.

DISCUSSION

We show the feasibility of integrating a forbidden region VF into a 3D Slicer-based navigation platform for BCS. More generally, we present an example image-guided robotic system that can be deployed using SlicerROS2 with minimal customization. This approach can be readily extended to support a broader range of applications. Future work includes scaling this application to other devices and testing on physical models.

REFERENCES

- [1] I. Fleming, M. Balicki, J. Koo, I. Iordachita, B. Mitchell, J. Handa, G. Hager, and R. Taylor, “Cooperative robot assistant for retinal microsurgery,” in International conference on medical image computing and computer-assisted intervention. Springer, 2008, pp. 543–550.
- [2] J. J. Abbott, P. Marayong, and A. M. Okamura, “Haptic virtual fixtures for robot-assisted manipulation,” in Robotics research. Springer, 2007, pp. 49–64.
- [3] G. Gauvin, C. T. Yeo, T. Ungi, S. Merchant, A. Lasso, D. Jabs, T. Vaughan, J. F. Rudan, R. Walker, G. Fichtinger et al., “Realtime electromagnetic navigation for breast-conserving surgery using naviknife technology: A matched case-control study,” The Breast Journal, vol. 26, no. 3, pp. 399–405, 2020.
- [4] L. Connolly, A. Deguet, S. Leonard, J. Tokuda, T. Ungi, A. Krieger, P. Kazanzides, P. Mousavi, G. Fichtinger, and R. H. Taylor, “Bridging 3d slicer and ros2 for image-guided robotic interventions,” Sensors, vol. 22, no. 14, p. 5336, 2022.
- [5] J. Tokuda, G. S. Fischer, X. Papademetris, Z. Yaniv, L. Ibanez, P. Cheng, H. Liu, J. Blevins, J. Arata, A. J. Golby et al., “Openigtlk: an open network protocol for image-guided therapy environment,” The International Journal of Medical Robotics and Computer Assisted Surgery, vol. 5, no. 4, pp. 423–434, 2009.

Optimizing Heart Valve Surgery with Model-Free Catheter Control

A. Bicchi¹, M. Quaquarelli¹, F. Fati¹, E. Votta¹, and E. De Momi¹

¹*Politecnico di Milano, Department of Electronics Information and Bioengineering*

INTRODUCTION

Currently, cardiac catheters for Structural Heart Disease (SHD), are maneuvered manually through the vascular pathway to the chambers of the heart by skilled surgeons. Given the complexity of these maneuvers, we aim at introducing a variable shared autonomy robotic platform for intra-procedural support, by robotizing the commercial MitraClip™ System (MCS). The MCS allows the treatment of mitral regurgitation by percutaneously implanting a clip that grasps the valve leaflets. In light of that, the aim of this paper is to propose a position control strategy that guarantees good trajectory tracking. In the field of control of catheter robots, having a good model is a key point in order to obtain reliable control. A model-based approach on the assumption of a constant curvature (CC) model has been proposed by [1]. The CC model, however, involves simplifying assumptions about catheter shape and external loading, moreover, nonlinearities of the catheter (as dead zones and tendon slack) are usually neglected. In order to include such nonlinearities, the Cosserat Rod model has been exploited by [2]; however, this complicates the model and involves high computational costs which makes the control not feasible in real-time. Model-free controllers based on machine learning represent a valid alternative to analytical models, considering their potential in model uncertainties that strongly influence soft robot control [3]. In [4] they proposed a formulation for learning the inverse kinematics of a continuum manipulator while integrating the end-effector position feedback. We developed a Neural Network based Inverse Kinematic Controller (IKC) shown in the scheme in Fig. 1. The inputs of the net are the target tip pose, \bar{p}_{k+1} at the next time instant, the current servomotors position, q_k , and the current tip pose p_k , while the output is the position of the servomotor at the next time instant q_{k+1} . Our goal is to build a robust control starting from the state-of-the-art control applied to the MCS presented in [5] by X. Zhang et all and adding to it the control also in the orientation of the tip. Moreover, we characterize the control model proposed, by testing its robustness at different motors' velocities.

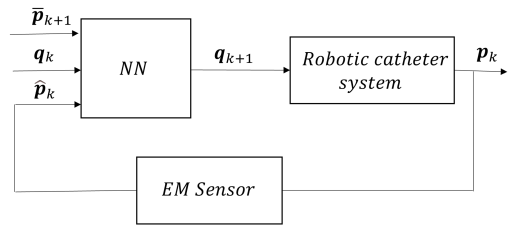


Fig. 1 Scheme of the Inverse Kinematic Controller. The inputs are the desired pose at $k + 1$, \bar{p}_{k+1} , the current servomotors position, q_k , and the current tip pose \hat{p}_k measured by the EM sensor. The output is the position of the servomotor at the next time instant, q_{k+1} .

MATERIALS AND METHODS

The proposed control exploits the Multi-Layer Perceptron (MLP) neural network to learn the non-linear map:

$$(\bar{p}_{k+1}, q_k, \hat{p}_k) \rightarrow (q_{k+1}). \quad (1)$$

As expressed by eq. 1, the inputs are the current measured tip pose, the corresponding motors position, and the tip target pose, while the outputs are the predicted number of motor steps needed to reach it. The data set used for training the NN IKC was generated on the real system by exploring the whole workspace of the catheter. The tip poses associated with motors positions were registered by using the Electromagnetic Sensor Aurora NDI, with a 0.48 mm accuracy on position and 0.30 degrees accuracy on orientation. The Aurora sensor system is composed of an EM field generator and of two 6 DoF sensors, one placed on the base of the system, in order to have a fixed reference frame, and one on the tip of the catheter.

A total of 3500 points covers the complete mapping of the whole workspace (shown in Fig. 2), processed and reduced in order to discard all tip poses where tendons show a slack behavior (no motion produced after actuation). The implemented MLP has 17 input and 3 output neurons with linear activation functions and two hidden layers. The system is composed of a set of two Nema 23 Stepper motors (JoyNano), and one linear actuator Nema 17 Bipolar Stepper Motor (Sainsmart) that are used respectively to pull tendons, for bending the catheter in mediolateral (ML) and anteroposterior (AP) planes, and to move the tip in the forward direction (LIN). Each motor is controlled by a DM556 driver (Jadeshay).

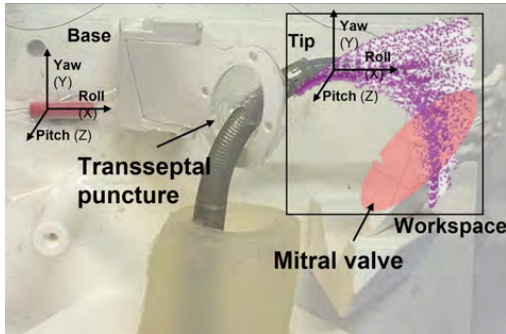


Fig. 2 MitraClip™ System. The image shows the entire catheter workspace after the transseptal puncture approaching the mitral valve. The reference systems of the base (fixed point) and tip are also shown.

and connected to an Arduino Uno microcontroller. In order to test and validate the performances of the proposed method, five different trajectories composed of five points each were tested for real-time kinematic control of the manipulator with the proposed IKC, with respect to the state-of-the-art control of the system [5]. The experiments were conducted for evaluating the performance of the control for path following and target reaching in terms of the Euclidean Distance (ED) :

$$ED = \|\hat{p}_k - \bar{p}_k\|, \quad (2)$$

between the desired position of the tip and the measured one. For all the experiments, the manipulator starts from the home position, and the final target is on the mitral valve, see Fig. 2. Moreover, to test the robustness of control, the tests were performed at 2 different motors' velocities.

RESULTS

To study the performance of the proposed IK controller, the system was tested in tracking five desired trajectories. Two different motors' velocities (60 rpm for AP and ML motors, 120 rpm for LIN one, 90 rpm for AP and ML, then 270 rpm for LIN) were set to simulate slow and fast actuation to characterize the control approach proposed. Each trajectory was repeated 3 times at each speed, and the results were averaged. Our study compared also the performance of data-driven control with the PID model-based control proposed by [5]. The box plots in Fig. 3 show the distribution of the estimated position error (ED) with the proposed IKC applied for the two motors' velocities. It can be noticed that the median of the error with slower motors' velocities is about 2mm, with respect to the 5.5 mm obtained at higher velocity. Moreover in Fig. 3 is reported with a red line the mean value of the error obtained with the PID controller in [5], which is around 5 mm. The data-driven controller outperformed the PID when the motors velocities are set to small values, with an average improvement in tracking error of 3 mm. Moreover, the orientation control in the IKC, reaches an

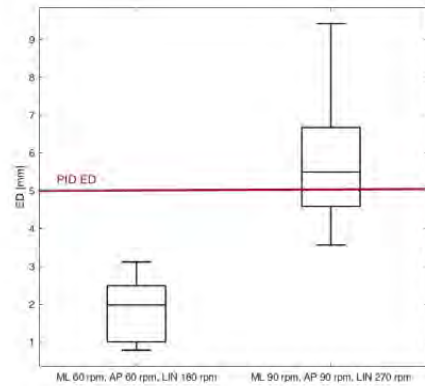


Fig. 3 Box plot of ED, eq. 2 using the IK controller at two motors' velocities and with respect to the results obtained with the PID controller in [5]

accuracy of 1.58 ± 1.02 degrees on the Y-axis (yaw), 1.03 ± 0.35 degrees on the Z-axis (pitch), and 0.59 ± 0.29 degrees on the X-axis (roll). Overall, the results suggest that data-driven control can be a promising alternative to model-based control in challenging scenarios.

DISCUSSION

In conclusion, this paper introduces a machine learning-based kinematic controller for continuum robots and the preliminary validation results of a robotic-assisted system in comparison with a PID state-of-the-art control. Experimental results demonstrated the effectiveness of the proposed method in path tracking if we stay under a certain motor's velocity. In addition, further testing is needed to assess the speed of the motors at which the control begins to degrade performance.

REFERENCES

- [1] Y. Bailly, Y. Amirat, and G. Fried, "Modeling and control of a continuum style microrobot for endovascular surgery," *IEEE Transactions on Robotics*, vol. 27, no. 5, pp. 1024–1030, 2011.
- [2] A. A. Alqumsan, S. Khoo, and M. Norton, "Robust control of continuum robots using cosserat rod theory," *Mechanism and Machine Theory*, vol. 131, pp. 48–61, 2019.
- [3] T. George Thuruthel, Y. Ansari, E. Falotico, and C. Laschi, "Control strategies for soft robotic manipulators: A survey," *Soft robotics*, vol. 5, no. 2, pp. 149–163, 2018.
- [4] T. George Thuruthel, E. Falotico, M. Manti, A. Pratesi, M. Cianchetti, and C. Laschi, "Learning closed loop kinematic controllers for continuum manipulators in unstructured environments," *Soft robotics*, vol. 4, no. 3, pp. 285–296, 2017.
- [5] X. Zhang, M. C. Palumbo, F. Perico, M. Magro, A. Fortuna, T. Magni, E. Votta, A. Segato, and E. De Momi, "Robotic actuation and control of a catheter for structural intervention cardiology," in *2022 IEEE/RSJ International Conference on Intelligent Robots and Systems (IROS)*. IEEE, 2022, pp. 5907–5913.

Percutaneous focal tumour ablation assisted by mini-stereotactic frame: proof-of-concept

Joeana Cambranis-Romero^{1,2}, Terry M. Peters^{1,2,3}, and Elvis C. S. Chen^{1,2,3}

¹*School of Biomedical Engineering, Western University, London, Ontario, Canada,*

²*Robarts Research Institute, Western University, London, Ontario, Canada,*

³*Department of Medical Biophysics, Western University, London, Ontario, Canada*

jcambran@uwo.ca

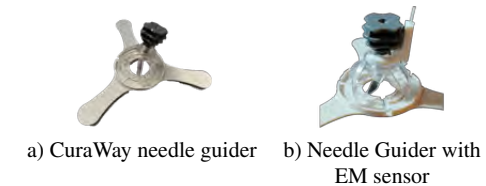
INTRODUCTION

The success of percutaneous focal tumour ablation largely depends on precise needle placement: an ablation zone, typically described as an ellipsoid centred on the ablation active needle tip, needs to completely enclose the tumour with a positive margin [1]. To facilitate precise needle placement, many types of needle guidance devices were developed, providing mechanical support and improving the targeting of the lesion [2]. Designs of these guiding apparatuses vary, including those that are rigidly attached to the Ultrasound (US) probe, enforcing the “in-plane” needle insertion. This type of targeting device forcefully maintains the needle within the US plane with the potential to improve the targeting accuracy, but at the same time, limits the entry angles of the needle and US probe placement. Other designs include mechanical and robotic (i.e., with electronic characteristics) guiders, which are large and need to be attached/positioned close to the surgical table, potentially restricting the range of movement of the healthcare providers (i.e., physicians and nurses) [3]. In this paper, we present a proof-of-principle surgical navigation system based on a disposable mini-stereotactic frame, which provides mechanical support for precise needle guidance. The pose of this stereotactic needle guider is magnetically tracked and calibrated, allowing the surgeon to visualize the potential needle trajectory in a 3D Virtual Reality (VR) environment prior to needle insertion.

MATERIALS AND METHODS

A 3D Slicer module was developed as a VR platform for surgical navigation based on streaming US images, and a patient-attached “mini” aiming device (CuraWay Medical Technology, China) with stereotactic characteristics as shown in Figure 1a. A magnetic tracking system (Aurora, Northern Digital Inc., CA) was deployed to track all the surgical apparatuses.

The main component of our approach is the aiming device which comprises a gimble mechanism with a metallic hollow tube at the turntable allowing a range of angular

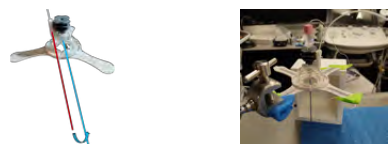


a) CuraWay needle guider b) Needle Guider with EM sensor

Fig. 1 Patient-attached “mini” aiming device.

movement of $\approx 180^\circ$. The turntable has an easy locking mechanism that rigidly secures the angular positioning of the metallic tube relative to its base. A magnetic pose sensor was attached to the turntable, using a custom clamp (Figure 1b), to track the guider. A 3D needle model is then displayed within the VR 3D Slicer module acting as a virtual path/pointer.

To ensure the correct display of the virtual path, we devised a spatial calibration technique to align the long axis of the metallic tube to the magnetic pose sensor using a least-squares solution. To perform the calibration a pre-calibrated needle (Aurora 5 DOF Needle, 18G, NDI, Canada) was slowly inserted into the guider tube, acting as a stylet and ground truth. The transformation matrices, relating the pose of the needle with respect to the guider, were used to perform the calibration. As shown in Figure 2b, the needle was subject to no bending.



a) Incorrect path display (red), b) Calibration setup. correct path display (blue).

Fig. 2 Calibration explanation and setup.

The visualization within the 3D Slicer module is customized based on the geometry of the ablation applicator

and the ablation zone (based on the manufacturer's specification). The accuracy of the virtual path projection, i.e. calibration of the stereotactic frame, was assessed by performing two analyses: a rotational and a translational error. For both experiments, a pre-calibrated needle (ground truth) was completely inserted into the guider without bending, then the guider was positioned in ten different orientations around the device's range of angular movement. For each position, both transformation matrices, the needle, and the calibrated sensor in the guider were saved to perform the error analyses. The resultant calibration matrix was applied to the real-time tracking information of the guider sensor, adjusting the virtual path position, as shown in Figure 2a.

RESULTS

A typical surgical navigation using the stereotactic frame is visualized in Figure 3: the virtual path (green) follows the same direction, and position, as the ground truth model (yellow), when the latest is inserted into the aiming device. The virtual path depth can be adjusted in the 3D Slicer module depending on the needs of each ablation case.

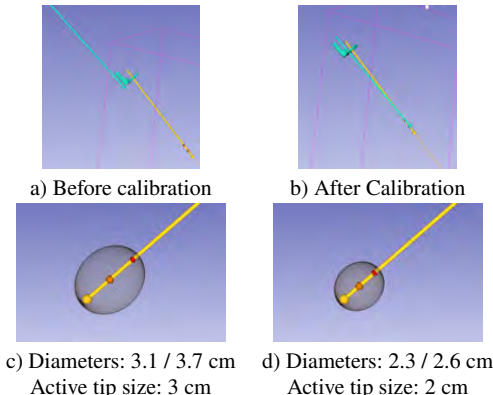


Fig. 3 Guider calibration visual results. Virtual path position (green) and ground truth, needle model (yellow).

Figure 3c and 3d show the visualization of two different estimated ablation zone at the active tip of the needle. The geometry of the ablation zone can be updated by changing the parameters in the 3D Slicer module, always maintaining its center on the needle's active tip. The visualization of the ablation zone can be turned on and off, and its opacity can be adjusted depending on the user's needs. A slice-intersection was applied so the ablation zone periphery is superimposed on the 2D US images in real-time.

Figure 4 shows an example of the visualization of the estimated ablation zone and virtual path in a virtual environment (3D) and superimposed upon the 2D US image of a liver phantom designed in our lab.

Table I summarizes the rotational and translational error results. The angular accuracy of the path projected by the



Real-life setup and virtual environment

Fig. 4 Ablation zone and virtual path surrounding the tumour, in a virtual environment and superimposed to the US image of a phantom. The real-life setup is at the right.

guider is $(2.19 \pm 0.16^\circ)$ and the accuracy of the active tip position is $(2.76 \pm 1.11 \text{ mm})$.

TABLE I Guider accuracy analysis results

Position #	Rotation analysis	Euclidean distance between tips.
1	2.14°	0.75 mm
2	2.36°	1.6 mm
3	2.09°	2.45 mm
4	2.56°	1.71 mm
5	1.95°	2.77 mm
6	2.18°	3.55 mm
7	2.14°	3.68 mm
8	2.20°	3.21 mm
9	2.11°	4.18 mm
10	2.13°	3.7 mm

DISCUSSION

The work presented here demonstrates a successful validation of the use of a mini-stereotactic frame as a guidance system. The pre-aiming given by the needle guider allows an "out of plane" approach, offering the exploration of alternative entry points while not limiting the US probe placement and the guider small size suggests non-interference with the healthcare providers. The 3D Slicer module's possibility of adjusting the parameters of the needle and ablation zone provides a wide guidance system for percutaneous procedures. While further testing is required to assess the clinical viability, these initial results suggest that the combination of the path projection and ablation zone display can assist percutaneous ablation procedures in the accurate placement of the active tip while ensuring complete tumour coverage.

REFERENCES

- [1] J. A. Collins, J. S. Heiselman, L. W. Clements, D. B. Brown, and M. I. Miga, "Multiphysics modeling toward enhanced guidance in hepatic microwave ablation: a preliminary framework," *Journal of Medical Imaging*, vol. 6, no. 2, pp. 1 – 10, 2019.
- [2] D. Wallach, G. Toporek, S. Weber, R. Bale, and G. Widmann, "Comparison of freehand-navigated and aiming device-navigated targeting of liver lesions," *The International Journal of Medical Robotics and Computer Assisted Surgery*, vol. 10, no. 1, pp. 35–43, 2014.
- [3] N. Hungr, I. Bricault, P. Cinquin, and C. Fouard, "Design and Validation of a CT-and MRI-Guided Robot for Percutaneous Needle Procedures," *IEEE Transactions on Robotics*, vol. 32, no. 4, pp. 973–987, 2016.

finding the sequence of proximal controls $\pi_{(t+1, \dots, t+n)}^{prox}$ that minimizes estimation cost C . Then, the problem follows:

$$\hat{\pi}^* = \underset{\pi_{(t+1, \dots, t+n)} \in \Pi}{\operatorname{argmin}} C(\pi_t^{prox}, \hat{x}_{(t+1, \dots, t+n)}^{tip} | \mathbf{p}, \mathbf{e}), \quad (3)$$

where t is the current time and n is the long-term time step. Creating a scalable environment is an important step in getting a better quality of learning-based controls for intelligent agents. Physics-based simulators are commonly used nowadays in various practical fields (*e.g.*, self-driving cars, pick-and-place) to improve the qualities of controls. Similarly, we create the pre-processing pipeline with 3D CTA images and 3D device simulation to create a scalable environment. Figure 3 shows the overall pre-processing pipeline for scalable data. First, given 3D CTA images (Fig. 3(a)), the corresponding 3D segmentation of the whole coronary vessels is computed (Fig. 3(b)). Then, the 3D level set distance map that contains the minimum distance to the vessels at each 3D point is computed to define the boundary conditions (Fig. 3(c)). Finally, we apply the desired force to the proximal section of the wire using the Cosserat-rod model in the simulator, which interacts with the defined boundary conditions by solving partial differential equations. Finally, this provides the scalable simulated device states inside the vessel (Fig. 3(d)).

We reformulate the control problem to a sequence-to-sequence learning problem, which we address using attention-mechanism-based architecture, Transformer model [6]. We use created data from the pre-processing pipeline to train the Transformer model. Our system inherently requires an open loop where spatial feedback of devices is not continuously available due to the radiation limit of X-rays. We train \mathcal{FF} and \mathcal{IF} as dual Transformer models to iteratively update each history of states over time. The input/output are described in Eq (1)(2). Then, we can finally estimate a long sequence of state information (*i.e.*, $\hat{x}_{(t+1, \dots, t+n)}^{tip}$ and $\pi_{(t+1, \dots, t+n)}^{prox}$, $\hat{\pi}_{(t+1, \dots, t+n)}^{prox}$).

We used 100 CTA images for the right coronary artery as a simulator environment, and applied 1000 randomly generated continuous sequential controls of π^{prox} for 60 seconds, which generated 120 sequence sample points for each set. We used 80% data as the training set and used 20% for the testing set. We then present the safety ratio and difference between the estimated force and the ground-truth in the test set.

Both forward/inverse transformer models are learned with 30 sequences of states as inputs, 1 output (Many-to-one), 12 heads, 4 encoder/decoder layers, 128 dimensions of feedforward, and 0.1 dropouts. The learning rate was set



Fig. 3 Pre-processing pipeline from 3D CTA to simulated catheter insertion: (a) 3D CTA images, (b) 3D segmentation, centerline, and vessel sectional labeling, (c) Vessel boundary distance map, (d) Physics-based simulation of an inserted catheter after proximal force application

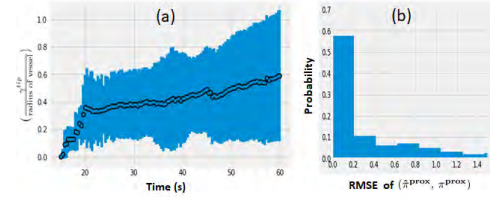


Fig. 4 Performance evaluation: (a) The safety ratio from $\frac{y^{tip}}{\text{radius of vessel}}$ for operation time, and (b) Histogram of RMSE between $\hat{\pi}^{prox}$ and π^{prox}

to be $1e^{-3}$ for 20 epochs with Adam optimizer in Pytorch.

RESULTS

We assumed the first 30 states of \hat{x}^{tip} are given as measurements. Then, we update states using \mathcal{FF} and \mathcal{IF} iteratively over time. Figure 4 (a) shows a ratio of $\frac{y^{tip}}{\text{radius of vessel}}$ for the test set, where 0 means the tip is located in the centerline while approaching to 1 represents the tip is close to the vessel wall, which means we might need to obtain new measurements from X-ray in time. The radius of the vessel that we tested is between 0.7 mm and 2 mm. Figure 4 (b) shows the distribution of our control output errors by computing errors between the ground-truth of π^{prox} and our estimation $\hat{\pi}^{prox}$.

DISCUSSION

Based on our results, our AI-based agents might provide an efficient approach to indicate when to turn on/off X-ray. As a future work, we plan to investigate more sophisticated controls for complicated scenarios with a systematic evaluation. In addition, we plan to apply various parameters to handle uncertainty.

DISCLAIMER

The concepts and information presented in this paper are based on research results that are not commercially available. Future availability cannot be guaranteed.

REFERENCES

- [1] H. Rafii-Tari, C. Payne, and G.-Z. Yang, "Current and emerging robot-assisted endovascular catheterization technologies: A review," *Annals of biomedical engineering*, vol. 42, 11 2013.
- [2] W. Duan, T. Akinyemi, W. Du, J. Ma, X. Chen, F. Wang, O. Omisore, J. Luo, H. Wang, and L. Wang, "Technical and clinical progress on robot-assisted endovascular interventions: A review," *Micromachines*, vol. 14, no. 1, p. 197, Jan 2023.
- [3] R. Madder, W. Lombardi, M. Parikh, D. Kandzari, J. Grantham, and S. Rao, "Impact of a Novel Advanced Robotic Wiring Algorithm on Time to Wire a Coronary Artery Bifurcation in a Porcine Model," *Journal of the American College of Cardiology*, vol. 70, no. 80, 2017.
- [4] Y.-H. Kim, A. Kapoor, R. Finocchi, and E. Girard, "Evaluation of High-Speed Dynamic Motions for Robotic Guidewire Crossing Techniques," in *Hamlyn Symposium on Medical Robotics*, London, UK, 2018.
- [5] ———, "An experimental validation of behavior-based motions for robotic coronary guidewire crossing techniques," in *Proceedings of the International Symposium on Experimental Robotics*, Buenos Aires, Argentina, 2018, pp. 14–23.
- [6] A. Vaswani, N. Shazeer, N. Parmar, J. Uszkoreit, L. Jones, A. N. Gomez, L. u. Kaiser, and I. Polosukhin, "Attention is all you need," in *Advances in Neural Information Processing Systems*, vol. 30, 2017.

AI-based Agents for Automated Robotic Endovascular Guidewire Manipulation

Young-Ho Kim¹, Èric Lluch¹, Gulsun Mehmet¹, Florin C. Ghesu¹, and Ankur Kapoor¹

¹Digital Technology & Innovation, Siemens Healthineers, Princeton, NJ, USA,
(young-ho.kim, eric.lluch, akif.gulsun, florin.ghesu, ankur.kapoor)@siemens-healthineers.com

INTRODUCTION

An endovascular guidewire manipulation is essential for minimally-invasive clinical applications; Percutaneous Coronary Intervention (PCI) is used to open narrowed coronary arteries and restore arterial blood flow to heart tissue, Mechanical thrombectomy techniques for acute ischemic stroke (AIS) to remove blood clots from the brain veins, and Transjugular intrahepatic portosystemic shunt (TIPS) for liver portal hypertension use a special needle and position a wire between the portal vein through the liver. All procedures commonly require 3D vessel geometries from 3D CTA (Computed Tomography Angiography) images (Fig. 1). During these procedures, the clinician generally places a guiding catheter in the ostium of the relevant vessel and then manipulates a wire through the catheter and across the blockage. The clinician only uses X-ray fluoroscopy intermittently to visualize and guide the catheter, guidewire, and other devices (*e.g.*, angioplasty balloons and stents). Various types of endovascular robot-assisted systems [1, 2] are being developed to provide efficient positional control of devices, helping clinicians to mitigate therapeutical risks. The primary motions that a clinician can use to control the movement and direction of the wire are rotation and pushing/retracting from the proximal end of the wire outside the insertion point on the patient's body.

Even with these robotic devices, clinicians passively control guidewires/catheters by relying on limited indirect observation (*i.e.*, 2D partial view of devices, and intermittent updates due to radiation limit) from X-ray fluoroscopy. Modeling and controlling the guidewire manipulation in coronary vessels remains challenging because of the complicated interaction between guidewire motions with different physical properties (*i.e.*, loads, coating) and vessel geometries with lumen conditions resulting in a highly non-linear system. Thus the recent literature has focused on behavior-based automated motion controls; Madder et al. [3] proposed the first known automatic guidewire retraction motions with a rotation of 180° to cannulate a coronary artery bifurcation; In addition, robotic crossing techniques

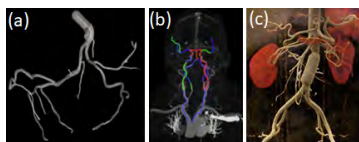


Fig. 1 3D vessel geometries are used for the clinical planning of various endovascular treatments: 1) Percutaneous Coronary Intervention (PCI) in a coronary vessel, 2) Cerebral thrombectomy for acute ischemic stroke (AIS), 3) Transjugular intrahepatic portosystemic shunt (TIPS) for liver portal hypertension

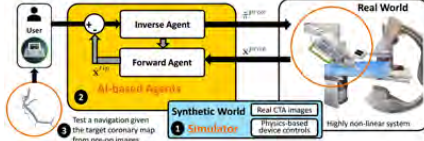


Fig. 2 An overview of the proposed AI-based agents, trained by created synthetic data using real CTA images and physics-based device controls.

have demonstrated to generate distal guidewire motions that take advantage of the fast response of the robot system, and it's autonomous and collaborative controls [4, 5].

This paper introduces a scalable learning pipeline to train AI-based agent models toward automated endovascular predictive device controls. Figure 2 shows an overview of an endovascular predictive control workflow. Specifically, we create a scalable environment by pre-processing 3D CTA images, providing patient-specific 3D vessel geometry and the centerline of the coronary. Next, we apply a large quantity of randomly generated motion sequences from the proximal end to generate wire states associated with each environment using a physics-based device simulator. Then, we reformulate the control problem to a sequence-to-sequence learning problem, in which we use a Transformer-based model, trained to handle non-linear sequential forward/inverse transition functions.

MATERIALS AND METHODS

At the torquer's attachment point to the robot, the wire's proximal state, $\mathbf{x}^{prox} \equiv (\Delta, \phi)$, has a translation Δ and rotation ϕ . At the distal (tip) of the wire, the state \mathbf{x}^{tip} is defined by its position and orientation in $SE(3)$. The physical parameters of the wire are defined as \mathbf{p} , including diameter, Poisson ratio, Young modulus, number of elements, etc. Let $\mathbf{e} \in \mathcal{E}$ represent the spatial environment of the vessel, including 3D vessel geometry, 3D vessel centerline, and sectional labels.

Since we do not have a direct measurement for the tip of the guidewire, we simplify $\mathbf{x}^{tip} \in \mathbb{R}^3$ with regard to the 3D vessel centerline by projecting it into known 3D vessel centerline. Then, $\mathbf{x}^{tip} \approx \hat{\mathbf{x}}^{tip} = \langle \Delta^{tip}, \gamma^{tip} \rangle$ where Δ^{tip} and γ^{tip} represent the translation along the centerline and the distance from the centerline to the tip, respectively.

Then our manipulation system can be treated as a forward/inverse transition function \mathcal{FF} and \mathcal{IF} with control $\pi^{prox} \in \Pi$ to transition from one state to another state given physical parameters \mathbf{p} and the spatial environment of vessel \mathbf{e} :

$$\hat{\mathbf{x}}_{t+1}^{tip} = \mathcal{FF}(\hat{\mathbf{x}}_t, \mathbf{x}_{t+1}^{prox}, \pi_{t+1}^{prox}; \mathbf{p}, \mathbf{e}), \quad (1)$$

$$\hat{\mathbf{x}}_{t+1}^{prox}, \hat{\pi}_{t+1}^{prox} = \mathcal{IF}(\hat{\mathbf{x}}_{t+1}^{tip}, \mathbf{x}_t^{prox}, \pi_t^{prox}; \mathbf{p}, \mathbf{e}) \quad (2)$$

Given \mathbf{p} and \mathbf{e} , manipulate the wire to the desired tip state $\hat{\mathbf{x}}_{(t+1, \dots, t+n)}^{tip}$, making all state transitions via π^{prox} and

Losing Focus: Can It Be Useful in Robotic Laser Surgery?

N.E. Pacheco, Y.A. Garje, A. Rohra, L. Fichera

*Department of Robotics Engineering
Worcester Polytechnic Institute, USA
nepacheco@wpi.edu*

INTRODUCTION

Lasers are an essential tool in modern medical practice, and their applications span a wide spectrum of specialties. In laryngeal microsurgery, lasers are frequently used to excise tumors from the vocal folds [1]. Several research groups have recently developed robotic systems for these procedures [2-4], with the goal of providing enhanced laser aiming and cutting precision.

Within this area of research, one of the problems that has received considerable attention is the automatic control of the laser focus. Briefly, *laser focusing* refers to the process of optically adjusting a laser beam so that it is concentrated in a small, well-defined spot – see Fig. 1. In surgical applications, tight laser focusing is desirable to maximize cutting efficiency and precision; yet, focusing can be hard to perform manually, as even slight variations ($< 1 \text{ mm}$) in the focal distance can significantly affect the spot size. Motivated by these challenges, Kundrat and Schoob [3] recently introduced a technique to robotically maintain constant focal distance, thus enabling accurate, consistent cutting. In another study, Geraldès et al. [4] developed an automatic focus control system based on a miniaturized varifocal mirror, and they obtained spot sizes as small as $380 \mu\text{m}$ for a CO₂ laser beam.

Whereas previous work has mainly dealt with the problem of creating – and maintaining – small laser spots, in this paper we propose to study the utility of defocusing surgical lasers. In clinical practice, physicians defocus a laser beam whenever they wish to change its effect from cutting to heating – e.g., to thermally seal a blood vessel [5]. To the best of our knowledge, no previous work has studied the problem of robotically regulating the laser focus to achieve controlled tissue heating, which is precisely the contribution of the present manuscript.

In the following sections, we first briefly review the dynamics of thermal laser-tissue interactions and then propose a controller capable of heating tissue according to a prescribed temperature profile. Laser-tissue interactions are generally considered hard to control due to the inherent inhomogeneity of biological tissue [6], which can create significant variability in its thermal response to laser irradiation. In this paper, we use methods from nonlinear control theory to synthesize a temperature controller capable of working on virtually any tissue type without any prior knowledge of its physical properties.

MATERIALS AND METHODS

Problem Formulation. Let us consider a scenario where a tissue specimen is exposed to a laser beam of intensity

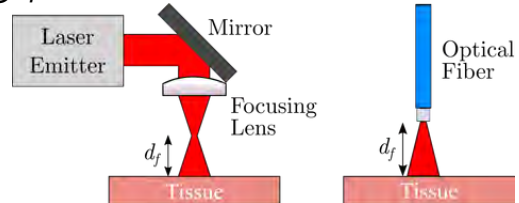


Fig. 1: The goal of laser focusing is to create a spot size of prescribed width via the control of d_f , i.e., the distance between the laser beam's focal point and the tissue surface. (Left) In *free beam* systems, the location of the focal point depends on the characteristics of the lenses used to focus the beam. (Right) In fiber-based systems, laser light diverges immediately upon exiting the fiber, with an angle determined by the numerical aperture of the fiber itself. In this manuscript, we study how regulating d_f can be used to produce controlled tissue heating.

$\mathbf{I} (\text{W/cm}^2)$. The problem we wish to solve is to control the tissue temperature at the point of incidence of the laser. We assume that the laser beam can only be moved vertically with respect to the tissue, i.e., that the only variable we can control is the distance d_f between the tissue surface and the beam's focal point – refer to Fig. 1.

Preliminaries. From [7], the temperature dynamics of laser-irradiated tissue can be modeled as:

$$c_v \frac{\partial \mathbf{T}}{\partial t} = \kappa \nabla^2 \mathbf{T} + \mu_a \mathbf{I} \quad (1)$$

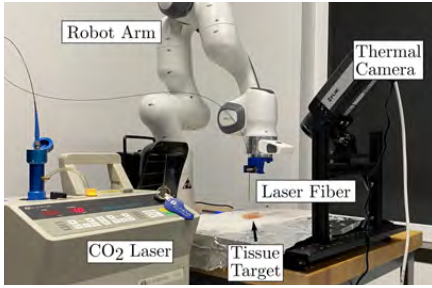
where \mathbf{T} represents the tissue temperature as a function of space and time, and c_v , κ , and μ_a are three tissue-specific physical parameters – namely, the *volumetric heat capacity*, the *thermal conductivity*, and the *coefficient of absorption*. We note that these parameters are rarely known with certainty, as different types of tissue will generally have different physical properties, and significant variations are possible even within specimens of the same tissue type [6].

We can regulate the beam intensity \mathbf{I} in Eq. (1) by varying d_f . Most surgical lasers produce a Gaussian beam with peak intensity I_{peak} , which can be related to d_f through simple optics calculations [7]:

$$d_f = \frac{\pi w^2}{\lambda} \sqrt{\frac{2P}{I_{\text{peak}} \pi w^2} - 1} \quad (2)$$

Here, w is the beam waist (i.e., the radius at which the beam intensity fades to $1/e$ of its peak value, measured at the focal point), λ is the laser wavelength, and P is the laser optical power.

Controller Synthesis. To control the tissue temperature, we synthesize an adaptive controller – this is a well-known family of control methods for systems with uncertain or time-varying parameters. Let us define a control law for the intensity I_{peak} as follows:

**Fig. 2:** Experimental Setup.

$$I_{peak}(t) = \hat{a}_T T_{peak} + \hat{a}_f f(T_{surf}) + \hat{a}_r r(t) \quad (3)$$

where t represents time, $r(t)$ is a prescribed temperature profile that we wish to create at the laser point of incidence, T_{surf} is the tissue surface temperature, and T_{peak} is the surface temperature at the point of incidence – these latter two quantities are assumed to be measurable with a suitable sensor. In the equation above, $f(T_{surf})$ numerically approximates the heat conduction term in Eq. (1), while \hat{a}_T , \hat{a}_f , and \hat{a}_r are three scalar coefficients. As sequential temperature measurements become available over time, the adaptive controller updates \hat{a}_T , \hat{a}_f , and \hat{a}_r in such a way to minimize the error between the observed temperature T_{peak} and the desired temperature r .

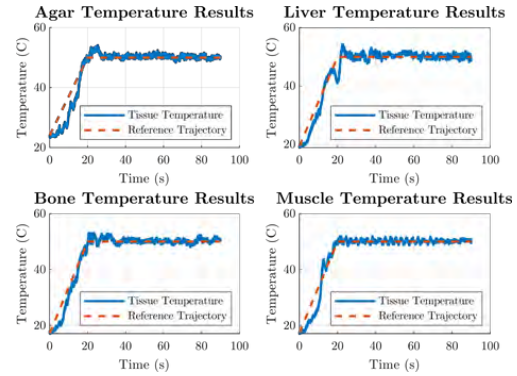
Ex-vivo Experiments. The controller's performance was verified in experiments on ex-vivo tissue, using the setup shown in Fig. 2. The experiments used a surgical CO₂ laser, the Sharplan 30C (Lumenis Ltd., Israel), whose beam is delivered through an optical fiber. The distance d_f between the fiber tip and the tissue is controlled by a Panda robotic arm (Franka Emika GmbH, Germany). The tissue surface temperature is monitored with an A655sc thermal camera (Teledyne FLIR, Oregon, USA) at a rate of 100 fps.

We carried out experiments on four different types of tissue, namely, soft tissue phantoms (2% agar gelatin), bovine liver, bovine bone, and chicken muscle. We note that these tissue types are not representative of what is normally encountered in laryngeal microsurgery and that our goal in this proof-of-principle study is to evaluate the controller's performance for a wide range of optical and thermal tissue properties.

In each experiment, we prescribed a temperature profile $r(t)$ which linearly ramps up to 50 °C, then remains constant for 70 seconds. We carried out five repetitions for each experimental condition, for a total of 20 experiments. All experiments used the same initial values for the controller's parameters, i.e., $\hat{a}_T = 0.152$, $\hat{a}_f = -0.288$, and $\hat{a}_r = 1$, which were obtained by tuning the controller's response on the gelatin phantoms.

RESULTS

Results are shown in Fig. 3. We observed a tracking error (RMSE) of 2.46 °C on gelatin, 1.95 °C on liver, 1.84 °C on bone, and 2.07 °C on muscle, with standard deviations of 0.2 °C, 0.09 °C, 0.25 °C, and 0.29 °C, respectively.

**Fig. 3:** Experimental results. Of the five trials performed on each tissue type, here we report the ones where we observed the median within-group RMSE.

DISCUSSION

Results indicate the viability of controlling tissue heating by robotically regulating the laser focus. The proposed controller achieved consistent temperature tracking across all four experimental conditions, suggesting that it is robust to variations in the physical properties of the tissue being irradiated. While these results have been obtained with a specific laser (CO₂), the proposed controller can be rapidly adapted to work with other types of surgical lasers, so long the wavelength λ is known.

An obvious limitation of the proposed controller is that it can only regulate the temperature at a single spot. In future work, we plan to extend the approach presented herein to enable temperature control of a user-defined region of interest. This will require (a) extending the controller to generate 3D motion profiles for the laser and (b) extending the temperature dynamics formulation of Eq. (1) to account for the movement of the laser.

REFERENCES

- [1] Rubinstein M, Armstrong WB. Transoral laser microsurgery for laryngeal cancer: A primer and review of laser dosimetry. *Lasers Med Sci*. 2011 Jan;26(1):113-24.
- [2] Mattox LS et al. μRALP and Beyond: Micro-Technologies and Systems for Robot-Assisted Endoscopic Laser Microsurgery. *Front Robot AI* 2021;8
- [3] Kundra D, et al. Toward Assistive Technologies for Focus Adjustment in Teleoperated Robotic Non-Contact Laser Surgery. *IEEE Transactions on Medical Robotics and Bionics*. 2019 Aug;1(3):145-57.
- [4] Geraldes A, et al. A focus control system based on varifocal mirror for CO₂ Fiber-coupled laser surgery. *IEEE Transactions on Medical Robotics and Bionics*. 2021;3(4):878-87.
- [5] Giglio NC, et al. Reciprocating side-firing fiber for laser sealing of blood vessels. *Proc. SPIE*. 2022 March 03; 1193602.
- [6] Jacques SL. Optical properties of biological tissues: a review. *Phys Med Biol*. 2013 Jun 7;58(11):R37-R61.
- [7] Lee HC, et al. When the end effector is a laser: a review of robotics in laser surgery. *Advanced Intelligent Systems*. 2022 Sep 13;4(10):2200130.

Design and Evaluation of a Sealing Valve Mechanism for Stoma Patients

Maleeha Al-Hamadani¹, Carlo A. Seneci¹

¹Institute for Biomedical Engineering and Imaging Sciences, King's College London
{maleeha.al-hamadani, carlo.seneci}@kcl.ac.uk

INTRODUCTION

Bowel cancer and other bowel conditions are becoming increasingly dominant in the UK across all age groups. Every year, around 21,000 patients undergo stoma formation surgery, leading to either a temporary or permanent stoma being fitted [1]. Stoma management presents many complications that lead to extensive physical and psychological burdens, including aesthetics, leakage, production of unpleasant odour, skin blistering and infection, all contributing towards a more complex social life [2][3]. The current state-of-the-art technology failed to produce a solution that overcomes the aforementioned complications and research in the field is only addressing some complications without providing a solution to address them all.

In this study, we have designed and manufactured a proof-of-concept prototype of a controllable valve, aiming to overcome the physical and psychological burden by eliminating the use of an actual stoma bag and allowing the patient to have full control over the stool release. With the sealable valve, stoma patients would be able to improve their quality of life. The proof-of-concept valve is then evaluated through two different experiments for validating the leakage-free mechanism, one through a static experiment and the second through a dynamic motion experiment.

MATERIALS AND METHODS

Design and Fabrication of the valve - The valve design consists of an hourglass-shaped silicone valve with an upper ring and a lower ring as seen in Figure 1. The sleeve was moulded with the silicone Ecoflex 00-30 (Bentley Advanced Materials, Feltham, England) in 3D printed moulds. The silicone was left for four hours to be cured and was removed from the mould manually. The upper ring, lower ring and stoma plug are plastic rigid parts that were manufactured using the Selective Laser Sintering (SLS) 3D printing technique. The Silicone valve was then inserted into the stoma plug and the lower ring was fixed in place, whereas the upper ring was free to rotate in an anticlockwise motion (closing the valve) and clockwise motion (opening the valve).

Static Experiment for Valve Sealing – The first experiment aimed to test the valve under static motion and to consider the angle required to seal the valve. First, the stoma plug was fixed to a water bag with a known water volume and a known weight of the bag. The sleeve

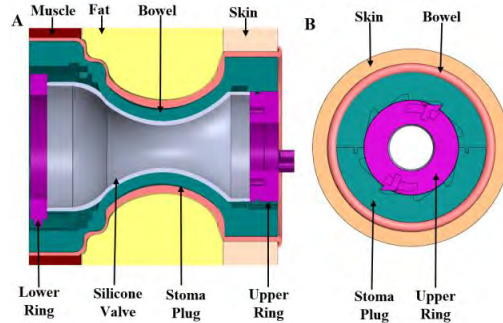


Fig. 1 A) CAD assembly of the silicone valve inserted in a stoma plug. The stoma lug is inserted into a conventional stoma site though the abdominal wall. B) Front view of the stoma plug showing the manual user interface upper ring.

was rotated at various degrees and for each number of degrees chosen, the valve was left for 24 hours before the water bag was weighed again. The setup experiment can be seen in Figure 2.



Fig. 2 Stoma Plug is fit into the filled water bag and was tested over 3 consecutive angle degrees. For each amount of degree, the water bag was weighed before the experiment timeline and after the timeline to determine the rotation degree required to seal the valve completely.

Dynamic Motion Experiment for Valve Sealing – KUKA Framework – To evaluate the valve in a dynamic environment, we have designed a framework using a 7 DoF KUKA arm robot (KUKA LBR, Augsburg, Germany). First, to mimic human motion, an Aurora Sensor (NDI, Ontario, CA) was attached to a participant and the position of the sensor in x, y and z directions were recorded while the participant was performing a jumping motion. The jumping motion was chosen due

to the kinetic energy being applied to the valve would be higher compared to walking or jogging. Therefore, the valve can be tested under an extreme condition. The data was recorded, analyzed, and mapped into the KUKA arm using various software including MATLAB for analysing the data, and C++ for controlling the motion of the robot arm.

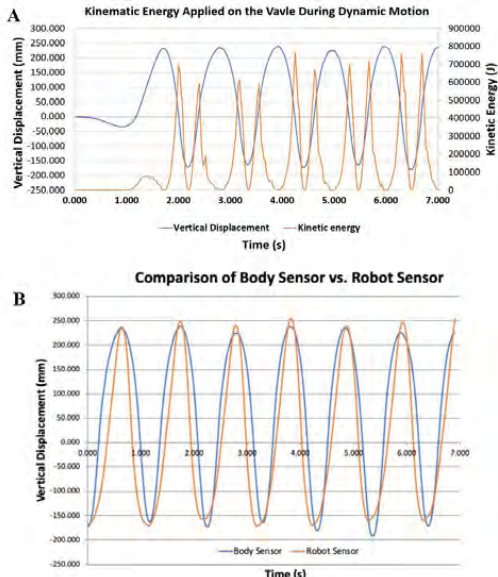


Fig. 3 A) Kinetic Energy is applied to the valve during the dynamic motion of the KUKA robot over time. B) Comparison of the vertical displacement of KUKA motion compared to the Aurora sensor over time.

The stoma plug was then inserted into an abdominal wall phantom made of different silicone materials to resemble the skin, fat, and muscles as seen in Figure 4. Alongside the phantom, a water bag was filled with water and attached to the back of the stoma plug. The entire assembly was then inserted into a box which then the box was connected to the KUKA arm shown in Figure 4.

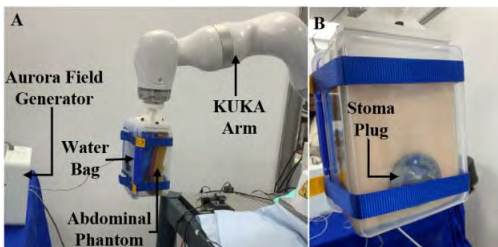


Fig. 4 A) KUKA Arm robot carrying the assembly box with abdominal wall phantom and valve inside while performing the motion in front of Aurora Field Generator for motion recording. B) close-up front view of the assembly box showing the stoma plug. The user interface was not yet incorporated, however, the silicone valve was rotated in the same manner and fixed in place using screws.

RESULTS

The results from the static experiment are shown in Table 1. The table shows the weight of the water bag before and after the experiment showing the best degree of rotation to achieve a fully sealed valve is 720° rotation.

Table. 1 Number of rotation degrees for choosing the optimal degree for achieving a fully sealable valve.

Day	Degrees (°C)	Weight 1 (g)	Weight 2 (g)	Weight Loss (g) (mL)
1	360	698.2	238.3	459.9 459.9
2	540	690.0	228.6	461.4 461.4
3	720	690.1	688.4	1.7 1.7

During the dynamic motion experiment, the valve was subjected to the jumping motion at different speeds by controlling the speed of the KUKA arm. During the series of rounds, there was no leakage detected inside the box which validates the number of rotations required to seal the valve fully and the capability to withstand the jumping motion at different speeds without damaging the valve.

DISCUSSION

In this work, we have described the process of manufacturing a sealable silicone valve to prevent leakage for stoma patients. Two experiments were designed including the validation of the valve functionality based on a static condition and dynamic motion condition. Both experiments have shown promising results in achieving a leakage-free valve aiming to eliminate the use of a stoma bag. Therefore, allowing patients to gain control over stool release. Future work includes further investigation and testing the valve in various motions such as sitting and standing up, walking, jogging and other activities performed on daily basis. Moreover, designing a mechanism for the stoma plug to be fixed inside the stoma site.

ACKNOWLEDGMENTS

The authors would like to thank the Cancer Bowel Research UK for supporting the project and providing us with valuable information regarding stoma management and ostomy care.

REFERENCES

- [1] Hubbard, G., Taylor, C., Beeken, B., Campbell, A., Gracey, J., Grime, C., Fisher, A., Ozakinci, G., Slater, S. and Gorely, T. "Research priorities about stoma-related quality of life from the perspective of people with a stoma: A pilot survey," *PMC*, vol. 20, no. 6, pp.1421-1427, 2017.
- [2] Krishnamurti, D., Blatnik, J. and Mutch, M. "Stoma Complications," *PMC*, vol. 30, no. 3, pp.193-201, Jul 2017.
- [3] Reese, J., et al. "Gastrointestinal ostomies and sexual outcomes: a comparison of colorectal cancer patients by ostomy status," *Supportive Care in Cancer*, vol. 22, no. 2, pp.461-468, Feb 2014

Simulating Mesh Cutting with the dVRK in Unity

Kanishkan M. Senthilkumar^{1,2}, Radian Gondokaryono^{2,3,4}, Mustafa Haiderbhai^{2,3,4}, and Lueder A. Kahrs^{2,3}

¹*Indian Institute of Technology Madras, India*

²*Medical Computer Vision and Robotics Lab, University of Toronto, Canada*

³*Department of Computer Science, University of Toronto, Canada*

⁴*The Wilfred and Joyce Posluns CIGITI, SickKids, Toronto, Canada*

INTRODUCTION

Research in surgical robotics and automation has made remarkable advancements in recent years thanks to new methods in computer vision, control, and deep learning. Autonomous end-effector manipulation is a challenging task in surgical robotics, and cutting with scissor tools is largely unexplored. A concurrent work explored path and trajectory generation for cutting deformable materials using the da Vinci Research Kit (dVRK) [1]. However, an efficient and realistic simulation is necessary for methods such as reinforcement learning (RL) or learned trajectory planning. Our previous work built a simulation for the dVRK in Unity for training RL algorithms on rigid body tasks [2]. To our knowledge, there is no dVRK simulation available that includes the cutting of deformable materials. This paper introduces a cutting simulation of a deformable mesh, which can represent a tissue layer, built onto our Unity dVRK simulation.

MATERIALS AND METHODS

Tissues can be roughly approximated with a collection of elastic strands that are woven together. We use this principle to create a simulation of a thin deformable mesh composed of multiple single ropes, so that cutting can be efficiently calculated. We use Obi Rope from the Unity Asset Store, a particle-based simulation method for ropes¹. A customizable mesh-like structure was created, where particles from different ropes are pinned at specific locations to create the desired resolution mesh structure. Factors such as rope length, resolution, thickness, appearance, bending, stretching, and tearability can be adjusted to match real-life behavior.

Single Rope: A single rope environment was developed and initial rope parameters as well as cutting logic were tested in this setting. The kinematics of the dVRK

¹<http://obi.virtualmethodstudio.com/>



Fig. 1 dVRK Round Tip Scissor tool cutting a rope

Round Tip Scissor tool was implemented, with accurate imported visual models, and efficient convex collision meshes for non-cutting interaction with the rope. By experimental exploration, the best possible rope parameters and cutting mechanisms were determined to match realistic behavior. A sample cutting sequence with the dVRK and a single rope can be seen in Fig. 1.

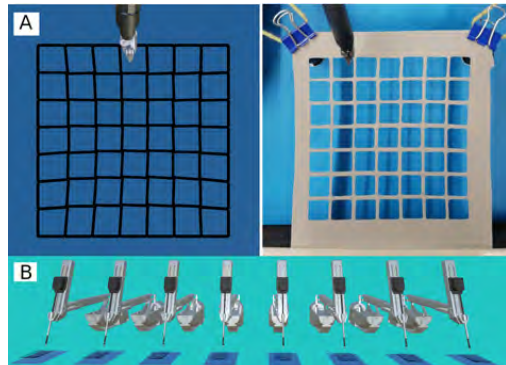


Fig. 2 A) dVRK Round Tip Scissor tool interacting with Multi-rope setup: sim vs real, B) 8 parallel PSM simulation for cutting task

Multi-Rope: To simulate a 2D mesh similar to a real mesh as shown in Fig. 2A, we compose the mesh of multiple ropes that are joined together like strands. Each rope is deformable and tearable, but pinned at specific locations based on the desired mesh resolution. Such a configuration's goal is to replicate a thin tissue simulation or cloth simulation, but remain more efficient and flexible for a cutting implementation. We choose to arrange the ropes as a cubic mesh, as the mass-spring model [3] with four vertices was found to be straightforward and a computationally efficient model for simulating cloth after extensive research on computer graphics. In Unity, each rope contains 15 particles, and the number of particles added to the scene grows by $15(2n+1)$ for a resolution step of 1. Since this system is CPU-dependent, adding particles slows simulation update time.

Sim2Real: A real mesh similar to the virtual rope mesh was created as illustrated in the right part of Fig. 2A

[1]. In our RL setting [2] we can train across multiple parallel environments for better convergence of results, the number of particles increased to $15(2n+1)*M$ where M is the number of environments (Fig. 2B).

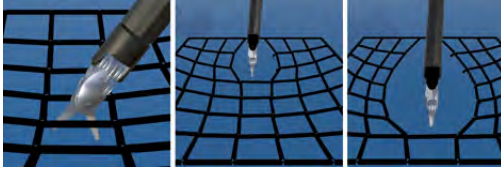


Fig. 3 Deformation of mesh for a straight line cut

Cutting implementation: Our previous Sim2Real work [2] using the dVRK dealt with pushing a block where the jaw open-close behavior was not taken into consideration. In this case of cutting, an interface was developed to accept jaw open and close commands implemented with an underlying interpolation for max speed to account for real hardware constraints. To cut the rope, the bond between particles is broken once a specified object comes into contact. The rope is torn at the contact point if it is in between the jaws and the jaw is closing above a threshold joint velocity. We show a flow chart of our cutting logic in Fig. 4.

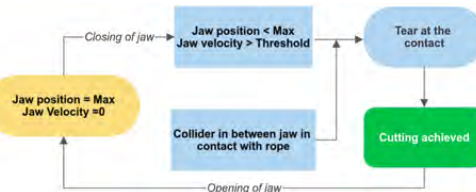


Fig. 4 Cut detection algorithm in the simulation

RESULTS

We can change the resolution of our mesh by simulating more or less ropes in the grid. More ropes effect the simulation speed, which can be observed in Fig. 5, where the effect of changing mesh resolution on simulation frame rate and physics convergence is observed. The final setup chosen is a 7×7 mesh with 1680 particles after addressing the tradeoffs between frame rate and mesh settling time. This virtual scene is tested by cutting the mesh with different trajectories as seen in Fig. 6. This shows how the mesh layer deforms depending on the cut being made. Three types of cuts that are considered are a straight line cut, a diagonal cut, and a square cut. The cuts are made by tele-operating the dVRK Round Tip Scissor tool.

DISCUSSION

In this work, we simulate the cutting of a deformable mesh structure using simple rope primitives. This setup can be used for reinforcement learning, and eventually applied to the Sim2Real transfer of learned cutting behavior from simulation. There are a couple of limitations present in this cutting simulation:

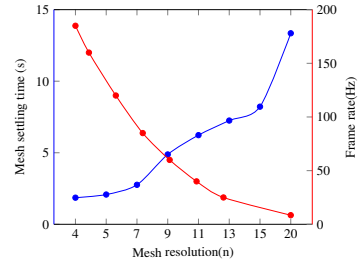


Fig. 5 Effect of mesh resolution on settling time and frame rate of simulation

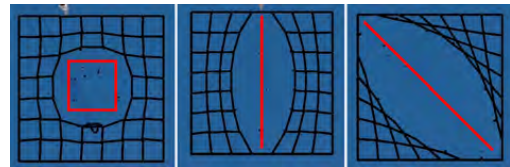


Fig. 6 Square, straight, and diagonal cuts respectively

- Our simulated cutting mechanism assumes that when the jaws close, the cut is successful. This may not be the case for materials that are difficult to cut, which would cause a Sim2Real gap.
- Matching Sim2Real material cutting behavior is difficult, and our simulation is based on observations and not based on any analytical comparison.
- Settling time plays an important role in the performance/quality tradeoff, which is a critical component when considering RL training that is done across multiple environments and multiple instances. The slower the update, the longer the RL steps, and the longer the training wall clock time.

Our future work will focus on training an RL agent for the cutting of this mesh, and the Sim2Real transfer of this RL agent. Other work will compare simulated mesh cutting with path and trajectory generated cutting [1]. We will also improve the simulation to include multi-layer 3D mesh configurations.

ACKNOWLEDGEMENTS

We thank Dr. Thomas Looi at The The Wilfred and Joyce Posluns CIGITI Lab at SickKids Hospital for his support in this research.

REFERENCES

- [1] P. Bawedi, R. Gondokaryono, and L. A. Kahr, "Experimental trials with a shared autonomy controller framework and the da vinci research kit: Pattern cutting tasks using thin elastic materials," in *International Symposium on Medical Robotics*. IEEE, 2023.
- [2] M. Haiderbhai, R. Gondokaryono, T. Looi, J. M. Drake, and L. A. Kahr, "Robust sim2real transfer with the da vinci research kit: A study on camera, lighting, and physics domain randomization," in *IEEE/RSJ IROS*, 2022, pp. 3429–3435.
- [3] J. Zhang, L. Gu, P. Huang, J. Dworzak, F. Chen, and X. Kong, "Real-time cutting and suture simulation using hybrid elastic model," in *2007 29th Annual International Conference of the IEEE Engineering in Medicine and Biology Society*. IEEE, 2007, pp. 3646–3649.

Design and Calibration of a Robot-Driven Catheter Actuation System

N. Feizi¹, F. C. Pedrosa¹, E. Arefinia¹, J. Jayender², and R. V. Patel¹

¹*Canadian Surgical Technologies & Advanced Robotics (CSTAR)*

and University of Western Ontario, London, Canada

²*Brigham and Women's Hospital Harvard Medical School, Boston, USA*

nfeizi@uwo.ca

INTRODUCTION

Flexible steerable tendon-driven systems are crucial in medical interventions, due to their ease of access to narrow spaces and safe operation [1]. Two examples of these systems are ablation and intra-cardiac echocardiography (ICE) catheters, used for non-invasive ultrasound imaging and ablation in cardiac procedures inside the heart. However, precise positioning of these devices to obtain optimal anatomical views is challenging for the cardiologist and requires specialized training [2]. Custom-made tendon-driven robots have been developed and modeled using Cosserat rod theory [3], [4]. However, most of these efforts have been directed towards creating new flexible robots with known parameters rather than adapting pre-existing tendon-driven systems, such as conventional ICE or ablation catheters. In [5] a 4-DoF robot was developed to manipulate and control a 4-tendon ICE catheter by actuating the knobs on the catheter handle. Nevertheless, the dynamics of the catheter's knob introduce friction and dead zones in the system. In our study, we developed a novel robot for catheter control and experimentally determined the parameters of a 2-DoFs quasi-static model of the ICE catheter. Our design eliminates the complexity of catheter knob dynamics by employing direct tendon actuation, distinguishing it from existing literature. The proposed robot will later be used in a visual-servoing mode to autonomously follow an ablation catheter.

MATERIALS AND METHODS

A 6-DoF robot has been developed to actuate a 4-tendon ICE catheter (see Fig. 1). The tendons are individually manipulated utilizing four custom linear actuation units. Each actuation unit consists of a linear bearing mounted on a cylindrical guide, and a ball nut that is coupled with a 2 mm pitch ball screw driven by a BXTH 2214 Brushless Motor (Faulhaber, Baden-Wuerttemberg, Germany). The linear bearing, ball nut, and tendons are connected by a connecting part. The four linear stages have been integrated to form a 4-DoF tendon actuation unit. A grasper is installed at the distal end of the tendon actuation unit to securely hold the catheter's body, and the tendons are connected to the carriages using a screw-tightened gripper.

The tendon actuation unit is mounted on two ball bearings, which enable rotation of the unit. These bearings are held in place by a U-shaped frame. The tendon actuation unit and the catheter are rotated by a pair of pulleys, which are coupled by a timing belt. The driving pulley is actuated by a Faulhaber BXTH 2214 Brushless Motor coupled with a 1:20 gearbox. The U-frame is installed on a custom-made linear motion stage consisting of a bearing mounted on a guide and a ball nut paired with a 1 mm pitch ball screw, which is driven by a Faulhaber BXTH 3216 Brushless Motor.

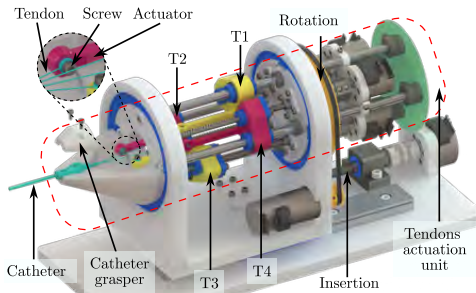


Fig. 1 Robot design for catheter actuation.

The motion of the motors is monitored using Faulhaber IEF3-4096 rotary encoders, and the position of the motors is controlled by EPOS2 controllers (Maxon, Sachseln, Switzerland) commanded from a computer through a CAN bus.

The actuation range of the robot is specified in Table I.

TABLE I Robot actuation range and accuracy

Actuator	Range	Accuracy	Force/Torque
Tendon	0-70 mm	0.005 mm	28 N
Rotation	> 720 deg	0.8 deg	0.8 Nm
Insertion	88 mm	0.01 mm	203 N

The location of the catheter tip within the catheter frame is determined through the use of two electromagnetic (EM) tracker sensors. A 6-DoF reference sensor is attached to the distal end of the catheter support (see Fig. 2), and its position relative to the catheter frame

is calculated through a 12-point registration process. This process involves placing the EM sensor on 12 pre-defined points on a registration frame with known locations determined from the CAD model of the frame. The transformation matrix is then computed by minimizing the error between the EM and computed positions. Subsequently, a 5-DoF EM sensor is mounted on the tip of the catheter, and the relative position of the tip is calculated using the determined transformation. A quasi-static catheter model, based on Cosserat slender rod theory as described in [4], was developed to predict the tip position of the catheter. Measurable model parameters, such as the length of the bending section (L) and the outer radius (r_2), were determined through direct measurement. The material density (ρ) was calculated by measuring the weight and volume of a piece of the catheter. Other kinematic parameters, including the elastic modulus (E), tendon compliance (C), tendon offset (r), inner radius (r_1), and Poisson's ratio (ν), were determined through calibration. To record calibration data, the catheter was positioned such that the tip of the catheter moved in a horizontal plane. The catheter was then moved to two sets of 100 positions by actuating one tendon twice with a sinusoidal position signal while the antagonist tendon was actuated with the same negative values. The position of the tip of the catheter $p_{k_{\text{expt}}}$ was recorded and the model parameters were calibrated through minimizing the error of the model-predicted position of the distal end of the catheter $p_{k_{\text{model}}}$, i.e.,

$$P = \arg \min_{P \in \Omega} \left\{ \sum_{k=1}^{200} \|p_{k_{\text{model}}} - p_{k_{\text{expt}}} \|_2 \right\} \quad (1)$$

The parameter calibration was carried out utilizing Interior-point algorithm employing 40 random initial points in a 5-dimensional space.

RESULTS

Fig. 2 illustrates the fabricated setup. Fig. 3 shows the recorded tip position of the catheter vs tendon actuators and the calibrated model. A mean absolute error of $4.56 \pm 2.86 SD$ mm was obtained using this method. Table II shows the calibrated and measured parameters.

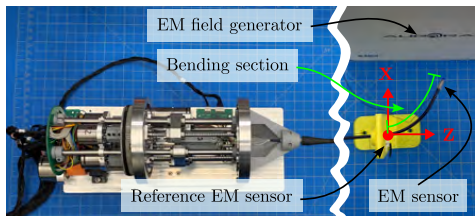


Fig. 2 Top view of the experimental setup.

DISCUSSION

As shown in Figure 3, the model tracks the average path of the catheter's tip; however, the experimental measurements reveal distinct loading and unloading curves due to the hysteresis generated by the internal friction

TABLE II Measured and calibrated parameters. The calibrated values are indicated in bold font.

E	3.32 GPa	r	1.12 mm	ν	0.41
C	0.29 N/mm	r_1	1.01 mm	r_2	1.4 mm
ρ	1570 Kg/m ³	L	78 mm		

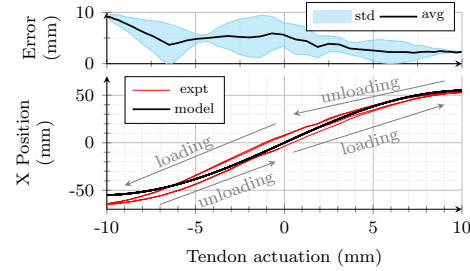


Fig. 3 Experimental data and analytical model.

of the catheter. This friction is different from the robot friction which was minimized through employing a high-lead ball screw approach for the tendon actuation units. This experiment highlights the importance of modeling the internal friction of the catheter. Additionally, it can be observed that although the initial position of the catheter's tip was set to zero, the magnitude of the motion of the tip in the negative direction was 21% greater than that in the positive direction, even though the same tendon actuation range was applied. This disparity could be due to differences in the mechanical properties of the tendons, which may have changed as a result of fatigue. Furthermore, it was noted that the optimization process of the calibration method is highly influenced by the initial estimate, and the optimizer may converge to a local minimum. It is therefore recommended to reduce the order of the optimization problem by direct measurement of the quantifiable parameters such as L , r_2 , and ρ . In our future research, we will incorporate a dynamic model that will be implemented to operate in 3D space, and the model parameters will be extended and calibrated accordingly. Furthermore, our future work will focus on estimating the tendon pull from the motor current.

REFERENCES

- [1] P. E. Dupont, N. Simaan, H. Choset, and C. Rucker, "Continuum robots for medical interventions," *Proceedings of the IEEE*, vol. 110, no. 7, pp. 847–870, 2022.
- [2] A. Ali, D. H. Plettenburg, and P. Breedveld, "Steerable catheters in cardiology: Classifying steerability and assessing future challenges," *IEEE Transactions on Biomedical Engineering*, vol. 63, no. 4, pp. 679–693, 2016.
- [3] D. C. Rucker and R. J. Webster III, "Statics and dynamics of continuum robots with general tendon routing and external loading," *IEEE Transactions on Robotics*, vol. 27, no. 6, pp. 1033–1044, 2011.
- [4] J. Till, V. Alois, and C. Rucker, "Real-time dynamics of soft and continuum robots based on cosserat rod models," *The International Journal of Robotics Research*, vol. 38, no. 6, pp. 723–746, 2019.
- [5] P. M. Loschak, L. J. Brattain, and R. D. Howe, "Algorithms for automatically pointing ultrasound imaging catheters," *IEEE Transactions on Robotics*, vol. 33, no. 1, pp. 81–91, 2016.

Handheld Concentric Tube Robot for Percutaneous Nephrolithotomy

Filipe C. Pedrosa^{*1}, Ruisi Zhang^{*2}, Navid Feizi¹, Dianne E. Sacco³, Rajni Patel¹, and Jagadeesan Jayender²

¹Western University, Canada

²Brigham and Women's Hospital, Harvard Medical School, USA

³Massachusetts General Hospital, Harvard Medical School, USA

^{*} Equal contribution, fpedrosa@uwo.ca

I. INTRODUCTION

The field of continuum robotics continues to advance rapidly, giving these manipulators potential to change the paradigm of minimally invasive medical surgery (MIS) in a near future. As MIS techniques are refined to improve recovery and cosmesis and reduce invasiveness and co-morbidity, continuum robot requirements in MIS applications have become ever stricter.

One such application is Percutaneous Nephrolithotomy (PCNL), a first-choice minimally invasive urological procedure for the extraction of large renal calculi (kidney stones) > 2 cm. The standard of care in PCNL entails the percutaneous insertion of a nephroscope via a small incision in the lumbar or lateral abdominal wall regions, followed by accessing a renal calyx to allow direct manipulation of the stone using specialized lithotripsy devices such as ultrasonic or laser equipment, which aids in reducing blood loss during surgery [1].

This study proposes a lightweight, compact handheld Concentric Tube Robot (CTR) as an alternative to the conventional straight and rigid PCNL tools. Unlike Girerd *et al.* [2] our design was conceived solely for the use in PCNL. Our envisaged device aims to provide an alternative to the conventional rigid nephroscopes by flexibly maneuvering the handheld CTR through a prescribed renal calyx and reaching clinical targets while safeguarding sensitive anatomical structures, as illustrated in Fig. 1. Additionally, it is designed to deliver an energy source through its lumen to the renal calculi for laser ablation.

II. MATERIALS AND METHODS

A. Description of the Handheld CTR

The handheld CTR consists of a cylindrical outer shell that can be grasped directly by the user Fig. 2. Its handle-free design results in a compact and lightweight device weighing only 500 ± 0.1 grams. Apart from the control units, the outer shell houses all components including the motor, actuation units, and sensors. The robot is designed to manipulate three Nitinol tubes assembled telescopically, with the outer tube being straight and

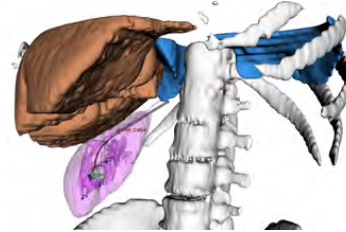


Fig. 1 Anatomically constrained CTR delivered to a clinical target (green marker) while traversing through the renal calyx (red marker), and ensuring avoidance of nearby pleura (blue), liver (amber), bony structures (grey).

stationary. Both the inner and middle tubes have two degrees of freedom each (translation and rotation) and comprise straight and curved sections.

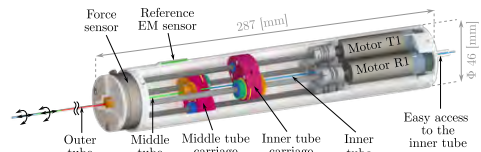


Fig. 2 Section view and dimensions of the handheld CTR

The outer tube is firmly attached to the distal end of the robot by a clamping shaft collar. An ATI MINI40 6-DOF force/torque sensor at the distal end of the robot enables monitoring the reaction forces on the outermost tube during the CTR deployment into the anatomy. The motion of both the inner and middle tubes is delivered by their respective carriages Fig. 2. The translational motion of the carriages is guided by a 4mm diameter splined shaft and a linear bearing. The translational motion is achieved through a flanged nut paired with a 4mm diameter fast-travel, ultra-precision lead screw with a 10mm travel/turn. With a linear bearing in between the 24-tooth gears attached to the tube and the splined shaft, each tube is rotated by a pair of 24-tooth gears. The splined shaft provides both linear guidance and transfers rotational

motion. Ball bearings secure the distal end of two splined shafts while couplings connect them to individual motors at the proximal end. To reduce weight, we employ four CXR 1727 DC micromotors with corresponding gearheads (91:1 planetary 17/1) and IEH3-4096L encoders from Faulhaber to actuate leadscrews and splined shafts. Our design minimizes the volume of the robot, making it possible for the entire device to be held ergonomically by a human hand, as evidenced by the dimensions in Fig. 2. A cylindrical canopy encloses the robot's shaft bearings and supports its four motors. A longitudinal canal in the center of the motor assembly guides an inner tube out of the proximal end for insertion of fiber optic and electromagnetic (EM) sensors during procedures (Fig. 3).



Fig. 3 (a) CXR 1727 DC micromotor (b) Motors & translational/revolute carriages (c) Fully assembled prototype

B. Hardware and Software Interface

The robot's motors are powered by an MC5005SET Faulhaber motion controller and TwinCAT, a soft real-time software suite. Analog signals from the ATI MINI40 force/torque sensor are obtained by a USB-6210 National Instruments data acquisition device. EM tracking system signals are acquired via USB port and analyzed using NDI Aurora's C++ library. The CTR requires both a low-level and high-level code, which communicate via UDP. The former runs on TwinCAT as a PLC, while the latter runs as a C++ application on the PC.

C. User Interface

Handheld robotic systems require effective means to relay user inputs to the robot. We are working on two approaches for merging user interfaces with our robotic solution: one that is integrated with the handheld CTR and allows surgeons to manipulate it through push buttons located on the device's top shell; and another stand-alone interface whereby a passive arm supports the CTR once deployed into the anatomy. Thereafter, the surgeon can pass commands to the robot through two push buttons and a joystick.

D. Kinematic Model Calibration

The CTR tip position is tracked by a 5-DoF EM sensor at the distal end of the innermost tube while a 6-DoF inertial reference EM sensor was installed on the body of the robot. The transformation between the CTR and field generator coordinate frames is computed via an 8 point-registration procedure using landmarks on a registration jig and recorded EM sensor positions at each landmark with respect to the inertial EM frame.

III. RESULTS

A. Calibration Results

The parameters of the tubes used in the experiments are as shown in Table I. To calibrate the quasi-static model of the CTR [3], the proximal ends of the innermost ($s = \beta_1$) and intermediate ($s = \beta_2$) tubes were actuated to the 5 positions listed in Table II. At each position, a full revolution of the innermost tube in 30° increments resulted in 60 configurations.

TABLE I Kinematic parameters of the CTR tubes

	ID [mm]	OD [mm]	ℓ_s [mm]	ℓ_c [mm]	R [mm]
Tb1	0.80	1.27	201.00	60.00	52.00
Tb2	0.97	1.85	113.00	70.00	87.00
Tb3	1.20	2.54	101.00	0.00	–

TABLE II Translational actuation configurations

β_1 [mm]	-135.00	-115.00	-105.00	-95.00	-90.00
β_2 [mm]	-82.00	-62.00	-52.00	-42.00	-40.00

The calibration is achieved by means of an unconstrained optimization over the kinematic parameter set $\Omega = \{E_1I_1, E_2I_2, E_3I_3, G_1J_1, G_2J_2\}$ minimizing the prediction error for the CTR's distal-end position $p(s = \ell)$ implementing (1) using the Nelder-Mead simplex algorithm available in the NLOpt C++ library [4].

$$P^* = \arg \min_{P \in \Omega} \left\{ \sum_{k=1}^{60} |p_k(\ell)_{\text{model}} - p_k(\ell)_{\text{empirical}}| \right\} \quad (1)$$

B. Open-loop accuracy

The calibrated model's yielded a prediction error of 6.21 ± 1.8 mm. As expected, the prediction error increases with the overall length of the backbone. However, in the worse case scenario, the prediction error corresponds to 3.60% the overall length of the backbone.

DISCUSSION

The prediction errors observed are due in part to the friction and non-negligible clearance between tubes in the concentric arrangement as well as systematic errors in positioning the tubes in an initial configuration before each run. The performance of this design under closed-loop control as well as a follow-the-leader like deployment into the anatomy is part of our ongoing work.

REFERENCES

- [1] F. C. Pedrosa, N. Feizi, R. Zhang, R. Delaunay, D. Sacco, J. Jagadeesan, and R. Patel, "On Surgical Planning of Percutaneous Nephrolithotomy with Patient-Specific CTRs," in *Medical Image Computing and Computer Assisted Intervention-MICCAI 2022*. Springer, September 2022, pp. 626–635.
- [2] C. Girerd and T. K. Morimoto, "Design and Control of a Hand-Held Concentric Tube Robot for Minimally Invasive Surgery," *IEEE Transactions on Robotics*, pp. 1–17, 2020.
- [3] P. E. Dupont, J. Lock, B. Itkowitz, and E. Butler, "Design and control of concentric-tube robots," *IEEE Transactions on Robotics*, vol. 26, no. 2, pp. 209–225, apr 2010.
- [4] S. G. Johnson, "The NLOpt nonlinear-optimization package [Software]," URL: <http://github.com/stevengj/nlopt>, 2014.

Non-local Dependencies and Contextual Information in the Interpretation of Procedural Surgical Text

Maria-Camilla Fiazza¹

¹*Department of Computer Science, University of Verona,
mariacamilla.fiazza@univr.it*

INTRODUCTION

Efforts to automate mining of procedural information from surgical texts are enabling technology for future autonomous surgical robots. In building their knowledge base (or seeking to augment it if they encounter unexpected circumstances), these robots need to interface with surgical resources so far intended for human use—such as textbooks, case reports, published medical literature. Knowledge mined from surgical texts forms the backbone of higher cognition mechanisms that support surgical situation awareness and autonomous decision-making, as well as verbal interaction with humans.

Great progress in natural language understanding is required. Regardless of whether the information is intended to support monitoring processes, surgeon or performance evaluation, or (in the future) autonomous decision-making, the safety-critical nature of the domain requires a careful study of the information landscape. Surgical textbooks contain descriptions of surgical procedures that are presented semi-algorithmically, often organized in phases and occasionally also in steps. Surgeons can understand and execute the procedure from the description, so it is possible at least in principle to derive a high-level executable representation of the procedure, one which could be suitable for an autonomous robot. However, even assuming that the robot already have executable routines corresponding to elementary surgical instructions such as incising an anatomical structure, placing an object in an anatomical location (and so on), not all information necessary to parametrize a surgical action is found directly in the text, and when it is, it is not always local to where the instruction is mentioned. Some parameters that cannot be found in the text are not missing per se; rather, they are patient-specific and thus available only when the abstract procedure is instantiated. Their values can only be determined from the direct perception of the surgical scene or from patient-specific imaging. Examples are the exact location in space of a target anatomical structure, or the values of conditions involving spatial relationships; for example, which between vein and corresponding artery obstructs the view of the other can depend on anatomical variants or on the direction of approach.

In this short paper, we discuss the problem of missing

information, and where to find it.

MATERIALS AND METHODS

We examined 6 texts describing the surgical technique for kidney-related interventions within the paradigm of robot-assisted surgery, published between 2014 and 2020 and written in English (e.g., [1], [2], [3]). We chose partial nephrectomy as our case study, covered by 5 of the 6 descriptions.

We selected a small number of verbs that describe surgical actions (elementary actions such as *incise* or complex such as *mobilize*) and determined what information is both (a) required to parametrize the action and (b) abstract enough to be conveyed via text. This information can be used to determine arguments that co-occur frequently with the verb—in a PropBank-style annotation as done in [4]—or, as we propose, to extend the PropBank annotations with additional labels (required arguments), should one want to specialize PropBank-style annotations specifically for use as mining templates for the surgical domain.

To determine patterns of usage, we examined a database of roughly 100 sentences per verb. Sentences were first extracted from the SPKS database [5]. If there were fewer than 100 samples, the set was augmented with instances from the 6 descriptions, and then with instances from a general robotic-surgery manual [6]. The results and examples in this paper refer to the lemma *mobilize*.

For every procedural instance of the target verb, we collected in-sentence execution parameters, then examined the sentences immediately preceding and following for additional (implicit or explicit) execution parameters, then examined non-local dependencies and the contribution of non-linguistic information (anatomical knowledge, reasoning).

RESULTS

In the context of abdominal surgery, *mobilize* is used exclusively to indicate that access to a desired location is obstructed by an anatomical structure, which then becomes the target of mobilization precisely in order to allow access. The stop conditions for the motion, the extent of mobilization (and the part of the organ to mobilize, if it is extensive) are all determined by the

goal of gaining access. As soon as the desired visibility is achieved and can be maintained, mobilization is completed.

We identified three required high-level parameters for **mobilize**: the anatomical structure to mobilize, the direction in which to move it after releasing its attachments, and the purpose of the mobilization (desired access). The triad what-where-to-why, in combination with information on patient anatomy, is sufficient to characterize the set of surgical actions that can successfully meet the specification. Worthy of note is that the specific how (which attachments to release, how far and in what order) even when described in the text is not presented as an exhaustive checklist, but as important nodes to visit. When not mentioned, the attachments to release are *whatever resists the movement* of the target structure in the desired direction to the extent necessary to achieve access.

We observed three different types of sentences containing the lemma **mobilize**: (1) the mobilization is presented as an *instruction* (“The kidney is mobilized outside of Gerota’s fascia, followed by defattening of perinephric fat around the tumor site.”); (2) it is presented as a *goal* for other actions (“The kidney is exposed by incising along the white line of Toldt to mobilize the colon”) and (3) it is presented in reference to some other considerations (“The advantage of this technique is that it requires less mobilization of the transverse colon.”). In type-3 contexts, execution is not intended and therefore the missing parameters are irrelevant. In type-2, the mobilization is in fact a “higher-order” surgical action comprised of smaller surgical actions. An instrument is never specified and only the direct object is normally found in-text in the same sentence. The neighboring sentences hold directional information in fewer than a third of the cases and the purpose of the mobilization must be deduced from wider context and from prior knowledge of the anatomical relations. On the other hand, type-2 occurrences are typically accompanied by an in-sentence mention of a surgical action which (partially) implements the mobilization (“This [space] should be incised to mobilize the cecum”).

In type-1 occurrences, the direct object is nearly always present in-sentence and always present within a 1-sentence distance. Directional information about the resulting motion is present explicitly in roughly half the cases (off/away from or toward a structure or in a given body-reference direction such as medially or caudad). In roughly a fourth of the cases a stop condition that can be used to infer the purpose is present. Occasionally **mobilize** occurs with manner information (“gentle and blunt mobilization of X”). This is not a parameter for **mobilize** but for the implied verb **dissect**, an elementary component action (rewrite as “use gentle and blunt dissection to mobilize X”).

DISCUSSION

Information relevant to determining missing or incomplete execution parameters (object, direction and pur-

pose) can be found non-locally to the current sentence or its two neighbors. Mining it requires retaining lexical and conditional information from prior sentences as well as being able to query non-linguistic knowledge. Successfully parametrizing actions also requires having built from the text a structure of partial goals, which serves as a representation of the procedure and as a working abstraction. The 4 classes of considerations below allow deriving the missing high-level parameters.

Lexical: Dropped qualifiers can be necessary to identify the entities (“incise the kidney” vs “incise the *left* kidney”). The ambiguity is resolved by backing up to the last instance in which the noun occurred with a qualifier. We use a parser to retain the (last) qualifying adjectives with which each noun occurred, and carry it over to the current instance. **Case-related:** The previous sentences may have constrained the context to a specific case (e.g., right- or left-sided procedures, anatomical variants). We use a tree structure of contexts to represent the workflow’s dependencies on cases and manage “local” instructions. **Anatomical:** At times it is necessary to combine knowledge of the semantics and pragmatics of the specific verb with anatomical knowledge, to query the projected intraoperative spatial relationships between anatomical objects. Access to an ontology is not sufficient, because intraoperatively spatial relationships may differ from those represented in an ontology, assumed immutable. The most important relationship is occlusion in reference to the field of view where the camera would be at this stage of the surgery. **Physical modeling:** Directional parameters may be missing because gravity is causing the desired motion of the mobilized organ, as a result of the patient’s pose.

ACKNOWLEDGEMENTS

This work has received funding from the European Research Council (ERC) under the European Union’s Horizon 2020 research and innovation programme (grant agreement No. 742671 “ARS”).

REFERENCES

- [1] J. S. Parihar and C. Lau, *Robot-Assisted Partial Nephrectomy*. Cham: Springer International Publishing, 2018, pp. 103–111.
- [2] J. H. Kaouk, A. Khalifeh, S. Hillyer *et al.*, “Robot-assisted laparoscopic partial nephrectomy: Step-by-step contemporary technique and surgical outcomes at a single high-volume institution,” *European Urology*, vol. 62, no. 3, pp. 553–561, 2012.
- [3] A. A. Raheem, K. D. Chang, M. J. Alenzi *et al.*, “Robot-Assisted Partial Nephrectomy for Totally Endophytic Renal Tumors: Step by Step Standardized Surgical Technique and Long-Term Outcomes with a Median 59-Month Follow-Up,” *Journal of Laparoendoscopic & Advanced Surgical Techniques*, vol. 29, no. 1, pp. 1–11, Jan. 2019.
- [4] M. Bombieri, M. Rospocher, S. P. Ponzetto, and P. Fiorini, “The robotic surgery procedural framebank,” in *Proceedings of the 13th Language Resources and Evaluation Conference*, Marseille, France: European Language Resources Association, Jun. 2022, pp. 3950–3959.
- [5] M. Bombieri, M. Rospocher, D. Dall’Alba, and P. Fiorini, “Automatic detection of procedural knowledge in robotic-assisted surgical texts,” *Int. J. Comput. Assist. Radiol. Surg.*, vol. 16, no. 8, pp. 1287–1295, 2021.
- [6] Y. Fong, Y. Woo, W. Hyung *et al.*, *The SAGES Atlas of Robotic Surgery*, 01 2018.

Miniaturisation, Modularization and Evaluation of the SoftSCREEN System

Vanni Consumi¹, Danail Stoyanov¹, and Agostino Stilli¹

¹Wellcome/EPSRC Centre for Interventional and Surgical Sciences (WEISS), University College London

INTRODUCTION

Early detection of precancerous forms in the intestine, e.g. adenomatous polyps, can be achieved with regular screening programmes of the lower gastro-intestinal tract (GI) by means of flexible sigmoidoscopy and colonoscopy. Screening of the GI tract is of paramount importance to reduce the high death rate of patients affected by colon cancer worldwide. Nonetheless, colonoscopy typically causes discomfort and often requires sedation for the patient because of its invasiveness and abdominal pain associated with it. Research on robotic-assisted colonoscopy is advancing in the design of minimally invasive devices aimed at the inspection of the GI, with the goal of reducing the discomfort caused to the patient while resulting in a safer and more successful procedure [1]. Multiple locomotion strategies have been explored to enable front-head locomotion of endoscopes, to minimise the interaction forces between the scope and the intestine wall, as these forces are typically the first cause of discomfort for the patient. Extensive studies have been conducted in the context of track-based miniaturised robots such as [2] and [3]. However, due to the fixed geometry of these systems, adapting to the variable and irregular lumen of the colon to enable full body track-based navigation is not possible. Furthermore, as per many of the robotic solution presented to date for GI screening, there is also a need to drag a tether, the frictional resistance of which grows the more the robot advances in the intestine. Soft materials properties have inspired research of mechanism to accomplish a compliant interaction with the tissue, such as the use of inflatable balloons for double balloon endoscopy. In our previous work [4], we have presented a novel robotic system for colonoscopy called SoftSCREEN. The proposed system relies on track-based locomotion and shape reconfiguration enabled by two inflatable chambers capable of displacing the elastic tracks to conform to the local geometry of the lumen, enabling full-body track navigation. In this seminal paper we have validated the proposed design in a 2:1 scale system and demonstrated that not only is possible to reconfigure our system to always match the lumen navigated, but also to control the force applied on the walls by means of pressure regulation, and, as a result, fine tuning the traction force of our system. In this work, we present the first miniaturised and modularised prototype of the SoftSCREEN system, designed to create a sterilisable reusable expensive component and a cheap disposable component. We then evaluate this first prototype in a 1:1 scale phantom.

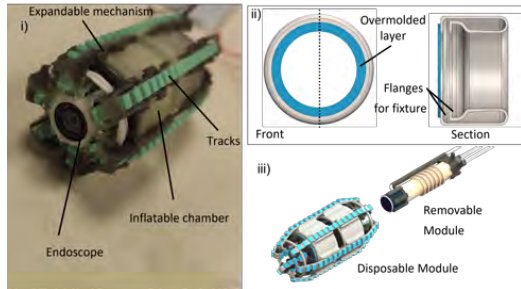


Fig. 1: Overview of the SoftSCREEN system. Picture of the robot mounting a front endoscope (i). Design of the of the inflatable chambers with reinforced-flange obtained by overmolding hard silicone (in blue) on the inflatable membrane (in white) (ii). Assembly of the robot by the insertion of a removable/resuable module into a disposable module (iii).

MATERIALS AND METHODS

The design presented in this work builds on the one firstly proposed by the authors in [4]. Here we are presenting a small-scale version (30 mm in diameter) of this system. As in our previous design the system is composed of a rigid chassis, a motor-powered worm-gear mechanism, six elastic tracks and two inflatable toroidal chambers, as shown in Fig 1-i). The robot mounts a 0.5 W DC Motor with gearbox (both from Maxon Motor™, Sashseln, Switzerland) and a full-HD endoscope (Misumi Electronics Corp., Taiwan) front facing and with integrated illumination. The rotation of the motor cause the rotation of the worm gear which displace all the elastic tracks that move in loop around the chassis and generating the linear movement of the robot by engaging with walls. Direction of motion of the robot depends on the direction of rotation of the motor. Inflation of the toroidal chambers is used to displace and deform the tracks to ensure contact with the lumen, thus traction. To enable shape reconfigurability flanges were embedded on the external surface of the chassis on the distal ends to facilitate chambers installation, sealing, maximise radial expansion and minimise the axial one. Flexibility of the distal ends of the track guides on the rigid chassis was also achieved by means of an expandable mechanism comprising multiple segments connected by hinges, as discussed in [4]. In the design presented here we have optimised this expandable mechanism, creating a chain of three links that provides laterally constraints the movement of the tracks while conforming to the system's inflated shape. In our design, we connect soft chambers subjected to high deformation to a rigid structure using screws

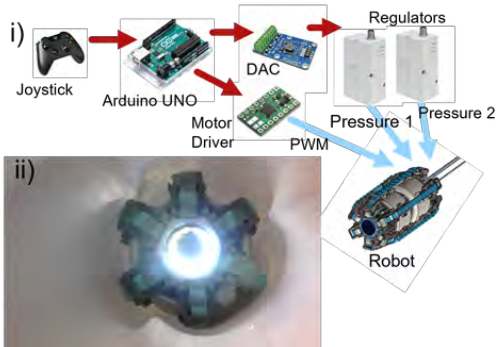


Fig. 2: Control scheme of the robot for the experimental setup. The user controls the robot using a joystick controller. The Arduino board controls the DC motor driver and the two pressure regulators to enable track motion and independent inflation of the chambers (i). Picture of the SoftSCREEN inside the phantom (ii).

passing through it. Both from simulation and from experiments this connection was found to be the point of higher stress concentration in the chambers that could lead to failure. To reinforce the membrane at the position of the screws, multi-material inflatable chambers were created by overmolding a layer of hard silicone on the flanges of the soft membrane, as shown in Fig 1-ii), to guarantee both high deformation and a robust fixture. Envisioning the robot being used in a clinical settings, we decided to modularise our system creating two modules depicted in Fig 1-iii: the first module is disposable being composed of a plastic chassis and silicone-based inflatable chambers; the second module is reusable after sterilization, and this embeds all the expensive components, namely the motor, the worm-gear and the optics. In the deflated state, the prototype is 32 mm in diameter and 60 mm long. The rigid parts are made of photopolymer resin, printed with a 3D-printer (Formlabs™, Somerville, MA, US). The toroidal chambers are 0.60 mm thickness membranes made of Dragon Skin™ 10 NV silicone rubber (Smooth-On Inc., Easton, PA, US), flange-reinforcement and tracks are made of Smooth-Sil 960™ from the same brand. The tracks are composed by two silicones combined together with overmolding, Dragon Skin™ 30 for the body of the track and Smooth-Sil™ 960 for the teeth. The users can control speed and pressure of the two chambers by using a joystick as shown in Fig 2-i). The two chambers are actuated pneumatically via pressure regulators (VPPX-6F-L-1-F-0L10H-S1, FESTO GmbH, Esslingen, Germany), where the pressure is controlled via a Arduino UNO microcontroller connected to a DAC (DA4C010BI, APTINEX Ltd., Maharagama, Sri Lanka). The motor is driven by a DC (DRV8876, Pololu, Las Vegas, NV, US). An experimental setup was assembled to assess the shape-shifting capability of the flange-reinforced actuators. The diametrical expansion of the robot was monitored by image analysis through a camera (C922, Logitech, Switzerland). The locomotion of the robot was then tested inside a straight segment of tubular phantom made of EcoFlex™ 30, 25 cm long with circa 30 mm in diameter (Fig 2-ii).

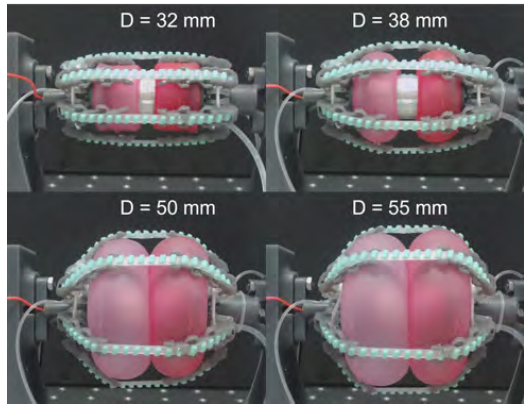


Fig. 3: Pictures of the experimental setup for the robot to assess the capability of reconfigure its shape. The soft chambers (red membranes) are inflated at 4 different levels of pressure, with the robot fixed on a rigid stand. The overall maximum diameter of the robot is displayed in the figure. The inflation of the chambers displaces the tracks (clear green) outward while the expandable mechanism sits below the tracks and above the chambers.

RESULTS

A selection of images captured during the data acquisition for are presented in Fig. 3, showing the deformation of the system at different pressure levels. The robot was assembled as described and fixed to a rigid structure to assess the inflation in a static condition. The overall enlargement of the robot was measured from the initial diameter of 32 mm to circa 55 mm, meaning that the design of the inflatable chambers as proposed allows the robot to almost double its diameter. Inside the phantom, the robot moved forward and backward as fast as 3 mm/s and provided clear image recording of the lumen.

CONCLUSIONS AND DISCUSSION

In this work We presented the first miniaturised version of the SoftSCREEN system for colonoscopy, demonstrating track locomotion and reconfiguration capabilities, and optimising the design for modularisation. In the experimental setup, the robot has demonstrated to be able to expand its diameter in a wide range and to move inside a straight silicone phantom. In future, a closed-loop control strategy will be considered to match the robot diameter to that of the lumen, and the locomotion of the robot will be extensively tested in more complex phantom settings.

REFERENCES

- [1] G. Ciuti, R. Caliò, D. Camboni, L. Neri, F. Bianchi, A. Arezzo, A. Koulaouzidis, S. Schostek, D. Stoyanov, and C. M. Oddo, “Frontiers of robotic endoscopic capsules: a review,” *Journal of Micro-Bio Robotics*, vol. 11, no. 1-4, pp. 1–18, 2016.
- [2] G. A. Formosa, J. M. Prendergast, S. A. Edmundowicz, and M. E. Rentschler, “Novel Optimization-Based Design and Surgical Evaluation of a Treaded Robotic Capsule Colonoscope,” *IEEE Transactions on Robotics*, vol. 36, no. 2, pp. 545–552, 2020.
- [3] D. Lee, S. Joe, J. Choi, B. I. Lee, and B. Kim, “An elastic caterpillar-based self-propelled robotic colonoscope with high safety and mobility,” *Mechatronics*, vol. 39, pp. 54–62, 2016. [Online]. Available: <http://dx.doi.org/10.1016/j.mechatronics.2016.08.002>
- [4] V. Consumi, L. Lindenroth, J. Merlin, D. Stoyanov, and A. Stilli, “Design and evaluation of the softscreen capsule for colonoscopy,” *IEEE Robotics and Automation Letters*, pp. 1–8, 2023.

Surface-Enhanced Raman Spectroscopy and Transfer Learning Toward Accurate Reconstruction of the Surgical Zone

Ashutosh Raman^{1,2}, Ren A. Odion^{1,2}, Kent Yamamoto¹, Weston Ross^{2,4}, Tuan Vo-Dinh^{1,2,3}, Patrick J. Codd^{2,4}

¹*Department of Biomedical Engineering, Duke University, Durham, NC, USA*

²*Fitzpatrick Institute for Photonics, Duke University, Durham, NC, USA*

³*Department of Chemistry, Duke University, Durham, NC, USA*

⁴*Department of Neurosurgery, Duke University School of Medicine, Durham, NC, USA*

ashutosh.raman@duke.edu

INTRODUCTION

Raman spectroscopy is a photonic modality defined as the inelastic backscattering of excitation coherent laser light. It is particularly beneficial for rapid tissue diagnosis in sensitive intraoperative environments like those involving the brain, due to its nonionizing potential, point-scanning capability, and highly-specific spectral fingerprint signatures that can characterize tissue pathology [1]. While Raman scattering is an inherently weak process, Surface-Enhanced Raman Spectroscopy (SERS), which is based on the use of metal nanostructure surfaces to amplify Raman signals, has become a compelling method for achieving highly specific Raman spectra with detection sensitivity comparable to conventional modalities such as fluorescence [2]. A unique plasmonics-active nanoplatform, SERS gold nanostars (GNS) have previously been designed in our group to accumulate preferentially in brain tumors [2]. Raman detection, when combined with machine learning and robotics, stands to enhance the diagnosis of surface-level ambiguous tissue during tumor resection surgery, with the potential to improve extent-of-resection and rapidly reconstruct the dynamic surgical field.

Here we demonstrate preliminary results from the use of a SERS-based 2-DOF translational platform to efficiently recreate a tumor embedded in healthy tissue, which is modeled here as a GNS-infused phantom. Transfer learning, specifically through use of the open-source RRUFF mineral database, is employed here to address the dearth of collected biomedical Raman data [3].

MATERIALS AND METHODS

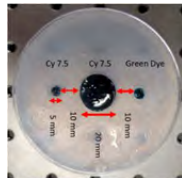


Fig. 1 Cancer Mimicking Phantom Used in Experiment, with Cy 7.5 regions containing SERS particles

The overall goals of this study were two-fold:

- Combine a Raman system and classification algorithm to discern SERS signal from

surrounding tissue-mimicking material, even with changes in material color, and

- Evaluate the ability of a robotic Raman system to reconstruct a sample field rapidly and accurately, with relative dimensions intact.

The experimental setup consists of a portable Raman system, translational stages, and a cancer-mimicking phantom with selectively infused SERS regions.

A. Phantom Design: A 3% agarose tissue-mimicking phantom was created for controlled testing of the platform. A 20 mm diameter circular hole was situated in the center of the mold, with two 5 mm diameter holes (fiducials) situated 10 mm edge-to-edge from the middle hole and along the diameter of the overall mold. 1 mL of 1-nM GNS-Cyanine 7.5 (Cy 7.5) solution was mixed with approximately 20 mL of the liquid agarose solution and used to fill the central hole (target), as well as one fiducial. The other fiducial was filled with green tissue dye and no Cy 7.5, to serve as a visually similar control and test the ability of the Raman system to differentiate targets of the same color with and without SERS particles. This is all shown in Fig. 1.

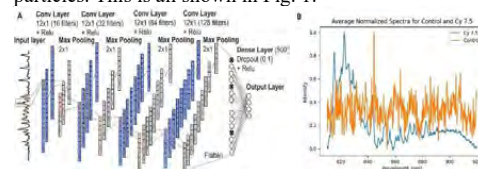


Fig. 2 A) Neural Network Architecture Adapted from [4] **B)** Normalized and Iterative Polynomial Fitted Spectral Classes

B. Neural Network and Transfer Learning: A convolutional neural network (CNN) was built with the structure shown in Fig. 2A. For the classification of Raman spectra in a biological context, the RRUFF open-source Raman spectra mineral database [3] was first utilized to pre-train the network. Once a validation accuracy of 90% was achieved following classification of the four most prevalent RRUFF mineral classes, all CNN layers were frozen and the final fully-connected layer was replaced with a trainable two-neuron layer.

Using a miniaturized Hamamatsu C13560 Raman system with 15-mW laser power, an integration time of 350 ms, and a sample distance of 10 mm, Raman spectra ($n = 100$ per class) were collected from solidified agarose and Cy 7.5-infused agarose samples similar in consistency to those used in the experimental phantom. Each spectrum

was filtered to only contain intensity values from 810–920 nm, then fit with a 3rd order iterative modified multi-polynomial to remove baseline signal. Then the spectra were min-max normalized, and finally interpolated to 3397 values each, to match the required input feature size for the pre-trained CNN. The average spectra for both classes are shown in Fig. 2B.

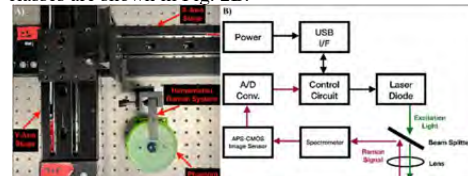


Fig. 3 A) Experimental Setup Used for Reconstruction and B) Schematic of Hamamatsu Raman System

C. Translational System Setup: The Hamamatsu system was attached to two linear translation Stages (Thorlabs LTS300). A 3D-printed mount was used to position the phantom precisely and reproducibly at 10 mm under the laser. The setup is shown in Fig. 3A, with the Hamamatsu Raman system schematic shown in Fig. 3B.

D. Raster and Reconstruction: A linear raster within a grid of 30x60 mm was implemented to completely scan the region of interest (ROI) in the phantom, including the tumor-mimicking zone and both fiducials. The stage was moved in 1 mm increments, pausing each time for 350 ms, during which the Raman system automatically captured a spectrum. Each spectrum was then post-processed in the same manner as the training Raman dataset used for CNN fine-tuning. Finally, each spectrum was given a prediction classification of 0 (Control) or 1 (Cy 7.5), and this was assigned to the location from which the sample was taken, to reproduce the ROI. A ground truth reconstruction was also created by manually establishing an origin on the phantom, using the stages to position the laser at the bottom-most edge of the target Cy 7.5 region.

RESULTS

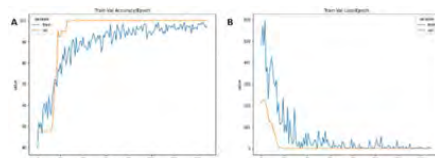


Fig. 4 A) Accuracy and B) Loss curves for the pre-trained CNN during fine-tuning on Cy 7.5 and Control Agarose Loss and accuracy curves from fine-tuning are provided in Fig. 4. The CNN had 100% test accuracy without evident overfitting in the binary classification task. Fig. 5 demonstrates the reconstructed phantom after the raster and prediction. Much like the majority of the surrounding agarose control, the non-Cy 7.5 green dye was not classified as SERS and thus is not visible in the reconstruction. The predicted approximate distance between the two Cy 7.5 samples remains 10mm edge-to-edge, and the general shape of the center sample is preserved at 19mm diameter, while the Cy-7.5 fiducial is

slightly misshapen due to misclassification at boundaries. The grid raster lasted 10.2 minutes.

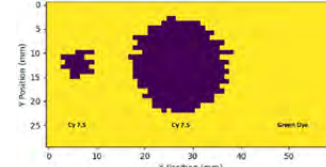


Fig. 5 Reconstructed Phantom from Raman Raster and CNN Predictions, with Same Orientation as Fig. 1

The ROI area is 1800mm² and the expected area of the Cy 7.5 regions is 333.8mm². The predicted area was 328mm² and thus the accuracy was 98.2%. Comparing the ground truth mask to the predicted reconstruction, the Intersection-over-Union (IoU) score was 84.3%. Comparing boundaries after edge filtering yielded a Boundary IoU of 53%.

DISCUSSION

This study achieved high accuracy and IoU, providing a proof-of-concept for a SERS and transfer learning-based pipeline that can aid neurosurgeons seeking rapid noninvasive sensing in vital areas like the brain. This study also shows that SERS does not differentiate between colors, but rather based on presence of GNS agents, which have previously been designed to accumulate in specific brain tumors.

The Boundary IoU was moderate due to the large 1 mm step size, but this can be corrected at the expense of overall raster time; this improved margin detection would make the system more applicable in surgical oncology, primarily in the diagnosis of surface tissue. Furthermore, though the fine-tuning training set was very similar to the phantom, this pipeline still offers value in surgeries for which a biopsy specimen already exists to train CNNs. Future studies make use of a 6-DOF manipulator to scan on non-flat samples and to simulate system deployment in surgical environments. Studies will also utilize animal tissue to explore effects of tissue structure on classification metrics. In conclusion, the preliminary results support the use of rapid and precise robotic biophotonics to aid intraoperative surface-level diagnosis and margin detection during oncologic surgery.

REFERENCES

- [1] Jermyn, Michael, et al. "A review of Raman spectroscopy advances with an emphasis on clinical translation challenges in oncology." *Physics in Medicine & Biology* 61.23 (2016): R370.
- [2] Vo-Dinh, Tuan, et al. "SERS nanosensors and nanoreporters: golden opportunities in biomedical applications." *Wiley Interdisciplinary Reviews: Nanomedicine and Nanobiotechnology* 7.1 (2015): 17-33.
- [3] RRUFF Project (2017) RRUFF database of minerals, rocks, and meteorites: University of Arizona, Tucson, USA. Available at <http://rruff.info>.
- [4] Li, Joy Qiaoyi, et al. "Machine learning using convolutional neural networks for SERS analysis of biomarkers in medical diagnostics." *Journal of Raman Spectroscopy* 53.12 (2022): 2044-2057.

Breast surface reconstruction utilising autonomous robotic assisted ultrasound image acquisition

A.G. de Groot¹, V. Groenhuis¹, S. Stramigioli¹, and F.J. Siepel¹

¹*Robotics and Mechatronics group, University of Twente,
a.g.degroot@utwente.nl*

INTRODUCTION

One in eight females will be diagnosed with breast cancer in their lifetime, making it the most diagnosed cancer globally [1]. Three phases are essential for the outcome of breast cancer; early detection, accurate diagnosis and treatment. Magnetic resonance imaging (MRI) has proven to be highly sensitive in detecting possible tumors lesions compared to other image modalities. However, ultrasound (US) guided biopsies are the standard and biopsies on MRI detected lesions is challenging, because these lesions may not be visible on US images. Registration of pre-operative MRI with the intraoperative US combines the benefits of both imaging modalities and subsequently improve tumor localisation. Therefore, this work presents an US image-based surface reconstruction based on autonomous acquired US images to increase the accuracy of MRI/US registration. Thereby the proposed work eliminates the need for inter-sensor calibration as would be needed if stereo camera-based, depth camera-based or marker-based breast surface reconstruction would be used.

MATERIALS AND METHODS

Experimental setup

The experimental setup as presented in Figure 1 consists of a seven degree-of-freedom manipulator (KUKA LBR Med 7 800, KUKA GMBH, Germany) with an end-effector that holds a linear US probe (L12-5L40S, Telemed UAB, Lithuania). The US probe is connected to a MicrUS EXT-1H (Telemed UAB, Lithuania) which streams the US images with 40Hz to the confidence driven controller which runs on a workstation.

A polyvinylchloride/plasticiser (PVCP) (Bricoleurre, France) breast phantom was fabricated shaped by segmenting MRI patient data. The phantom is made with a 70 %/30 % ratio of PVCP to mimic breast tissue. The five markers were made by adding green colouring (LUPA colouring, LureParts, The Netherlands) to a 100 %/0 % PVCP mixture.

Finally, the breast phantom is attached to an aluminium profile in prone position which resembles the position of the breast during MR-imaging. The golden standard is based on a camera scan of the makers on the breast phantom to place the MRI segmented breast surface in

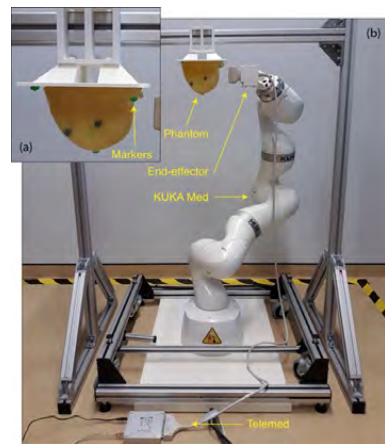


Fig. 1 (a) The phantom with skin markers. (b) An overview of the setup with the relevant parts indicated.

space, this golden standard is only used to validate the outcome of the US image-based surface reconstruction.

Image acquisition

The presented work utilises the ultrasound image acquisition strategy presented by Welleweerd et al. [2]. In which the initial reference trajectory of the US probe is planned around the breast and corrected based on the amount of contact between the US probe and breast surface. Additionally, the US probe is rotated in respect to the breast to ensure the contact is centred around the center scan-line of the US probe. This approach limits the need of prior knowledge of the breast shape and position, but provides a high quality US image acquisition stream of 40Hz.

Contact between the US probe and the breast surface is evaluated based on the confidence map [3] of each acquired US image. The confidence map provides a pixel-wise representation of the uncertainties in the US images and therefore provides useful inside in the acoustic coupling of a given US scan-line with the breast surface. During the image acquisition the amount of scan-lines in contact with the breast surface (C_s) is set at 30 %, 50 % and 65 % or ($C_s = 0.3, 0.5, 0.65$).

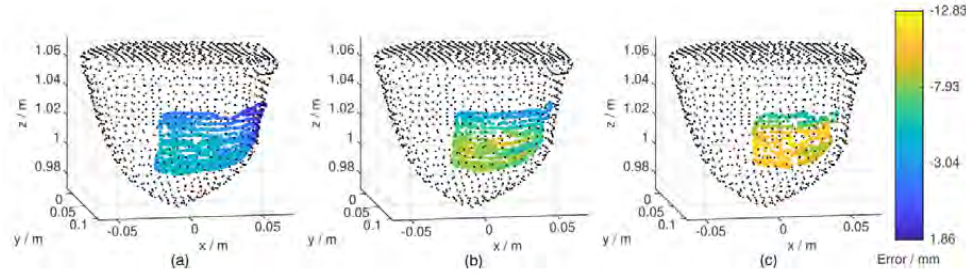


Fig. 2 Point-cloud registration of the MRI data (black dots) with the generated surface reconstruction (coloured dots) for the set-points: (a) $C_s = 0.3$, (b) $C_s = 0.5$ and (c) $C_s = 0.65$. The colours of the dots represent the error between the surface reconstruction and the golden standard as seen in the error bar (far right).

Surface reconstruction

The US images are processed offline by first, creating a binary vector of the original US image with zeros for non-acoustic coupled scan-line and ones for acoustic coupled scan-lines, this evaluation is similar to the control approach presented in Welleweerd et al. [2]. Second, three point clouds are constructed two low-knowledge high density point clouds and a high-knowledge low density point cloud. The two low-knowledge point clouds contain the location in Euclidean space of either the non-acoustic coupled points or the acoustic coupled points, these point clouds are low-knowledge as the undeformed breast surfaces lays somewhere between them. The non-acoustic coupled point provide the knowledge that the breast surface is not there and the acoustic coupled points provide the knowledge that the undeformed breast surface is in an outward direction seen from these scan-lines. The high-knowledge point cloud contains the location of the points that are formed by transition from non-acoustic coupled to acoustic coupled scan-line or vice versa, because these locations contain the undeformed shape of the breast as no deformation is applied by the US probe to ensure acoustic coupling.

The initial estimation of the undeformed breast surface is placed between the two low-knowledge point clouds and adjusted based on the high-knowledge point cloud.

RESULTS

Thirty scans of the breast phantom were made with the robotic setup, ten for each confidence set-point and a surface reconstruction was made for each data set. The average surface error in respect with the golden standard was -3.78 ± 1.08 mm for $C_s = 0.3$, -5.28 ± 1.30 mm for $C_s = 0.5$ and -8.45 ± 1.77 mm for $C_s = 0.65$. Note the minus sign means inward deformation compared to the golden standard.

Figure 2 shows the average surface error for all three confidence set-points. The lowest error for all three surface reconstructions is found in the top right and an increasing error is shown till the maximum error is reached at the bottom left. This pattern is shown for all three surface reconstructions, however the lowest error and maximum error are dependent on the confidence set-point.

DISCUSSION

This work presents an approach to reconstruct the breast surface in the undeformed state using autonomously acquired ultrasound data. The robotic setup which acquired these ultrasound images is not dependent on prior knowledge about the breast shape and location, because the controller sets an initial path based on an half-sphere and updates this initial path based on ultrasound images evaluation as presented in Welleweerd et al. [2].

The smallest average reported error was -3.87 ± 1.08 mm compared to the golden standard. However, it should be noted that Welleweerd et al. [2] presents a 1.74 mm error for the golden standard, marker-based registration of the MRI data with the phantom, this error is incorporated in the error found in this work. Possibly a second inaccuracy of the golden standard is shown in the form of a rotational error around the z-axis as shown in figure 2. This results in an uneven spread of the error along the reconstructed surface for all three confidence set-points.

An increase in the amount of contact between the breast and the US probe results in an increase in the reported error, because during scanning the breast is more deformed due to the contact with the US probe. Other techniques such as stereo camera-based registration, depth camera-based surface reconstruction or marker reconstruction do not have this disadvantage, but have issues with inter-sensor calibration. This is seen in the golden standard as it tends to show a rotational error around the z-axis, thereby showing the advantages of a single sensor setup.

REFERENCES

- [1] M. Arnold, E. Morgan, H. Rumgay, A. Mafra, D. Singh, M. Laversanne, J. Vignat, J. R. Gralow, F. Cardoso, S. Siesling, and I. Soerjomataram, "Current and future burden of breast cancer: Global statistics for 2020 and 2040," *Breast*, vol. 66, no. June, pp. 15–23, 2022. [Online]. Available: <https://doi.org/10.1016/j.breast.2022.08.010>
- [2] M. K. Welleweerd, A. G. de Groot, S. O. H. de Looijer, F. J. Siepel, and S. Stramigoli, "Automated robotic breast ultrasound acquisition using ultrasound feedback," in 2020 *IEEE International Conference on Robotics and Automation (ICRA)*. IEEE, may 2020, pp. 9946–9952. [Online]. Available: <https://ieeexplore.ieee.org/document/9196736/>
- [3] P. Chatelain, A. Krupa, and N. Navab, "Confidence-Driven Control of an Ultrasound Probe," *IEEE Transactions on Robotics*, 2017.

From 4D Transesophageal Echocardiography to Patient Specific Mitral Valve Models

Patrick Carnahan^{1,2}, Elvis C.S. Chen^{1,2,3}, and Terry M. Peters^{1,2,3}

¹*Imaging Laboratories, Robarts Research Institute, London, Canada*

²*School of Biomedical Engineering, Western University, London, Canada*

³*Department of Medical Biophysics, Western University, London, Canada*

pcarnah@uwo.ca

INTRODUCTION

Mitral valve regurgitation is the most common valvular disease, affecting 10% of the population over 75 years old [1]. Current standard of care diagnostic imaging for mitral valve procedures primarily consists of trans-esophageal echocardiography (TEE) as it provides a clear view of the mitral valve leaflets and surrounding tissue. Heart simulator technology has been adopted widely by both industry for evaluation of technologies for imaging heart valves [2], and academia for the assessment of modelled heart valves [3]. Recently, developments have been made on a workflow to create 3D, patient-specific valve models directly from trans-esophageal echocardiography (TEE) images. When viewed dynamically using TEE within a pulse duplicator simulator, it has been demonstrated that these models result in pathology-specific TEE images similar to those acquired from the patient's valves in-vivo [4]. However, producing a mesh model of the valve geometry from TEE imaging remains a challenge. Previously, producing a valve model included a labor intensive series of steps including manual leaflet segmentation, and computer-aided design (CAD) manipulation to derive a 3D printable mold from a raw segmentation. Our objective is to automate the workflow and reduce the labor requirements for producing these valve models. To address the leaflet segmentation problem, we developed DeepMitral, a fully automatic valve leaflet segmentation tool. Following leaflet segmentation, we have developed tools for automatically deriving mesh models that can easily be integrated into a mold base.

MATERIALS AND METHODS

We have developed a module for 3D Slicer¹ that incorporates the automated steps towards patient specific valve models. Our module integrates with SlicerHeart, which provides additional tools for valve mold creation, as well as a platform for delineating the mitral annulus[5]. The first step towards producing a 3D printable valve

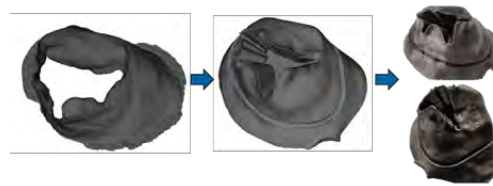


Fig. 1 Extracted atrial surface (left) to generated 3D mesh (middle) to 3D printed positive molds (right).

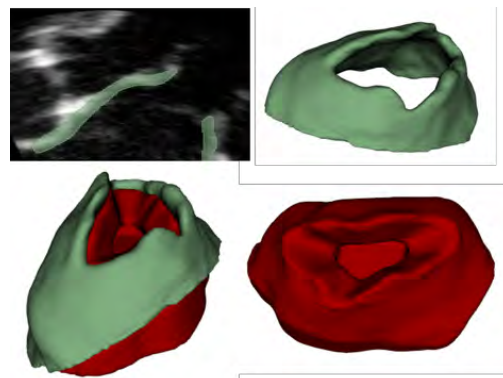


Fig. 2 Cross section of 3D TEE volume (top-left). 3D representation of leaflet segmentation shown in green (top-right, bottom-left), positive mold generated from atrial surface shown in red (bottom-left, bottom-right).

model mold from a TEE volume is leaflet segmentation. We have developed DeepMitral, a Residual U-Net model that can accurately label the mitral leaflets [6]. This model was originally trained using 40 patient cases, and since the original work, we have added an additional 90 cases for a total of 130. This has been done through the ongoing use of the network within our 3D Slicer module on new patient images, under the supervision of an expert clinical user who provides manual editing to the output segmentations as needed.

¹<https://www.slicer.org/>

Following leaflet segmentation, additional processing is necessary to produce a 3D printable mesh. For our purposes, we desire a positive mold of the inside, or atrial surface of the segmentation. Before proceeding, we utilize the segmentations modules of 3D Slicer to produce a closed-surface mesh representation of the leaflet segmentation. All processing following is done using VTK² on PolyData meshes. The atrial surface algorithm is described in [algorithm 1](#), and an example of the resulting extracted surface can be seen in [Figure 1](#).

Algorithm 1: Algorithm to extract only atrial surface portion of segmentation mesh

```

Data:  $m$  segmentation mesh
Result: extracted atrial surface mesh
Construct OBBTree from  $m$ ;
Construct cylinder  $c$  with midplane normal as
axis, at midplane center, with height 40mm and
radius 10mm;
for each point  $p$  in  $m$  do
    if  $p$  is above midplane then
        Use OBBTree to compute intersection
        between  $m$  and line from  $p$  to midplane
        center;
        Discard point if self-intersection;
    else
        Find line  $l$  from  $p$  to closest point on
        cylinder;
        Compute angle  $a$  between mesh normal at
         $p$  and line  $l$ ;
        Discard point if angle  $a > 1.5$  rad
    end
end

```

The extracted atrial surface is then thickened inwards towards the midplane center by 2mm, and the portion below the midplane center is filled in. To construct an even, flat base, the bottom half of the mold is also extruded downwards and clipped to account for any regions with a short segmentation. The results of this process can be seen in [Figure 2](#).

RESULTS

Through use in our 3D Slicer module with manual user intervention on cases with poor predictions, we have increased the available data for training our deep learning model. This has resulted in an improvement in accuracy for the mean-absolute-surface distance from 0.59 ± 0.23 mm to 0.57 ± 0.20 mm and a 95% Hausdorff distance from 1.99 ± 1.14 mm to 1.90 ± 0.92 mm. This largely represents an improvement in consistency of the model, which we particularly note in cases of poor image quality. Our 3D Slicer module has been used to produce patient specific valve models for 105 patient cases by clinical users. In all cases where image quality is deemed sufficient to attempt modelling automatic segmentation

²<https://vtk.org/>

and mold creation is successful. The time required for the steps within our Slicer module range from 10 to 20 minutes, depending on the amount of manual intervention needed on the automated leaflet segmentation. Manual segmentation takes roughly 1 hour, and manually extracting the atrial surface to produce a mold takes 1 to 3 hours depending on the complexity of the valve.

DISCUSSION

Our 3D Slicer module enables fast and accurate creation of 3D printable meshes directly from patient image data. By integrating our deep learning model into a 3D Slicer module, a user can generate a segmentation with one click in less than 5 seconds and then leverage the 3D Slicer platform to view and edit the segmentation as needed. This allows us to deploy our model, while keeping a user in the loop to verify the quality of the segmentations. Through continued use of this module to generate valve models, we can increase the available data to improve our deep-learning based methods, and further automate steps in the workflow such as annulus identification. With further development, we aim to incorporate further steps into the 3D Slicer module to include automatic creation and positioning of parametric mold and flange components, with the ultimate goal of eliminating any need for external CAD software. Our 3D Slicer module simplifies the overall workflow for valve modelling by automating previously manual steps and incorporating them into a single user interface. We demonstrate an algorithm for extracting the atrial surface from an automatic leaflet segmentation, enabling creation of a positive mold mesh that can easily be 3D printed. By simplifying this workflow, we aim to improve the clinical translatability of patient-specific heart valve modelling.

REFERENCES

- [1] P. M. Shah, "Current concepts in mitral valve prolapse—Diagnosis and management," *Journal of Cardiology*, vol. 56, no. 2, pp. 125–133, sep 2010. [Online]. Available: <https://www.sciencedirect.com/science/article/pii/S0914508710001309>
- [2] P. Kozlowski, R. S. Bandaru, J. D'hooge, and E. Samset, "Real-time catheter localization and visualization using three-dimensional echocardiography," in *Medical Imaging 2017: Image-Guided Procedures, Robotic Interventions, and Modeling*, R. J. Webster and B. Fei, Eds., SPIE, mar 2017.
- [3] A. Mashari, Z. Knio, J. Jegannathan, M. Montealegre-Gallegos, L. Yeh, Y. Amador, R. Matyal, R. Saraf, K. Khabbaz, and F. Mahmood, "Hemodynamic Testing of Patient-Specific Mitral Valves Using a Pulse Duplicator: A Clinical Application of Three-Dimensional Printing," *Journal of Cardiothoracic and Vascular Anesthesia*, vol. 30, no. 5, pp. 1278–1285, oct 2016.
- [4] O. K. Ginty, J. T. Moore, M. Eskandari, P. Carnahan, A. Lasso, M. A. Jolley, M. Monaghan, and T. M. Peters, "Dynamic, patient-specific mitral valve modelling for planning transcatheter repairs," *International Journal of Computer Assisted Radiology and Surgery*, vol. 14, no. 7, pp. 1227–1235, may 2019.
- [5] A. Lasso, C. Herz, H. Nam, A. Cianciulli, S. Pieper, S. Drouin, C. Pinter, S. St-Onge, C. Vigil, S. Ching, K. Sunderland, G. Fichtinger, R. Kikinis, and M. A. Jolley, "SlicerHeart: An open-source computing platform for cardiac image analysis and modeling," *Frontiers in Cardiovascular Medicine*, vol. 9, sep 2022.
- [6] P. Carnahan, J. Moore, D. Bainbridge, M. Eskandari, E. C. S. Chen, and T. M. Peters, "DeepMitral: Fully automatic 3d echocardiography segmentation for patient specific mitral valve modelling," in *Medical Image Computing and Computer Assisted Intervention – MICCAI 2021*. Springer International Publishing, 2021, pp. 459–468.

3-D Visualization and Inter-Session Comparison for Robotic Assisted Bladder Cancer Screening

V. Groenhuis¹, A.G. de Groot¹, E.B. Cornel², S. Stramigioli¹, and F.J. Siepel¹

¹*Robotics and Mechatronics, University of Twente*

²*Department of Radiology, Ziekenhuisgroep Twente*

v.groenhuis@utwente.nl

INTRODUCTION

Over 570,000 new cases of bladder cancer are diagnosed worldwide every year[1]. It is essential to detect new tumors as early as possible to reduce the mortality rate. In addition, the muscle invasiveness of lesions should be quantified to determine the optimal treatment plan. Within the "Next-gen in-vivo cancer diagnostics" research project we propose a new cystoscopy instrument consisting of an optical coherence tomography (OCT) sensor, a camera and a light source, mounted on the tip of a concentric tube robot (CTR). The camera images could then be used to create 3-D reconstructions of the bladder wall and to quantify changes in its texture between successive cystoscopy sessions. In addition, the camera could guide the OCT sensor to investigate the bladder wall structure at the locations of possible tumors in order to investigate the malignancy and muscle invasiveness.

This research specifically reports on creating 3-D reconstructions of bladder phantoms and co-registration of successive sessions, in order to automatically detect and indicate changes in texture which might be related to the onset and growth of tumors.

Several research groups performed 3-D reconstruction of the bladder based on monocular images, often in combination with a different sensor or with structured light. Lurie et al. used monocular images (2700 on average) and sophisticated algorithms to create 3-D reconstructions with sufficiently sharp textures such that thin blood vessels are made visible without interruptions [2]. Suarez-Ibarrola et al. also performed detailed 3-D reconstructions of the bladder, but an additional sensor (electromagnetic tracker or inertial measurement unit) was required [4]. Up to date no automatic detection of texture changes in successive cystoscopy sessions has been reported in literature.

MATERIALS AND METHODS

A video of an in-vivo human bladder was recorded using a CV-170 cystoscope (Olympus Corp., Tokyo, Japan). A partial 3-D reconstruction of the bladder wall was made by stitching a representative subset of 351 video frames using Structure-from-Motion (SfM) algorithms

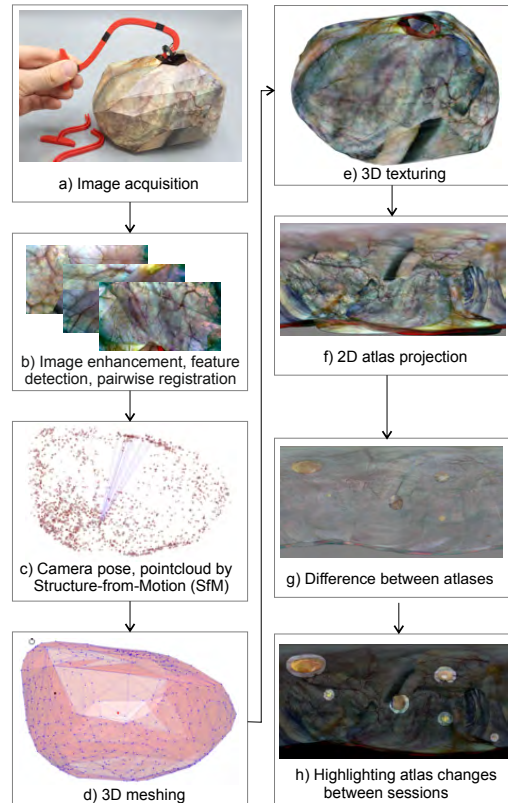


Fig. 1. Workflow in this research. Images from a bladder phantom are enhanced, co-registered and reconstructed to construct a textured surface model and project it to a 2-D atlas. Successive atlases are co-registered and its differences highlighted.

by a combination of COLMAP software [3]. Based on the stitched textures a realistic phantom (150% scale, 1.2L volume) was created by printing a mosaic of representative bladder wall texture segments and folding it into a bladder model. Changes between successive scanning sessions were simulated by attaching six pictures

of tumors (size 5 mm to 30 mm) to different locations of the phantom.

Videos were recorded from the bladder phantom at the two sessions, using a camera of type FXD-VB20903L-76 (MISUMI Electronics Corporation, Taipei, Taiwan) with outer diameter 3.8 mm, image size 1280×720 pixels and diagonal field of view 76° . After acquisition approximately 125 individual frames were selected and undistorted, its brightness leveled using a Gaussian-smoothed mask and the contrast enhanced. The 3-D reconstruction process was conducted by a combination of COLMAP software [3] and a Matlab application. The estimated camera positions were imported in Matlab and the 3-D pointcloud converted to a surface mesh on which the camera frames were projected. A 2-D atlas was also created by projecting the bladder wall onto a sphere and then a plane using equirectangular projection. The 3-D reconstructions of the two successive sessions were co-registered and deformed using the thin plate spline (TPS) algorithm to make the co-registered features coincide with each other. The corresponding 2-D atlases were subtracted and regions with significant color differences highlighted.

RESULTS

Figure 1 shows the workflow showing the different steps in the acquisition, reconstruction and inter-session comparison processes.

In the first session 124 camera frames were recorded. 780 pairwise registrations were found with an average of 34.9 inlier feature pairs per registration, leading to 2041 robust homologous points in the bi-connected connectivity graph. Three camera frames were discarded in the 3-D reconstruction. A pointcloud was constructed consisting of 2041 points, as shown in Figure 1(b). The mean reprojection error was 0.081 mm (range 0 mm to 0.79 mm). The pointcloud was subsequently converted to a surface mesh with 623 vertices and 674 faces (Figure 1(c)). The textured model is shown in Figure 1(e) and the corresponding atlas in Figure 1(f). The average time needed for reconstructing one session was 15 minutes. The difference between both sessions is shown in Figure 1(g), with highly saturated regions representing relatively large changes in texture. By smoothing and thresholding the saturation channel six regions are filtered and used to highlight the corresponding regions shown in Figure 1(h). Approximately 30 minutes were needed to conduct the necessary steps to perform inter-session registration, resolve any inaccuracies in the registration and choose the right filtering parameters to properly highlight the changes in texture.

DISCUSSION

The results show that cystoscopy images of the bladder could be reconstructed in 3-D and subsequently projected to a 2-D atlas. Registrations of successive sessions were effectively co-registered with help of the TPS algorithm and the system was able to automatically detect all six images of tumors which were added between the two sessions.

While the original textures were acquired from an in-vivo cystoscopy video, comparison of two successive sessions was based on images of a realistic ex-vivo phantom. A next step in this research is to acquire and process in-vivo cystoscopy images at different sessions from the same patient in order to detect and quantify texture changes *in vivo*.

The research envisages the use of a concentric tube robot for manipulating the an end-effector consisting of a miniature camera along with an OCT sensor and a light source. The integration of multiple sensors into one robotically-steered minimally-invasive instrument potentially allows for a versatile bladder cancer screening method with direct assessment of muscle invasiveness of any tumors. The development of such a device is challenging given the small diameter of the urethra through which the bladder is to be accessed. In any case the results presented in this paper could in principle also be applied to standard cystoscopy procedures, as long as a proper video is acquired.

Approximately one hour was needed to create 3-D reconstructions of both sessions and perform the inter-session comparison. This can be primarily attributed to the time required by the structure-from-motion and bundle adjustment algorithms to create a proper 3-D reconstruction, and it is in line with state-of-art reconstruction techniques [4], [2]. The 3-D reconstruction process is particularly difficult due to the presence of floating particles in the fluid, bladder wall deformations, uneven lighting, blurry frames and other effects.

Many manual interventions were needed, e.g. in selecting the proper range of input frames and at different steps in inter-session comparison. More sophisticated algorithms should be implemented to streamline the workflow and alleviate the need for manual interventions.

In current clinical practice usually only a couple of cystoscopy images are stored, which is insufficient for automatic comparison of successive sessions. When each cystoscopy session would be recorded on video by default and automatically reconstructed in 3-D and compared to earlier sessions, urologists could be presented with powerful new tools to detect suspicious changes in texture, and be quicker on average in detecting new bladder tumors. Especially when combined with robotic steering and/or an OCT sensor, this may bring the standard of bladder cancer diagnostics to a higher level and improve the quality of life of bladder cancer patients.

REFERENCES

- [1] F. Bray, J. Ferlay et al. *Global cancer statistics 2018: GLOBOCAN estimates of incidence and mortality worldwide for 36 cancers in 185 countries*. CA, 68(6):394–424, 2018.
- [2] K. L. Lurie, R. Angst et al. *3D reconstruction of cystoscopy videos for comprehensive bladder records*. Biomedical Optics Express, 8(4):2106, 2017.
- [3] J.L. Schonberger, J.M. Frahm, *Structure-from-motion revisited*. In Proceedings of the IEEE conference on computer vision and pattern recognition, pp. 4104–4113, 2016.
- [4] R. Suarez-Ibarrola, M. Kriegmair et al. *A novel endoimaging system for endoscopic 3D reconstruction in bladder cancer patients*. Minimally Invasive Therapy & Allied Technologies, 31(1), 34-41, 2020.

A New Suture Needle State estimation Method Based on Electrical Impedance Sensing

Kim L. Schwaner, Zhuoqi Cheng, and Thiusius R. Savarimuthu

*SDU Robotics, The Mærsk Mc-Kinney Møller Institute, University of Southern Denmark
kils@mmti.sdu.dk*

INTRODUCTION

Autonomous surgical task execution has the potential to improve surgeons' working conditions, increase hospital throughput, and better patient outcomes in the future. While fully autonomous robotic minimally invasive surgery (RMIS) is currently unrealistic for several reasons, partly automated surgery – or *task autonomy* [1] – is being explored for different surgical tasks.

One such task is suturing, which involves complex motions in a challenging environment. Automating the suturing task using surgical robots has been attracting research interest (see, e.g., [2]–[4] for recent studies). Despite these advances, automated suturing is still limited to controlled environments and is not yet applicable in realistic surgical settings.

This paper presents a step towards autonomous robotic suturing. Specifically, we propose a method for suture needle state estimation during insertion into soft tissue based on electrical bioimpedance (EBI) sensing. EBI is an advantageous sensing modality in RMIS, given that it is non-invasive and requires only minor modifications to existing surgical instruments. In this study, we equip a surgical robot with EBI sensing capabilities, allowing the robot to measure the electrical impedance between a needle driver instrument and a common ground electrode. The proposed method requires a suture needle with insulation coating except for its tip, end, and notch in the middle. We conducted an experiment for concept validation based on ex vivo animal tissue where we obtained a 98.8% prediction accuracy on four different suture needle insertion states. Most interestingly, we could accurately determine when the needle tip exits after being pushed through soft tissue, which is challenging to do with, e.g., computer vision due to the needle's small size and occlusions. The needle tip exiting is valuable information as often one wishes to grasp the needle tip with a second manipulator to complete the suture throw by pulling the needle through the tissue.

MATERIALS AND METHODS

The proposed method is based on a monopolar EBI sensing configuration where the electrical impedance of a material is measured through one electrode and a

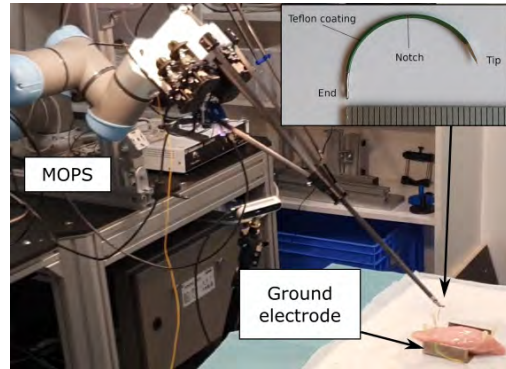


Fig. 1 Overview of our experimental setup for suture needle insertion state estimation using electrical impedance sensing and a Teflon coated needle.

ground electrode for current return and as a potential reference.

The method was validated on the MOPS surgical robotic platform [5]. To enable EBI sensing capabilities on the MOPS system, we integrated a Quadra electrical impedance spectroscopy analyzer (Eliko OÜ, Estonia). The Quadra is able to sample impedance data at 15 frequencies from 1 kHz to 349 kHz in real time. The current stimulation pin and voltage measurement pins were shorted and connected to one of the needle driver's jaws. A metal plate was placed under the tissue and acted as the ground electrode. The suture needle ($\frac{3}{8}$ circle, 24 mm in diameter) is coated with a layer of Teflon, as shown in Fig. 1. The coating layer does not cover the needle tip, end, and a 1 mm notch in the middle (15 mm from the tip).

With this coating, we are able to observe a distinct change in the EBI signal as the needle enters and exits the tissue: Before contacting the tissue, the sensing circuit is open, and the measured impedance value is high. The moment the needle comes in contact with the tissue, a decrease of the measured impedance values can be seen. A slight decrease of the EBI value may occur during the insertion since the contact area between the needle and tissue increases [6].

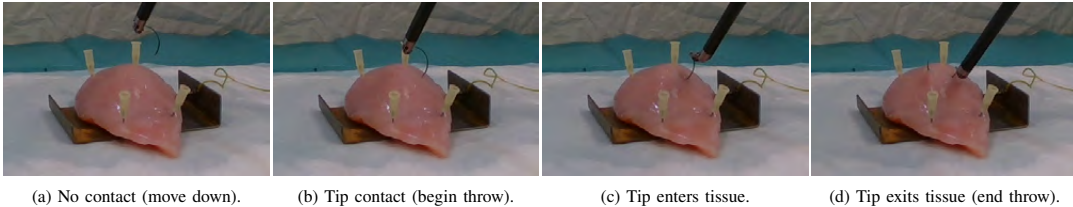


Fig. 2 The MOPS robot system performing an autonomous suture throw while collecting impedance data using the needle driver's jaws and metal plate as sensing electrodes.

To verify our method, we set up an experiment where we autonomously performed eight suture throws on a chicken breast while recording sensor signals from the robot system, camera, and Quadra device. Fig. 2 depicts the scenario: Initially, the needle driver would move the pre-grasped needle downward, tip-first, with a velocity of 0.8 mm s^{-1} until reaching a threshold impedance magnitude of 3000Ω at the 1000kHz excitation frequency. The needle was then moved along a circular trajectory to push it through the tissue. After one-half revolution (after which the needle tip had exited the tissue), the motion was reversed to pull the needle back. Throughout this, we recorded impedance spectrograms from the Quadra sensor at a rate of 1kHz and video from a RealSense camera at 30Hz . Based on the video recordings we manually annotated when changes between the following states occurred:

- 1) *No contact*: no contact between needle and tissue.
- 2) *Contact*: needle tip touching tissue (not inserted).
- 3) *Tip entry*: needle tip inserted in tissue (middle/back outside).
- 4) *Tip exit*: needle tip exited on other side of tissue (middle/back inside).

This let us create a dataset of 640 data points, evenly selected from the eight trials (20 data points per state from each trial), annotated with ground-truth states according to the list above.

To test whether the recorded impedance spectrograms is suitable for determining the needle insertion state, we use a simple two-nearest neighbors classification scheme with features being 15 impedance magnitude values for excitation frequencies between 1kHz and 349kHz . The dataset was shuffled and randomly split with 60 % of samples using for training, and 40 % used for testing.

RESULTS

Using the proposed scheme for estimation a suture needle's insertion state, we obtain an exact match metric of 98.8 %, indicating that almost all samples had their labels classified correctly. In three cases the *contact* state was wrongly predicted as the *no contact* state but otherwise predictions on the test set were entirely correct.

DISCUSSION

In this research, we presented a novel method for suture needle insertion state estimation based on EBI sensing.

Given the sensed EBI signal, the system could accurately detect whether the needle tip contacts, enters or exits the tissue accurately on pre-recorded data (offline). This important information can be used guide control autonomous robotic suturing. The two-nearest neighbors method achieved very good results. However, the method will not generalize well to other tissue types which have different electrical properties.

It is interesting to observe that the EBI magnitude was slightly lower when middle notch was inserted into the tissue and the value increased after the middle notch exited. In this work we did not use this information though this indicates that we can achieve more fine-grained state estimation by manipulating the needle's insulation coating.

Future work will investigate using the proposed method for online feedback control to autonomously complete full suture throws, including pulling the needle out from tissue after its tip exits. Additionally, we plan to extend the method to an increasingly realistic surgical environment.

REFERENCES

- [1] G.-Z. Yang, J. Cambias, K. Cleary, *et al.*, "Medical robotics—regulatory, ethical, and legal considerations for increasing levels of autonomy," *Science Robotics*, vol. 2, no. 4, Mar. 2017. doi: [10.1126/scirobotics.aam8638](https://doi.org/10.1126/scirobotics.aam8638).
- [2] K. L. Schwamer, I. Iturrate, J. K. H. Andersen, P. T. Jensen, and T. R. Savarimuthu, "Autonomous bi-manual surgical suturing based on skills learned from demonstration," in *2021 IEEE/RSJ International Conference on Intelligent Robots and Systems (IROS)*, Prague, Czech Republic: IEEE, Oct. 2021, pp. 4017–4024. doi: [10.1109/IROS51168.2021.9636432](https://doi.org/10.1109/IROS51168.2021.9636432).
- [3] S. A. Pedram, C. Shin, P. W. Ferguson, J. Ma, E. P. Dutson, and J. Rosen, "Autonomous suturing framework and quantification using a cable-driven surgical robot," *IEEE Transactions on Robotics*, vol. 37, no. 2, pp. 404–417, Apr. 2021. doi: [10.1109/TRO.2020.3031236](https://doi.org/10.1109/TRO.2020.3031236).
- [4] S. Leonard, J. Operfmann, N. Uebel, *et al.*, "Vaginal cuff closure with dual-arm robot and near-infrared fluorescent sutures," *IEEE Transactions on Medical Robotics and Bionics*, vol. 3, no. 3, pp. 762–772, Aug. 2021. doi: [10.1109/TMRB.2021.3097415](https://doi.org/10.1109/TMRB.2021.3097415).
- [5] K. L. Schwamer, I. Iturrate, J. K. H. Andersen, C. R. Dam, P. T. Jensen, and T. R. Savarimuthu, "MOPS: A modular and open platform for surgical robotics research," in *2021 International Symposium on Medical Robotics (ISMР)*, Atlanta, GA, USA: IEEE, Nov. 2021. doi: [10.1109/ISMР48346.2021.9661539](https://doi.org/10.1109/ISMР48346.2021.9661539).
- [6] Z. Cheng and T. R. Savarimuthu, "Monopolar, bipolar, tripolar, and tetrapolar configurations in robot assisted electrical impedance sensing," *Biomedical Physics & Engineering Express*, vol. 8, no. 5, p. 055014, 2022.

A			
Abolfathi, Kiana	95	Christiansen, Michael G.	131
Aktas, Ayhan	35	Citi, Luca	123
Al-Hamadani, Maleeha	133	Civati, Lorenzo	35, 115
Alarcón de la Lastra, Ángela	1	Clarkson, Matthew	1
Alterovitz, Ron	19	Cleary, Kevin	15
Alvarez, Pablo	71	Codd, Patrick	111, 145
Arefinia, Elaheh	137	Connolly, Laura	123
Ashkan, Keyoumars	95	Connor, Peter	19
Atalla, Mostafa A.	23	Consumi, Vanni	143
Austin, Ryan	91	Cornel, Erik B.	151
Avery, James	99	Corrales, C. Eduardo	3
Aviles-Espinosa, Rodrigo	17	Cotin, Stéphane	71
Ayyala, Haripriya	1	Cui, Zejian	7
B		D	Guenette, Jeffrey
Balakuntala, Mythra	75	Daffara, Claudia	3
Barralet, Jake	25	Damian, Dana	47
Barrett, Tristan	11	Dang, Khoa	101
Bartholomew, Ryan	3	Dargahi, Javad	19
Bicchi, Anna	125	Davidor, Nitsan	147, 151
Billatos, Ehab	91	Davies, Brian	33, 65
Binyamin, Yair	79	de Groot, A.G.	79
Boreel, Maud	3	de Kater, Esther P.	79
Borvorntanajanya, Korn	115	De Momi, Elena	79
Bosi, Giorgia	37	De Rossi, Giacomo	79
Botha, Abrie		Deguet, Anton	67
Breedveld, Paul	57	Deng, Kaizhong	125
Brown, Jeremy D.	83	Deo, Akhil	47
Broyles, Justin	1	Dillenseger, Jean-Louis	123
Burdet, Etienne	109	Diller, Eric	71
Burriesci, Gaetano	37	Dimitrakakis, Emmanouil	121
C		Donder, Abdulhamit	Hooshiar, Amir
Cambranis-Romero, Joeana	127	Dowrick, Thomas	73
Cannon, Piper	9	Drake, James	5, 29
Carnahan, Patrick	149	Drew, Daniel S.	59
Carroll, Sean	97	Dupont, Pierre E.	147, 151
Casals, Alicia	51	Dwyer, George	59
Cecere, Renzo	25	E	27
Chandler, James	95	Elson, Daniel S.	117
Chen, Elvis	127, 149	Esendag, Kaan	117
Chen, Longrui	109	F	43
Chen, Rongwan	21	Fan, Hongyi	43
Cheng, Truman	41	Fati, Francesca	101
Cheng, Zhuoqi	153	Feizi, Navid	101
Chitalia, Yash	27	Fekri, Pedram	85
Chiu, Philip Wai Yan	39, 41	Fiazza, Maria-Camilla	85
D		J	Jan, Victor
Daffara, Claudia		Jacovacci, Veronica	69
Damian, Dana		Iacobucci, Michele	91
Dang, Khoa		Jannin, Pierre	77
Dargahi, Javad		Jayender, Jagadeesan	77
Davidor, Nitsan		Jeong, Gwoon	1, 3, 137,
Davies, Brian		Jeung, Deokgi	139
de Groot, A.G.		Jha, Prashant	21
de Kater, Esther P.		Jin, Kaizhe	49
De Momi, Elena			
De Rossi, Giacomo			
Deguet, Anton			
Deng, Kaizhong			
Deo, Akhil			
Dillenseger, Jean-Louis			
Diller, Eric			
Dimitrakakis, Emmanouil			
Donder, Abdulhamit			
Dowrick, Thomas			
Drake, James			
Drew, Daniel S.			
Dupont, Pierre E.			
Dwyer, George			
E			
Elson, Daniel S.			
Esendag, Kaan			
F			
Fan, Hongyi			
Fati, Francesca			
Feizi, Navid			
Fekri, Pedram			
Fiazza, Maria-Camilla			
G		G	Gaeta, Leah
Guenette, Jeffrey			97
Guerin, Sonia			75
Gupta, Saksham			3
Gwisai, Tinotenda			105
H		H	Haiderbhai, Mustafa
Haiderbhai, Mustafa			135
Harlé, Antoine			81
Hayuni, Tamar			79
He, Changyan			5
Herrell, S. Duke			9
Hess, Donald			97
Ho, Ming Ho			39
Hong, Jaesung			49
Hooshiar, Amir			25, 65
Hu, Zhaoyang Jacopo			109
Hu, Zhenxuan			
Huang, Baoru			69
Huang, Xiaoyu			17
Huang, Yanpei			109
Huaulmé, Arnaud			77
I		I	Iacobucci, Veronica
Iacobucci, Veronica			89
Ibrahimi, Michele			89
J		J	Jan, Victor
Jan, Victor			77
Janke, Taylor			91
Jannin, Pierre			77
Jayender, Jagadeesan			
Jeong, Gwoon			
Jeung, Deokgi			
Jha, Prashant			
Jin, Kaizhe			

<u>Julia Wise, Frank</u>	87	<u>Majewicz-Fey, Ann</u>	61	<u>Podolsky, Dale</u>	13
<u>K</u>		<u>Marcus, Hani</u>	117	<u>Pomahac, Bohdan</u>	1
<u>Kafash Hoshiar, Ali</u>	95	<u>Masoumi, Navid</u>	65	<u>Q</u>	
<u>Kahrs, Lueder</u>	135	<u>Mattos, Leonardo S.</u>	53, 55, 113	<u>Qin, Tony</u>	19
<u>Kang, Paul H.</u>	29	<u>McAlindon, Mark</u>	101	<u>Quacquarelli, Mariagrazia</u>	125
<u>Kapoor, Ankur</u>	129	<u>McCandless, Max</u>	87	<u>Quevedo-Moreno, Diego</u>	93
<u>Kaptijn, Tjalling G.</u>	57	<u>McDonald, Kevin</u>	97	<u>R</u>	
<u>Kavoussi, Nicholas</u>	9	<u>Mehmet, Gulsun</u>	129	<u>Raina, Deepak</u>	75
<u>Kazanzides, Peter</u>	85	<u>Mencattelli, Margherita</u>	27	<u>Raman, Ashutosh</u>	145
<u>Kazanzides, Peter</u>	121	<u>Menciassi, Arianna</u>	89	<u>Ranzani, Tommaso</u>	97
<u>Kazemipour, Negar</u>	25, 65	<u>Mirkhani, Seyed Nima</u>	105	<u>Rathi, Anushka</u>	97
<u>Kessler, Dimitri</u>	11	<u>Miyashita, Shuhei</u>	101	<u>Rendon-Morales, Elizabeth</u>	17
<u>Khan, Danyal</u>	117	<u>Morel, Guillaume</u>	81	<u>Roche, Ellen</u>	93
<u>Kim, Hee-June</u>	49	<u>Mountris, Konstantinos</u>	51	<u>Rodriguez Y Baena, Ferdinando</u>	7, 67, 73, 109, 115
<u>Kim, Young-Ho</u>	129	<u>Mousavi, Parvin</u>	123	<u>Rohra, Akash</u>	131
<u>Kinnicutt, Lorenzo</u>	97	<u>Munawar, Adnan</u>	85	<u>Roshanfar, Majid</u>	33
<u>Ko, Seong Young</u>	21	<u>Muradore, Riccardo</u>	47	<u>Ross, Weston</u>	145, 111
<u>Kocaturk, Ozgur</u>	103	<u>Murray, Julia</u>	119	<u>Rubio Solis, Adrian</u>	63, 107
<u>Koskinopoulou, Maria</u>	55	<u>Mylonas, George</u>	65, 99, 107, 119	<u>Rucker, Caleb</u>	19
<u>Krieger, Axel</u>	123	<u>N</u>		<u>Runciman, Mark</u>	99, 119
<u>Kumar, Aravind</u>	123	<u>Naik, Ravi</u>	63, 107	<u>Rus, Daniela</u>	101
<u>Kuntz, Alan</u>	59	<u>Neri, Alberto</u>	113	<u>Russo, Sheila</u>	87, 91
<u>L</u>		<u>Newall, Nicola</u>	117	<u>S</u>	
<u>Lam, Chun Ping</u>	39	<u>Ng, Calvin Sze Hang</u>	41	<u>Sacco, Dianne</u>	139
<u>Lam, Ryan</u>	59	<u>Nguyen, Anh</u>	67	<u>Saghbiny, Elie</u>	81
<u>Lasso, Andras</u>	123	<u>Nguyen, Robert</u>	5, 29	<u>Sahu, Manish</u>	85
<u>Lau, Ka Chun</u>	39	<u>Niknam Maleki, Aryan</u>	119	<u>Sakes, Aimée</u>	23, 57
<u>Law, Jones</u>	13	<u>Nisky, Ilana</u>	79	<u>Samur, Evren</u>	103
<u>Laws, Stephen</u>	67	<u>Norton, Christine</u>		<u>Santangelo, Andrea</u>	53, 55
<u>Leavitt, Alexandra</u>	59	<u>Nyangoh Timoh, Krystel</u>	77	<u>Savarimuthu, Thiusius</u>	153
<u>Lecomte, Francois</u>	71	<u>O</u>		<u>Sayadi, Amir</u>	25, 65
<u>Lee, Daniel</u>	3	<u>O'Brien, Anthony</u>	73	<u>Scaroni, Valentina</u>	71
<u>Lee, Harin</u>	91	<u>Oden, Janae</u>	97	<u>Schilling, Richard</u>	51
<u>Lee, Hyun-Joo</u>	49	<u>Odion, Ren</u>	145	<u>Schuerle, Simone</u>	105
<u>Lee, Jungjae</u>	97	<u>Onorati, Simone</u>	89	<u>Schwaner, Kim</u>	153
<u>Lee, Megan</u>	97	<u>Orakwue, Chisom</u>	97	<u>Scutelnic, Dumitru</u>	47
<u>Leonard, Simon</u>	123	<u>P</u>		<u>Semproni, Federica</u>	89
<u>Li, Gang</u>	15	<u>Pacheco, Nicholas</u>	131	<u>Seneci, Carlo</u>	133
<u>Li, Jixiu</u>	41	<u>Paladini, Dario</u>	53	<u>Senthilkumar, Kanishkan</u>	135
<u>Li, Zheng</u>	41	<u>Patel, Rajni V.</u>	137, 139	<u>Setia, Shaan</u>	9
<u>Liang, Haipeng</u>	11	<u>Pedrosa, Filipe C.</u>	137, 139	<u>Shafiq, Babar</u>	15
<u>Lim, Zi Heng</u>	97	<u>Penza, Veronica</u>	53, 113	<u>Shi, Jialei</u>	31
<u>Lluch, Eric</u>	129	<u>Peters, Terry</u>	127, 129	<u>Siepel, F.J.</u>	147, 151
<u>Looi, Thomas</u>	5, 29	<u>Piccinelli, Nicola</u>	47	<u>Siewerssen, Jeffrey</u>	15
<u>M</u>		<u>Pittiglio, Giovanni</u>	27	<u>Siracusano, Salvatore</u>	47
<u>Machaca, Sergio</u>	83			<u>Sitti, Metin</u>	45
<u>Maglio, Sabina</u>	89				

<u>Siu, Shi Pan</u>	39	X	
<u>Souipas, Spyridon</u>	67	<u>Xochicale, Miguel</u>	43
<u>Stilli, Agostino</u>	143	Y	
<u>Stoyanov, Danail</u>	117, 143	<u>Yam, Yeung</u>	39
<u>Stramigioli, S.</u>	147, 151	<u>Yamamoto, Kent</u>	145, 111
<u>Sun, Zhijun</u>	99	<u>Yang, Jianlin</u>	99
<u>Sunderland, Kyle</u>	123	<u>Yao, Junke</u>	37
<u>Suresh, Krish</u>	3	Z	
T		<u>Zachem, Tanner</u>	111
<u>Tagoe, Jonathan</u>	93	<u>Zhang, Ruisi</u>	1, 139
<u>Talas, Seref Kemal</u>	103	<u>Zhang, Tao</u>	41
<u>Taylor, Nichols Crawford</u>	59	<u>Zhao, Jianchang</u>	
<u>Taylor, Russell</u>	85, 123	<u>Zheng, Yi</u>	61
<u>Thompson, Alexander</u>	119	<u>Zhou, Haoyin</u>	1, 3
<u>Thompson, Stephen</u>	43	<u>Zou, Yuelin</u>	
<u>Torkaman, Tannaz</u>	65	<u>Zuo, Wanli</u>	11
<u>Tozun, Nurdan</u>	103		
<u>Treratanakulchai, Shen</u>	115		
<u>Tse, Zion Tsz Ho</u>	11		
<u>Tuijp, Jeroen J.</u>	23		
<u>Tutcu, Cem</u>	103		
U			
<u>Uneri, Ali</u>	15		
<u>Ungi, Tamas</u>	123		
V			
<u>Vafadar, Saman</u>	81		
<u>Valdastri, Pietro</u>	95		
<u>Van Lewen, Daniel</u>	91		
<u>Verde, Juan</u>	71		
<u>Vibert, Eric</u>	71		
<u>Vijayan, Rohan</u>	15		
<u>Vo-Dinh, Tuan</u>	145		
<u>Votta, Emiliano</u>	125		
<u>Voyles, Richard</u>	75		
W			
<u>Wachs, Juan</u>	75		
<u>Wang, Shuxin</u>	47		
<u>Wang, Tianlu</u>	45		
<u>Webster, Robert</u>	9, 19		
<u>Wiertlewski, Michaël</u>	23		
<u>Wurdemann, Helge</u>	31, 37, 51		

The Hamlyn Symposium on Medical Robotics

26 - 29th June 2023

Imperial College London and

the Royal Geographical Society, London

ISSN: 2755-0036

